Available online at www.sciencedirect.com
ScienceDirect
Progress in Solid State Chemistry 35 (2007) 1–159
Progress in Solid State Chemistry
www.elsevier.com/locate/pssc

# Size dependence of nanostructures: Impact of bond order deficiency

Chang Q. Sun [a,b,*]

[a] *School of Electrical and Electronic Engineering, Nanyang Technological University, Singapore 639798*
[b] *Institute of Advanced Materials Physics and Faculty of Science, Tianjin University, China 300072*

Received 9 January 2006; received in revised form 7 February 2006; accepted 6 March 2006

**Abstract**

This report deals with the mechanism behind the unusual behavior of nanostructures in mechanical strength, thermal stability, acoustics (lattice dynamics), photonics, electronics, magnetism, dielectrics, and chemical reactivity and its indication for designing and fabricating nanostructured materials with desired functions. A bond-order-length-strength (BOLS) correlation mechanism has been initiated and intensively verified, which has enabled the tunability of a variety of properties of a nanosolid to be universally reconciled to the effect of bond order deficiency of atoms at sites surrounding defects or near the surface edges of the nanosolid. The BOLS correlation indicates that atomic coordination imperfection causes the remaining bonds of the under-coordinated atom to contract spontaneously associated with bond strength gain and the intraatomic trapping potential well depression. Consequently, localized densification of charge, energy and mass occurs to the surface skin, which modify the atomic coherency (the product of bond number and the single bond energy), electroaffinity (separation between the vacuum level and the conduction band edge), work function, and the Hamiltonian of the nanosolid. Therefore, any detectable quantity can be functionalized depending on the atomic coherency, electroaffinity, work function, Hamiltonian or their combinations. For instances, the perturbed Hamiltonian determines the entire band structure such as the band-gap expansion, core-level shift, Stokes shift (electron-phonon interaction), and dielectric suppression (electron polarization); The modified atomic coherency dictates the thermodynamic process of the solid such as self-assembly growth, atomic vibration, phase transition, diffusitivity, sinterbility, chemical reactivity, and thermal stability. The joint effect of atomic coherency and energy density dictates the mechanical strength (surface stress, surface energy, Young's modulus), and compressibility

* School of Electrical and Electronic Engineering, Nanyang Technological University, Singapore 639798. Tel.: +65 6790 4517; fax: +65 6792 0415.
*E-mail address:* ecqsun@ntu.edu.sg
*URL*: http://www.ntu.edu.sg/home/ecqsun/

0079-6786/$ - see front matter 
doi:10.1016/j.progsolidstchem.2006.03.001

(extensibility, or ductility) of a nanosolid. Most strikingly, a combination of the new freedom of size and the original BOLS correlation has allowed us to gain quantitative information about the single energy levels of an isolated atom and the vibration frequency of an isolated dimer, and the bonding identities in the metallic monatomic chains and in the carbon nanotubes. A survey and analysis of the theoretical and experimental observations available to date demonstrated that the under-coordinated atoms in the surface skin of 2-3 atomic layers dictate the performance of nanostructures yet atoms of the interior remain as they are in the bulk counterpart. Further extension of the BOLS correlation and the associated approaches to atomic defects, impurities, liquid surfaces, junction interfaces, and amorphous states and to the temperature domain would be more challenging, fascinating, and rewarding.


*Keywords:* Nanostructures; Low-dimensional system; Surface and interface; Mesoscopic; Chemical bond; Coordination number; Bond contraction; Mechanical strength; Compressibility; Acoustics; Thermal stability; Optics; Dielectrics; Magnetism; Phase transition; Diffusivity; Reactivity; Crystal growth

**Contents**

**Nomenclature**

| | |
|---|---|
| $\omega$ | The angular frequency |
| $\mu$ | Atomic magnetic momentum |
| $\beta$ | Compressibility/extensibility |
| $\chi$ | Dielectric susceptibility |
| $\sigma$ | Surface stress/conductivity |

| | |
|---|---|
| $\Phi$ | Work function |
| $\varepsilon'_{\mathrm{r}}$ | Imaginary part of dielectric constant |
| $\varepsilon_0$ | Dielectric permittivity of vacuum |
| $\eta_1$ | Specific heat per coordinate |
| $\eta_2$ | Thermal energy per coordinate for evaporating a molten atom |
| $\mu_{\mathrm{B}}$ | Bohr magneton |
| $\gamma_{ij}$ | Atomic portion in the $i$th atomic shell over the entire solid of size $D_j$ |
| $\delta_{\mathrm{K}}$ | Kobo gap |
| $\varepsilon_{\mathrm{r}}$ | Real part of dielectric constant |
| BBB | Bond-band-barrier correlation |
| BOLS | Bond-order-length-strength correlation |
| CN($z$) | Coordination number |
| CNT | Carbon nanotube |
| $d_0$ | Atomic diameter or bond length |
| DFT | Density functional theory |
| $D_j$ | Diameter of $j$th spherical nanosolid |
| DOS | Density of state |
| $E_\nu$ | Core-level energy |
| $E_\nu(1)$ | Single energy level of a statically isolated atom |
| $E_{\mathrm{B}}$ | Atomic cohesive energy/vacancy formation energy |
| $E_{\mathrm{b}}$ | Cohesive energy per bond |
| $E_{\mathrm{G}}$ | Band gap |
| e–h | Electron–hole |
| e–p | Electron–phonon |
| GB | Grain boundary |
| HOPG | Highly oriented pyrolytic graphite |
| IHPR | Invere Hall–Petch relationship |
| $k_{\mathrm{B}}$ | Boltzmann constant |
| $K_j$ | Dimensionless form of the radius of a sphere or the thickness of a plate |
| MC | Monte Carlo |
| MD | Molecular dynamics |
| $M_{\mathrm{S}}$ | Saturation magnetization |
| PDF | Pair distribution function |
| $P$ | Stress |
| p-Si | Porous silicon |
| Q($K_j$) | Measurable quantity of a nanosolid |
| QC | Quantum confinement |
| $R$ | Radius/resistance |
| RCL | Resistance–capacitance–inductance |
| RT | Room temperature |
| SIMS | Secondary ion mass spectroscopy |
| SMAT | Surface mechanical attrition treatment |
| SPB | Surface potential barrier |
| STE | Self-trapping exciton |
| STM/S | Scanning tunneling microscopy/spectroscopy |

| | |
|---|---|
| $T_C$ | Critical/Curie temperature |
| TEM | Transition electronic spectroscopy |
| $T_m$ | Melting point |
| $W$ | Stokes shift |
| XAFS | X-ray absorption fine structure spectroscopy |
| XPS | X-ray photoelectron spectroscopy |
| XRD | X-ray diffraction |
| $Y$ | Young's modulus |

## 1. Introduction

### *1.1. Scope*

The contribution starts with Section 1 that presents a brief overview on the unusual behavior of a nanometer-sized solid. The intriguing phenomena are highlighted. Deeper and consistent insights into the mechanism behind the phenomena is the challenge of the current survey. Understanding the nature and factors dominating the general trends and limitations of the size-induced property change is of fundamental importance for advancing technological applications. Section 2 describes the bond-order-length (BOL) correlation premise of Pauling [1] and Goldschmidt [2] and its extension to the bond-order-length-strength (BOLS) correlation mechanism that correlates the bond strength to the spontaneous process of bond contraction of the under-coordinated atoms at sites surrounding a defect or in the surface skin. The effect of surface passivation with electronegative elements such as O, N, and C on the density of states (DOS) and surface potential barrier [3,4] is also briefly summarized. A general scaling relationship is introduced to describe the core-shell structure and the shape and size dependence of a nanosolid of various shapes. In Sections 3–10, efforts in both experimental observations and theoretical considerations are comparatively analyzed and quantified in terms of the BOL correlation and its consequences on bond strength, atomic cohesive energy (per discrete atom, or so-called atomic coherency), electroaffinity, and the density of energy and charge (per unit volume) in the region of surface skin. Section 11 summarizes the main contributions of this work with suggestions for future directions in extending the developed knowledge and the associated approaches. Further investigation of liquid surfaces, structural defects, substitution impurities, junction interfaces, and amorphous state, as well as transport dynamics would stimulate new discoveries in materials research.

### *1.2. Overview*

Nanosolids, or so-called nanoparticles, nanoclusters, nanocrystallites, nanograins, etc., are defined as substances or devices that are in the shape of spherical dot, rod, thin plate, or void of any irregular shape smaller than $10^2$ nm across or substances consisting of such voids or grains that are weakly linked one to another [5]. Substances of nanosolids can be composites, compounds, alloys, or elemental solids. From a fundamental point of view, nanostructures bridge the gap between an isolated atom and its bulk counterpart in its chemical and physical behavior. The key difference between a solid and its elementally isolated atom is the involvement of interatomic interaction. Without interatomic interaction, neither a solid nor even a liquid could form. The interatomic

interaction causes a solid to be completely different from an isolated atom in performance. Compared with its bulk counterpart, on the other hand, a nanosolid has a high portion of under-coordinated atoms in the surface skin. For a spherical dot of 1 μm across, the sum of the volumes containing all surface atoms is only 1% of the volume of the entire solid. For a 10 nm-sized dot, the surface-to-volume ratio is 25% and it reaches 100% when the solid is around 1 nm across, or consists of three atomic shells or less. Therefore, interatomic interaction and the changing fraction of the under-coordinated atoms should be the key factors dictating why the behavior of a nanosolid is different from that of an isolated atom or its bulk counterpart.

The discovery of nanosolids of various shapes and their assemblies has been quite surprising and has thus generated enormously ever-increasing interest for scientific insight and technological thrusts. Properties of solids determined by their shapes and sizes are indeed fascinating and form the basis of the emerging field of nanoscience and nanotechnology that has been recognized as the key area of significance in science, technology, and economics in the 21st century. Nanoscaled materials are offering a variety of novel features. New physical and chemical properties are expected to occur in such systems, arising from the large fraction of the under-coordinated atoms at the surface and from the confinement of electrons to a rather small volume, or surface skins according to the presently reported understanding.

The study of nanocrystalline materials is an active area of research in physics, chemistry, and materials engineering as well as biomedical engineering [6,7]. The striking significance of miniaturizing a solid to nanometer scale is the tunability of the measurable quantities of the solid in all aspects. In transport dynamics, quantized and resonant features due to size effect become apparent. In addition to the large surface-to-volume ratios, the surface, interface, and quantum effects take on a significance that is normally inconsequential for bulk materials. Varieties of physical properties such as mechanical strength, plasticity [8], sintering and alloying ability [9], diffusivity [10], chemical reactivity [11,12], as well as the mode of crystal growth (self-assembly) have been found to be dependent upon particle size. Property tunability also includes thermodynamics (critical temperatures for phase transitions such as liquidation, evaporation, and heat transport), lattice dynamics (optical and acoustic modes of lattice vibration), optics (photoemission and absorption) [13–15], electronics (work function, energy-level positions, electron–phonon coupling) [16,17], magnetic (magnetization tailoring or enhancement) and dielectric performance. Surfaces passivated by electronegative additives such as C, N, and O, also affect the performance of the nanosolids [18]. A recent review [19] suggests that not only size-dependent phase transition but also chemical interaction between the core of the nanoparticle and its surfactant molecules are responsible for the observed X-ray absorption fine structure (XAFS) spectral changes, which can be explained when constructing detailed models of core–surfactant interaction.

Materials composed of nanosolids possess unusual features, leading to new phenomena that are indeed surprising [20–22]. For instance, the structural and electronic properties are modified near and at the surface, resulting from a breaking of lattice symmetry or surface dangling bond formation, giving rise to site-specific surface anisotropy, weakened exchange coupling, and surface spin disorder [23]. Moreover, spin–spin coupling at the interface and interaction between the surface and the core magnetic structures can give rise to exchange anisotropy [24]. An individual defect-free silicon nanosphere with a diameter of 40 nm is measured to be four times harder than bulk silicon (12 GPa) at the ambient temperature [25]. The elastic modulus of ZnO nanowires was measured to increase when the wire diameter is reduced [26]. Single-walled carbon nanotubes (SWCNTs) with dispersed nanotube composite fibers [27] had a tensile strength of 1.8 GPa and an energy-to-break value of 570 J/g. The fibers are four times tougher than spider silk and 17 times tougher than the Kevlar fibers used in bulletproof vests. The fibers also have twice the stiffness and

strength and 20 times the toughness of the same weight of a steel wire. As artificial muscles, nanotube fibers are some 100 times the force of natural muscle with the same diameter [28]. The hardness of nanocrystalline (nc)/amorphous (a) composites such as nc-TiN/a-$Si_3N_4$, nc-TiN/a-$Si_3N_4$/nc-$TiSi_2$, nc-$(Ti_{1-x}Al_x)$N/a-$Si_3N_4$, nc-TiN/$TiB_2$, nc-TiN/BN, approaches that of diamond [29,30]. Generally, mechanical strength of a particle increases inversely with the square root of its size and then becomes soft at sizes around 10 nm, which is termed as the inverse Hall–Petch relationship [31]. While most coarse-grained ceramics are brittle, nanograined ceramics can exhibit significant ductility before failure. Such ductility is suggested to be primarily contributed by the grain-boundary phase, but in grains of certain ceramic phase, some plastic deformation has been found to occur and contribute to the overall plastic strain [32]. Ceramic blocks made of such nanometric grains can be moulded into engine parts or other useful shapes without shattering during the process, as do ceramics made from larger particles. The ductility of metallic nanowires such as Cu is $\sim$50 times higher than that of the bulk counterparts [8,33,34]. Pure copper samples with a high density of nanoscale grains show a tensile strength about 10 times higher than that of conventional coarse-grained copper, while retaining an electrical conductivity comparable to that of pure bulk copper [35]. Super plasticity (280% strain) of SWCNTs has been observed at elevated temperature [36]. If platinum is formed containing a continuum network of nanometer-sized pores, the porous Pt can generate reversible strain with amplitudes comparable to those of commercial materials through surface-charging effects under potentials of about 1 V [37]. The conversion of an external electrical signal into a volume change, and hence mechanical force, known as actuation, is of considerable importance in the development of small-scale devices. The sinterability of a zeolite crystal increases at the ambient temperature as the solid size is reduced. On heating nanocrystallites of 40–80 nm at 80 °C, solution-mediated mass transport results in additional substantial crystal growth that occurs at $10^{2-3}$ °C for large bulk [9]. A CNT is much stiffer than the bulk graphite [38,39], while a SWCNT melts at $\sim$1600 K [40], being 0.42 times the melting point ($T_m(\infty) = 3800$ K) of bulk graphite. A CdS nanodot of $\sim$2.5 nm across melts at 600 K [13]; this is much lower than the bulk value of 1675 K. The size-induced $T_m$ suppression is quite common to nanosolids [15,41].

Grains of semiconductors of a few nanometers across emit blue-shifted light than do slightly larger chunks of the same material [42,43]. The band gap ($E_G$) of CdSe can be tuned from deep red (1.7 eV) to green (2.4 eV) by simply reducing the solid diameter from 20 to 2 nm [44]. The $E_G$ [45,46] and the core-level shift ($\Delta E_\nu$) [47] of nanosemiconductors increase whereas the dielectric susceptibility ($\chi$) decreases when the solid size is reduced. Without triggering the electron–phonon (e–p) interaction or electron-hole (e–h) production, scanning tunneling spectroscopy/microscopy (STS/M) measurement revealed that at 4 K the $E_G$ expands from 1.1 to 3.5 eV when the diameter of Si nanorod reduces from 7.0 to 1.3 nm associated with some 10% of Si–Si surface bond contraction [48].

Magnetic nanocomposites also manifest enhanced or tailored magnetic properties under various conditions [49]. At low temperatures, the saturation magnetization ($M_S$) of a small solid is higher than that of the bulk with oscillation features when the solid size is reduced; however, at the ambient temperatures, an opposite trend dominates. Nitriding occurs at a much lower temperature (300 °C for 9 h) for a Fe surface covered with nanoparticles compared with that for a smooth Fe surface where nitriding may occur at 500 °C or higher when the Fe is held for more than 48 h under an atmospheric pressure of ammonia [50]. The diffusivity of Ag into Au nanoparticles at the ambient temperature is much higher when the particle size is reduced [51]. Decreasing the particle size of tin oxide particles in the range of 10–35 nm leads to an increase of the sensitivity to gas conditions [52].

As found by Hu et al. [53], nanometer-sized (27 nm) $SrTiO_3$ obtained by high-energy ball milling could lower substantially the temperature for sensor operation from 970 to 310 K, close to the temperature of the human body. The grain size and the electric conductivity of the $SrTiO_3$ nanosolid increase with the annealing temperature [54]. Size-enhanced gas sensitivity of $SnO_2$ nanoparticles [52] and size-enhanced ionicity of $Cu_2O$ nanoparticles have also been observed [55]. Introducing ferroelectric materials of different sizes into a photonic crystal could modulate its refractive index and hence the photonic band gap, $E_G$, which is sensitive not only to the external stimuli such as temperature or electric field, but also to the particle sizes. Zhou et al. [56,57] filled up the colloid crystal matrix of silicon-dioxide with barium titanate ($BaTiO_3$) and lead lanthanum zirconate titanate and found that, near the ferroelectric phase-transition point of $BaTiO_3$ (100–150 °C), the photonic $E_G$ of the resulting assembly exhibits strong temperature dependence. At the Curie point ($T_C$), a 20-nm red shift of the $E_G$ has been detected. The photonic $E_G$ gradually shifts to longer wavelength with the increase of the applied electric field, suggesting that the refractive index increases with the applied voltage. The photonic $E_G$ tunability could be used not only for simple on–off switching, but also in devices requiring more localized control of light propagation. Lu [58] has demonstrated in his review that the thermal expansion coefficient, resistivity, and specific heat of metallic nanosolids, or alloys, increase with the inverse of solid size whereas the temperature coefficient of resistivity and the critical temperature for magnetic transition drop with the inverse of solid size. Indeed, the new freedom of size has led to dramatic change of many physical and chemical properties that are conventionally unchangeable for a bulk specimen. The examples of the effect of size on various properties are endless, as reviewed by many researchers [59–68].

The size-induced property change of nanostructures has inspired numerous theoretical models, all discussed from various perspectives. For instance, the following models describe the size-induced blue shift in photoluminescence (PL) of semiconductor nanosolids.

(i) *Quantum confinement* theory [69–72] suggests that the Coulomb potential and kinetic energies of electron–hole pairs (usually called excitons) are responsible for the PL blueshift of nanometric semiconductor; the PL blueshift is dictated by joint effect of the intrinsic band gap expansion and electron-phonon coupling.
(ii) *The free-exciton collision* model [73] proposes that, during the PL measurement, the excitation laser heats the free-excitons which then collide with the boundaries of the nanometer-sized fragments. The PL blueshift is suggested to originate from the activation of hot-phonon-assisted electronic transitions rather than from the effect of quantum confinement.
(iii) *The impurity luminescent center* model [74] assumes that different impurity centers in the solid take responsibility for the PL blueshift. The density and types of impurity centers vary with particle size.
(iv) *Surface states and surface alloying* mechanisms [75] consider that the extent of surface catalytic reaction and measurement temperature determine the PL blueshift and the passivation effect varies with the processing parameters and aging conditions [76].
(v) *An intercluster interaction and oxidation* [77] argument is also proposed to explain the dominance of the PL blueshift.

Another significant phenomenon is the size dependence of thermal stability. The critical temperature for melting ($T_m$) of an isolated nanosolid, or a system with weakly linked nanoparticles, drops with solid size (called undercooling), while the $T_m$ may rise (called overheating) for an embedded nanometric system due to the interfacial effect. The $T_m$ was characterized by either the

Lindermann's criterion [78] of abruption of atomic vibration or Born's criterion [79] of disappearance of the shear modulus at melting. The modes for nanosolid melting are of typical form as for the models of (i) homogeneous melting and growth [80,81], (ii) liquid shell nucleation [82–85], (iii) liquid nucleation and growth [82,86,87], and (vi) random fluctuation melting [88]. The origins for nanosolid melting are ascribed as (i) lattice-vibrational instability [41,89–93], (ii) liquid-drop formation [94], and (iii) the surface-phonon instability [95–97].

### *1.3. Challenge*

An overwhelming contribution has been made to the development of nanotechnology by the advent of methods such as atomic imaging and manipulating, nanosolid synthesizing, functioning, and characterizing as well as structural patterning for device fabrication. However, insight into the mechanism behind and factors dominating the general trend of the tunability remains in its infancy. It is quite often that a single phenomenon corresponds to numerous models yet a comprehensive model reconciling all observations is a high challenge.

Predictable design and controllable growth of nanostructured materials or devices are of foremost importance to scientific and technological communities. One needs not only to understand the performance, but also to know the origin, the trend, and the limitation of the change and the interdependence of various properties in order to predict and control the process for fabricating materials and devices.

Furthermore, structural miniaturization provides us with an additional freedom that not only allows us to tune the properties of a solid by changing its shape and size, but also, challenges us to gain quantitative information by making use of the new freedom of size, which is beyond traditional approaches. A combination of the new freedom of size with the freedoms of temperature and pressure, etc. would vastly amplify the space of exploration in condensed matter physics and chemistry.

### *1.4. Objectives*

In earlier experimental work reported in Ref. [3], the practitioner uncovered the reality of surface bond contraction in decoding the very-low-energy electron diffraction (VLEED, in the energy range of 6.0–16.0 eV) data from O–Cu(001) surface reaction kinetics. This finding coincides surprisingly well with the atomic-coordination–atomic-size correlation notations of Pauling [1] and Goldschmidt [2] (see Appendix A). It was proposed [1,2] that the atomic CN reduction could cause shrinkage of atomic size, or the contraction of the remaining bonds. The coincidence of VLEED measurement with BOL correlation stimulated the currently reported effort in surveying and analyzing the size and confinement effects on the performance of nanostructures. Apparently, only atomic CN imperfection occurs at sites surrounding defects (point defects, voids, dislocations, etc.), at the flat surface skin of a bulk material, at the curved surface of a small solid, or in amorphous state consisting of atoms with CN imperfection distributed randomly. Therefore, it is reasonable to apply the BOLS correlation to such cases.

The main objective of this contribution is to present a survey and consistent analysis on the advancement of both modeling considerations and experimental observations on the size dependence of nansolid materials. We will show that all modeling considerations are valid from different perspectives and the models and measurements can be consistently understood in terms of the BOLS correlation. We also suggest that the BOLS correlation could be applied to liquid

surfaces, structural defects, substitution impurities, junction interfaces, and transport dynamics, which could stimulate new topics and exciting findings in future investigations.

For simplicity, the report will use the dimensionless form to express the relative change (%) of a detectable quantity and the dimensionless form of size $K_j$ (being the number of atoms lined along the radius of a sphere or across the thin film) unless indicated otherwise. The dimensionless approach also allows the generality of the formulation and minimizes the contribution from impurities and errors in measurement. An attempt will be made to minimize and simplify numerical expressions and focus more on physical understanding.

## 2. Principles: atomic CN imperfection

### 2.1. Bond relaxation

#### 2.1.1. Effects of lattice periodicity termination

*2.1.1.1. Barrier confinement—quantum uncertainty.* The termination of the lattice periodicity in the surface normal direction, or at a grain boundary, has two effects. One is the creation of the surface potential barrier (SPB, called work function or contact potential) and the other is the reduction of the atomic CN. The CN of an atom in a highly curved surface is lower compared with the CN of an atom at a flat surface. For a negatively curved surface (such as the inner side of a pore or a bubble), the CN may be slightly higher. Therefore, from the atomic CN imperfection point of view, there is no substantial difference in nature between a nanosolid, a nanovoid and a flat surface. This premise can be extended to the structural defects or faults such as voids surrounding with atoms experiencing CN loss.

The work function is expressed as $\Phi = E_0 - E_F(\rho(E)^{2/3})$ [98], which is the energy separation between the vacuum level, $E_0$, and Fermi energy, $E_F$. The value of $\Phi$ depends on the charge density ($\rho(E)$) in the surface region and varies with energy around which the DOS is centered. The charge density varies with the valence states of the surface atoms. If dipoles form at the surface through reaction with electronegative elements such as nitrogen or oxygen, the $\Phi$ of a metal surface can be reduced (by some 1.2 eV) [99]. However, if a hydrogen bond like forms with more addition of the adsorbate at the surface, the $\Phi$ will restore to the original value or even higher because the metal dipoles donate the polarized electrons to the additional electronegative additives to form a '+/dipole' at the surface [3]. The shape and the saturation degree of the SPB depend on the surface atomic-valence states [100] but the height of the SPB approaches the muffin-tin inner-potential-constant of atoms inside the solid, $V_0$ [101]. The real (elastic) and imaginary (inelastic) parts of the SPB take the following forms [101,102,103]:

$$\mathrm{Re}\,V(z) = \begin{cases} \dfrac{-V_0}{1 + A\exp[-B(z - z_0)]}, & z \geq z_0 \text{ (a pseudo-Fermi-}z\text{ function)} \\ \dfrac{1 - \exp[\lambda(z - z_0)]}{4(z - z_0)}, & z < z_0 \text{ (the classical image potential)} \end{cases}$$

$$\mathrm{Im}V(z,E) = \mathrm{Im}[V(z) \times V(E)] = \gamma \times \rho(z) \times \exp\left[\frac{E - \phi(E)}{\delta}\right] = \frac{\gamma \times \exp\left[\dfrac{E - \phi(E)}{\delta}\right]}{1 + \exp\left[-\dfrac{z - z_1}{\alpha}\right]} \quad (1)$$

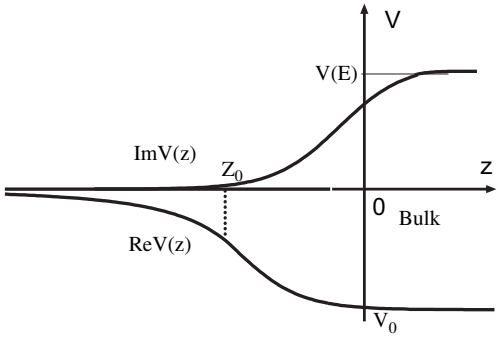


Fig. 1. One-dimensional SPB model showing that the real and imaginary parts are functions of the distance $z$ from the surface. The $z$-axis is directed into the crystal and $z_0$ is the origin of the image plane [101–103].

where $A$, $B$, $\gamma$, and $\delta$ are constants, $\alpha$ and $\lambda$ describe the degree of saturation, $z_0$ is the origin of the image plane inside which electron is located, $\phi(E)$, the energy-dependent local $\Phi(E)$ depends on the density of states $\rho(E)$. The $\nabla^2[\mathrm{Re}\ V(z)] = -\rho(z) \propto \mathrm{Im}\ V(z)$ describes the spatial distribution of charges (Fig. 1).

The intrinsic SPB confines only electrons that are freely moving inside the solid. However, the SPB has nothing to do with the *strongly localized* electrons in deeper bands or with those that form sharing electron pairs in a bond. According to the principle of quantum uncertainty, reducing the dimension ($D$) of the space inside which energetic particles are moving increases the fluctuation, rather than the average value, of the momentum, $p$, or kinetic energy, $E_k$, of the moving particles

$$\begin{aligned} &\Delta p \propto \hbar/D; \quad p = \overline{p} \pm \Delta p \\ &E_k = \overline{p}^2/(2m) \end{aligned} \tag{2}$$

where $\hbar$, being the Plank constant divided by $2\pi$, corresponds to the minimal quanta in energy and momentum spaces and $m$ is the mass of the moving particle. Therefore, SPB confinement causes energy rise of neither the freely moving carriers nor the localized ones. Hence, the kinetic energies of carriers or e–h pairs change little with solid dimension according to the principle of quantum uncertainty.

*2.1.1.2. Atomic CN imperfection.* Fig. 2 illustrates situations of atomic CN imperfection. The CN of an atom in the interior of a monatomic chain and an atom at the open end of a SWCNT is 2; while in the CNT wall, the CN is 3. For an atom in the fcc unit cell, the CN varies from site to site. The CN of an atom at the edge or corner differs from the CN of an atom in the plane or inside the unit cell. Atoms with deformed bond lengths or deviated angles in the CNT are the same as those in amorphous states. The CN imperfection is not limited to the number loss, which should cover situations of bond angle distortion. The CN imperfection is referred to the standard value of 12 in the bulk without distortion irrespective of the bond nature or the crystal structure. For example, the CN of an atom in diamond tetrahedron is the same as that in an fcc structure as a tetrahedron unit cell is an interlock of two fcc unit cells.

### *2.1.2. BOLS correlation and its consequences*

*2.1.2.1. Bond order–length correlation.* Pauling [1] and Goldschmidt [2] indicated that, if the CN of an atom is reduced, the ionic and the metallic radius of the atom would shrink

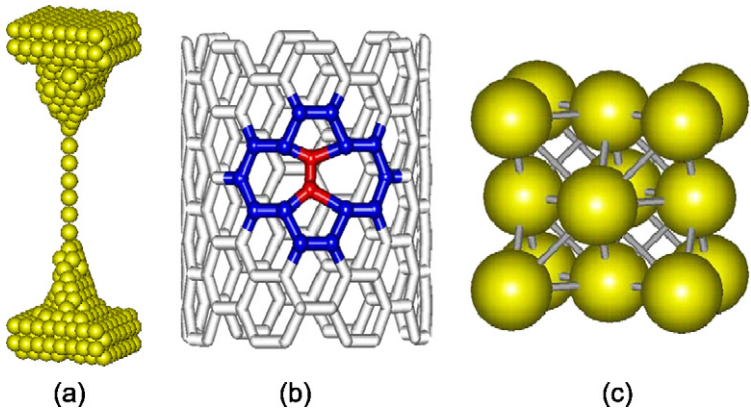


Fig. 2. Atomic CN of (a) monatomic chain ($z = 2$); (b) single-walled CNT ($z = 2$, 3); and (c) an fcc unit cell ($z$ varies from site to site).

spontaneously. Therefore, the CN imperfection will shorten the remaining bonds of the under-coordinated atom, which is independent of the nature of the specific chemical bond [104] or the structural phase, even a liquid [105,106]. For example, 10% contraction of spacing between the first and the second atomic surface layers has been detected in the liquid phase of Sn, Hg, Ga, and In [105]. Evidence of phase changes occurring at the surface of droplets but not in the bulk for *n*-alkane emulsions suggests that the phase changes result from the formation of a monolayer thick solid solution of the oil phase [106]. A substitutional As dopant impurity has induced 8% bond contraction around the impurity (acceptor dopant As) at the Te sublattice in CdTe, as observed using EXAFS (extended X-ray absorption fine structure) and XANES (X-ray absorption near edge spectroscopy) [107]. The finding of dopant-induced bond contraction could provide an atomic scale understanding of the bond in a junction interface that has been a puzzle for decades. Interestingly, recent theoretical calculations, confirmed by electron microscopy measurement [108], revealed that homo-junction dislocations in aluminum have either compact or dissociated core interlayers. The calculated minimum stress ($\sigma_P$) required for moving an edge dislocation is approximately 20 times higher for the compact dislocations than for the equivalent dissociated dislocations. The dopant-induced bond contraction may provide insights into the deformation of ultra-fine-grained metals and the twin grain boundaries as well. The finding of liquid surface bond contraction could serve as the origin of surface strain and stress, which provide understanding of the driving force for liquid-drop formation. Therefore, the bond-order loss induced bond contraction can be applied to a liquid surface and junction interface as well.

Fig. 3a shows the CN dependence of the bond-contraction coefficient, $c_i(z_i)$. The solid curve formulates the Goldschmidt premise indicating that an ionic radius contracts by 12%, 4%, and 3% if the CN of the atom reduces from 12 to 4, 6 and 8, respectively. Feibelman [109] has noted a 30% contraction of the dimer bond of Ti and Zr, and a 40% contraction of the dimer bond of vanadium, which is also in line with the formulation. The premise of Goldschmidt–Pauling–Feibelman bond contraction and the associated bond-strength gain from the subject of the BOLS correlation mechanism that can be expressed as:

$$\begin{cases} c_i(z_i) & = d_i/d_0 = 2/\{1+\exp[(12-z_i)/(8z_i)]\} & \text{(BOLS-coefficient)} \\ E_i & = c_i^{-m}E_b & \text{(Single-bond-energy)} \\ E_{B,i} & = z_iE_i & \text{(Atomic-coherency)} \end{cases} \quad (3)$$

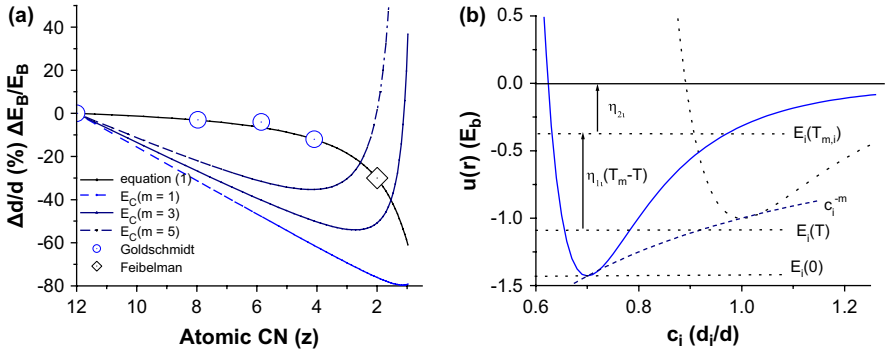


Fig. 3. Illustration of the BOLS correlation. Solid curve in (a) is the contraction coefficient $c_i$ derived from the notations of Goldschmidt [2] (open circles) and Feibelman [109] (open square). As a spontaneous process of bond contraction, the bond energy at equilibrium atomic separation will rise in absolute energy, $E_i = c_i^{-m}E_b$. The $m$ is a parameter that represents the nature of the bond. However, the atomic cohesive energy, $z_iE_i$, changes with both the $m$ and $z_i$ values. (b) Atomic CN imperfection modified pairing potential energy. CN imperfection causes the bond to contract from one unit (in $d_0$) to $c_i$ and the cohesive energy per coordinate increases from one unit to $c_i^{-m}$ unit. Separation between $E_i(T)$ and $E_i(0)$ is the thermal vibration energy. Separation between $E_i(T_{m,i})$ and $E_i(T)$ corresponds to melting energy per bond at $T$, which dominates the mechanical strength. $T_{m,i}$ is the melting point. The energy required to break the bond at $T$ is $\eta_{1i}\,(T_{m,i} - T) + \eta_{2i}$.

Subscript $i$ denotes an atom in the $i$th atomic layer, which may be counted up to three from the outermost atomic layer to the center of the solid as no CN reduction is expected for $i > 3$. The index $m$ is a key parameter that represents the nature of the bond. For Au, Ag, and Ni metals, $m \equiv 1$; for alloys and compounds $m$ is around four; for C and Si, the $m$ value has been optimized to be 2.56 [110] and 4.88 [47], respectively. The $m$ value may vary if the bond nature evolves with atomic CN [111]. If the surface bonds expand in certain cases, we simply expand the $c_i$ from a value that is smaller than unity to greater, and the $m$ from positive to negative to represent the spontaneous process for which system energy is minimized. The $c_i(z_i)$ should be anisotropic and depend on the effective CN rather than a certain order of CN. The $z_i$ also varies with the particle size due to the change of the surface curvature. Experience reveals that the $z_i$ takes the following values [47]:

$$z_1 = \begin{cases} 4\left(1 - 0.75/K_j\right) & \text{curved-surface} \\ 4 & \text{flat-surface} \end{cases} \tag{4}$$

Generally, $z_2 = 6$ and $z_3 = 8$ or 12 would be sufficient. The BOLS correlation illustrated in Fig. 3 has nothing to do with the particular form of the pairing potential as the approach involves only atomic distance at equilibrium.

From a study of interatomic distances of the C–C bonds in organic chemistry, Pauling derived the relation [1]:

$$r(1) - r(v/z_0) = 0.030\log(v/z_0) \quad (\text{nm}) \tag{5}$$

where $r(1)$ is the radius of a single atom or the length of a dimer bond. The $r(v/z)$ is the radius of an $s$-fold bond and $s = v/z$, where $v$ is the number of valency bonds and $z_0$ is the number of the equivalent coordinate. As an illustration of the use of this relation, the radius of Ti has been computed as an hcp from the data of Ti as bcc. As a bcc, the radius of Ti is 0.1442 nm, and there are eight bonds of this length. The next closest bonds are six situated 0.1667 nm from any given Ti atom. These

values are calculated from the known lattice parameter of 0.333 nm. The valence, $v$, of Ti is four. The problem is to determine what fraction of these bonds is associated with the eight near neighbors and with the six others removed from these. From Eq. (5)

$$r(1) - r(x/8) = 0.030 \log(x/8) \tag{6}$$

and, for the next-nearest neighbors,

$$r(1) - r[(4-x)/6] = 0.030 \log[(4-x)/6] \tag{7}$$

where $x$ is the number of bonds associated with the eight near neighbors and $(4-x)$ the number associated with the other six bonds. Subtracting Eq. (6) from Eq. (7) and using the value (0.1667−0.1442) obtained from the lattice parameter, one can find that $x = 3.75$ and the dimer bond length $r(1) = 0.13435$ nm, which contracts by 0.00985 nm. For a CN = 12 in the hcp structure, the bond number $v/z$ is 4/12, and the corresponding bond length is $r(4/12) = 0.13435 - 0.03\log(4/12) = 0.1486$ nm. From Eq. (5), one can also deduce the bond length of an atom with a reduced CN($z_i$):

$$r(v/z_i) = r(v/z_0) + 0.030 \log(z_i/z_0) \tag{8}$$

Appendix A combines Goldschmidt and Paulings' notations of electronegativity ($\eta$), metallic (ionic) valencies, and metallic (ionic) radii of the elements. Pauling's theory introduced here contains numerous assumptions and it is somewhat empirical in nature. Compared to the formulation (3), Pauling's notation is $d_0$ dependent and somewhat complicated, which gives:

$$c_i = 1 + 0.06 \log(z_i/z_0)/d_0(v/z_0) \tag{9}$$

However, this notation does give some surprisingly good answers in certain cases, as commented by Sinnott [104]. Both Eqs. (3) and (9) should be valid but here we prefer relation (3), as it covers Feibelmen's notation and it is element ($d_0$) independent.

*2.1.2.2. Bond length–strength correlation.* Fig. 3b illustrates schematically the BOLS correlation using the pairing atomic potential, $u(r)$. When the CN of an atom is reduced, the equilibrium atomic distance will contract from one unit (in $d_0$) to $c_i$ and the cohesive energy of the shortened bond will increase in magnitude from one unit (in $E_b$) to $c_i^{-m}$. The solid and the broken $u(r)$ curves correspond to the potentials of the pairing atoms with and without CN imperfection. The $u(r)$ curve slides towards shorter atomic distance along the $c_i^{-m}$ line. The bond length–strength correlation herein is consistent with the trend reported in Ref. [112] though the extents of bond contraction and energy enhancement therein vary from situation to situation.

There are several characteristic energies in Fig. 3b, which correspond to the following facts:

(i) $T_{m,i}$ being the local melting point is proportional to the atomic cohesive energy, $z_iE_i(0)$ [113], per atom with $z_i$ coordinate [114].
(ii) The separation between $E = 0$ and $E_i(T_m)$, or $\eta_{2i}$, is $1/z_i$ fold energy that is required for atomization of an atom in molten state.
(iii) Separation between $E = 0$ and $E_i(T)$, or $\eta_{1i}(T_{m,i} - T) + \eta_{2i}$, corresponds to the cohesive energy per coordinate, $E_i$, at $T$, being required for the bond fracture under mechanical or thermal stimulus. $\eta_{1i}$ is the specific heat per coordinate.

Table 1
Relation between the bond energy and the $T_m$ of various structures

| | fcc | bcc | Diamond structure |
|---|---|---|---|
| $\eta_{1b}$ ($10^{-4}$ eV/K) | 5.542 | 5.919 | 5.736 |
| $\eta_{2b}$ (eV) | −0.24 | 0.0364 | 1.29 |

$E_b = \eta_{1b} T_m + \eta_{2b}$ [94], see Fig. 4. The value of $\eta_{2b} < 0$ for an fcc structure means that the energy required for breaking all the bonds of an atom in molten state is included in the term $\eta_{1b} z T_m$ and therefore the $\eta_{2b}$ deviates from the true specific heat per CN. The $\eta_{2b}$ should also be a linear function of the $T_m$.

(iv) The spacing between $E_i(T)$ and $E_i(0)$ is the thermal vibration energy.
(v) The energy contributing to the mechanical strength is the separation between the $E_i(T_m)$ and the $E_i(T)$, or $\eta_{1i}(T_{m,i} - T)$, as a molten phase is extremely soft and highly compressible.

Values of $\eta_{1i}$ and $\eta_{2i}$ can be determined with the known $c_i^{-m}$ and the bulk $\eta_{1b}$ and $\eta_{2b}$ values that have been determined for various crystal structures as given in Table 1 (Fig. 4).

*2.1.2.3. Potential well of trapping.* As the relaxation (either contraction or expansion) is a spontaneous process, the binding energy of the relaxed bond will be lowered (rise in magnitude) to stabilize the system. The relaxed bond will be stronger. Bond expansion might happen but the process must proceed towards lowering the system energy, unless the relaxation is realized under external stimulus such as heating, pressing or stretching.

Fig. 5 illustrates the potential well of a nanosolid because of the BOLS correlation. Compared with the QC convention that extends the mono-center trapping potential well of an isolated atom by rescaling the size, the BOLS potential well covers contributions from the

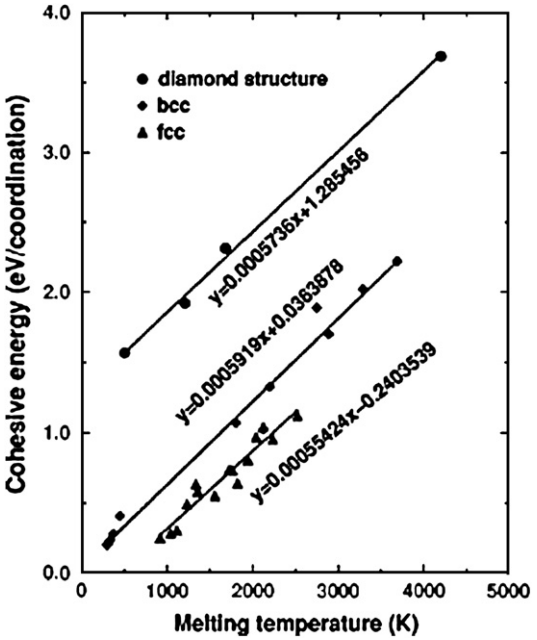


Fig. 4. Correlation between the cohesive energy per coordinate and the $T_m$ of different elements and crystal structures [94]. The data for cohesive energy per atom are taken from Refs. [115,116].

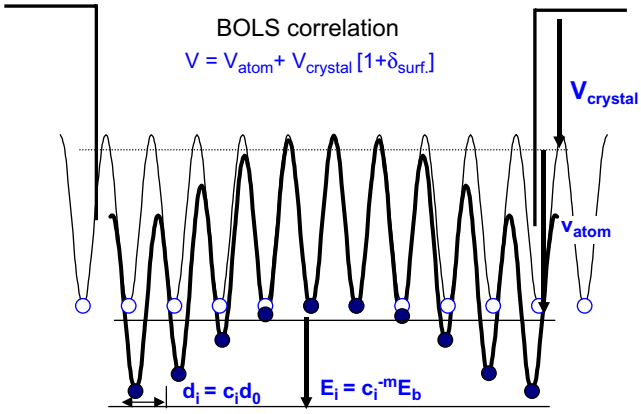


Fig. 5. Schematic illustration of the BOLS derived nanosolid potential with multi-trap centers and CN imperfection induced features. In the relaxed surface region, the density of charge, energy and mass will be higher than at the other sites due to atomic CN imperfection [122]. However, atomic cohesive energy for the under-coordinated atoms will be lowered, whereas the core interior remains as it is in the bulk counterpart.

individual atoms with multi-center trapping potential wells and the effect of atomic CN imperfection in the surface region. Atomic CN imperfection induced bond contraction and the associated bond-strength gain deepens the potential well of trapping in the surface skin. Therefore, the density of charge, energy, and mass in the relaxed surface skin are higher than those at other sites inside the solid. The charge localization and energy densification have been observed using STM/S at the end of gold atomic chains on a Si substrate [117]. Because of energy densification, surface stress that is in the dimension of energy density will increase in the relaxed region. Electrons in the relaxed region are more localized because of the depressed potential well of trapping, which lowers the work function and conductivity in the surface region due to boundary scattering [118,119], but enhances the angular momentum of the surface atoms [120]. The densification of mass, charge and energy in the surface skin should have an important impact on the surface science and the thermal and electrical transport dynamics [121].

*2.1.2.4. Atomic coherency and electron affinity.* Because of bond-order loss, the cohesive energy or atomic coherency (being the sum of single bond energy over all the coordinates of a specific atom) of an under-coordinated atom will drop. On the other hand, electron affinity, or the separation between the vacuum energy level and the bottom of conduction band will increase because of the energy level shift caused by the enhanced energy density [123]. Atomic coherency determines structural stability and the electron affinity represents the ability to catch electrons from other atoms. Therefore, the increased affinity will enhance the chemical reactivity or ionicity of a nanosized specimen.

## *2.2. Surface passivation*

Besides the effect of atomic CN imperfection induced bond relaxation, surface passivation by adsorbing electronegative elements also contributes to the behavior of a nanosolid. The chemical-bond–valence-band–potential-barrier (BBB) correlation mechanism [3,4] indicates that it is necessary for an atom of oxygen, nitrogen, and carbon to hybridize its sp orbitals upon interacting with atoms in the solid phase. Because of tetrahedron formation, nonbonding

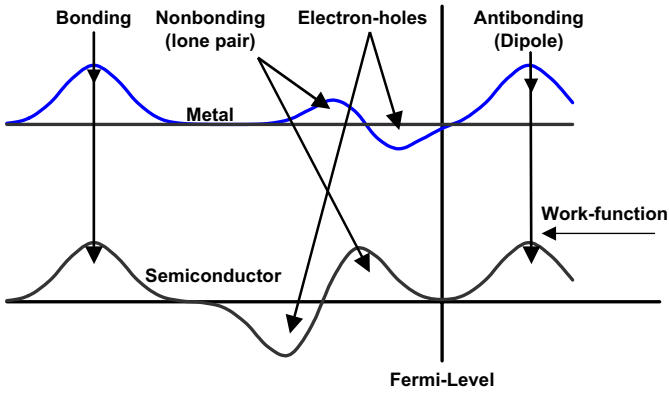


Fig. 6. N and O induced DOS differences between a compound and the parent metal (upper) or the parent semiconductor (lower). The lone-pair polarized antibonding state lowers the $\Phi$ and the formation of bonding and antibonding generates holes close to $E_F$ of a metal or near the valence band edge of a semiconductor. For carbide, no lone-pair features appear but the ion induced antibonding states will remain [4].

lone pairs, antibonding dipoles and hydrogen-like bonds are produced, which add corresponding features to the density of states (DOS) of the valence band of the host, as illustrated in Fig. 6 [124]. Bond forming also alters the sizes and valences of the involved atoms and causes a collective dislocation of these atoms. Alteration of atomic valences roughens the surface, giving rise to corrugations of surface morphology. Charge transportation not only alters the nature of the chemical bond but also produces holes below the $E_F$ and thus creates an $E_G$ for metals or enlarges the existing $E_G$ of semiconductors [125]. In reality, the lone-pair-induced metal dipoles are often directed into the open end of a surface due to the strong repulsive forces among the lone pairs and among the dipoles as well. The outward orientation of dipoles leads to the surface dipole layer that lowers the $\Phi$ with localized feature. For a nitride tetrahedron, the single lone pair may be directed into the bulk center, which produces the ionic layer at the surface. The ionic surface network deepens the well depth, or increases the value of $\Phi$, as the host surface atoms donate their electrons to the acceptors. For carbides, no lone pair is produced but the weak antibonding feature exists due to the ion-induced polarization. However, hydrogen adsorption neither adds DOS features to the valence band nor expands the $E_G$ as hydrogen adsorption terminates the dangling bond at a surface, which minimizes the midgap impurity DOS in the case of silicon [126]. An addition of light elements such as S and F is expected to produce dipoles but this anticipation is subject to confirmation. Although the effect of hydroxyl termination of the surface is not so clear, the HO may modify the electronic structure at the surface but it could be less significant than the effect of bond contraction or C, N, and O addition.

## 2.3. Shape and size dependence

### 2.3.1. Surface-to-volume ratio

It is easy to derive the volume or number ratio of a certain atomic layer, denoted $i$, to that of the entire solid as:

$$\gamma_{ij} = \frac{N_i}{N_j} = \frac{V_i}{V_j} \cong \frac{\tau c_i}{K_j} \tag{10}$$

where $K_j = R_j/d_0$ is the dimensionless form of size, which is the number of atoms lined along the radius of a spherical dot, a rod, or across the thickness of a thin plate. $\tau$ is the dimensionality of a thin plate ($\tau = 1$, and monatomic chain as well), a rod ($\tau = 2$) and a spherical dot ($\tau = 3$) of any size. For a hollow system, we have to introduce a size $L_j$ that is the number of atomic layers being not occupied by atoms in a hollow structure. For a solid system, $L_j = 0$; while for a hollow sphere or a hollow tube, $L_j < K_j$. For a hollow system, the sum of $\gamma_{ij}$ should count both external and internal sides of the hollow system. With reduced particle size, the performance of surface atoms will dominate because at the smallest size ($K_j \to 3$) $\gamma_1$ approaches unity. At $K_j = 1$, the solid will degenerate into an isolated atom. The definition of dimensionality herein differs from conventional excercises in transport considerations in which a nanosphere is defined as zero dimension (quantum dot), a rod as one dimension (quantum wire), and a plate as two dimensions (quantum well). Fig. 7 illustrates the derivation of the surface-to-volume ratio. As the $K_j$ is an integer, the property change will show quantized oscillation features at small particle sizes, which varies from structure to structure, as illustrated in Fig. 7c.

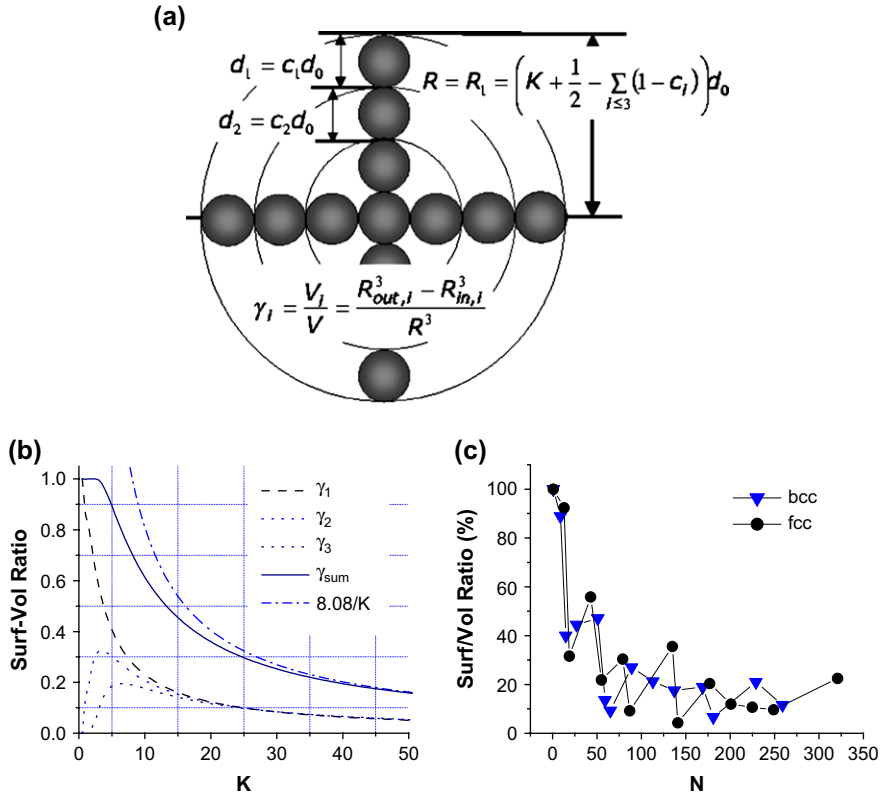


Fig. 7. Illustration of (a) the surface-to-volume ratio ($\gamma_{ij}$) of a nanosolid with involvement of CN imperfection-induced bond contraction. (b) The $\gamma_{ij}$ drops from unity to infinitely small when the solid grows from atomic scale, $K_j = 1$, to infinitely large, $K_j = \infty$. At the lower end of the size limit, the solid degenerates into an isolated atom. (c) The number ratio shows oscillatory features for fcc and bcc small solids.

*2.3.2. Scaling law*

Generally, the mean relative change of a measurable quantity of a nanosolid containing $N_j$ atoms, with dimension $K_j$, can be expressed as $Q(K_j)$, and as $Q(\infty)$ for the same solid without the effect of CN imperfection contribution. The $Q(K_j)$ relates to $Q(\infty) = N_j q_0$ as follows:

$$Q(K_j) = N_j q_0 - \sum_{i\le 3} N_j q_0 + \sum_{i\le 3} N_i q_i = N_j q_0 + \sum_{i\le 3} N_i (q_i - q_0) \tag{11}$$

The $q_0$ and $q_i$ correspond to the local density of $Q$ inside the bulk and in the region of the $i$th atomic layer, respectively. Eq. (11) leads to the immediate relation:

$$\frac{\Delta Q(K_j)}{Q(\infty)} = \sum_{i\le 3} \gamma_{ij} (\Delta q_i / q_0) = \Delta_{qj} \tag{12}$$

The weighting factor, $\gamma_{ij}$, represents the geometrical contributions from dimension ($K_j$, $L_j$) and dimensionality ($\tau$) of the solid, which determines the magnitude of change. The quantity $\Delta q_i/q_0$ in the surface skin is the origin of change. The $\sum_{i\le 3} \gamma_{ij}$ drops in a $K_j^{-1}$ fashion from unity to infinitely small when the solid dimension grows from atomic level to infinitely large. For a spherical dot at the lower end of the size limit, $K_j = 1.5$ ($K_j d_0 = 0.43$ nm for an Au spherical dot example), $\gamma_{1j} = 1$, $\gamma_{2j} = \gamma_{3j} = 0$, and $z_1 = 2$, which is identical in situation to an atom in a monatomic chain despite the bond orientation. Actually, the bond orientation is not involved in the BOLS modeling iteration. Therefore, the performance of an atom in the smallest nanosolid is a mimic of an atom in an MC of the same element without the presence of an external stimulus such as stretching or heating. At the lower end of the size limit, the property change of a nanosolid relates directly to the behavior of a single bond.

Generally, the experimentally observed size-and-shape dependence of a detectable quantity follows a scaling relation. Equilibrating the scaling relation with the BOLS prediction, Eq. (12), one has:

$$Q(K_j) - Q(\infty) = \begin{cases} bK_j^{-1} & \text{(measurement)} \\ Q(\infty) \times \Delta_{qj} & \text{(theory)} \end{cases} \tag{13}$$

where the slope $b \equiv Q(\infty) \times \Delta_{qj} \times K_j = Q(\infty) \times \sum_{i\le 3} \tau c_i \Delta q_i / q_0 \cong$ constant is the focus of various modeling attempts. The $\Delta_{jq} \propto K_j^{-1}$ varies simply with the $\gamma_{ij}(\tau, K_j, c_i)$ if the functional dependence of $q(z_i, c_i, m)$ on the atomic CN, bond length, and bond energy is given.

Physical quantities of a solid can normally be categorized as follows:

(i) Quantities that are related directly to bond length, such as the mean lattice constant, atomic density, binding energy, and length of transporting free path.

(ii) Quantities that depend on atomic coherency, $E_{B,i} = \sum_{zi} E_i = z_i E_i$, such as self-organization growth, thermal stability, Coulomb blockade, critical temperature for liquidation, evaporation and phase transition of a nanosolid and the activation energy for atomic dislocation, diffusion, and bond unfolding [127].

(iii) Properties that vary with the binding energy density in the relaxed continuum region such as the Hamiltonian that determines the entire band structure and related properties such as band gap, core-level energy, magnetization, and phonon frequency. The binding energy density is proportional to the single bond energy $E_i$ because the number of bonds per

circumferential area between neighboring atomic layers in the relaxed region does not change.

(iv) Properties related to the electron affinity such as reactivity, toxity, and ionicity.

(v) Properties that are contributed from the joint effect of the binding energy density and atomic cohesive energy such as mechanical strength, Young's modulus, surface energy, surface stress, extensibility and compressibility of a nanosolid, as well as the magnetic performance of a ferromagnetic nanosolid.

(vi) Transport dynamics and scattering process such as thermal conductivity and electric conductivity, relate to the depth of trapping potential well. The localized and depressed potential well will govern the transport processes.

Therefore, if one knows the functional dependence of the $q$ on atomic separation or its derivatives, the size dependence of the quantity $Q$ is then definite. This approach means that one can design a nanomaterial with desired functions based on the prediction as such by simply tuning the shape and size of the solid.

### 2.4. Summary

We have addressed the event of atomic CN imperfection and its effect on the bond length and bond strength of the under-coordinated atoms and the effect of chemical reaction with atoms of electronegative elements. In using the BOLS correlation, one needs to consider the cohesive energy per bond or per discrete atom when dealing with thermally activated process such as phase transition and crystal growth. One also needs to consider the binding energy density in the surface skin region when dealing with the Hamiltonian of the system that dictates the change of the entire band structure of a nanosolid. Some properties such as mechanical strength and magnetization and both atomic cohesion and energy density come into competition. An additionally depressed trapping potential well near the surface is critical in transport dynamics. As we know, the performance of a material is determined by the bond and band structures. Chemical reaction with electronegative additives also affects the bond length and the DOS in the valence band [3]. In the following sections, we will apply the BOLS premise to available experimental and theoretical observations towards consistent insight into the size and shape induced property change of nanosolids, aiming at predictable design and controllable growth of nanostructures with designed functions.

## 3. Surface relaxation and nanosolid densification

### 3.1. Surface relaxation

#### 3.1.1. Monolayer relaxation

There exists sufficient evidence for the bond contraction in the skin of a flat surface (see samples in Table 2). For instance, LEED and density functional theory (DFT) investigations revealed some 10% reduction of the first layer spacing ($d_{12}$) of the hcp $(10\bar{1}0)$ surface of Ru [128], Co [129] and Re [130]. The $d_{12}$ of diamond (111) surface was reported to be $\sim$30% smaller than the (111) spacing in the bulk with a substantial reduction of the surface energy [131]. It has been discovered

Table 2
Bond length relaxation for typical covalent, metallic and ionic solids and its effect on the physical properties of the corresponding solid or surface

| Bond nature | Medium | $c_1 = d_1/d_0$ | Effect |
|---|---|---|---|
| Covalent | Diamond {111} [131] | 0.7 | Surface energy decrease |
| Metallic | hcp $(10\bar{1}0)$ surface of Ru [128], Co [129], and Re [130] | 0.9<br>0.9 | |
| | Fe-W, Fe-Fe [139] | 0.88 | Atomic magnetic momentum enhancement by (25–27)% |
| | Fe(310) [140], Ni(210) [141] | 0.88 | |
| | Al(001) [142] | 0.85–0.9 | Cohesive energy rises by 0.3 eV per bond |
| | Ni, Cu, Ag, Au, Pt and Pd dimer [112] | 0.7 | |
| | Ti, Zr [109] | 0.6 | Single bond energy increases by 2–3 times |
| | V [109] | | |
| Ionic | O–Cu(001) [132] | 0.88–0.96 | |
| | O–Cu(110) [133] | 0.9 | |
| | N–Ti/Cr [136] | 0.86–0.88 | 100% rise in hardness |
| Extraordinary cases | (Be, Mg) (0001) surface Zn, Cd, and Hg dimer bond [109], Nb [143] | >1.0 | No report is available about its effects on physical properties |

$d_0$ and $d_1$ are the bond lengths for atoms inside the bulk and for atoms at the surface, respectively. The $c_1$ is the bond-contraction coefficient that varies from source to source.

[132], with VLEED that the O–Cu bond contraction (from 4% to 12%) forms one of the four essential stages of the O–Cu(001) bond forming kinetics and, about 10% O–Cu bond contraction for the O–Cu(110) surface is necessary [133–135]. A 12–14% contraction of TiCrN surface has been confirmed by measuring the enhanced surface stress and Young's modulus of TiCrN films [136]. Theoretical calculations [137] confirmed that the interatomic distance drops significantly associated with rise of cohesive energy per bond as the dimensionality decreases from three to one for Ag, Au and Cu nanosolids, as shown in Fig. 8.

However, the $d_{12}$ of the Be(0001) and Mg(0001) surfaces and the dimer bonds of the II-b elements of Zn, Cd, and Hg have been reported to expand. With a reduction of Se grain size from 70 to 13 nm, the $a$ lattice was found to expand by 0.3%, but the $c$ lattice spacing decreases slightly, and the unit-cell volume increases by about 0.7% at $D = 13$ nm [138]. The reported expansion appears not in line with notations of Goldschmidt and Pauling who emphasized that the global bond contraction depends uniquely on the reduction of atomic CN and it is independent of the bond nature and the constituent elements (Appendix A).

### *3.1.2. Multilayer relaxation*

In some numerical calculations and diffractional data optimizations, bond contraction and expansion coexist, extending to more than 10 atomic layers in depth for a number of clean metals though the physical ground is ambiguous [144]. For instance, calculations suggested that [145] atomic relaxations on the stepped Ag(410) and Cu(320) surfaces extend several layers into the bulk with a non-uniform character in damping magnitudes of interlayer relaxations. LEED analysis for Ag(410) initially suggested [146] that there was no measurable

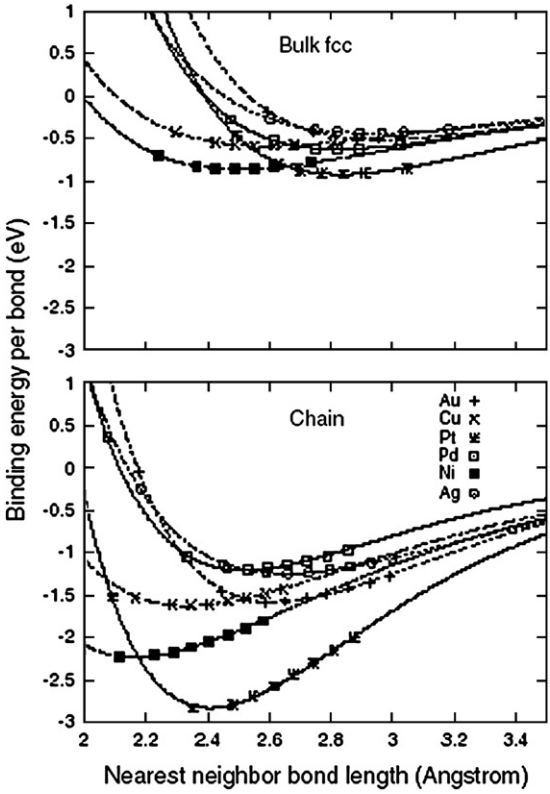


Fig. 8. DFT calculation of the bond-length–strength relation for bulk fcc crystals and straight atomic chains [112]. The bond length contracts and the binding energy per bond in the chains are about 2–3 times that of the bulk fcc crystals, which complies with the current BOLS correlation albeit the absolute amounts of variation.

relaxation of the interlayer spacings. However, later analysis of the same set of LEED data showed a 36% contraction for $d_{23}$ and 18% expansion for $d_{34}$. Theoretical calculations suggested that 11.6, 5.3, and 9.9% contraction for the top three interlayer separations of Ag(410) are followed by lattice expansion of 2.1% and 6.7% for the subsequent two interlayer spacings. Investigations [147] of the temperature dependence of the first three interlayer spacings of Ag(110) using LEED and DFT and molecular dynamics (MD) calculations suggested that the $d_{12}$ contracts by 8% at 133 K and by 0.2% at 673 K associated with Debye temperature rise from $150 \pm 65$ K to $170 \pm 100$ K compared with the bulk value of 225 K. For a Cu(320) surface, 13.6% and 9.2% contractions of the first two interlayers are followed by an expansion of 2.9%, and then an 8.8% contraction, and finally a 10.7% expansion for the subsequent three. The $d_{12}$ of the Au(110) surface is reduced by 13.8%, the $d_{23}$ is expanded by 6.9%, and finally the $d_{34}$ is reduced by 3.2% [148]. On the other hand, LEED measurements of Cu(320) revealed a 24% contraction for $d_{12}$ and 16% contraction for $d_{23}$, followed by 10% expansion for $d_{34}$. Therefore, physical constraints may be necessary to specify a unique solution from the numerous solutions given by pure mathematics as numerous adjustable parameters are involved. According to the BOLS correlation, the surface bond contracts by 12% if we take the effective CN of four, which agrees with most reported cases.

### 3.2. Nanosolid densification

#### 3.2.1. Observations and interpretations

For an isolated nanosolid or a complex consisting of highly dispersed nanosolids, the measured lattice constants are often found to contract while for a nanosolid embedded in a matrix of different materials or passivated chemically, they may expand [149]. For example, oxygen chemisorption could expand the first metallic interlayer by up to 10–25% due to the penetration of oxygen atoms into the interlayer spacing for tetrahedron formation [3]. Lattice expansion in nanocrystalline copper due to size and surface effect has also been observed [150]. A 0.4 nm thick Ni surface oxide skin has caused the lattice expansion and $M_S$ suppression of Ni nanosolids in the diameter range of 6–27 nm [151,152]. The magnetization of 16-nm $La_{0.7}Sr_{0.3}MnO_3$ nanoparticles is significantly lower than that of a bulk sample [153]. Using extended XAFS, Montano et al. [154] measured the nearest-neighbor distance for silver particles of 2.5–13 nm sizes isolated in solid argon and found a noticeable contraction of the nearest-neighbor atomic distance. Lamber et al. [155] have measured the lattice contraction of Pd particles of 1.4–5.0 nm sizes using LEED. Mi et al. [156] resolved an offset of high-resolution TEM diffraction patterns of 14 nm FePt nanoparticles embedded in an amorphous carbon matrix, which corresponds to 4% contraction of lattice constant. XRD measurements [157] revealed that the mean lattice constants of Sn and Bi nanoparticles contract with decreasing the particle size and the absolute amount of contraction of the *c*-axis lattice is more significant than that of the *a*-axis lattice, showing anisotropy of lattice contraction. Using XRD, Reddy and Reddy [158] measured ~8% contraction of the lattice parameter of a 12.5 nm sized ZnMnTe nanosolid. GAXRD studies of the as-deposited Pd overlayer on the hydrogen-induced changes in the Gd switchable mirrors reveal a positive shift in the XRD peak position indicating lattice contraction with decrease in Pd nanoparticle size [159]. Extended XAFS investigation revealed that the Cu–Cu distance in copper nanosolids with 0.7–1.5 nm mean diameter contracts with size in a $D^{-1}$ way and the Cu–Cu dimer bond is reduced by 13% from 0.2555 to 0.221 nm of the 0.7 nm-sized particle [160].

In comparison, an effective-medium theory approximation [161] suggested that the bond lengths of small (100–1000 atoms) Cu particles at various temperatures suffer only slight changes. DFT calculations [162] predicted that the atomic distance of Ge and Si expands in the central sites while the bond length contracts in the surface skins, and therefore, the mean lattice constants of the whole Ge and Si nanosolids are smaller than the bulk values. Recent calculations conducted by Liu et al. [163] suggested that the mean layer spacing of atomic clusters containing 7–617 atoms contract monotonically with size. The extent of contraction decreases when the cluster size is increased. In DFT calculations, Kara and Rahman [161] found that distances between neighboring atoms of Ag, Cu, Ni, and Fe in different CNs follow a strong bond-order–bond-length correlation. The bond lengths of Ag, Cu, Ni, and Fe diameters are 2.53, 2.22, 2.15, and 2.02 Å [164], being shorter than the nearest-neighboring atomic distances in their respective bulk by 12.5% for Ag, 13.2% for Cu, 13.6% for Ni, and 18.6% for Fe.

Mechanisms for the nanosolid densification are quite controversial. The lattice contraction was previously ascribed to the effect of hydrostatic pressure arising from surface stress [165] and the intrinsic compressibility of the material [154,166–168]. The central lattice expansion is expected to be the consequence of surface oxidation. The mean lattice strain is also explained in terms of incorporation of impurities like hydrogen, carbon, and oxygen, or

pseudomorphism in the case of crystalline supports [155]. Nanda et al. [169] adopted a liquid-drop model to illustrate the lattice strain and indicated that the anisotropic lattice contraction in Bi and Sn arises from the anisotropy of both the compressibility and the thermal expansion coefficient of the corresponding bulk counterpart in the $c$ and in the $a$ axes. Jiang et al. [170,171] developed a model for the size-induced lattice contraction based on the Laplace–Young's equation and the size dependence of the solid–liquid interfacial energy. Yu et al. [157] attributed such lattice variation to the super-saturation of the vacant lattice sites inside the particle. Reddy and Reddy [158] suggested that both the atomic density and the refractive index in the core region are higher than those in the surface skin. Both the atomic density and the refractive index slowly decrease as one moves away from the center of the solid to the surface. Nevertheless, from numerical point of view, all the modeling arguments could fit the experimental data well despite different physical origins.

Actually, surface stress and surface energy result intrinsically from, rather than in, the bond contraction as no external pressure is applied to the surface. For instance, the compressibility that is the inverse of Young's modulus and the thermal expansion coefficient

$$\beta = -\frac{1}{V}\left(\frac{\partial V}{\partial P}\right)\Big|_T = \left(-V\frac{\partial^2 u}{\partial V^2}\Big|_T\right)^{-1} = Y^{-1}; \quad \alpha = \frac{1}{V}\left(\frac{\partial V}{\partial T}\right)\Big|_P \tag{14}$$

are intrinsic properties of a solid and they depend functionally on the interatomic interaction and atomic size. These measurable quantities describe the response of the lattice ($V \propto d^3$) to the external stimuli such as pressure, $\Delta P$, or temperature change, $\Delta T$.

$$\frac{\Delta V}{V} = 3\frac{\Delta d}{d} = \begin{cases} \beta \times \Delta P \\ \alpha \times \Delta T \end{cases}$$

The external stimulus simply provides a probe detecting the responses: compression or expansion. It may not be applicable to assume a constant compressibility or a constant thermal expansion coefficient when dealing with a nanometric solid. In fact, the surface stress and interfacial energy are derivatives of the binding energy that is enhanced at the surface by the spontaneous process of bond contraction. Therefore, the fact of surface atomic density increase with reduced particle size could explain the lattice and property change of a nanosolid, as at the lower end of the size, no 'core interior' remains.

### *3.2.2. BOLS consideration*

The BOLS correlation mechanism indicates that the contraction of the mean lattice constant of the entire solid originates from the CN imperfection induced bond shortening in the surface region and the portion of surface atoms of the entire solid, which can be easily derived in a core-shell structure as follows:

$$\begin{cases} \overline{d} & = d_0[1+\Delta_d] \\ \Delta_d & = \sum_{i\le 3} \gamma_{ij}(c_i - 1) < 0 \end{cases} \tag{15}$$

The BOLS consideration is compared with other analytical models for the mean lattice contraction as follows [169,170]:

$$\frac{\Delta d(K_j)}{d_0(\infty)} = \begin{cases} \Delta_d & \text{(BOLS)} \\ -(2\beta\sigma)/(3K_j) & \text{(liquid-drop)} \\ -(\beta\gamma_{s-l}d_0)^{1/2}/K_j & \text{(surface-stress)} \end{cases} \tag{16}$$

where $\beta$ is the compressibility and $\sigma$ the surface stress of the corresponding bulk solid. $\gamma_{s-l} = (2d_0 S_{vib} H_m)/(3VR_j)$ is the solid–liquid interfacial energy, which is a function of the bulk melting enthalpy, $H_m$, and molar volume, $V$, and the vibrational part of melting entropy, $S_{vib}$. All the models fit the measured data numerically well for solids larger than a critical size. The relative change in the mean lattice constant of a particle in the present BOLS premise simply depends on the $\gamma_{ij}$ and the bond-contraction coefficient $c_i$ without needing other quantities that may vary with the solid size.

With a given shape and size and the known atomic diameters of the constituent atoms of a nanosolid, one can easily predict the lattice contraction of the nanosolid using Eq. (15). In the particular ZnMnTe case [158] in which the nanosolid was assumed as a spherical dot with diameter $D$, the diameters of the constituent atoms are taken as 0.1306(Zn), 0.1379(Mn), and 0.1350(Te) nm, and the effective CN of the outermost three atomic layers are taken as 4, 6, and 8, respectively. Results calculated agree fairly well with the observation ($\sim$8% contraction for 12.5 nm sized ZnMnTe solid) and show that the lattice constant reaches its bulk value only when the solid dimension is sufficiently large. At the lower end of the size limit, the mean lattice contraction of the solid approaches the value for a dimer bond of the same atomic constituents. Furthermore, predictions based on the BOLS premise also agree with the observed trends of lattice contraction for ZnS:Mn films [172] and Sn and Bi nanoparticles [157]. Measurements [164] show that the Ag-Ag atomic distance becomes shorter than the bulk value for the 2.0, 2.5, and 3.5 nm sized Ag crystals. For the 5.0 nm crystal, 60% of the atoms have the bulk value but 40% have a shorter atomic distance. Consistency between predictions and observations of lattice contraction for a number of metals has been achieved as shown in Fig. 9. One can see that the average atomic distance for the three elements, Ag, Cu, and Ni, is shortened by as much as 1.6–2.0% for small nanocrystals and about 0.6% for relatively larger ones, as compared to the bulk value. In the current approach using the dimensionless form of size, $K_j$, as the lateral axis, the observed anisotropy of Bi lattice contraction does not exist if one considers the relative change of $c$ and $a$ axes, $\Delta a/a$ and $\Delta c/c$, instead of the absolute amount of variation.

### *3.2.3. Further evidence: strain induced stiffness*

Discrepancy on the mechanism for structural deviations in nanoparticles remains because the deviation is hard to resolve experimentally. Theoretically, nanoparticles have bulk-like interior structure [180] with surface relaxation [163,181] in a manner comparable to that of bulk surfaces. However, classical and quantum MD simulations have suggested that disorder may pervade throughout nanoparticles [182,183]. Combining the pair distribution function (PDF) derived from wide-angle X-ray scattering and EXAFS analyses, Gilbert et al. [184] investigated the intermediate-range order in $3.4 \pm 0.3$-nm-diameter ZnS nanoparticles. They found the structural coherence loss over distances beyond 2 nm rather than at 3.4 nm. Fig. 10 shows that the PDF for real ZnS nanoparticles is distinct from that of ideal ZnS nanoparticles in the following aspects [184]:

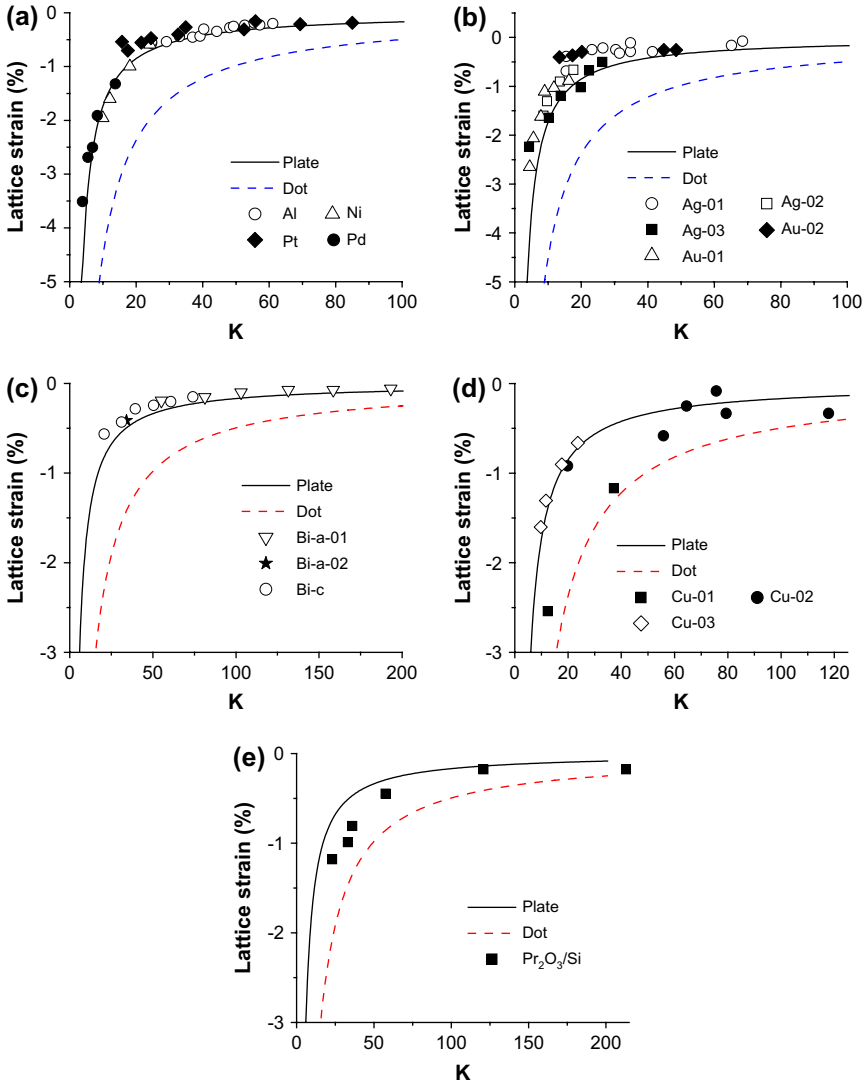


Fig. 9. Comparison of BOLS predations with measured size dependence of mean lattice contraction of (a) Al [173], Ni [164], Pd [155], and Pt [174]; (b) Ag-01 [168], Ag-02 [164], Ag-03 [154], Au-01 [166], Au-02 [175]; (c) Bi-a-01 [157], Bi-a-02 [176], Bi-c [157]; and (d) Cu-01 [177], Cu-02 [178], and Cu-03 [164] nanoparticles. (e) Thickness dependence of lattice constant of $Pr_2O_3$ films on Si substrate [179]. No anisotropy is present when using $\Delta a/a$ and $\Delta c/c$ to calibrate the Bi lattice contraction.

(i) The PDF peak intensity of the first shell is lower than that for the ideal case.
(ii) The intensities of the PDF peaks at higher correlation distances diminish more rapidly than the ideal nanoparticle.
(iii) PDF peak widths are broader in the real nanoparticle.
(iv) The PDF peak positions are shifted closer to the reference atom. The shift is more apparent at $r = 1.0$ nm and 1.4 nm (shortened by 0.008 and 0.02 nm, respectively), indicating a contraction of mean bond length of the nanoparticle.

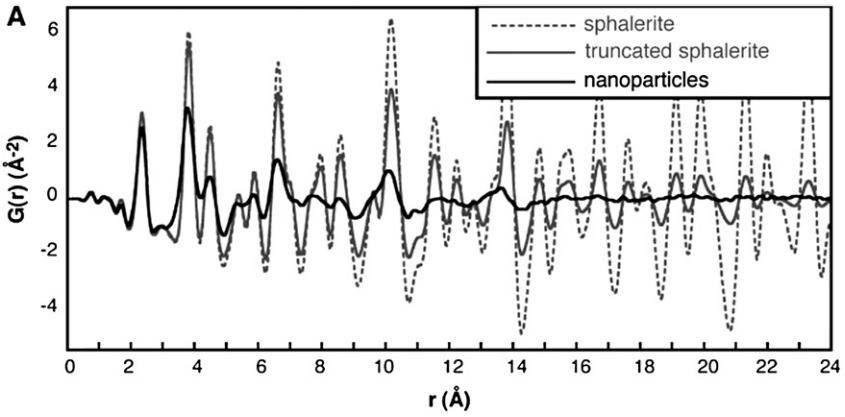


Fig. 10. Comparison of the pair distribution function of ZnS bulk solid, calculation for ideal nanosolid and the measurement for real nanosolid show the cohesive length loss of nanosolid [184].

The frequency of lattice vibration for the ZnS nanoparticles is measured to increase from the bulk value of $7.12 \pm 1.2$ to $11.6 \pm 0.4$ THz, implying bond stiffening.

The findings of ZnS nanosolid straining and stiffening agree appreciably well with the BOLS prediction suggesting that the surface relaxation is dominantly caused by atomic CN reduction, and therefore, PDF intensity weakening or diminishing results from the volume loss of high-order CN atoms. The PDF peak shifting and broadening arise from the broad range of bond contraction in the outermost two or three atomic layers and the non-uniformity of nanosolid sizes. As the XRD and the EXAFS present statistic information from a collection of nanosolids, one could only tell the existence of structure deviation but hardly conclude whether the structure distortion arises from surface skin or from the core region. However, the diameter difference of (3.4–2.0) 1.4 nm coincides with the thickness of the skins composing the outermost atomic capping and surface layers [185] ($3 \times 2 \times 0.255$ nm) of which atoms are subject to CN imperfection. Compared with the PDF of an amorphous solid of which the structure coherence extends only to a couple of atomic distances [126], the detected PDF of ZnS nanosolid coincides with the core size of the measured solid. Therefore, the surface layers should dominate the bond length distortion. As illustrated in the next section, the strengthening of the shortened bonds is responsible for the stiffening of the entire nanosolid. The difference between a solid composed of nanoparticles and a solid in an amorphous state is the distribution of atoms with CN imperfection. For the former, under-coordinated atoms are located at the surface; for the latter, they distribute randomly inside the solid and the distribution of CN imperfection is sensitive to processing conditions. In collecting statistical information, the low-CN atoms contribute identically irrespective of their locations. It is anticipated that the PDF correlation length, or core size, increases with solid dimension and further verification by measuring different sizes would provide affirmative evidence for the shell strain induced stiffness.

### *3.3. Impact of bond-order loss*

The bond-order loss induced bond contraction at a surface has indeed enormous effects on various physical properties of a nanosolid because of the localization and densification of

electrons and energies in the surface skins and the lower atomic coherency, as addressed earlier. Besides the magnetic enhancement [139–141], the relaxation of Al, Ag, Cu, and Pd surfaces has been found to lead to a shift in the frequencies of the surface states and to a change in the number and localization of the states [186]. For Ag nanocrystals, densification stiffens the atomic force constants by up to 120% when compared to that for bulk silver [164]. The vibrational energy and the heat capacity of the step and the terrace atoms on the Cu(711) surface are sensitive to the local atomic environment, and vibrational contribution to the excessive free energy of the step atoms near room temperature is a significant fraction of the kink formation energy [187]. The Al(001) surface relaxation expands the bandwidth for the relaxed monolayer by 1.5 eV compared with the value for the bulk-truncated monolayer with 0.3 eV enhancement of atomic cohesive energy [142]. The lattice constant of Au nanoparticles capped in n-dodecanethiol contracts by 1.4%, 1.1% and 0.7% with an association of 0.36, 0.21, and 0.13 eV 4f-core-level shift for 1.6, 2.4, and 4.0 nm sized Au particles, respectively [188]. Therefore, the impact on physical properties of atomic CN imperfection and the associated bond-strength gain is indeed enormous especially for a system with a large portion of undercoordinated atoms.

## 4. Mechanical strength

### *4.1. Surfaces*

#### *4.1.1. Outstanding models*

*4.1.1.1. Surface stress and surface energy.* Surface stress ($P$), being the same in dimension to hardness ($H$), reflects the internal energy response to volume strain at a given temperature. Hardness is the ability of one material to resist being scratched or dented by another. The former often applies to the elastic regime while the latter to plastic deformation. Surface stress is an important concept, which links the microscopic bonding configuration at an interfacial region with its macroscopic properties [189,190], such as the threshold of cold-cathode field emission in carbon [191]. The stress also plays a central role in the thermodynamics and acoustics of solid surfaces. During the past decades, increasing interest has been paid to processes that are strongly influenced by surface stress effects such as reconstruction and relaxation, interfacial mixing, segregation, and self-organization at solid surfaces. However, surface stress and hardness are not so easily determined at the atomic scale, and there is no theory that could tell us how to arrange atoms to make a hard structure. Therefore, detailed knowledge underlying the atomistic processes of surface stress is highly desirable [189,190].

Comparatively, surface energy ($\gamma$) representing a fundamental material property is normally defined as half the energy needed to cut a given crystal into two halves. As such, the surface energy naturally depends on the strength of the bonding and on the orientation of the surface plane. Despite its importance, the value of surface energy is difficult to determine experimentally. Most of the experiments are performed at high temperatures where the surface tension of the liquid is measured, and the results are extrapolated to 0 K. This kind of experiment contains uncertainties of unknown magnitude [192] and corresponds to the $\gamma$ value of an isotropic crystal only [193]. Documented data determined by the contact angle of metal droplets or from peel tests conflict one another. Errors can be induced by the presence of impurities or by mechanical contributions, such as dislocation slip or the transfer of material across the grain boundaries [194].

Numerical attempts have been made to calculate the $\gamma$ values of metals using ab initio techniques [193,195,196], tight-binding parameterizations [197], and semi-empirical methods [198]. The $\gamma$ values, work functions, and surface relaxation for the whole series of bcc and fcc 4d transition metals have been studied using the full-potential (FP) linear muffin-tin orbital (LMTO) method in conjunction with the local-spin density approximation to the exchange-correlation potential [195]. In the same spirit, the values of $\gamma$ and work function of most elemental metals including the light actinides have been calculated using Green's function and the LMTO method [196,199]. A documented database shows a mean deviation of 10% for the 4d transition metals from FP methods [193]. In conjunction with the pair-potential model [200], the database has been further extended to estimate the formation energy of monatomic steps on low-index surfaces for an ensemble of the bcc and fcc metals [193].

The traditional broken-bond model is often used to estimate the $\gamma$ values of the transition and the noble metals with different facets [148]. The simplest approach to estimate the $\gamma$ values at $T = 0$ K is to determine the broken-bond number $z_{(hkl)} = z_b - z_S$ for creating a surface area by cutting a crystal along a certain crystallographic plane with a Miller index $(hkl)$ where $z_S$ is the CN of a surface atom and $z_b$ the corresponding bulk one. Galanakis et al. [148] investigated the correlation between the broken bond and the surface energy of noble metals using two different full-potential ab initio techniques. They introduced a simple rule based on the number of broken nearest-neighbor bonds to determine the surface energies of Cu, Ag, and Au metals. The physical argument for the bond-broken rule is derived from a tight-binding approximation, which relates the surface energy to the atomic cohesion energies. In a nearest-neighbor TB model, the $\gamma$ value for a transition metal surface is given by [148]

$$\gamma \cong \frac{W_S - W_B}{20} n_d (n_d - 10)$$

where $n_d$ is the number of d-electrons. $W_S$ and $W_B$, being the bandwidths for the surface and bulk DOS, are assumed to have rectangular forms. The $\gamma$ value of the Au(110) surface was calculated to be reduced by 6.5% compared with the energy in the bulk region [148].

Using the Kelvin equation [201], the relation between the atomic cohesive energy, $E_B$, and the activation energy, $E_A(N)$, for removing an atom from a nanosolid is given as [202]

$$\begin{cases} \dfrac{P_s(D)}{P_s(\infty)} = \exp\left(\dfrac{4\gamma m_a}{\rho_P k_B T D}\right), & \text{(Kelvin)} \\ E_A(N) = E_B - \dfrac{2\pi d^2 \gamma}{3N^{1/3}}, & (E_A - E_B) \end{cases} \tag{17}$$

where $P_s(D)$ and $P_s(\infty)$ are the vapor pressures of the nanosolid and the corresponding bulk surface, respectively; $m_a$ is the atomic mass, and $\rho_P$ is the mass density of the particle. Nanda et al. [203] developed a method based on this approach to determine the $\gamma$ value of Ag and PbS nanosolids by measuring the onset temperature ($T_{onset}$) of evaporation:

$$\frac{\Delta T_{\text{onset}}(K_j)}{T_{\text{onset}}(\infty)} = -\frac{8\pi d_0^2}{3E_B K_j}\gamma \tag{18}$$

Using $E_B = 2.95$ eV and $d_0 = 0.158$ nm, a $\gamma$ value of 7.37 J m$^{-2}$ has been derived by analyzing the measured size-dependent $T_{\text{onset}}$ of free-standing Ag nanosolids, which is 5–6 times higher than that of the bulk value, though this value might be overestimated [204].

Multiplying the broken-bond number with the cohesion energy per bond $E_b = E_B/z_b$ in the bulk for the non-spin-polarized atom at 0 K, $\gamma$ is also suggested to follow [190]

$$\gamma = (1 - z_s/z_b)E_B = E_b(z_b - z_s) \tag{19}$$

where $\gamma$ corresponds actually to the energy loss due to CN reduction, which is always lower than the cohesive energy of the bulk atom. On the other hand, the broken-bond rule seems to contradict the basic knowledge about the electronic structure since $E_B$, in general, does not scale linearly with $z_S$. Nevertheless, the above estimation provides the order of magnitude of $\gamma$ and shows a possible relationship between $\gamma$ and atomic binding strength. Despite the absence of verification from experiments, such a rule has been used to give a reasonable description of the $\gamma$ value of Al [148].

In the second-moment TB approximation, the width of the local DOS on an atomic scale with $z_S$, leads to an energy gain that is proportional to $\sqrt{z_S}$ due to the lowering of the occupied states [205]. Neglecting the repulsive terms, the energy per nearest neighbor is then proportional to $\sqrt{z_S}$. By assuming that the total crystalline energy is a sum of contributions from all bonds of an atom, the surface energy is suggested to follow the relation [205]:

$$\gamma \cong \left(1 - \sqrt{z_s/z_b}\right)E_B \tag{20}$$

According to this model, the rearrangement of the electronic charge does not practically change the nature of the remaining bonds when one bond is broken. Thus, the energy needed to break a bond is independent of the surface orientation, so that the $\gamma$ value is proportional to the square root of the number of the nearest-neighbor broken bonds.

Eq. (19) or (20) has been widely used to estimate the $\gamma$ value of a surface. However, Eq. (19) fails to consider the variation of bond strength with CN reduction, while Eq. (20) is less complete because only attractive forces are taken into account [195]. Namely, Eq. (19) neglects while Eq. (20) overestimates the effect of relaxation on $\gamma$ when the $\gamma$ value is directly related to the number of broken bonds. Neither of them could alone give satisfied predictions for $\gamma$ values in comparison with the experimental and theoretical results [195]. To obtain a more general expression, Jiang et al. [206] assumed that an average of Eqs. (19) and (20) could make up the deficiency of each. Thus, the $\gamma$ values may be determined by averaging them without requiring an estimate of the relaxation energy. They also considered the contribution from the high-order CN to the bond energy and suggested a form

$$\gamma = \frac{\left[2 - z_s/z_b - (z_s/z_b)^{1/2}\right] + \lambda\left[2 - z'_s/z'_b - \left(z'_s/z'_b\right)^{1/2}\right]}{2 + 2\lambda}E_B \tag{21}$$

where the prime denotes the next-nearest CN of the surface atoms and $\lambda$ is the total bond strength ratio between a next-nearest neighbor and a nearest neighbor [207]. The approach apparently improves the values of both of them [206].

### 4.1.2. BOLS consideration

*4.1.2.1. Surface energy.* Apparently, the approaches mentioned above give inconsistent trends of surface energy change compared with the bulk binding energy because of the difference in definition. Actually, Kelvin's equation describes energy density in the surface region while the bond-broken arguments describe energy loss upon surface formation. Kelvin's equation suggests an elevation while the broken-bond arguments suggest a suppression of the surface energy. The key problem is the clarification of surface energy. It must be clear that the surface energy is the (i) energy density in the surface skin of a couple of atomic layers, (ii) cohesive energy of the under-coordinated surface atoms, or (iii) energy loss due to bond number loss. The different definitions will lead to different values of $\gamma$ change.

We should prefer the definition of surface energy as the energy density in the surface skin. The fact of surface bond contraction and its effect on the bond energy may provide us with the possible physical origin for surface energy and interfacial stress, even if it is an effect of chemical passivation. As the number of bonds in the relaxed region does not change apparently, the surface energy, or the binding energy density in the relaxed region, should increase by:

$$\begin{aligned} &\gamma_i = \mathrm{E}_i/d_i^3 = \gamma c_i^{-(m+3)} \\ &\Delta\gamma_i/\gamma \cong c_i^{-(m+3)} - 1 > 0 \end{aligned} \tag{22}$$

For a defect-free metallic surface ($m = 1$), the surface energy is expected to increase by $0.88^{-4} - 1 \cong 67\%$ in magnitude, if we define the surface energy as the energy density in the relaxed outermost surface region.

*4.1.2.2. Young's modulus and surface stress.* Young's modulus ($Y$) is the stress of a material divided by its strain in the elastic deformation region, meaning physically how much the material yields for each kilogram of load put on it. The $Y$ and $P$ at a surface can be expressed as functions of the binding energy, $E_\mathrm{b}$, volume, $v$, and the atomic distance, $d$. They share the same dimension:

$$\left\{ \begin{array}{ll} P & = -\dfrac{\partial u(r)}{\partial v}\Big|_{r=d} \\ Y & = v\dfrac{\partial P}{\partial v} = v\dfrac{\partial^2 u(r)}{\partial v^2}\Big|_{r=d} \end{array} \right\} \propto \gamma_i \propto \left\{ \begin{array}{ll} \dfrac{E_i}{d^3} & (T \ll T_{\mathrm{m},i}) \\ \dfrac{\eta_i(T_{\mathrm{m}i} - T)}{d^3} & (\text{otherwise}) \end{array} \right. \tag{23}$$

The relative change of the local $Y_i$, $P_i$ and $\gamma_i$ shares a commonly dimensionless form at $T \ll T_{\mathrm{m}i}$:

$$\frac{\Delta Y_i}{Y} = \frac{\Delta P_i}{P} = \frac{\Delta\gamma_i}{\gamma} = \left\{ \begin{array}{ll} c_i^{-(m+3)} - 1 & (T \ll T_{\mathrm{m}i}) \\ [\eta_{1i}(T_{\mathrm{m}i} - T)/\eta_{1\mathrm{b}}(T_{\mathrm{mb}} - T)]c_i^{-3} - 1 & (\text{otherwise}) \end{array} \right. \tag{24}$$

This relation implies that the $Y$, the $P$ and the $\gamma$ at a surface be higher than the bulk values because of the strength gain of the shortened surface bond at temperatures, ideally, far below the melting point. However, at a temperature that is sufficiently high, the situation may change because the $\eta_{1i}$ is larger than $\eta_{1\mathrm{b}}$ but $T_{\mathrm{m}i}$ is lower than $T_{\mathrm{mb}}$. The competition between the $\eta_{1i}$ and the $T_{\mathrm{m}i} - T$ determines the mechanical strength of a surface [205]. The $d_i$ is also subject to change under thermal expansion, mechanical stretching or pressing:

$$d_i = d \times c_i(z) \times (1 + \alpha T) \times (1 + \beta P)$$

One may note that the Young's modulus describes the elasticity while its inverse, or the extensibility or compressibility, covers both the elastic and plastic deformations. However, any of the elastic or plastic processes is related to the process of bond distortion with energy consumption (integrating the area in the stress vs. strain plot). No matter how complicated the actual process of deformation (with linear or nonlinear response) or recovery (reversible or irreversible) is, a specific process consumes a certain portion of bond energy, and the exact portion for a specific process does not come into play in the numerical expression for the relative change. Therefore, relations (23) and (24) are valid for any substance in any phase such as the gaseous, liquid, or solid state and any scale as well, as they are dimensionless quantities. It might not be appropriate to think about the stress of a single atom but instead the stress at a specific atomic site.

There is massive evidence for the surface-enhanced mechanical strength of inorganic thin films. An examination of the hardness (also stress) and the Young's modulus using nanoindentation revealed that the surface of the TiCrN thin film (2 μm thick) is 100% higher than its bulk value [136]. The same trend holds for amorphous carbon [209] and AlGaN surfaces [210]. Ni films also show maximal hardness in ~5 nm depth of the surface, though the peak maxima vary with the shapes of nanoindentor tips [211]. Low-dielectric thin films also show 2–3 times higher value of hardness and Young's modulus near the surface at the ambient temperature. When the measuring temperature rises, the stress drops and changes from tensile to compressive [212]. However, the $Y$ values for the polymer nanostructures drop with size according to the relation $Y = 0.014 \ln(x) + 0.903 \pm 0.045$ [213], with $x$ being the particle size. The $Y$-suppression indicates the importance of the $(T_m - T)$ contribution in determining the size effect on mechanical strength. The $T_m$ of organic material is much lower than that of inorganic systems.

Solving Eq. (24) with the measured value of $\Delta P/P = (50 - 25)/25 = 1$ in Fig. 11 gives rise to the $c_i$ values of 0.860 and 0.883 associated with $m = 3$ and 4, respectively. Lower $P$ values were also observed in measurement, which arise from grain boundaries or from sites near defects. Fig. 12 shows the indentation profiles of N doped tetrahedron carbon films [214]. The thickness dependence of both the $Y$ and the $P$ follows a similar

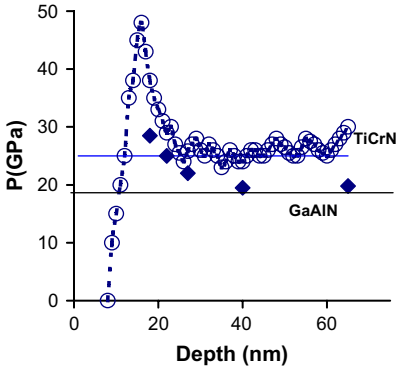


Fig. 11. Nanoindentation hardness–depth profile for TiCrN [136] and GaAlN [210] thin films. The peak shift corresponds to the surface roughness (Ra = 10 nm as confirmed by AFM).

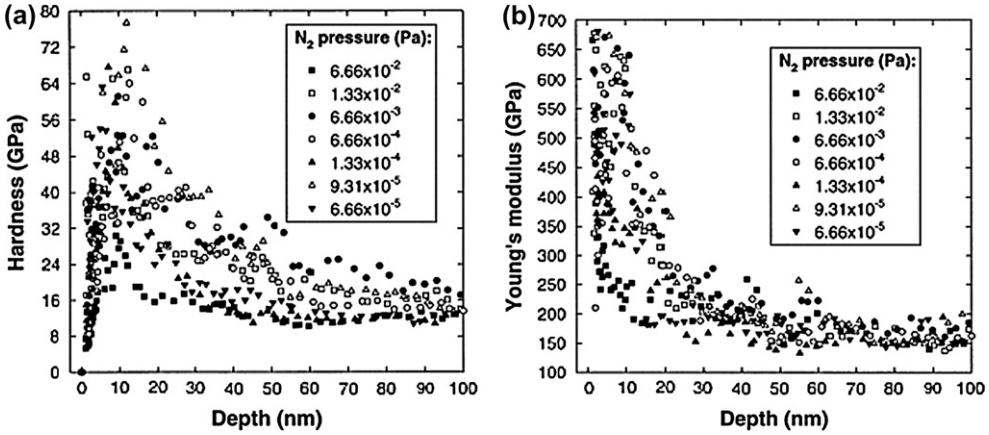


Fig. 12. Nitrogen partial pressure dependence of (a) the hardness and (b) Young's modulus of ta-C:N films versus penetration depth measured using a continuous stiffness method [214].

trend and that is independent of the nitrogen content, showing the validity of relation (24), though the Young's modulus is defined for the elastic deformation and the hardness is for plastic deformation. Fig. 13a shows the indentation depth dependence of the hardness of Ag, Ni, Cu, Al, $\alpha_2$-TiAl, and $\gamma$-TiAl films [215]. The measured strain-gradient plasticity was explained in terms of the material characteristic length that depends functionally on quantities of the Burger's vector, the shear modulus, and the material reference stress. Fig. 13b compares predictions with the theoretically calculated thickness dependence of Young's modulus for Ni-I and Cu-I [216], Ni-II, Cu-II, and Ag [217] thin films by summing Eq. (24) over the top three atomic layers. Agreement is reached with $z_1 = 4$, $z_2 = 6$, and

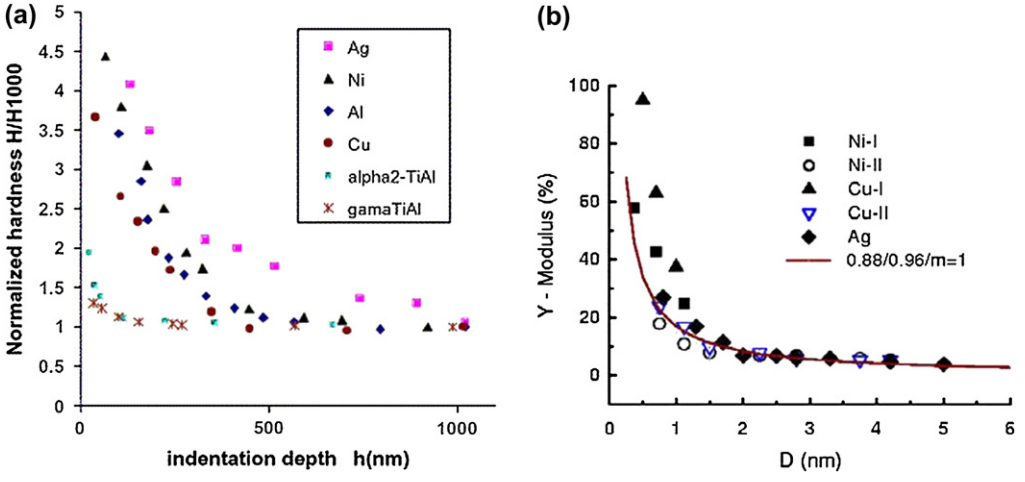


Fig. 13. (a) Comparison of indentation size effect. The hardness $H$ is normalized by its value, $H_{1000}$, at a depth of 1000 nm [215]. (b) Agreement between predictions and theoretically calculated size dependence of the Young's modulus of Cu-I and Ni-I, Ni-II and Cu-II and Ag thin films [216,217].

$m = 1$ for the pure metals. At the thinnest end (two atomic layers), the Young's modulus of Cu is 100% higher than the bulk value, which agrees with the values measured for a TiCrN surface.

### 4.2. Nanospheres

By squeezing Si nanospheres of different sizes between a diamond-tipped probe and the sapphire surface, Gerberich et al. [25] measured that a defect-free silicon nanosphere with a diameter of 40 nm is ~3 times (50 GPa) harder than bulk silicon (12 GPa). The smaller the sphere, the harder it was: spheres with a diameter of 100 nm had a hardness of around 20 GPa. For comparison, sapphire has a hardness of about 40 GPa, and diamond 90–100 GPa. The silicon nanospheres are comparable in hardness with materials such as nitrides and carbides, which typically have hardness values in the range of 30–40 GPa. Fig. 14a–c shows the loading curves and the derived hardness of different particle sizes. Liu et al. [218] measured, as shown in Fig. 14d, that the $Y$ value of nanograined steel increases from 218 to 270 GPa associated with lattice contraction from 0.2872 to 0.2864 nm in the grain-size range of 700 nm and smaller.

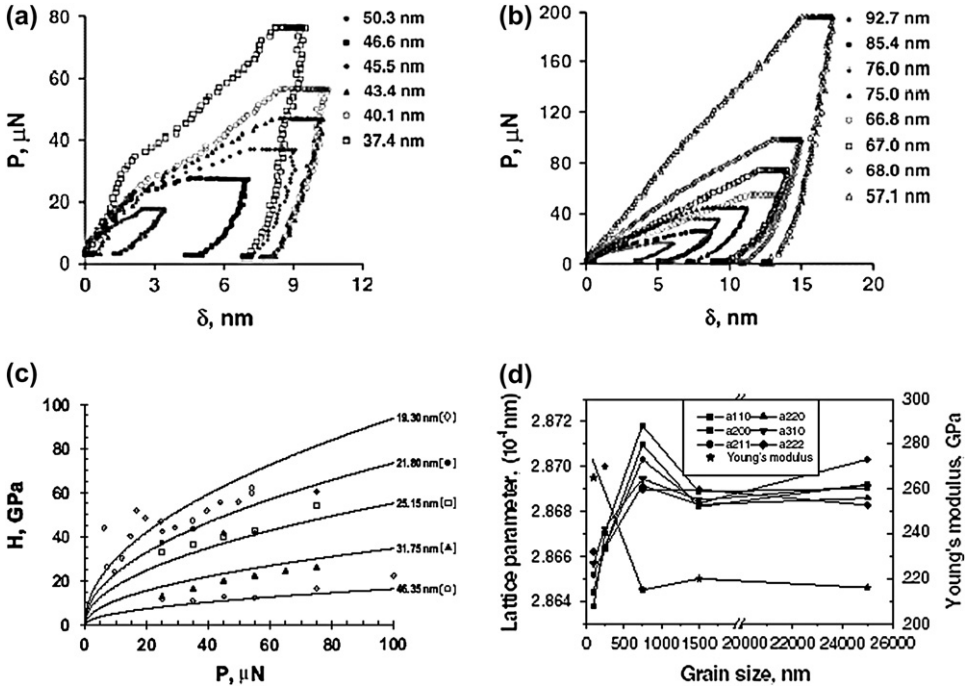


Fig. 14. (a) Load–displacement curves for a Si particle with an original height of 50.3 nm exhibiting a strain reversal of approximately 34%. (b) Load–displacement curves for a particle with an original height of 92.7 nm exhibiting a strain reversal of approximately 19%. (c) Hardening curves for silicon nanospheres of various dimensions. The right-hand column lists the particle radii [25]. (d) Correlation between the Young's modulus and lattice constant of various planes of nanograined steel [218].

The above-mentioned findings coincide with a recent flurry of activity in the nanotechnology community, which has focused on the indentation size effect [25,219] and the mechanical behavior of small volumes [220,221]. Small volumes include mechanically milled iron powders with hardness of 8.4 Gpa [222], and nanocrystalline composite films of $TiN/Si_3N_4$ reportedly having hardness in the range of 20–100 GPa [223]. The hardness of Ti, Zr, and Hf carbide films on a silicon substrate increases from bulk value of 18 GPa to 45 GPa when the film thickness decreases from 9000 to 300 nm [224]. MD simulations [225] of 105–106 atoms of nanocrystalline aluminum under an applied stress of 2–3 GPa suggest that the stress is substantially higher than can be sustained by their normal bulk counterparts, and they are believed to have unique properties at least partially due to their small length scales. These seemingly widely disparate material systems have a common thread in that line defects or dislocations in these refined microstructures are generated at very high pressures. In the process of testing, dislocations that are generated and squeezed closely together result in extremely high internal stress, which is suggested to be responsible for resisting plastic deformation in these fine microstructures. A single edge dislocation has an elastic shear stress field distribution that could produce a stress of nearly 3 GPa at a distance of 1 nm from the line. The consequences of these very high internal stresses have potential for the design of superhard materials. Evaluation of such materials becomes in question, as substrate, contact area, or pressure effects represent confounding aspects in measuring hardness.

The size-dependent hardness and the Young' modulus enhancement at temperature far below the $T_m$ of the addressed samples are in good accordance with the BOLS prediction. From Eqs. (23) and (24), one may realize that the factors enhancing the $Y$ and $P$ simultaneously are the shortened bond length and the associated bond-strength gain. Atoms in the surface skin, or at an interface, should dominate the hardness due to the atomic CN induced bond contraction and bond-strength gain.

Applying $m = 4.88$ for Si in Eq. (24) gives immediately $c_1 = (15 \pm 1)\%$ and the corresponding $z_1 \approx 3.60 \pm 0.25$. The $z_1$ is slightly lower than $z_1 = 4$ for a flat surface and the $c_1$ is slightly greater than that of the TiCrN flat surface $(13 \pm 1)\%$. The bond contraction (from 0.263 nm to 0.23 nm) and band gap expansion (from 1.1 to 3.5 eV) of a Si nanorod with the rod diameter reduction [48] is direct evidence of the BOLS correlation that could consistently dictate the Young's modulus and the hardness of Si nanosolids. For steel, Liu et al. [218] proposed a functional dependence of $Y$ value on the lattice constant, which-agrees with the BOLS prediction of $Y(D)/Y(\infty) = c_i^{-(m+3)}$ with $m = 1$ for metals. The $c_i$ is estimated to be 94.8% according to the measured maximal $Y$ value, as given in Fig. 14d.

### 4.3. Compounds and alloys

Blending different types of atoms in a solid could enhance the hardness of the solid preferably in an amorphous state, to form the so-called high entropy materials [226]. Gao et al. [227] proposed a formula based on the concept of ionicity to predict the hardness of several compounds. Ionicity ($f_i$) is a measure of the degree of charge sharing: covalent bonds have the lowest ionicity, and ionic bonds have the highest. The hardness, or the activation energy required for plastic gliding, was related to the band gap $E_G$. The hardness of a covalent solid is empirically described as:

$$\begin{cases} H_v = AN_aE_G = 556N_ad_0^{-2.5}\exp(-1.191f_i)(\text{GPa}) \\ f_i = 1 - E_h^2/E_G^2 \end{cases}$$

where $A$ is a constant coefficient and $N_a$ is the number of covalent bonds per unit volume. The $E_G$ for a binary polar covalent system can be separated into both covalent or homopolar gap $E_h$ ($=39.74d_0^{-2.5}$) [228] and ionic or heteropolar gap C. The $d_0$ is the covalent bond length in angstrom. Philips [229], Liu and Cohen [230], and Korsunskii and Pepekin [231] have proposed another relationship for the bulk modulus $B$ of a compound solid, which follows:

$$B = N_c/4 \times (19.71 - 2.20f_i)d_0^{-3.5}(\text{Mbar})$$

$N_c$ is the nearest atomic CN. The parameter $f_i$ accounts for the reduction in $B$ arising from increased charge transfer. The value of $f_i = 0$, 1 and 2 for groups IV, III–V, and II–VI solids in the periodic table, respectively. For a tetrahedral system, $N_c = 4$, otherwise, the $N_c$ is an average of atomic CN. For diamond, $f_i = 0$, $d = 1.54$ Å, and hence $B = 4.35$ Mbar, compared with an average experimental value of 4.43 Mbar. This relationship was applied to BN and β-$Si_3N_4$ with corresponding prediction of $B = 3.69$ and 2.68 Mbar. Litovchenko [232] also derived that the $E_G \propto d^{-2}$ and then the elastic modulus follows the relation $B \propto d^{-5}$. These predictions stimulated tremendous interest in the experimental search for the superhard carbon-nitride phase worldwide [233–236], as the diameter of an N atom is 0.14–0.148 nm shorter than that of carbon in the C–C bond in a diamond.

In spite of the difference in the power index, −2.5, −3.5, −5, and $-(m+3)$ in the current approach, all the expressions indicate that shorter and denser chemical bonds as well as smaller ionicity should favor hardness. In order to obtain a compound with large bulk modulus, one must find such a covalent compound that has both shorter bond length and smaller ionicity, and high compactness in atomic arrangement inside. Thus, the atomic CN imperfection induced bond contraction should contribute directly to the hardness at the surface or sites surrounding defects. Therefore, a nanometer sized diamond is expected to be 100% ($0.88^{-5.56}-1$) harder than the bulk nature diamond but the hardness should be subject to the inverse Hall–Petch relationship [237].

### 4.4. Inverse Hall–Petch relation

The mechanical strengthening with grain refinement of crystals with mean grain size of 100 nm or bigger has been traditionally rationalized with the so-called T-unapparent Hall–Petch relationship (HPR) [238] that can be simplified in a dimensionless form:

$$P(x_j, T)/P(0, T) = 1 + A'x_j$$

The $P(x_j, T)$ is the yield strength (or flow stress), and the slope $A'$ is an adjustable parameter for data fitting. The $x_j = K_j^{-1/2}$ and $K_j$ are the dimensionless forms of size. $P(0, T)$ is the bulk strength measured at the same $T$. The dimensionless form should be independent of processing condition.

The pile-up of dislocations at grain boundaries is envisioned as a key mechanistic process underlying the enhanced resistance to plastic flow from grain refinement. As the crystal is refined from the micrometer regime into the nanometer regime, this process invariably breaks down and the yield strength versus grain size relationship departs markedly from that seen at

larger grain sizes. With further grain refinement, the yield stress peaks at a mean grain size in the range of 10 nm or so in many cases. Further decrease in grain size can cause softening of the solid, and then the HPR slope turns from positive to negative in the nanometer range, which is called the inverse Hall–Petch relationship (IHPR).

There is a concerted global effort underway using a combination of novel processing routes, experiments and large-scale computations to develop deeper insights into these phenomena. It has been suggested that the grain boundaries consisting of under-coordinated atoms contribute to the grain-boundary strengthening [239]. The strength maximum of Cu at a grain size of 10–15 nm is attributed to a switch in the microscopic deformation mechanism from dislocation-mediated plasticity in the coarse-grain interior to grain boundary sliding in the nanocrystalline regime [240,241]. An investigation of the flow stress of Ag clusters [242] suggest that the dislocation density model governs the grain-size dependence of the flow stress in the regime between 10 and 500 nm and that dislocation pile-up applies in the regime of 500 nm or higher. A significant portion of atoms resides in the grain boundaries and the plastic flow of the grain-boundary region is responsible for the unique characteristics displayed by such materials [243]. In the HPR regime, crystallographic slips in the grain interiors govern the plastic behavior of the polycrystalline, while in the IHPR regime, the plastic behavior is dominated by the grain boundaries. During the transition, both grain interiors and grain boundaries contribute competitively. The slope in the HPR is suggested to be proportional to the work required to eject dislocations from grain boundaries [244]. Wang et al. [245] proposed two mechanisms that influence the effective stiffness and other mechanical properties of nanomaterials. One is the softening effect due to the distorted atomic structures and the increased atomic spacings in the interface region, and the other is the baffling effect due to the existence of boundary layers between the interface and the crystalline interior. The mechanical performance of a nanocrystallite depends on the competition between these two origins. Molecular dynamics simulations suggest that the IHPR arises from sliding-accommodated grain-boundary diffusion creep [246]. The critical size depends strongly on the stacking-fault energy and the magnitude of the applied stress [247]. However, the mechanism for transition from grain interior to grain boundary is yet unclear. Unfortunately, an analytical form for the IHPR was absent until recently when Zhao et al. [31] firstly modified the HPR by introducing the activation energy that can be related directly to the $T_m$ and to the slope $A'$ [114].

Although there is a growing body of experimental evidence pointing to such unusual deformation responses in the nanometer regime, the underlying mechanisms are not fully understood. As pointed out by Kumar et al. [248], the physical origin of the IHPR has been a long-standing puzzle and the factors that dominate the critical size at which the HPR transits are yet poorly known.

It is possible to incorporate the BOLS correlation to the IHPR by considering the competition between the effect of bond-order loss on atomic cohesive energy and energy density in the continuum skin region on the mechanical strength. Atomic cohesive energy determines the temperature of melting at which the materials become extremely soft while the energy density determines the hardness. Therefore, the surface is harder at low temperatures but melts easily. A competition between the specific heat and the separation between the operation temperature and the $T_m(K_j)$ dictates the strength. The smaller the difference $T_m(K_j) - T$, the softer the nanosolid. Explanations of the size and temperature effects on mechanical strength and extensibility of nanosolid and the factors dominating the critical size for different materials have been reported separately [208].

## 5. Thermal stability

### 5.1. Cohesive energy

#### 5.1.1. Definition

The cohesive energy of a solid ($E_{coh}$) is an important physical quantity to account for the binding strength of the crystal and is equal to the energy dividing the crystal into the individually isolated atoms by breaking all the bonds of the solid. The $E_{coh}$ is given as $E_{coh}(N_j) = N_j E_B = N_j z_b E_b$, if no atomic CN imperfection is considered. The cohesive energy for a single atom, or atomic coherency, $E_B$, is the sum of the single bond energy $E_b$ over all its atomic CN, $E_B = z_b E_b$, (or $E_{Bi} = z_i E_i$ for the $i$th specific atom) for the specific atom.

The heat required for loosening an atom is proportional to the atomic $E_B$ that varies with, not only the atomic CN, but also the CN reduction induced bond-strength gain. The under-coordinated surface atoms will be less thermally stable than those inside the core interior even though the strength gain occurring in the remaining bonds of the under-coordinated atoms. For large bulk materials, effects of surface CN imperfection can be ignored but, for small particles, surface effects become dominant because of the appreciably large portion of such under-coordinated atoms at the surface. Different values of the mean $E_B$ in different systems are responsible for the fall (undercooling) or rise (overheating) of the $T_m$ of a surface and a nanosolid. The $E_B$ is also responsible for other thermally activated behaviors such as phase transition, catalytic reactivity, crystal structural stability, alloy formation (segregation and diffusion), and stability of electrically charged particles (Coulomb explosion), as well as the crystal growth and atomic diffusion, atomic gliding displacement that determine the ductility of nanosolids.

#### 5.1.2. Outstanding models

*5.1.2.1. Surface-area difference.* One approach to determine the $E_{coh}$ of a nanosolid is to consider the difference between the surface area of a whole particle and the overall surface area of all the constituent atoms in isolated state [249]. For a spherical dot with radius $R_j$ and $N_j$ atoms of diameter $d_0$, the $E_{coh}$ equals the energy required to generate the area difference, $\Delta S$, between the isolated $N_j$ atoms and the nanodot without changing the volume:

$$\begin{cases} N_j 4\pi (d_0/2)^3/3 = 4\pi (R_j)^3/3 & \text{(volume-conservation)} \\ \Delta S = \pi \left[ N_j d_0^2 - (2R_j)^2 \right] & \text{(surface-area-difference)} \end{cases}$$

Let the surface energy per unit area at 0 K be $\gamma_0$, then the overall $E_{coh}(N_j)$ is

$$\begin{cases} E_{coh}(K_j) = \gamma_0 \Delta S & = \pi N_j d_0^2 \gamma_0 \left(1 - N_j^{-1/3}\right) \\ & = E_{coh}(\infty)\left(1 - \alpha/K_j\right) \end{cases}$$

$E_{coh}(\infty) = \pi N_j d_0^2 \gamma_0$ is the cohesive energy of the $N_j$ atoms without the effect of atomic CN imperfection. The factor $\alpha$ varies with the shape and dimensionality of the solid. For a cube, the factor is 9/4 [246]; for a spherical dot, it is 1/2.

Recent development of the model by Qi and coworkers [250] covers the situations of both isolated and embedded nanosolids by considering the contribution from interface/surface atom:

$$E_{\mathrm{B,s}} = [E_{\mathrm{B}} + 3\beta(E_{\mathrm{B}}/2 + kE_{\mathrm{m}}/2)]/4$$

and the mean atomic cohesive energy becomes

$$E_{\mathrm{B}}(K_j) = E_{\mathrm{B}} + \gamma_{ij}(E_{\mathrm{B,S}} - E_{\mathrm{B}}) = E_{\mathrm{B}} + 3\gamma_{ij}\left[k\beta E_{\mathrm{m}} - (2-\beta)E_{j\mathrm{B}}\right]/8$$

where $\beta$ is the ratio of the interface area to the whole surface area, $k$ denotes the degree of cohesion between the nanocrystal and the matrix with $E_{\mathrm{m}}$ atomic cohesive energy. For a nanocrystal wholly embedded in the matrix, $\beta = 1$ and $k = 1$; for an isolated crystal, $\beta = 0$ and $k = 0$. This model improves agreement between modeling calculations and measurement than their previous assumption that the surface atomic cohesive energy is $E_{\mathrm{B}}/4$ [251].

*5.1.2.2. Atomic CN-difference*. By considering the effect of CN imperfection, Tománek et al. [127] derived the $E_{\mathrm{B}}$ for an individual atom denoted $i$:

$$E_{\mathrm{B},i} = (z_i/z_{\mathrm{b}})^{1/2} E_{\mathrm{B}}(\infty) + E_{\mathrm{R}}$$

$E_{\mathrm{R}}$ is the repulsive interaction that can be replaced by a hard-core potential. $E_{\mathrm{R}}$ is neglected at equilibrium distances. The mean $E_{\mathrm{B}}$ in a nanosolid with $N_j$ atoms is obtained by summing all bonds over the $N_j$ atoms:

$$\langle E_{\mathrm{B}}(N_j)\rangle = \sum_{\langle i,N_j\rangle} (z_i)^{1/2} E_i/N_j$$

Based on the model for the latent heat, the size-dependent cohesive energy or boiling heat can be derived [252], which agrees reasonably well with experimental data of W and Mo nanosolids.

*5.1.3. BOLS consideration*

The BOLS correlation considers contribution from atoms in the skin shells. Using the same spherical dot containing $N_j$ atoms with $N_i$ atoms at the $i$th surface shell, the average $\langle E_{\mathrm{coh}}(N_j)\rangle$ or $\langle E_{\mathrm{B}}(N_j)\rangle$ is

$$\begin{aligned}\langle E_{\mathrm{coh}}(N_j)\rangle &= N_j z_{\mathrm{b}} E_{\mathrm{b}} + \sum_{i\le 3} N_i(z_i E_i - z_{\mathrm{b}} E_{\mathrm{b}}) = N_j E_{\mathrm{B}}(\infty) + \sum_{i\le 3} N_i z_{\mathrm{b}} E_{\mathrm{b}}(z_{i\mathrm{b}} E_{i\mathrm{b}} - 1)\\ &= E_{\mathrm{coh}}(\infty)\left[1 + \sum_{i\le 3}\gamma_{ij}\left(z_{i\mathrm{b}} c_i^{-m} - 1\right)\right] = E_{\mathrm{coh}}(\infty)(1+\Delta_{\mathrm{B}}) \text{ or}\\ \langle E_{\mathrm{B}}(N_j)\rangle &= E_{\mathrm{B}}(\infty)(1+\Delta_{\mathrm{B}})\end{aligned} \tag{25}$$

where $E_{\mathrm{coh}}(\infty) = N_j z_{\mathrm{b}} E_{\mathrm{b}}$ represents the ideal situation without CN imperfection. The $z_{i\mathrm{b}} = z_i/z_{\mathrm{b}}$ is the normalized CN and $E_{i\mathrm{b}} = E_i/E_{\mathrm{b}} \cong c_i^{-m}$ is the binding energy per coordinate of a surface atom normalized by the bulk value. For a free surface, $\Delta_{\mathrm{B}} < 0$; for an intermixed interface, $\Delta_{\mathrm{B}}$ may change depending on the interfacial interaction.

Summarizing all available models, one may find that the size dependence of $E_{\mathrm{B}}$ can be numerically estimated in the scaling relationships:

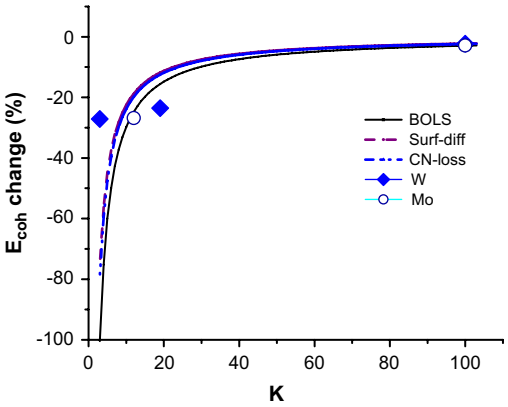


Fig. 15. Comparison of the modeling predictions with experimental results on the size-dependent $E_B$ of Mo and W nanosolids [253]. Numerical agreement is nearly identical for the compared models albeit the different physical origins.

$$\frac{\Delta E_B(K_j)}{E_B(\infty)} = \begin{cases} \sum_{i\le 3} \gamma_{ij}\left(z_{ib}c_i^{-m} - 1\right) = \Delta_B & \text{(BOLS)} \\ \sum_{i\le 3} \gamma'_{ij}\left[(z_{ib})^{1/2} - 1\right] = \Delta'_B & \text{(CN-loss)} \\ -\alpha/K_j = \delta_B & \text{(Area-difference)} \end{cases} \tag{26}$$

where $\gamma_{ij} \sim \tau c_i/K_j$ and $\gamma'_{ij} \sim \tau_i/K_j$ are the surface-to-volume ratios in the corresponding descriptions. Fig. 15 compares the modeling predictions with the measured size-dependent $\langle E_B(K_j)\rangle$ of Mo and W nanosolids [253]. From a numerical viewpoint, one could hardly tell which model is preferred to others though physical indications of the compared models are entirely different.

### *5.1.4. Atomic vacancy formation*

As an element of structural defects, atomic vacancies or point defects are very important in materials and have remarkable effects on the physical properties of a material such as electrical resistance, heat capacity, mechanical strength, etc. Atomic vacancy formation needs energy to break all the bonds of the specific atom to its surroundings, which is the same as the atomic $E_B$ in the current BOLS iteration though structure deformation or relaxation is involved upon atom evaporation. However, the structural deformation costs no additional external energy. The vacancy volume should be greater than the atomic size due to the effect of atomic CN imperfection on the bond length of atoms surrounding the vacancy. The $E_B$ values can be measured but the experimental values may have limited accuracy. For instance, the $E_B$ of a Mo atom has been measured over the large range from 2.24 to 3.3 eV [254]. Sophisticated theoretical efforts also predict the $E_B$ of metals and alloys but the theories are rather complicated and not generally applicable accurately to most metals [255].

*5.1.4.1. Brook's convention.* In the 1950s, Brooks [256] developed a semi-empirical method to calculate the $E_B$ of bulk materials. In this method, the crystal is assumed isotropic, and the formation of vacancy is considered equivalent to creating new surface, equal to the area of one unit cell, being approximately the spherical surface of the atomic volume. Meanwhile, it was assumed that the surface tension of the hole would squeeze the hole to contract in size by

distorting the rest of the crystal elastically. Then the $E_B$ equals the minimum of the sum of the increased surface energy and distortion energy. The $E_B$ for atomic vacancy formation inside a bulk solid is thus given as:

$$E_B = \pi d_0^3 \gamma_0 G(\gamma_0 + G d_0)^{-1}$$

$G$ is the shear modulus and $\gamma_0$ the surface energy per unit area surrounding the vacancy. Introducing the size effect to the $d_0$, $G$, and $\gamma_0$, the relative change of the mean $E_B$ in a nanoparticle becomes

$$\frac{E_p - E_B}{E_B} = \frac{d_p^3}{d_0^3}\left(\frac{G d_0 + \gamma_0}{G d_p + \gamma_0}\right) - 1$$

where $E_p$ and $d_p$ are the corresponding vacancy formation energy and mean atomic diameter in the nanosolid. Qi and Wang [257] have extended Brook's approach to nanostructures by assuming that the $G$ and the $\gamma_0$ of a nanosolid remain the bulk values. The key factor influencing the $E_p$ of a spherical dot of diameter $D$ is the size-dependent atom size. Assuming that a small size shrink of $\varepsilon D$ ($\varepsilon \ll 1$) results from the hole size contraction, the surface energy variation $\Delta\gamma$ and the strain-dependent elastic energy $f$ of the particle become

$$\begin{aligned} \Delta\gamma &= \pi D^2\left[(1-\varepsilon)^2 - 1\right]\gamma_0 \\ f &= \pi G D^3 \varepsilon^2 \end{aligned} \tag{27}$$

At equilibrium state, the total energy $F$, or the sum of $\Delta\gamma$ and $f$, is minimal, that is, $dF/d\varepsilon = 0$, and then the strain of the particle is:

$$\varepsilon = [1 + (G/\gamma_0)D]^{-1}$$

The average size $d_p$ of an atom shrinks due to the presence of $G$ and $\gamma_0$, $d_p = d_0(1-\varepsilon)$.

*5.1.4.2. BOLS analysis.* The bond strain derived from Brook's approximation is compared with the current BOLS correlation as follows:

$$\frac{\Delta d_p}{d_0} = \begin{cases} -[1 + (G/\gamma_0)D]^{-1} \cong -K_{dc}/(K_j + K_{dc}) & \text{(Brook)} \\ \sum_{i\le 3} \gamma_i(c_i - 1) = \Delta_d & \text{(BOLS)} \end{cases}$$

where $K_{dc} = \gamma_0/(2d_0G)$ is the critical value and $K_j$ remains its usual meaning of dimensionless form of size. Further simplification of Eq. (27) leads to the atomic vacancy formation energy in a nanometric system as given in comparison with the BOLS derivative:

$$\frac{\Delta E_B(K_j)}{E_B(\infty)} = \begin{cases} -(1 + K_j/\alpha)^{-1} & \cong -K_{Ec}/(K_{Ec} + K_j) \\ \sum_{i\le 3} \gamma_{ij}\left(z_{ib}c_i^{-m} - 1\right) & = \Delta_B \end{cases} \tag{28}$$

where $\alpha = (2gd_0 + 3)/[2d_0(g^2d_0 + g)]$ ($\sim 10^{-1}$ level) and $g = G/\gamma_0 \sim 10\ \mathrm{nm}^{-1}$. $K_{Ec} = \alpha/(2d_0)$ is the critical value of $K_j$. For Pd and Au nanosolids, the critical $K_{Ec}$ and $E_{dc}$ values are calculated based on the given $G$ and $\gamma_0$ bulk values as listed in Table 3. Fig. 16 compares the predictions of the two models. At the lower end of the size limit ($K_j = 1.5$), the particle contracts by 40% associated with 12% reduction of the $E_B$ according to Brook's convention [257]. In comparison, the BOLS correlation predicts a 25% bond contraction and 70% lower for the

Table 3
Shear modulus, surface energy and the calculated $\alpha$ values for Pd and Au

| | G ($10^{10}$ N/m$^2$) [258] | $\gamma_0$ (J/m$^2$) [259] | $\alpha$ (nm) | $K_{Ec}/K_{dc}$ |
|---|---|---|---|---|
| Pd | 4.36 | 2.1 | 0.104 | 0.1894/0.8770 |
| Au | 2.6 | 1.55 | 0.119 | 0.2066/1.035 |

$E_B$ of the smallest size. The approximation based on Brook's relation seems to overestimate the bond contraction and underestimate the $E_B$ suppression because of the assumption of size independent $G$ and $\gamma_0$. Actually, the atomic cavity should expand instead as the remaining bonds of the surrounding atoms will contract. The strain of the entire nanoparticle arises from surface bond contraction and has little to do with the atomic void inside. One may note that $E_B$ varies from site to site due to the difference of atomic CN environment at various locations of the solid.

### 5.2. Liquid–solid transition

#### 5.2.1. Outstanding models

The melting behavior of a surface and a nanosolid has attracted tremendous research interest both theoretically and experimentally for decades [13]. In many cases, surface melting and evaporation often occur at temperatures lower than the corresponding bulk values [260,261]. For substrate-supported nanosolids with relatively free surfaces, the $T_m$ decreases with particle size (termed as undercooling). In contrast, as per the existing experimental evidence for embedded nanosolids, the $T_m$ can be lower than the bulk $T_m$ for some matrices. However, the same nanosolids embedded in some other different matrices may exhibit overheating to temperatures higher than the bulk $T_m$. An MD calculation suggested that a 115 K overheating occurs to Pb(111) films confined in an Al(111) matrix [262]. The $T_m$ suppression for a free surface is attributed to the reduced degree of confinement, and hence the increased entropy of the molecules at the surface compared with atoms in the bulk, whereas the $T_m$ elevation or depression of the embedded nanosolids depends on the coherency between the nanosolids and the embedding matrix [263,264].

There is an extensive database describing surface and nanosolid $T_m$ suppression [265–270]. For instance, a photoelectron emission study [271] confirmed that lithium (110) surface melting

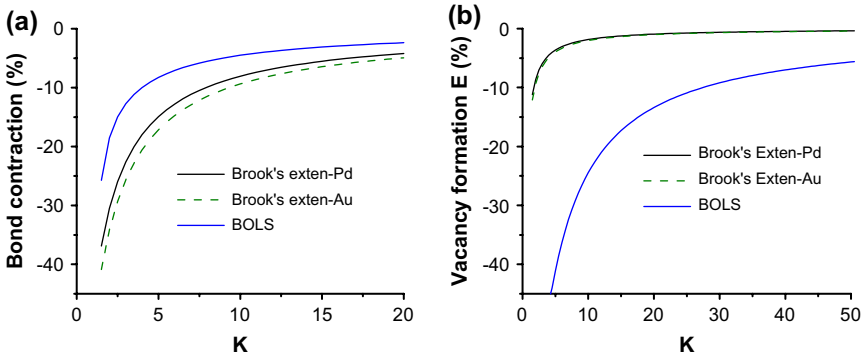


Fig. 16. Comparison of the bond (particle size) contraction and atomic vacation-formation energy derived from the BOLS premise and from Brook's approach for Pd and Au nanosolids.

occurs 50 K below the bulk $T_m$ (453.69 K). A thermal and temperature-resolved XRD analysis revealed that the $T_m$ of nanometer sized drugs (polymer) also drops (by 33 and 30 K for 7.5 nm-sized griseofulvin and 11 nm-sized nifedipine, respectively) in a $1/R$ fashion [272]. STM measurements of a reversible, temperature-driven structural surface phase transition of Pb/Si(111) nanoislands indicates that the transition temperature decreases with inverse of island and domain size and the phase transition is independent of the processes of cooling or heating [273]. It was found by calculation [274] that the melting temperature of a Pd nanowire is lower than the bulk value but higher than that of the cluster. Surface premelting at much lower temperatures than the near first-order transition temperatures noted above was observed in both Pd systems. The surface premelting temperature range was higher for the nanowire than for the cluster. A quasi-liquid skin grows from the surface in the radial direction for both cluster and wire, in the surface premelting regime, followed by the breakdown of order in the remaining solid core at the transition temperature.

Numerous models for the size effect on the nanosolid melting have been developed in terms of classical thermodynamics and atomistic MD simulations [41,80–88,96,275–280]. In general, the size-dependent $T_m(K_j)$ follows the empirical scaling relationship:

$$\frac{\Delta T_m(K_j)}{T_m(\infty)} = -\frac{K_C}{K_j} \tag{29}$$

where $K_C$ is the critical size at which the nanosolid melts completely, or the $T_m(K_C) = 0$ K. The physical meaning of the $K_C$ is complex and is the focus of modeling studies.

*5.2.1.1. Classical thermodynamics*. Classical thermodynamic theories based on the surface Laplace and the Gibbs–Duhem equations [277] have derived that $K_C$ obeys the following relations [275,278]:

$$K_C = \frac{-2}{H_m(\infty)} \times \begin{cases} \sigma_{sv} - \sigma_{lv}(\rho_s/\rho_l)^{2/3}, & \text{(HGM)} \\ \sigma_{sl}\left(1 - K_0/K_j\right)^{-1} + \sigma_{lv}(1 - \rho_s/\rho_l), & \text{(LSM)} \\ [\sigma_{sl}, 3(\sigma_{sv} - \sigma_{lv}\rho_s/\rho_l)/2] & \text{(LNG)} \end{cases}$$

where $H_m$ is the latent heat of fusion, $\rho$, the mass density and $\sigma$, the interfacial energy. Subscripts s, l, and v represent the phases of solid, liquid and vapor, respectively. The critical value of $R_C$ ($= K_C d_0$) is normally several nanometers. Expressions for $K_C$ correspond to three outstanding mechanisms in terms of classical thermodynamics:

(i) The homogeneous melting and growth (HMG) model [80,81] considers the equilibrium between the entire solid and the entire molten particle, which suggests that the melt proceeds throughout the solid simultaneously. This model describes well the case of smallest nanoparticle with $K_C$ equal to three or less or otherwise to larger values with void defects being involved.

(ii) The liquid shell nucleation (LSN) model [82] assumes that a liquid layer of thickness $K_0$ is in equilibrium at the surface, which indicates that the surface melts before the core of the solid.

(iii) The liquid skin nucleation and growth (LNG) model [86,87] suggests that melting starts by the nucleation of a liquid layer at the surface and moves into the solid as a slow process

with a definite activation energy. The LSN and LNG mechanisms describe the melting of a flat surface or larger nanoparticles.

*5.2.1.2. Atomistic models.* However, models based on atomistic/MD suggest that the critical $R_C$ follows:

$$R_C = \begin{cases} 5230 v_0 \gamma, & \left(v_0 = 4\pi d_0^3/3\right) \quad \text{(Liquid-drop)} \\ \alpha_m d_0, & \left(\alpha_m - \text{constant}\right) \quad \text{(Surf-phonon)} \\ R_0\left(\dfrac{1-\beta}{1-R_0/R_j}\right), & \text{(Surf-RSMD)} \end{cases} \tag{30}$$

The liquid-drop model [94] relates the $T_m$ to the $E_{coh}$ of the entire particle of $N_j$ atoms. With surface involvement, the $E_{coh}$ equals the difference between the volume cohesive energy ($N_j E_B$) and the surface energy ($4\pi d_0^2 N_j^{2/3}\gamma$). The mean cohesive energy per atom with volume $v_0$ in the solid is $E_B(R_j) = E_B - E_{B,S}N_j^{-1/3}$, where $E_{B,S} = 4\pi d_0^2\gamma$ is the cohesive energy for an atom at the surface. The relation between the $E_B$ and the $E_{B,S}$ is given empirically as $E_{B,S} = 0.82E_B$ [281]. Based on the Lindemann's criterion of melting, an expression for the $T_m$ of the bulk material is derived as [282]:

$$T_m(\infty) = nf_e^2 E_B/(3k_B Z) \propto E_B \tag{31}$$

where $n$ is the exponent of the repulsive part of the interaction potential between constituent atoms, $Z$ is the valence of the atom, which is different from the atomic CN. The coefficient $f_e$ is the thermal expansion magnitude of an atom at $T_m$. At $T_m$, the $f_e$ is less than 5% [283]. The fact that the bulk $T_m$ varies linearly with the $E_B$ and hence with the $E_{B,S}$ agrees with the data measured for metals [284]. Therefore, the $T_m$ of a solid can be simply related to the mean atomic $\langle E_B(K_j)\rangle$ of the solid. Replacing the $E_B$ with $E_B(K_j)$, Nanda et al. [94] derived the liquid-drop model for the size-dependent $T_m(K_j)$ based on the relation between the bulk $T_m$ and the cohesive energy per coordinate:

$$E_b(\infty) = \eta_{1b} T_m(\infty) + \eta_{2b} \tag{32}$$

where the constant $\eta_{2b}$ represents $1/z$ fold of enthalpy of fusion and atomization being required for evaporating an atom from the molten state. $\eta_{1b}$ is the specific heat per coordinate in the bulk. The $\eta_{1b}$ and $\eta_{2b}$ values, as tabulated in Table 1 (see Section 2), for various structures and elements have been obtained from fitting experimental data [94].

According to the liquid-drop model, the critical radius at which $T_m(K_C)$ approaches 0 K is in the range of 0.34 (for Mn)–1.68 nm (for Ga). The liquid-drop model underestimates the $T_m$ of Sn, Bi, In, and Pd nanosolids by 3–12%, due to the involvement of intercluster interaction and particle–substrate interaction [94].

The surface-phonon instability model [95,285] suggests that $T_m(K_j)$ varies with $T_m(\infty)$ and with the energy of intrinsic defect formation at the surface. Within the thermo dynamical limit (particle radius larger than 2 nm), the accumulated effect of size reduction and high electronic excitation combine [286].

The lattice-vibration instability model [89–93,96] was advanced based on Lindemann's vibrational-lattice instability criterion [78]. The melting behavior of a nanosolid is related to the ratio ($\beta$) of the root-mean-square-displacement (RMSD, $\delta^2$) of an atom at the surface to the RMSD of an atom inside a spherical dot. $\beta$ is assumed to be a size independent adjustable parameter:

$$\beta = \delta_s^2(D)/\delta_b^2(D) = \delta_s^2(\infty)/\delta_b^2(\infty)$$

The $K_C$ in the RMSD model is determined by $K_0 = \tau$ at which all the constituent atoms have surface features. This model indicates that if $\beta > 1$, the surface melts below the bulk $T_m$, and vice versa. According to the RMSD, a nanosolid with $K_C = \tau$ shells will melt at 0 K.

*5.2.1.3. Overheating*. In the case of embedded nanosolids, the coefficient of surface energy will be replaced by the interfacial energy if surfaces are completely saturated with atoms of the surrounding matrix. Nanda et al. [94] describe the overheating by introducing the ratio as a perturbation of surface energy between the matrix and the embedded specimen

$$\frac{\Delta T_m(K_j)}{T_m(\infty)} = -\frac{K_C}{K_j}\left(1 - \frac{\gamma_{Mat}}{\gamma}\right)$$

If the surface energy of the matrix $\gamma_{Mat} > \gamma$, the core nanosolid melts at a temperature that is higher than its bulk counterpart. This expression matches the experimental data of Pb particles embedded in an Al matrix but overestimates the $T_m$ for indium particles embedded in an Al matrix by some 10–20 K using the known $\gamma$ and $\gamma_{Mat}$ values. Based on the size-dependent magnitudes of the atomic vibrations, Jiang et al. [15,96] extended the $T_m(K_j)$ model for the overheating, according to which the overheating is possible if the diameter of the constituent atoms of the matrix is smaller than the atomic diameter in the embedded nanosolid. Therefore, both the overheating and undercooling of a nanosolid can be modeled simply by adjusting the $\beta$ value in the RMSD model. Overheating happens when $\beta < 1$, which means that the matrix confines the vibration of the interfacial atoms.

However, MD simulations [287] suggest that atoms in the bulk interior of an isolated nanosolid melt prior to the surface and the surface melting occurs at relatively higher temperatures. This prediction seems to be contradicted by existing evidence but it is possible if the bond nature changes upon CN reduction, as discussed shortly for the overheating of the smallest $Ge^+$ and Sn clusters. In contrast, MD calculations [288] of the melting evolution, atomic diffusion and vibrational behavior of bcc metal vanadium nanoparticles with diameters around 2–9 nm suggest that the melting proceeds in two stages. The stepwise premelting of a surface layer of 2–3 lattice constants thick was followed by the abrupt overall melting of the whole cluster. The heat of fusion of nanoparticles is also inversely proportional to the reciprocal of the nanoparticle size. The diffusion is mainly localized to the surface layer at low temperatures and increases with the reduction of nanoparticle size, with the temperature being held constant.

The models of LSN, HMG and LNG suit only the cases of $T_m$ suppression ($\Delta T_m < 0$) while the liquid-drop and the RMSD models cover both the undercooling and overheating. For particles larger than several nanometers, all the models worked sufficiently well in simulating the size-dependent melting despite the disputable mechanisms. However, a large number of independent parameters such as the latent heat of fusion, mass density and interfacial energy of different phases are to be considered when evaluating the melting behavior of a nanosolid.

*5.2.2. BOLS consideration*

It is known that the total energy of a pair of atoms (Section 2) can be expressed in a Taylor's series, which can be decomposed as energies of binding at 0 K, $E_b(r)$, and the thermal vibration energy, $E_V(T)$:

$$\begin{aligned} E_{\text{total}}(r,T) &= \sum_n \left(\frac{\mathrm{d}^n u(r)}{n!\mathrm{d}r^n}\right)_{r=d_0} (r-d_0)^n \\ &= u(d_0) + 0 + \frac{\mathrm{d}^2 u(r)}{2!\mathrm{d}r^2}\bigg|_{d_0} (r-d_0)^2 + \frac{\mathrm{d}^3 u(r)}{3!\mathrm{d}r^3}\bigg|_{d} (r-d_0)^3 \cdots \\ &= E_b(d_0) + \frac{k}{2}(r-d_0)^2 + \frac{k'}{6}(r-d_0)^3 + \cdots \\ &= E_b(d_0) + E_V(T) = \begin{cases} 0, & (\text{Evaporation}) \\ E_C, & (\text{Critical} - T_C) \end{cases} \end{aligned} \tag{33}$$

The term with index $n=0$ corresponds to the minimal binding energy at $T=0$ K, $E_b(d_0)<0$. The term $n=1$ is the force $[\partial u(r)/\partial r|_{d_0}=0]$ at equilibrium and terms with $n\geq 2$ correspond to the thermal vibration energy, $E_V(T)$. The $T_C$ can be any critical temperature for event such as liquid–solid, liquid–vapor, or other phase transition, like magnetic and ferroelectric transitions. By definition, the thermal vibration energy of a single bond is

$$\begin{aligned} E_V(T) &= \frac{\mathrm{d}^2 u(r)}{2!\mathrm{d}r^2}\bigg|_{d} (r-d)^2 + \frac{\mathrm{d}^3 u(r)}{3!\mathrm{d}r^3}\bigg|_{d} (r-d)^3 \cdots \\ &\cong \mu\omega^2 (r-d)^2/2 + 0\left[(r-d)^{n>2}\right] \\ &\approx k_v (r-d)^2/2 = \eta_1 T \end{aligned} \tag{34}$$

where $r-d_0$ is the magnitude of lattice vibration and $\mu$ is the reduced mass of a dimer of concern. The term $q_v=\mu\omega^2$ is the force constant for lattice vibration with an angular frequency of $\omega$.

The physical grounds for the BOLS iteration is that, if one wishes to peel off or loosen an atom in the solid thermally, one must supply sufficient thermal energy to overcome the cohesion that binds the specific atom to its surrounding neighbors. The thermal energy required to loosen one bond is the separation of $E_b(T_C)-E_b(T)$, as illustrated in Section 2. If the $E_V(T)$ is sufficiently large, all the bonds of the specific atom will break and this atom will leave the solid. At the evaporating point of any kind of solid, $E_{\text{total}}=0$; at the critical point, $E_{\text{total}}=E_C$. We may consider step by step the energies required for melting (or dissociating) a single bond, a single atom, and then shell-by-shell of a nanosolid of radius lined with $K_j$ atoms.

The thermal energy required for loosening a single bond of an atom in the $i$th atomic layer by raising the temperature from $T$ to $T_C$ is given as

$$E_T = E_b(T_C) - E_b(T) = \eta_1 (T_C - T) \propto E_b(0) \tag{35}$$

The energy required for melting the entire atom in a bulk is proportional to the $E_B(0)$, which is a sum of the single bond energy over all the atomic CN.

Melting a nanosolid comprising $N_j$ atoms in a shell-by-shell manner requires thermal energy that is proportional to the cohesive energy of the entire solid:

$$T_{\mathrm{m}}(K_j) \propto E_{\mathrm{coh}}(K_j) = N_j z_{\mathrm{b}} E_{\mathrm{b}} + \sum_{i\leq 3} N_i (z_i E_i - z_{\mathrm{b}} E_{\mathrm{b}}) \tag{36}$$

It is reasonable to assume a homogenous bond nature in the solid. The $E_{\mathrm{coh}}$ may vary from material to material but for a specific sample, the portion of $E_{\mathrm{coh}}$ needed for the specific phase transition should be fixed [282]. The relative change of $T_{\mathrm{m}}(K_j)$ and $T_{\mathrm{C}}(K_j)$ is then:

$$\frac{\Delta T_{\mathrm{m}}(K_j)}{T_{\mathrm{m}}(\infty)} = \frac{\Delta T_{\mathrm{C}}(K_j)}{T_{\mathrm{C}}(\infty)} = \frac{\Delta E_{\mathrm{B}}(K_j)}{E_{\mathrm{B}}(\infty)} = \sum_{i\leq 3} \gamma_{ij}\left(z_{i\mathrm{b}} c_i^{-m} - 1\right) = \sum_{i\leq 3} \gamma_{ij}(\alpha - 1) = \Delta_{\mathrm{B}} \tag{37}$$

It is not surprising that the temperature is always the same throughout the small specimen in operation whereas the intrinsic $T_{\mathrm{C},i}$ may vary from site to site if the sample contains atoms with different CN, such as atoms at the surface, grain boundary, or sites surrounding voids or stacking faults. This mechanism may explain why the latent heat of fusion of a solid has a broad range of measured values rather than appearing as a sharp peak [275,289]. For a solid with numerous randomly distributed defects, the mechanism of random fluctuation melting [88] could dominate because the energy required for breaking one bond and hence the energy needed to melt an individual atom with different CN is different. This mechanism also explains the broad temperature range for glass transition of an amorphous state as the random distribution of atomic CN imperfection in the amorphous solid. Glass transition happens in a range of temperatures and it is material processing condition dependent [290].

On the other hand, from a classical thermodynamic point of view, the thermal energy $E_{\mathrm{T}}$ required for the liquid–solid phase transition can be estimated by integrating the specific heat over the entire solid with and without CN imperfection from zero to the $T_{\mathrm{m}}$:

$$\frac{\Delta E_{\mathrm{T}}(K_j)}{E_{\mathrm{T}}(\infty)} = \frac{\int_0^{T_{\mathrm{m}}(K_j)} C_{\mathrm{p}}(K_j, T)\mathrm{d}T}{\int_0^{T_{\mathrm{m}}(\infty)} C_{\mathrm{p}}(\infty, T)\mathrm{d}T} - 1 \cong \frac{\Delta T_{\mathrm{m}}(K_j)}{T_{\mathrm{m}}(\infty)} = \Delta_{\mathrm{B}} \tag{38}$$

with the assumption that $C_{\mathrm{P}}(K_j, T) \cong C_{\mathrm{P}}(\infty, T) \cong C_{\mathrm{V}}(\infty, T) =$ constant in the entire measured temperature range [104]. It is true in fact that $C_{\mathrm{P}}(K_j, T) \neq C_{\mathrm{P}}(\infty, T) \neq C_{\mathrm{V}}(\infty, T) \neq$ constant. The Debye temperature and hence the specific heat $C_{\mathrm{P}}$ is size and temperature dependent [90,291]. This effect may lead to 3–5% deviation of the $C_{\mathrm{P}}$. Besides, $(C_{\mathrm{P}} - C_{\mathrm{V}})/C_{\mathrm{V}} \sim 3\%$ [104]. However, compared with the precision in determining the size and shape of a nanosolid such errors are negligible. Actually, measurements [292–294] show that the $C_{\mathrm{P}}$ varies insignificantly with the particle size in the measured temperature range. Therefore, it is acceptable to simplify the $C_{\mathrm{P}}$ as a constant in the integration. Such simplification may lead to slight deviation in the integration in Eq. (38) from the true value. Nevertheless, one should particularly note that the deviation of the integration from true value only affects the precision of the $m$ value or the effective $z_{i\mathrm{b}}$, it does not change the nature of the phenomenon. Actually, Eq. (37) extends classical thermodynamics (38) to include an atomistic approach.

### *5.2.3. Verification: liquidation and evaporation*

Eq. (37) indicates that the size-dependent $\Delta T_{\mathrm{m}}(K_j)/T_{\mathrm{m}}(\infty)$ originates from the relative change of the $E_{\mathrm{B},i}$ of a surface atom to the bulk value. The $\Delta T_{\mathrm{m}}(K_j)/T_{\mathrm{m}}(\infty)$ follows the scaling law given in Eq. (13) in Section 2. Fig. 17 compares predictions using parameters given in Table 4 with the measured size-dependent melting behavior of metals, semiconductors, inert

gases and methyl-chloride polymer (m-Cl), as well as embedded systems showing overheating effects. The size-dependent evaporating temperatures ($T_{eva}$) of Ag and CdS nanosolids also follow the trend of prediction.

It is interesting to note that Al nanosolids grown on an SiN substrate are more plate-like ($\tau = 1$) throughout the measured size but Sn on SiN and Au on C are more spherical-like ($\tau = 3$) at particle sizes smaller than 10 nm. The melting profiles show that at the smaller size range, the Au/W interface promotes more significantly the melting of Au (undercooling) than the Au/C interface. The silica matrix causes a slight overheating of the embedded Au solid compared with the curves for Au on the other two substrates. This understanding also provides information about the mode of epitaxial crystal growth and the bonding status between the nanosolid and the substrate. The deviation from theory and experiment may provide information about the difference in interfacial energy between the particles and the substrates, which is expected to be subject to the temperature of formation.

The curent exercise indicates that the overheating of In/Al ($T_{m,In}/T_{m,Al} = 530/932$), Pb/Al (600/932), Pb/Zn (600/692), and Ag/Ni (1235/1726) [295] systems originates from the interfacial bond strengthening. It is understandable that an atom performs differently at a free surface from an atom at the interface. Although the coordination ratio at the interfaces suffers little change ($z_{ib} \sim 1$), formation of the interfacial compound or alloy alters the nature of the interatomic bond that should be stronger. In this case, we may replace the $z_{ib}c_i^{-m}$ with a parameter $\alpha$ to describe the interfacial bond enhancement due to the interfacial effect, as indicated in panel (g). Numerical fitting leads to an $\alpha$ value of 1.8, indicating that an interfacial bond is 80% stronger than a bond in the core/bulk interior. If we take the bond contraction, 0.90–0.92 [105], as determined from the As and Bi impurities in CdTe compound into consideration, it is readily found that the $m$ value is around 5.5–7.0. The high $m$ value indicates that bond nature indeed evolves from a compound with $m$ around four to one with more covalent nature. Therefore, the deformed and shortened interfacial bond is much stronger. This finding means that electrons at an interface are deeply trapped and densified. Densification of energy and mass also happens as a result. Therefore, it is understandable that twins of nanograins [296] and the multilayered structures [297] are stronger and thermally more stable. It is anticipated that a thin insulating layer could form in a hetero-junction interface because of the interfacial bond nature alteration and the charge trapping effect. Interestingly, recent theoretical calculations confirmed by electron microscopy [108], revealed that junction dislocations in aluminum could have compact or dissociated core interlayers. The calculated minimum stress ($\sigma_P$) required for moving an edge dislocation is approximately 20 times higher for compact dislocations than for equivalent isolated dislocations. As anticipated, this finding provides new insight into the deformation of ultra-fine-grained metals. Density functional simulations at temperatures near the $T_m(\infty)$ suggested that the solid–liquid phase-transition temperature at the semiconductor surfaces can be altered via a monolayer coating with a different lattice-matched semiconducting material. Results show that a single-monolayer GaAs coating on a Ge(110) surface could raise the Ge melting temperature (1211 K) with an association of a dramatic drop of the diffusion coefficient of the Ge atoms to prevent melting of the bulk Ge layers. In contrast, a single-monolayer coating of Ge on a GaAs(110) surface introduces defects into the bulk and induces melting of the top layer of GaAs atoms 300 K below the GaAs melting point (1540 K). Therefore, overheating is subject to the configuration of the hetero-junction interface and their respective $T_m(\infty)$ as well.

The measured $T_m$ of Si and CdS nanosolids appeared to be lower than the expected values compared with the predicted curve with $m = 4.88$ for Si. The reason for the deviation could be

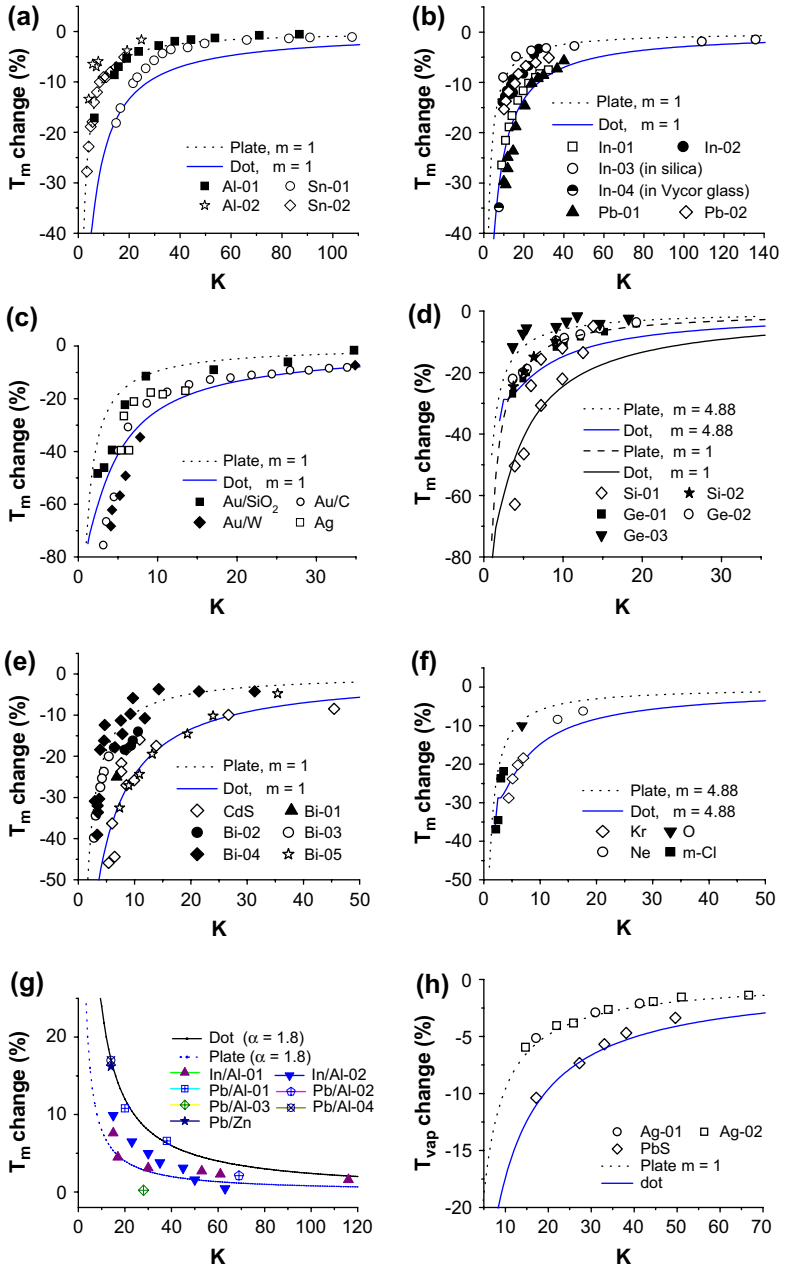


Fig. 17. Agreement between predictions (solid lines) and experimental observations of the size-and-shape dependence of the $T_m$ suppression of (a) Sn and Al on $Si_3N_4$ substrate [104,294], (b) In and Pd, (c) Au on C [81], W [80] and embedded in silica [300], (d) Ge and Si, (e) Bi and CdS, (f) Kr, Ne and O, and m-Cl, (g) overheating of embedded In and Pb, and (g) $T_{eva}$ of Ag and PbS nanosolids [203]. Parameters and references are given in Table 4.

Table 4
Parameters used in calculations presented in Fig. 17

| Medium | $T_m(\infty)$ | $T_m$ intercept | Data sources (Refs.) |
|---|---|---|---|
| Al-01 (on SiN) | 933.25 | | [293] |
| Al-02 | | | [301] |
| Sn-01 (on SiN) | 505.06 | | [302] |
| Sn-02 | | | [303] |
| Au/C | 1337.33 | | [81] |
| Au/$SiO_2$ | | | [300] |
| Au/W | | | [80] |
| Ag | 1234 | 947 | |
| In-01 | 429.76 | 438.9 | [268] |
| In-02 | | 433 | [303] |
| In-03 | | 443 | [304] |
| Pb-01 | 600.6 | 632.6 | [305] |
| Pb-02 | 600.6 | 607 | [268] |
| Si-01 | 1685 | 1510 | [306] |
| Si-02 | | | [307] |
| Ge-01 (beginning) | 930 | 910 | [308] |
| Ge-02 (ending) | – | 1023.3 | |
| Ge-03 (recrystallization) | – | 1260.8 | |
| CdS | 1678 | 1346 | [13] |
| Bi-01 | 544.52 | | [268] |
| Bi-02 | | 618.9 | [303] |
| Bi-03 | | 559.9 | [176] |
| Bi-04 | | 587.6 | [309] |
| Bi-05 | | 557.8 | [310] |
| Kr | 116 | 109.2 | [311] |
| O | 54.4 | | [312] |
| Ne | 24.6 | | [306] |
| Methyl chloride (m-Cl) | 175.6 | | [311] |
| In/Al-01 | 429.76 | 433 | [313] |
| In/Al-02 | 429.76 | 423.8 | [303] |
| Pb/Al-01 | 933.25 | 613.2 | [263] |
| Pb/Al-02 | | | [314] |
| Pb/Al-03 | | | [315] |
| Pb/Al-04 | | | [316] |
| Pb/Zn | 692.73 | | [312] |

For metals, $m = 1$. For embedded system, the $z_{ib}c_i^{-m}$ is replaced with a constant $\alpha$ that describes the bond strength enhancement due to the alloying at the interfaces. $T_m$ is the intercept of least-root-mean-square linearization of the experimental data, which calibrate the measurements. Atomic sizes are referred to in Appendix A.

the definition of melting temperature that may refer to temperature of coalescence or complete melting. For instance, molecular dynamics calculations revealed that [298] coalescence occurs at temperatures lower than the cluster melting point, and that the difference between coalescence and melting temperatures increases with decreasing cluster size. In the normalization of the scaling relation, the coalescence temperature is lower than the $T_m$ and the coalescence $T$ drops faster than $T_m$ with solid size. The size-dependent $T_m$ of Kr, Ne, and O solids follows the curve of $m = 4.88$ as well, despite the accuracy of measurement. The indium particle

encapsulated in the controlled-pore silica exhibits overheating while the indium embedded in Vycor glass shows no overheating effect. From the RMSD instability point of view, the interfacial binding constrains the RMSD of the interfacial atom to be smaller than that of a bulk atom [96].

Eq. (37) indicates that the quantity $\alpha = z_i/z_b c_i^{-m}$ dictates the process of overheating ($\alpha > 1$, $T_m$ elevation for chemically capped nanosolids) or undercooling ($\alpha < 1$, $T_m$ suppression of free-standing nanosolids). For a capped nanosolid, $z_i/z_b \sim 1$, the $\alpha$ represents the interfacial bond strengthening as no apparent bond-order loss can be recognized. For a free-standing nanosolid, there are two possibilities for $\alpha > 1$. One is that the $m$ increases as $z_i$ is reduced and the other is that the $c_i$ is much lower than the prediction [299].

As the particle size is reduced, the surface curvature will increase and the surface atomic CN will further decrease and the bond should be even shorter. Increasing the particle size, the area of interface between the particle and the substrate increases. Atoms at the interface perform quite differently from atoms at the free surface. These artefacts may bring errors in the measurement that deviate from ideal modeling expectations. As we noted, the possible errors affect the accuracy of the $m$ value and the effective $z_{ib}$ ratio in Eq. (37) but not the nature of the phenomenon or the general trend of change. Compared with the accuracy of size determination, these artefacts may be negligible. From the perspective of equilibration between the thermal energy of melting and the cohesive energy of an atom at different sites, the proposed BOLS correlation mechanism could incorporate with the existing models including mechanism of random fluctuation melting [88] and could link all the competent factors involved to the effect of atomic CN imperfection.

### 5.2.4. $T_m$ oscillation

*5.2.4.1. Observations.* Numerous studies show that the surface shells are indeed harder than the bulk interior but the surface melts easier than the core interior of the nanosolid. XRD in ultra-high vacuum [278] reveals that the $T_m$ of Pb nanosolids drops with crystallite size and favors the liquid skin melting mechanism. Such melting is demonstrated via the reversible growth of a 0.5 nm (2 atomic diameters) thick liquid skin on 50 nm-sized crystallites. It is surprising, however, that sophisticated experimental [266,317] and theoretical [318–320] efforts have uncovered recently that a freestanding nanosolid at the lower end of the size limit, or clusters containing 10–50 atoms of $Ga^+$ or atoms in group IV-A of the Periodic Table, IV-an elements, melt at temperatures that are 10–100% or even higher than the bulk $T_m(\infty)$. For example, $Ga^+_{39-40}$ clusters were measured to melt at about 550 K, while a $Ga^+_{17}$ cluster does not melt even up to 700 K compared with the $T_m(\infty)$ of 303 K [317]. Small Sn clusters with 10–30 atoms melt at least 50 K above the $T_m(\infty)$ of 505 K [266]. Advanced DFT MD simulations suggest that $Ga^+_{13}$ and $Ga^+_{17}$ clusters melt at 1400 and 650 K [318], and $Sn_n$ ($n = 6$, 7, 10 and 13) clusters melt at 1300, 2100, 2000, and 1900 K, respectively [320]. For an $Sn_{10}$ cluster, the structural transition is calculated to happen at 500 and 1500 K and the structural transition of an $Sn_{20}$ cluster occurs at 500 and 1200 K [321]. Recent calorimetric measurements [322] on unsupported $Sn^+_n$ particles clarified that the $Sn^+_{10}$ and $Sn^+_{11}$ clusters survive up to 1073 K while Sn clusters containing $n > 19$ and $n < 8$ atoms are less thermally stable as melting occurs at temperature around 773 K or below. $Sn_{19}$ can remain solid up to 673 K while $Sn_{20}$ melts below 673 K. Calculations [319] suggested that the IV-a elements, $C_n$, $Si_n$, $Ge_n$, and $Sn_n$ ($n \sim 13$) clusters melt at temperatures higher than their $T_m(\infty)$. The measured melting temperatures for Bi particles [323] of 7 nm in radius were similar, being up to 50 K above the value predicted by the homogeneous melting

model. The $C_{13}$ cluster prefers a monocyclic ring or a tadpole structure which is most probable to appear in the simulated annealing when the temperature is between 3000 and 3500 K. Theoretical calculation suggested that at the smallest sizes, carbon atoms tend to form tubes or fullerene rather than tetrahedron diamond [324]. Although the $T_m$ may be overestimated to some extent for the smallest clusters [320], the calculated $T_m$ elevation follows the trend of measurement.

The $T_m$ elevation of the smallest Ga and Sn nanosolid is attributed either to the bond nature alteration from covalent-metallic to pure covalent with slight bond contraction [318,325], or to the significant geometrical reconstruction as Ge, Si, and Sn clusters are found to be stacks of stable tricapped triagnal prism units [326]. However, consistent insight into the $T_m$ oscillation over the whole range of sizes (from single atom to the bulk crystal) is yet lacking though numerous outstanding models have been developed specifically for the $T_m$ elevation or suppression.

*5.2.4.2. Simulation.* We may fit the measured $T_m$ oscillation over the whole range of sizes for Sn and $Ga^+$ clusters by varying the bond character parameter $m$ with atomic CN. Optimization leads to the relation that expresses the $m$ value over the range from seven at $z = 2$ to one at $z > 4$:

$$m(z) = 1 + 12/\{1 + \exp[(z-2)/1.5]\}$$

It is seen from Fig. 18 that the $T_m$ curves drop generally with size and then bend up at $K_j \sim 3$ ($\log(K_j) \sim 0.5$ or $z_i \sim 3$) for higher $m$ values. If the $T_m$ rise originates from the $c_i$ deviation without bond nature change, the bond will contract to $c_i = 0.7^7 = 0.082$. A 92% bond contraction is strictly forbidden. Therefore, the $m$ value, or bond nature, must change with CN reduction. As the smallest clusters are not spherical in shape, the equivalent size specified herein might be subject to adjustment. It is surprising that evolution of $m(z)$ matches closely the measurement of $Ga_{17}^+$, $Ga_{39-40}^+$, $Sn_{19-31}$ and $Sn_{500}$ clusters and Sn nanosolids deposited on $Si_3N_4$ substrate as well [286]. Calculations [317] show that the $T_m$ transition for $Sn_{6-13}$ happens at $Sn_7$ though the estimated $T_m$ is subject to experimental confirmation.

Results indicate that the nature of the Sn–Sn and Ga–Ga bond indeed evolves from metallic-covalent to pure covalent as atomic CN reduces to much lower values, agreeing with that proposed by Chacko et al. [318]. This feature also complies with theoretical findings that the Al–Al bond for under-coordinated or distorted Al atoms at grain boundaries [327] and at free surfaces [328] becomes shorter (~5%) and stronger with some covalent characteristics [329]. However, bond nature evolution in $Al_{49-60}^+$ clusters appears not as significant as in Sn and Ga, as the $T_m$ for $Al_{49-63}^+$ is 300 K lower than the $T_m(\infty)$ of bulk Al. The abrupt $T_m$ rise (~180 K) for $Al_{51-54}^+$, $Sn_{10-11}^+$ and $Sn_{19-20}^+$ clusters [334] may be partly due to the closed shell structures that are highly stable [330,331]. Bond nature evolution should also cause conductor–insulator transition such as in a Pd solid containing 10–100 atoms [12], because of the depressed potential well of traps of all the involved atoms with low coordination. As anticipated by the BOLS correlation, strong localization of charges in the surface-trapping region should be responsible for bond nature evolution/alteration and conductivity reduction of small specimens. Results show that bonding to two neighbors is stronger for an IV-A atom than bonding with three or more atoms due to the bond nature evolution. This mechanism may explain why a $C_{13}$ cluster prefers a ring or a tadpole structure with each atom having two bonds, or the tubes or fullerene rather

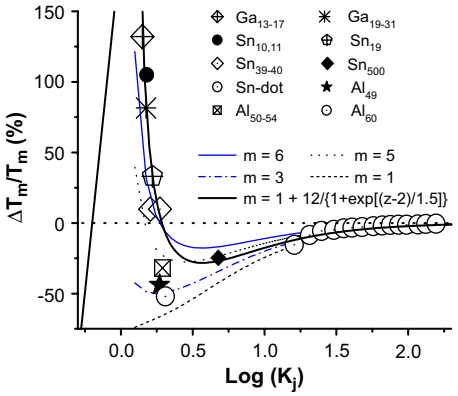


Fig. 18. Comparison of the predicted $T_m$ ossification with those measured from $Ga^{+}_{13-17}$ [317,318], $Sn_{10-19}$ [322], $Sn_{19-31}$ [266], $Ga^{+}_{39-40}$ [317], $Sn_{500}$ [333], and Sn nanosolid on $Si_3N_4$ substrate [289]. The $T_m$ deviation of $Al^{+}_{50-60}$ clusters [334] from the predictions indicates that the bond nature alteration of Al is less significant compared to Sn and Ga bonds. Ideal fit is reached with a function of $m(z) = 1 + 12/\{1 + \exp(z - 2)/1.5\}$ to let $m$ transit from 7 at $z = 2$ to 1 when $z > 4$ [111].

than the densely packed tetrahedron structure, as theoretically predicted [319,324]. It is expected that, the covalent Si ($m = 4.88$) and C ($m = 2.56$) clusters should also show the $T_m$ elevation (bending up) at $K_j < 3$. For a pure covalent system, the bond strength increases as the bond contracts without bond nature evolution. For Au, however, the value of $m$ remains unity throughout the course of CN reduction during monatomic chain formation [332]. Therefore, the bond nature evolution may be the unique property of the III-A and IV-A elements with a larger number of electrons as compared with Al ($m \sim 2$), Ga ($m = 6$–$7$), C ($m = 2.56$), Si ($m = 4.88$), and Sn ($m = 6$–$7$).

### 5.2.5. Remarks

Briefly, the BOLS correlation premise has enabled the observed suppression (undercooling), elevation (overheating), and oscillation of $T_m$ over the whole range of sizes of various specimens to be reconciled to the effect of atomic CN imperfection. The modified cohesive energy of the under-coordinated system also determines the geometrical reconstruction, surface lattice/phonon instability, and surface energy. Actually, the surface and interfacial energy, surface stress, the local mass density of liquid and solid are all functions of atomic separation and bond energy that are subject to the BOLS correlation. We relate the $T_m$ suppression directly to the atomic CN imperfection and its effect on the strength of interatomic bonding, and the $T_m$ enhancement of embedded system to the strengthening of the interfacial bond. The $T_m$ oscillation over the whole range of size results from atomic CN variation and its effect on bond strength. Compared with the existing models, the current BOLS premise is simpler and straightforward involving almost no assumptions or freely adjustable variables. The only parameter needed is the $m$ that denotes the bond nature and can be determined from measurement of other properties. It is seen that in the present premise, that $\Delta T_m(K_j)$ originates from $z_{ib}c_i^{-m} - 1$, compared with the RMSD premise in which $-(\beta - 1)$ dominates. If $z_{ib}c_i^{-m} < 1$, then $\beta > 1$. If the $E_B$ of a surface atom is weaker, its RMSD will be larger, and vice versa. For overheating, $z_{ib}c_i^{-m} > 1$ and $\beta < 1$. Therefore, the models of RMSD instability, LSN, LNG, surface-phonon instability, and the current

BOLS are in good accordance. All the modeling variables relating to the melting can be related functionally to the mean atomic $E_B$, which should provide a natural link among the various models. The BOLS mechanism quantizes statistically the so-called 'liquid shell' structure, as the contribution from individual atomic layers with different atomic CNs is different. The current model also supports the fluctuation for highly disordered system and the spontaneous melting at the lower end of the size limit. Therefore, all the proposed models are correct from a certain perspective.

### 5.3. Phase transition: ferroelectric, ferromagnetic and superconductive $T_C$

#### 5.3.1. Observations

With reduction of a solid size, the phase stability of the solid becomes lower as well. The $T_C$ of ferromagnetic [335–337], ferroelectric [243,338,339], and superconductive [340–342] nanosolids can be modified by adjusting the shape and size of the nanosolid. The tunable $T_C$ will be an advantage for sensors or switches that can be functioning in a designed temperature range. However, an understanding of the underlying mechanism for the $T_C$-tunability is yet primitive though numerous models have been developed.

*5.3.1.1. Ferromagnetic $T_C$.* For ferromagnetic nanosolids, such as Fe, Co and Ni and their alloys or compounds [343–345], the $T_C$ reduces with the particle size or with the thickness of the films [335,337,346–353]. The $T_C$ of Prussian blue nanowire is also found to be reduced with respect to Prussian blue bulk [354], resulting from the diminution of the average number of nearest magnetic interaction neighbors and magnetic exchange interaction constants as the diameters of nanowires decrease. According to the scaling theory [355], a spin–spin correlation length (SSCL, or $\xi$) limitation model [355,356] defines the SSCL as the distance from a point beyond which there is no further correlation of a physical property associated with that point. Values for a given property at distances beyond the SSCL can be considered purely random. The SSCL, depends functionally on temperature as $\xi = \xi_0(1-T/T_C)^{-\nu}$, where $\nu$ is a universal critical exponent. The SSCL limitation premise indicates that the $\xi$ is limited by the film thickness. If the $\xi$ exceeds the film thickness $K_j$, the $T_C$ will be lower compared with the bulk value. The SSCL mechanism gives rise to the power-law form of $T_C(K_j)$ that involves two freely adjustable parameters, $\lambda$ and $C$ (or $C_0$). The $\lambda$ value varies from unity to 1.59 for the mean field approximation and the three-dimensional Ising model, respectively [347,355,357]:

$$\frac{\Delta T_C(K_j)}{T_C(\infty)} = (C_0 K_j)^{-\lambda} \tag{39}$$

In order to match numerically to the measurement of ultrathin films, Eq. (39) was modified by replacing the reference $T_C(\infty)$ with the $K_j$-dependent $T_C(K_j)$ for normalization [335,358]:

$$\frac{\Delta T_C(K_j)}{T_C(K_j)} = (C' K_j)^{-\lambda'}$$

However, a convergence problem remains at the lower end of the size limit. An alternative non-continuous form was developed based on the mean field approximation to cover the thinner scales [359]:

$$\frac{\Delta T_C(K_j)}{T_C(\infty)} = \begin{cases} -\left(\dfrac{\xi+1}{2K_j}\right)^{\lambda}, & (K_j > \xi) \\ \dfrac{K_j-1}{2\xi} - 1, & (K_j < \xi) \end{cases} \tag{40}$$

Eq. (40) shows that $T_C$ varies linearly with $K_j$ and approaches zero at $K_j = 1$ (single atom). If $\lambda \neq 1$, there is a discontinuity at $K_j = \xi$.

Recently, Nikolaev and Shipilin [360] derived a simple model relating the $T_C$ change of a spherical nanosolid to the reduction of exchange bonds of surface atoms. It is assumed that, the number of exchange bonds per unit volume inside the bulk is equal to $z$. For the magnetically active surface atoms of a nanosolid, this number amounts to $z/2$ or less. The $T_C$ is assumed proportional to the mean number of exchange bonds per unit volume, and then the relative change of the $T_C$ due to size reduction is:

$$\frac{\Delta T_C(K_j)}{T_C(\infty)} = -\frac{\tau \Delta K_j}{2K_j} \tag{41}$$

where $\Delta K_j$ is the thickness of the layer with half-depleted exchange bonds. The quantity $\Delta K_j$ is an average that characterizes the features of the surface CN-deficient structure of a nanosolid. If $\Delta K_j$ is independent of the particle radius $K_j$, the $T_C$ drops with $K_j$ and the critical $K_C$ at which $T_C$ is zero is $\tau \Delta K_j/2$. This relation characterizes qualitatively the interrelation between the degree of magnetic structure disorder and the particle size for $Fe_3O_4$ spherical dots [361] by setting the critical thickness $\Delta K_j$ of half (for larger size) and two (for the smallest size) atomic sizes. However, the mechanism for the size dependence of $\Delta K_j$ remains yet unclear.

*5.3.1.2. Superconductive $T_C$.* Highly dispersed superconducting nanosolids can be coupled due to the proximity effect when the interparticle spacing is of the order of twice the penetration length of the superconducting order parameter in the normal phase [362,363]. The electronic energy levels of the sample are discrete, with a mean level spacing of Kobo gap $\delta_K$ for fine metallic particles [122,364]: $\delta_K = 4E_F/3n \propto 1/V \propto K_j^{-3}$. As pointed out by Anderson [365], superconductivity would not be possible when $\delta_K$ becomes larger than the bulk $E_G$. Based on this suggestion, the relation between the superconducting phase transition and the energy-level spacing for spherical granules is suggested to follow the relation [366,367]:

$$\mathrm{Ln}\left(T_C(K_j)/T_C(\infty)\right) = \sum \left[2/(2m_j+1)\right] \times \left[\tanh\left[(\pi/2)\left((2m_j+1)2\pi k_B T_C/\delta_K\right)\right] - 1\right]$$

Index $m_j$ is the magnetic quantum number. Estimation using this relation yields a 2.5 nm critical size for the disappearance of superconductivity of Pb nanosolid. Experiments of Giaever and Zeller [342] on Sn confirmed the existence of a metastable energy gap only for particles of sizes larger than 2.5 nm. However, the $T_C$ for Pb is detectable when the grown Pb atomic layers on Si substrate are four and more [368]. The $T_C$ suppression of Pb embedded in the Al–Cu–V matrix measured by Tsai et al. [341] could not fit the above prediction. Instead, the data can be fitted to an empirical equation:

$$T_C(K_j) = T_C(\infty)\exp(-K_C/K_j)$$

with $T_C(\infty) = 7.2$ K for Pb [340]. In the observed size region, due to the finite number of electrons in each particle (between 1000 and 64,000 depending upon the grain size) the conventional BCS approach loses its validity because the bulk BCS theory of superconductivity assumes an infinite number of electrons. Small size implies fewer electrons at the Fermi surface and the discreteness of the Kubo levels. Additionally, energy-level spacing may be larger compared to thermal energy $k_BT$. Therefore, the assumption of metallic behavior of these particles may be subject to examination [115].

Pogrebnyakov et al. [340,369] found that the $T_C$ of superconductive $MgB_2$ thin films decreases and the residual resistance increases when the thickness of the epitaxial $MgB_2$ thin films is decreased. At sizes larger than 300 nm, the $T_C$ saturates at 41.8 K. The resistivity also saturates to the bulk value of 0.28 Ωcm at 300 nm. The origin of the thickness dependence of the $MgB_2$ film properties is not clear at present. A possible explanation of higher $T_C$ is the strain in the film, while the grain size is not likely to be the direct cause of the thickness dependence of $T_C$. XRD measurement on a 230 nm-thick film shows a slight lattice expansion of $a = 0.3095 \pm 0.0015$ nm, compared with the value of 0.3086 nm for bulk $MgB_2$ [370]. The measured $c$ lattice constant contracts from 0.3524 to 0.3515 nm. This contraction suggests that the films are under tensile strain in c-plane epitaxial growth. Hur et al. [371] reported a higher-than-bulk $T_C$ in $MgB_2$ films on boron crystals and suggested that it is possibly due to tensile strain. Yildirim and Gulseren [372] have predicted an increase in $T_C$ by the $c$-axis compression in the first-principle calculations. Therefore, understanding of the size-induced $T_C$ suppression is still under debate.

*5.3.1.3. Ferroelectric $T_C$.* Unlike ferromagnetic and superconductive nanosolids that show smaller critical sizes for $T_C = 0$ K, a ferroelectric nanosolid often shows larger critical size at which the ferroelectric feature disappears [373]. Zhao et al. [374] observed a progressive reduction of tetragonal distortion, heat of transition, $T_C$, and relative dielectric constant on dense $BaTiO_3$ ceramics with grain size decreasing from 1200 to 50 nm. The correlations between grain size, extent of tetragonal distortion, and ferroelectric properties strongly support the existence of an intrinsic size effect. The critical size for disappearance of ferroelectricity has been estimated to be 10–30 nm. The strong depression of the relative permittivity observed for the nanocrystalline ceramics can be ascribed to the combination of the intrinsic size effect and of the size-dependent ''dilution'' effect of a grain boundary ''dead'' layer. It has been found [375] that the remnant polarization of nano-scale $Pb(Zr,Ti)O_3$ thin films decreases from 6 μC/cm$^2$ to 2.5 μC/cm$^2$, while the coercive field increases from 50 kV/cm to 150 kV/cm, with the decrease in film thickness from 152 to 32 nm. The suppression of ferroelectricity was attributed to the crystallinity degradation and the residual compressive stress.

Different theoretical approaches have been developed including (i) a microscopic pseudospin theory based on the Ising model in a transverse field, (ii) a classical and macroscopic Landau theory in which surface effects can be introduced phenomenologically, and (iii) a polariton model for the very-long-wavelength region. Taking the surface and nonequilibrium energy into consideration, Zhong et al. [243] extended the Landau-type phenomenological and classical theory by introducing a surface extrapolation length $\delta$ to the size-dependent $T_C$ suppression of ferroelectric nanosolids expressed using the Ising model, $J_{ij} = J/r_{ij}^{\sigma}$. $\sigma = 0$ corresponds to an infinite-range interaction and $\sigma = \infty$ corresponds to a nearest-neighbor interaction [376].

However, the model shows limitations in explaining the thermal properties of $PbTiO_3$ and $PbZrO_3$ nanosolids. After that, Jiang and Bursill [377] assumed the phenomenological Landau–Ginzburg–Devonshire (LGD) coefficients in the Gibbs energy to change with particle size to solve this problem. Huang et al. [378] combined the LGD phenomenological theory and the BOLS correlation to study the size effect of ferroelectrics. The model assumes that the surface bond contraction occurs only within three outermost nanoferroelectric layers whereas the core interior remains ferroelectric [379]. Recent experimental results seem to confirm this assumption. For example, barium titanate particles are found to consist of a shell of cubic material surrounding a core of tetragonal material [380]. Although such a core-shell structure has not been reported in the PZT system, an antiferrodistortive reconstruction of the (001) surface layer of $PbTiO_3$ has been found by in situ X-ray scattering measurements [381]. It is easy to understand that the rotation of the relatively rigid oxygen octahedra decreases the lattice parameter or the distance between neighboring Pb–Pb ions [382]. A surface stress is therefore expected due to the antiferrodistortive reconstruction of the surface. In Huang's model, such a surface stress can be treated as a hydrostatic pressure for a nanoparticle or a two-dimensional stress for a thin film [383].

An empirical equation widely used to fit the $T_C$ suppression of ferroelectric nanosolids is given as [338]

$$\Delta T_C(K_j)/T_C(\infty) = C/(K_j - K_C) \tag{42}$$

where $C$ and the critical $K_C$ are adjustable parameters. One may note that if $K_j = K_C$, Eq. (42) becomes singular. The proper form of the dividend seems to be $K_j + K_C$, instead, to shift the scaling relation towards larger critical size. More recently, Jiang et al. [384] adopted their model for $T_m$ suppression to the size-dependent $T_C$ of the ferroelectric nanosolids, which is expressed as:

$$\begin{cases} T_C(K_j)/T_C(\infty) = \exp\{-2S_0[3R_S(K_j/K_C - 1)]^{-1}\} \\ K_C = \alpha_{90}(2k_B\alpha\beta^2)^{-1} \end{cases}$$

where $S_0$ is the transition entropy, $R_S$, the ideal gas constant, $\alpha$, the thermal expansion coefficient and $\beta$, the compressibility. The constant $\alpha_{90}$ denotes the density of 90° domain walls. Numerical match for the $T_C$ suppression of $BaTiO_3$ and $PbTiO_3$ nanosolids has been realized with the documented $S_0$ values. Jiang et al. found a relation that larger $K_C$ value corresponds to a smaller value of $S_0$ in the simulation.

*5.3.1.4. Antiferromagnetic transition.* Zysler et al. [385] investigated the size and temperature dependence of the spin–flop transition in antiferromagnetic $\alpha$-$Fe_2O_3$ nanosolids. When a sufficiently large magnetic field is applied along the preferred axis, the so-called spin–flop reorientation occurs, i.e., a 90° rotation of the sublattice vectors. They found that both the spin–flop field, $H_{S-F}$ ($T = 0$), and the Morin transition temperature ($T_M$) decrease with particle size in a $K_j^{-1}$ way and tend to vanish below a diameter of 8 nm, for spherical particles [386]. Table 5 summarizes the size-dependent $H_{S-F}$ and $T_M$ values. Zysler et al. [385] related the change particularly to the distribution of CN for surface spins that determines a variety of reversal paths and in turn affects both the exchange and anisotropy fields. Therefore, the surface spins can undergo spin–flop instability at field that is much lower than the field for bulk. Weschke et al. [387] measured the thickness dependence of the helical antiferromagnetic

Table 5
Annealing temperature dependence of crystal size, Morin temperature ($T_M$), and spin–flop transition field at $T = 0$ ($H_{S-F,0}$) for the heminatite nanosolids [385]

| $D$/nm | $T_M$/K | $H_{S-F,0}/T$ |
|---|---|---|
| 36.4 | 186 | 1.7 |
| 40.0 | 200 | 2.5 |
| 82.7 | 243 | 5.4 |
| 159 | 261 | 6.6 |

ordering temperature, called Néel temperature ($T_N$), for Ho films by resonant magnetic soft X-ray and neutron diffraction and found the $T_N$ to decrease with film thickness. The offset thickness is 11 ML for metallic Ho films in comparison with the value of 16 ML for Cr in sputtered, epitaxial Fe/Cr(001) superlattice [388]. Superconducting quantum interference device (SQUID) magnetometry and electron magnetic resonance experiments reveal that in the $Pr_{0.5}Ca_{0.5}MnO_3$ nanowires, a ferromagnetic transition occurs at ~105 K. The antiferromagnetic transition disappears and the charge ordering transition is suppressed compared with the bulk charge ordering transition at 245 K. The antiferromagnetic transition at 175 K [389].

Briefly, the SSCL theory considers the correlation length whereas the CN imperfection model considers the loss of exchange bonds of atoms in the ferromagnetic surface region for magnetic $T_C$ suppression. A model for the $T_C$ suppression of superconductive $MgB_2$ nanosolids [390] is yet lacking. Mechanisms for the ferroelectric $T_C$ suppression are under debate. Nevertheless, all the models developed insofar could have contributed significantly to the understanding of $T_C$ suppression from various perspectives. Consistent insight and a unification of size-induced $T_C$ suppression of ferromagnetic, ferroelectric, and superconductive nanosolids as well as the $T_M$ and $H_{S-F}$ for antiferromagnetic heminatite are highly desirable. Here, we extend the BOLS correlation into the Ising model that involves atomic cohesive/exchange energy, which has led to consistent insight, with a general expression, into the $T_C$ suppression of these nanosolids.

### 5.3.2. BOLS consideration

*5.3.2.1. Ising model.* The Hamiltonian of an Ising spin system in an external field $B$ is expressed as [359]:

$$H_{ex} = \sum_{\langle i,j \rangle} J_{ij} S_i S_j - g\mu_B B \sum_{i=1}^{N} S_i \propto z_i d_i^{-1}$$

The $H_{ex}$ is identical to the atomic $E_B$ if zero external field is applied, $B = 0$. $S_i$ and $S_j$ are the spin operators in site $i$ and site $j$, respectively. $J_{ij}$ is the exchange strength between spins at site $i$ and site $j$, which is inversely proportional to atomic distance. The sum is over all the possible coordinates, $z_i$. For phase transition, the thermal energy required is in equilibration with a certain portion of the exchange energy. This mechanism leads to the case being the same as for $T_m$ suppression as described in Eq. (37).

*5.3.2.2. High-order CN imperfection.* For ferroelectric systems, the exchange energy also follows the Ising model, but the $S_j$ here represents the quanta of a dipole or an ion (may be called quasi-dipole) that is responsible for the ferroelectric performance. The difference in the correlation length is that the dipole system is longer than that of a ferromagnetic spin–spin system. Usually, dipole–dipole Van der Vaals interaction follows the $r^{-6}$ type whereas the superparamagnetic interaction follows an $r^{-3}$ relation. Hence, it is insufficient to count only the exchange bonds within the nearest neighbors for atoms with distant interaction in a ferroelectric system. A critical exchange correlation radius $K_C$ can be defined to count contribution from all atoms within the sphere of radius $K_C$. Therefore, the sum in Eq. (37) changes from the $z_i$ neighbors to atoms within the $K_C$ sized correlation volume.

For a ferroelectric spherical dot with radius $K_j$, we need to consider the interaction between the specific central atom and its surrounding neighbors within the critical volume $V_C = 4\pi K_C^3/3$, in addition to the BOLS correlation in the surface region. The ferroelectric property drops down from the bulk value to a value smaller than 5/16 (estimated from Fig. 19) when one goes from the central atom to the edge along the radius. If the surrounding volume of the central atom is smaller than the critical $V_C$, the ferroelectric feature of the central atom attenuates; otherwise, the bulk value remains. For an atom in the *i*th surface layer, the number of the exchange bonds loss is proportional to the volume $V_{vac}$, that is the volume difference between the two caps of the $V_C$-sized sphere as illustrated in Fig. 19a. Therefore, the relative change of the ferroelectric exchange energy of an atom in the *i*th atomic layer to that of a bulk atom due to volume loss becomes

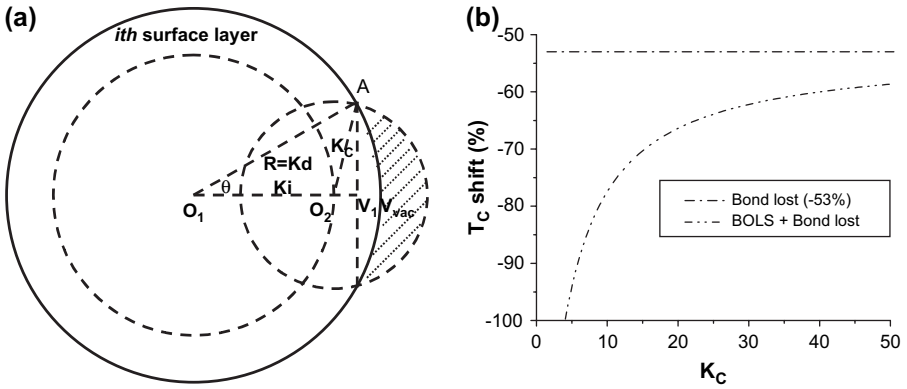


Fig. 19. (a) Schematic illustration of the high-order exchange bonds lost of an atom in a spherical nanosolid with radius $K_j$. $K_C$ is the critical correlation radius. The $V_{vac}$ loss (the shaded portion) is calculated by taking the difference in the volumes of the two spherical caps:

$$V_{vac,i} = \pi(K_C + K_i - K\cos\theta)^2\left(K_C - \frac{K_C + K_i - K\cos\theta}{3}\right) - \pi(K - K\cos\theta)^2\left(K - \frac{K - K\cos\theta}{3}\right)$$

where the angle θ is determined by the triangle $O_1O_2A$. (b) Critical correlation radius $K_C$ dependence of the $T_C$ shift of ferroelectric and superconductive alloying nanosolids. For $K_C = 5$ example, BOLS lowers the $T_C$ by −41.1% (follows the curve in Fig. 1a) and the high-order bond loss contributes to the $T_C$ suppression by −53% and the overall $T_C$ shift is −94%. $K_C \leq 4$, $T_C = 0$ [623].

$$\frac{\Delta E_{\mathrm{exc},i}}{E_{\mathrm{exc}}(\infty)}=\frac{V_{\mathrm{C}}-V_{\mathrm{vac},i}}{V_{\mathrm{C}}}-1=-\frac{V_{\mathrm{vac},i}}{V_{\mathrm{C}}}=\delta_{\mathrm{V},i} \tag{43}$$

*5.3.2.3. Generalization of $T_C$ suppression.* Considering the BOLS correlation for the nearest neighbors and the volume loss of long-order CN imperfection, we have a generalized form for the $T_C$ suppression for ferromagnetic, ferroelectric, and superconductive nanosolids ($m=1$ in the Ising model):

$$\frac{\Delta T_{\mathrm{C}}(K_j)}{T_{\mathrm{C}}(\infty)}=\frac{\Delta E_{\mathrm{exc}}(K_j)}{E_{\mathrm{exc}}(\infty)}=\begin{cases}\sum_{i\le 3}\gamma_{ij}\left(z_{i\mathrm{b}}c_i^{-1}-1\right)=\Delta_{\mathrm{B}} & \text{(short-order-CN)}\\ \sum_{i\le K_{\mathrm{C}}}\gamma_{ij}\delta_{\mathrm{V},i}+\Delta_{\mathrm{B}}=\Delta_{\mathrm{COH}} & \text{(long-order-CN)}\end{cases} \tag{44}$$

For a short-order spin–spin interaction, it is sufficient to sum over the outermost three atomic layers whereas for a long-order dipole–dipole interaction the sum should be within the sphere of the critical volume $V_C$, in addition to the BOLS effect. It is understood now why $\Delta K_j$ in Eq. (41) is not a constant. In the current BOLS premise, the $\gamma_{ij}$ is not always proportional to the inverse of the radius, which drops instead from unity to infinitely small when the particle grows from atomic scale to macroscopic size. Meanwhile, the $z_i$ and the $c_i$ vary with the curvature of the sphere. Fig. 19b shows the general $K_C$ dependence of the ferroelectric $T_C$ shift involving both volume loss and BOLS effect. For the $K_C=5$ example, bond contraction lowers the $T_C$ by $-41.1\%$ and the volume loss contribution lowers the $T_C$ by $-53\%$ and the overall $T_C$ shift is $-94\%$.

*5.3.3. Verification: critical size*

Least-root-mean-square linearization of the measured size-dependent $T_C$ represented by Eq. (44) gives the slope $B'$ and an intercept that corresponds to the bulk $T_C(\infty)$. Compared with Eq. (44), one would find that $B'=K_j\Delta_{\mathrm{COH}}$ for a ferroelectric system. For a ferromagnetic system, $B'=K_j\Delta_{\mathrm{B}}=$ constant without needing numerical optimization. Calculations based on Eq. (44) were conducted using the average bond length (Appendix A) and the $T_C(\infty)$ values as listed in Table 6.

Fig. 20 shows the match between the predicted curves and the measured $T_C$ suppression for a ferromagnetic nanosolid. For ultrathin films, the measured data are closer to the predicted curve for a spherical dot. This coincidence indicates that at the beginning of film growth, the films prefer island patterns that transform gradually into a continuous slab. For a ferroelectric system, we need to optimize the $K_C$ value by computation to match theoretical curves to the measured data. Fig. 21 shows the $T_C$ suppression of ferroelectric $PbTiO_3$ [243], $SrBi_2Ta_2O_9$ [339], $BaTiO_3$ [392] and anti-ferroelectric $PbZrO_3$ [393] nanosolids. For ferroelectric and superconductive nanosolids, $T_C=0$ K occurs at $V_{\mathrm{vac}}=V_C$, which means that $K_C$ corresponds not to $T_C=0$ K, but to a value that is much lower than room temperature. The difference in the optimized $K_C$ by different approaches, as compared in Table 6, lies in that the $\gamma_{ij}$ in the current approach is not a constant but changes with particle size.

Comparing the BOLS prediction to the measured $T_C$ suppression of superconductive $MgB_2$ nanosolids in Fig. 22 leads to an estimation of the critical radius $K_C=3.5$, which agrees with the value we determined recently ($R_C\sim 1.25$ nm) [393]. For the smallest $MgB_2$ crystals, the relative Bragg intensities of the allowed reflections can only be successfully matched during Rietveld refinement by introducing statistically distributed B-vacancies, with the refined value falling from 1 to 2/3. This finding means that the average coordination of Mg to B falls from 12

Table 6
Comparison of the BOLS predicted critical correlation radius ($K_C$) with the $R'_C$ derived from other observations

| Materials | $T_C(\infty)$/K | $K_C/R_C$(nm) | $R'_C$/nm (Refs.) |
|---|---|---|---|
| Fe | 1043 | 1 | 0 [337] |
| Co | 1395 | 1 | 0 [335] |
| Ni | 631 | 1 | 0 [335] |
| $Fe_3O_4$ | 860 | 1 | 0 [361] |
| $PbTiO_3$ | 773 | 4/1.04 | 6.3 [338], 4.5 [243] |
| $SrBi_2Ta_2O_9$ | 605 | 4/1.0 | 1.3 [339] |
| $PbZrO_3$ | 513 | 8/2.3 | 15 [393] |
| $BaTiO_3$ | 403 | 100/24.3 | 24.5 [396], 55 [392] |
| $MgB_2$ | 41.7 | 3.5/1.25 | 1.25 [394] |
| Pb | 7.2 | 3.5/1.25 | 1.25 [341] |

to 8, which provides direct evidence for the loss of superconductivity of the under-coordinated system [395]. Consistency between BOLS prediction with experiment data indicates that the long-range interaction dominates the superconductive $T_C$. For an Al–Cu–V embedded Pb nanosolid [341], the $K_C$ is around 1, being the same as for a ferromagnetic solid. This finding may provide possible mechanisms for the origin of the superconductive $T_C$ suppression of compound $MgB_2$ and metallic Pb nanosolids. For the antiferromagnetic $\alpha$-$Fe_2O_3$ a spin–flop

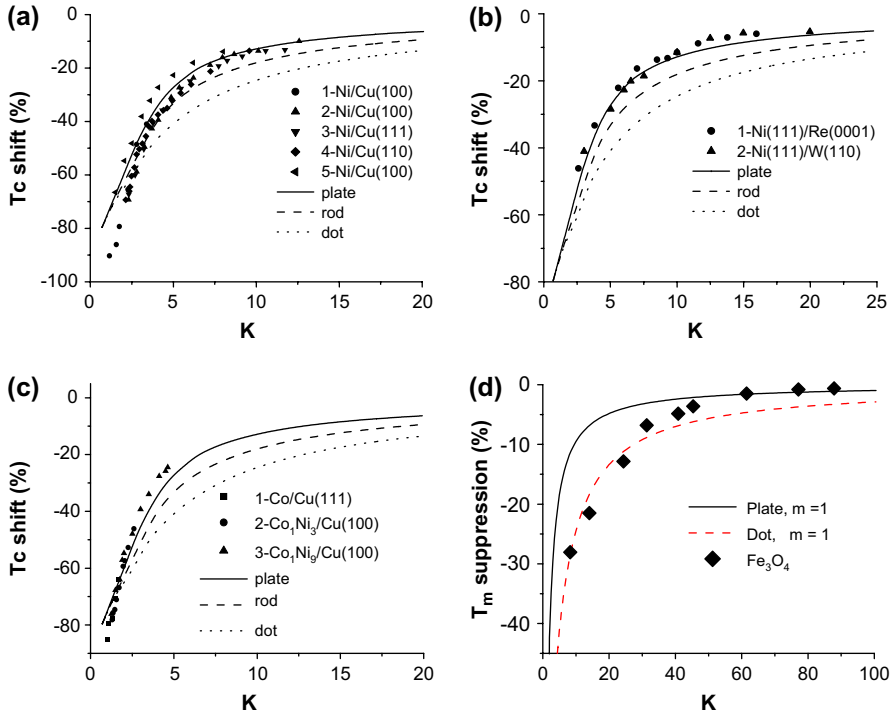


Fig. 20. Comparison of the predicted $T_C$ suppression with observations of (a) Ni thin films: data-1 [350], data-2, 3, and 4 [359], and data-5 [335]; (b) data-1 [391] and data-2 [349]; (c) Co films [335]; and (d) $Fe_3O_4$ nanosolids [361].

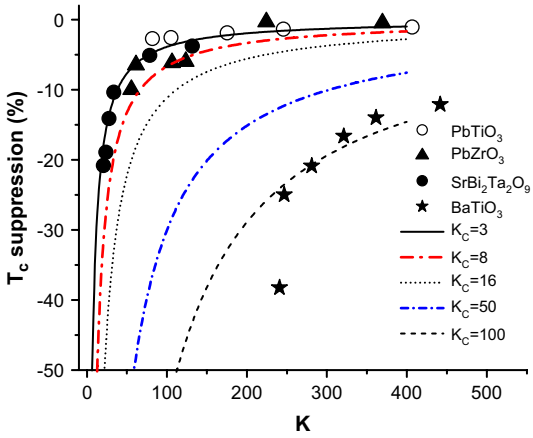


Fig. 21. Size-induced $T_C$ suppression of ferroelectric $PbTiO_3$ [243], $SrBi_2Ta_2O_9$ [339], $BaTiO_3$ [392], and anti-ferroelectric $PbZrO_3$ [393] nanosolids.

transition at a critical size of 8 nm can also be related to the high-order CN imperfection, which is the same for the ferroelectric and antiferroelectric compound nanosolids.

### *5.4. Other applications*

#### *5.4.1. Diffusivity and reactivity*

*5.4.1.1. Diffusivity*. The kinetics of diffusion processes occurring in nanostructured materials is a subject of intensive study [397,398]. Although the available database is ambiguous due to structural varieties during the process of diffusion experiments, there is no doubt regarding the sharp acceleration of diffusion in these materials [399]. The activation enthalpies for the interfacial diffusion are comparable to those for surface diffusion, which are much lower than those for diffusion along grain boundaries [400,401]. Measuring grain-boundary diffusion fluxes of Cu on creep behavior of coarse-grained and nanostructured Ni samples at 423 K and 573 K [402] revealed that the creep acceleration behavior is grain size dependent, which was attributed to higher diffusivity in the finer grain material. Experimental studies [403] of the Fe-tracer diffusion in submicrocrystalline Pd powders revealed that interfacial diffusion occurs at relatively low temperatures accompanied by a substantial recovery of grain growth. The recovery processes and the crystal growth occurring in a main recovery stage at 500 K are triggered by atomic defects. The under-coordinated atoms surrounding the defects become mobile in this temperature regime, which is suggested to be responsible for the onset of diffusion in the interfaces.

By means of surface mechanical attrition treatment (SMAT) to a pure iron plate, Wang et al. [404] fabricated a 5 μm-thick Fe surface layer composed of 10–25 nm sized grains without porosity and contamination on the Fe plate. They measured Cr diffusion kinetics within a temperature range of 573–653 K in the nano-Fe coated plate. Experimental results show that diffusivity of Cr in the nanocrystalline Fe is 7–9 orders higher in magnitude than that in a Fe lattice and 4–5 orders higher than that in the grain boundaries (GBs) of α-Fe. The activation energy ($E_A$) for Cr diffusion in the Fe nanophase is comparable to that of the GB diffusion, but the pre-exponential factor is much higher. The enhanced diffusivity of Cr was

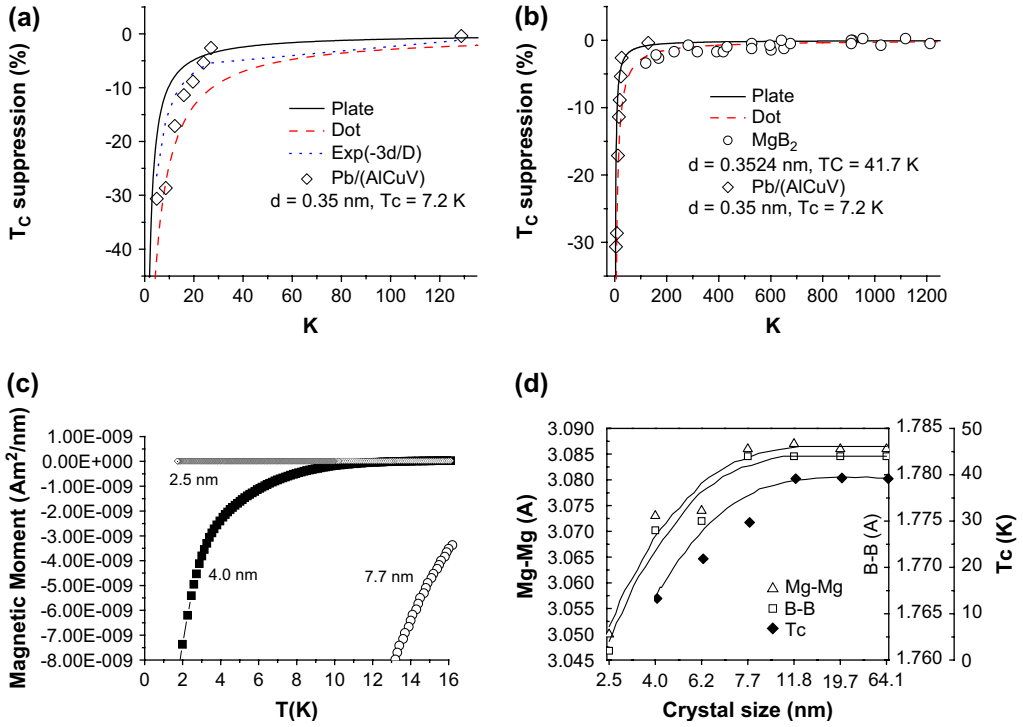


Fig. 22. Comparison of the prediction with the measured size-dependent $T_C$ suppression of (a) Pb particles embedded in Al–Cu–V matrix and (b) $MgB_2$ films [340]. (c) Size and temperature dependence of the magnetism of $MgB_2$ superconducting nanosolids and (d) size-induced $T_C$ and bond length suppression of $MgB_2$ nanosolids [394].

suggested to originate from a large volume fraction of nonequilibrium GBs and a considerable amount of triple junctions in the presence of the nanocrystalline Fe samples.

Under the given conditions, copper atoms were not detectable in the coarse-grained Ni even at a depth of 2 μm. However, the diffusive copper fluxes in nanostructured Ni penetrate into a depth greater than 25 and 35 μm at 423 and 573 K, respectively [402]. This information leads to the GB diffusion coefficients of copper in nanostructured nickel derived as follows.

Using Secondary Ion Mass Spectrometry (SIMS), at 423 K, no migration of the GBs in nanostructured Ni was observed, and hence, the diffusion coefficient, $D_b$, could be determined using the equation describing the change of the GB impurity concentration versus time $t$ of the diffusion annealing [405]:

$$c(x,t) = c_0 \mathrm{erfc}\left[x/\left(2\sqrt{D_b t}\right)\right]$$

where $c_0$ is the concentration of copper at the surface. The depth $x$ is the distance from the surface at which $\log c = -1$ ($c = 0.1\%$, which corresponds to the resolution limit of the SIMS unit). The value of $c_0$ was obtained by extrapolation of the experimental concentration curve at $x \to 0$. In this case, $D_b = 1 \times 10^{-14}$ m$^2$/s ($t = 3$ h).

Grain growth occurs in nanostructured nickel when the sample is annealed at 573 K and the grain-boundary migration occurs at the velocity of $V \sim 7 \times 10^{-11}$ m$^2$/s. In this case, the $D_b$ follows [405]:

$$c(x,V,\beta) = c_0 \exp\left(-x\sqrt{V/D_b\beta_b}\right)$$

Considering the diffusion width of the boundary $\beta_b = 10^{-8}$ m, one can obtain $D_b = 1.4 \times 10^{-12}$ m$^2$/s, which is two orders higher than that for the same sample annealed at 423 K. These experimental data demonstrate the increase in the GB diffusion coefficient of copper in nanostructured Ni in comparison with the coarse-grained nickel.

Systematic studies [51] of size-dependent alloy formation of silver-coated gold nanosolids in aqueous solution at the ambient temperature using XAFS reveal remarkable size-dependent interdiffusion of the two metals at the ambient temperature. The diffusion between Ag and Au is enhanced when the Au particle size is reduced. For the very small particles (<4.6 nm initial Au-core size), the two metals are almost randomly distributed within the particle. For larger particles, the diffusion boundary is only one monolayer. These results cannot be explained either by enhanced self-diffusion that results from depression of the $T_m(K_j)$ or by surface melting of the Au nanosolid. It was proposed that defects, such as vacancies, at the bimetallic interface enhance the radial migration (as well as atomic displacement around the interface) of one metal into the other [51].

Kim et al. [406] investigated the thickness dependence of Ag resistivity during temperature ramping as a means to access thermal stability of Ag thin films. In situ four-point probe analysis is used to determine the onset temperature at which the electrical resistivity deviates from linearity during the temperature ramping. At the deviation point, the Ag thin films become unstable due to void formation and growth during thermal annealing. In vacuum, Ag thin films thicker than 85 nm on $SiO_2$ substrates are thermally stable. Using the Arrhenius relation in terms of onset temperature and film thickness, an $E_A$ of $0.326 \pm 0.02$ eV is obtained for the onset of Ag agglomeration ramped at a rate of 0.1 °C per second. This value is consistent with the $E_A$ for surface diffusion of Ag in vacuum. Therefore, Ag agglomeration and surface diffusion share the same $E_A$, both of which should be related to the atomic cohesion.

The high diffusivity of a nanosolid also enhances diffusion of a liquid into the nanosolid, as observed first by Li and Cha [407]. Nanosolid surface adsorption and liquid diffusion are conventionally studied using planar electrodes in the field of catalytic chemistry. Cyclic voltammograms (CV) are often used to study surface adsorption of inorganic and organic molecules on metal nanosolids. However, normal-sized electrodes cannot study the fast electron transfer process because the potential scan rate is lower than 1 V/s. Solid ultramicroelectrodes can conduct fast CV but are not able to study powder nanosolids surface. Li and Cha [408] found much improved diffusion efficiency ($10-10^4$) in molding powder nanosolids as electrodes. Further, the powder ultramicroelectrode can significantly enhance the mass transportation rate from solution to the nanosolids' surface. A mass transportation rate generated by a 1-μm scale ultramicroelectrode is equivalent to that obtained at a conventional rotating disc electrode at a speed of 300,000 rounds per minute. The high efficiency of electronic behavior is general irrespective particular catalytic material [409]. Recently, the powder ultramicroelectrode has been used to biosensor to enhance the enzymatic catalysis process [410].

*5.4.1.2. Chemical reactivity*. It is known that nanocrystalline materials possess ultrafine grains with a large number of grain boundaries that may act as channels for fast atomic

diffusion [7]. Greatly enhanced atomic diffusivities in nanocrystalline materials relative to their conventional coarse-grained counterparts have been experimentally confirmed [8,411]. A large number of grain boundaries with various kinds of nonequilibrium defects constitute a high excess stored energy that may further facilitate their chemical reactivity. It has been demonstrated experimentally that chemical reaction (or phase transition) kinetics is greatly enhanced during mechanical attrition of solids, in which the grain size is significantly reduced to nanometer scale and large amount of structural defects are created by the severe plastic deformation [412], which is associated with the actual temperature rise.

Nitriding of iron happens when Fe powders were ball-milled in a nitrogen-containing atmosphere at the ambient temperature [413,414]. Considerable transient temperature rise (as high as a few hundred degrees) always accompanies the impacts of the milling balls, which may contribute to enhancing the chemical reactivity. However, enhanced chemical reactivity at lower temperatures [50] can happen by converting the surface layer of the metal such as Fe into nanostructures. Observations show that surface nanocrystallization greatly facilitates the nitriding process of Fe, which happens in ammonia at much lower temperature (300 °C for 9 h) compared with nitriding of smooth Fe surface that occurs at 500 °C or higher for 20–80 h [415]. The much-depressed nitriding temperature was attributed to the enhanced diffusion of nitrogen in the nanocrystalline surface layer compared to the coarse grains. In conventional nitriding of coarse-grained Fe, diffusion in the Fe lattice dominates. In the nanocrystalline Fe specimen, however, nitrogen mostly diffuses along Fe grain boundaries because of the much smaller $E_A$, being proportional to $E_B$, compared with that for the lattice diffusion. Nitrogen diffusivity at nanostructured surface layers ($5.4 \times 10^{10}$ cm$^2$/s) at 300 °C is about two orders of magnitude higher than that in a α-Fe lattice ($3.8 \times 10^8$ cm$^2$/s) at 500 °C. Therefore, the ultrafine-grained Fe phase in the surface layer provides a large number of defective grain boundaries (and other defects) that enhance the diffusion. Similarly, other surface chemical treatments by diffusing foreign atoms (such as chromium or aluminum) are useful in the industry to improve the performance of engineering materials. Greatly enhanced diffusivity of chromium in the SMAT Fe has also been observed at 350 °C that is about 300–400 °C lower than the conventional case. A combined STM and electrochemical reactivity measurements revealed that the catalytic activity towards electrochemical proton reduction is enhanced by more than two orders of magnitude as the diameter of the palladium particles parallel to the support surface decreases from 200 to 6 nm [416]. The sensitivity of $WO_3$ films to ozone depends on grain size and porosity: the sensitivity drastically decreases when the grain size increases at higher oxygen partial pressure during deposition [417]. DFT calculations combined with MD simulations suggest that the size effect is given by the thickness-variation of the support-induced strain at the surface of the palladium nanoparticles.

Pollution from automobiles is emitted in the first 5 min after startup. This is because Pt- or Pd-based catalysts currently used in automobile exhaust cleanup are inactive below a temperature of 200 °C. Interestingly, low-temperature gold catalysts are very inactive unless the gold is in the form of particles smaller than ~8 nm in diameter [418]. However, self-ignition and self-supporting combustion of Pt nanoparticles have been observed [419] at room temperature by exposing the particles to methanol/air or ethanol/air gas mixtures. The reaction is controlled by varying the fuel/air mixture and reducing particle size. An ordinary camera flash could burn the SWCNT under the ambient conditions, showing the higher chemical reactivity for oxidation of the SWCNT [420]. Chen and Goodman [421] discovered recently that a

1.33 ML ($3 \times 1$ reconstructed surface with every third row of Au adding to the fully covered surface) coverage of Au on $TiO_2$ surface could improve the efficiency of CO oxidation at room temperature by a factor of 50 times compared with the fully Au covered surface. The catalytic activity was attributed entirely to the presence of neutral gold atoms on the gold nanoparticles [418]. These surface atoms differ from atoms on bulk gold in three ways that might enhance their catalytic activity. (i) They have fewer nearest-neighbor atoms and possibly a special bonding geometry to other gold atoms that creates a more reactive orbital. (ii) They exhibit quantum size effects that alter the electronic band structure of gold nanoparticles. (iii) They undergo electronic modification by interactions with the underlying oxide that cause partial electron donation to the gold cluster. Another proposal is that positively charged gold ions on the oxide support are the key to the catalytic activity of these gold catalysts. The finding of Chen and Goodman [421] provides direct, atomistic evidence for the significance of bond-order unsaturation on the catalytic effect of gold atoms and offers challenges to determine the underlying mechanism.

Engineering alloys rely on the formation of protective oxide surfaces such as $Al_2O_3$ to resist corrosion at high temperature. Unfortunately, a relatively large (6 wt.% or higher) amount of Al or Cr is needed in bulk alloying to form a complete $Al_2O_3$ scale, which often reduces the mechanical strength of the alloys [422]. If too-low Al content is added, complex oxides consisting of $Cr_2O_3$, $NiCr_2O_4$ and internal $Al_2O_3$ could form, which result in high reactivity and poor oxidation resistance. Gao et al. [423] showed that diffusion and selective oxidation can be greatly enhanced by nano-structured coatings. With nanocrystal alloy coatings, the Al content can be substantially reduced to form a complete protective oxide scale. Experience shows that, when the grain size of Ni–20Cr–Al coatings are 60 nm or smaller, alloys containing $\sim$2 wt% Al could form a complete $\alpha$-$Al_2O_3$ scale at 1000 °C in air. Numerical methods suggest a mechanism in which simultaneous lattice and grain-boundary diffusion dominates the selective oxidation process in the nanograined structures [424].

*5.4.1.3. BOLS consideration.* In order to gain consistent insight into the size-enhanced diffusivity and reactivity, we extend the BOLS correlation to the $E_A$ that can be related to the atomic cohesion, leading to the conclusion that atomic CN imperfection suppressed atomic $E_B$ should be responsible for the $E_A$ for atomic diffusion, chemical reaction, and atomic agglomeration and glide dislocation as well.

The temperature dependence of the diffusion coefficient $D$ is expressed in the Arrhenius relation:

$$D(\infty, T) = D_0 \exp(-E_A(\infty)/k_B T) \tag{45}$$

where the activation enthalpy of diffusion is $E_A(\infty) = 1.76$ eV and the pre-exponential factor is $D_0 = 0.04\ \mathrm{cm^2\,s^{-1}}$ for gold. It is possible to incorporate the BOLS premise to the interdiffusion and nano-alloying by letting $E_A \propto E_B$ and hence the $E_A$ is atomic CN dependent. It is understandable that, to diffuse an atom into the solid, energy is needed to relax partially the bonds associated with atom dislocations. Applying Eq. (36) to (45) by considering the size effect, one has

$$\frac{D(K_j,T)}{D(\infty,T)} = \exp\left(-\frac{E_A(K_j)-E_A(\infty)}{k_BT}\right) = \exp\left(-\frac{E_A(\infty)}{k_BT}\left[\frac{E_B(K_j)}{E_B(\infty)}-1\right]\right)$$
$$= \exp\left(\frac{-E_A(\infty)}{k_BT}\Delta_B\right)$$

$$D(K_j,T) = D_0\exp\left(\frac{-E_A(\infty)}{k_BT}\frac{T_m(K_j)}{T_m(\infty)}\right) = D_0\exp\left(\frac{-E_A(\infty)}{k_BT}[1+\Delta_B]\right) \quad (46)$$

Therefore, the nano-diffusivity increases with the CN imperfection reduced atomic $E_B$ and hence the $T_m(K_j)/T_m(\infty)$ ratio drops in an exponential way. This understanding should provide a feasible mechanism for the nano-alloying, nano-diffusion, and nano-reaction in the grain boundaries where under-coordinated atoms dominate. However, oxidation resistance of a Si nanorod exhibits oscillation features [48]. At the lower end of the size limit, the Si nanorod can hardly be oxidized, as oxide tetrahedron formation is strongly subject to the atomic geometrical environment. For instance, oxidation happens preferentially at the densely packed diamond {111} plane rather than at the (110) surface [425]. The high surface curvature of the Si nanorod may provide an environment that resists the formation of a tetrahedron by the oxygen with Si atoms at the highly curved surface of a Si nanorod.

Fig. 23 compares the measured size-dependent $T_m$ suppression and diffusion-coefficient enhancement of silica-encapsulated gold particles [300], and the CO oxidation catalytic reactivity of Au/$TiO_2$ monatomic chains and Au/oxide [426] nanosolid in comparison with BOLS prediction of diffusivity. The similarity in the trends of diffusivity and reactivity shows the correlation between these two identities in terms of activation energy, though the former is related to atomic dislocation while the latter to charge capturing. The actual link between the activation energy for atomic dislocation and charge transportation is a challenging topic for further study.

### 5.4.2. Crystal growth

*5.4.2.1. Liquid–solid epitaxy*. Significant experimental and theoretical efforts aiming at identifying factors controlling nucleation, growth and subsequent microstructural evolution of nanocrystalline materials such as silicon have been motivated by the need to obtain high-quality materials for electronic and optical applications. However, little is yet known about the initial stages of growth of nanometer-sized crystals from the molten or amorphous matrix. This important issue largely determines the resulting microstructure of a polycrystalline material, which is extremely difficult to study experimentally due to the small size of the clusters and the small time scale involved. Intensive experiment and MD simulations have been conducted towards understanding the kinetics and thermodynamics of the homoepitaxial melting and solidification of a material. Results on the homoepitaxial growth and melting of Si, for example, are well understood in terms of the transition-state theory of crystal growth.

According to transition-state theory, the driving force, $F_C$, for the movement of the liquid–crystal interface is the free energy difference between the liquid and bulk crystal. This difference is approximately proportional to the magnitude of the undercooling, $T_m - T$. The velocity of the moving interface, $V$, is proportional to the driving force $V = kF_C$, where $k$ is the mobility

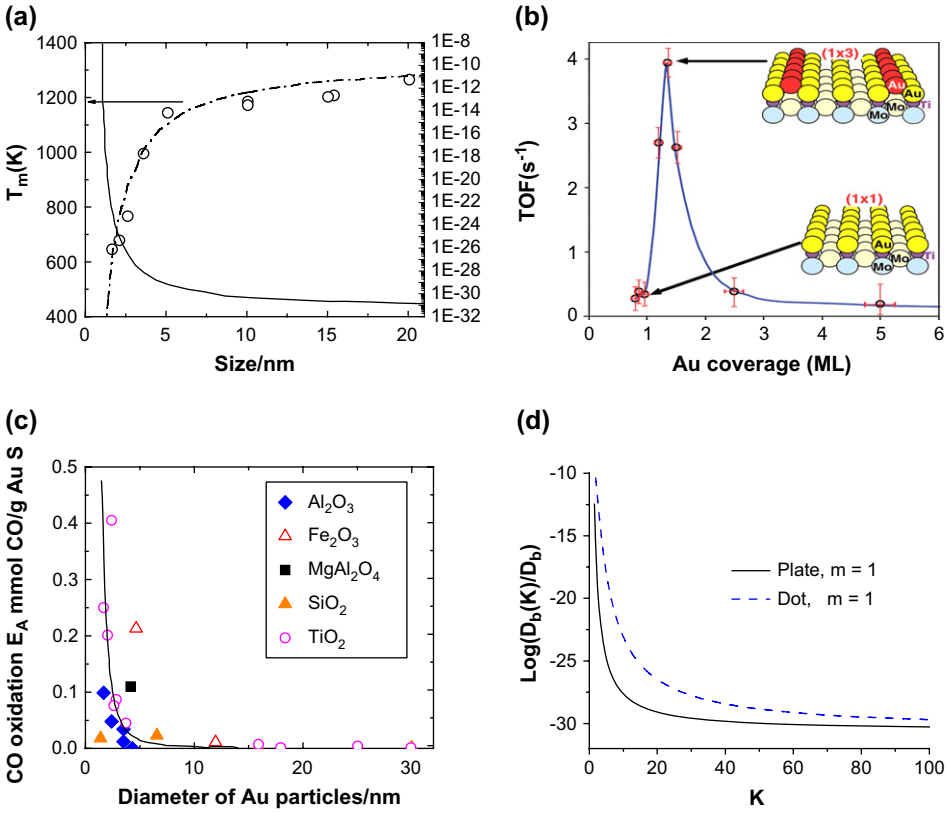


Fig. 23. (a) Size dependence of the $T_m$ and the diffusion coefficient of silica-encapsulated gold particles. The solid curve (right-hand side axis) is the calculated Au self-diffusion coefficient [300]. (b) Atomic CN imperfection enhanced catalytic reactivity (~50 fold) of Au/$TiO_2$ monatomic chains for CO room temperature oxidation [421]. (c) Au/oxide particle size dependence of CO room temperature oxidation activity [426]. (d) BOLS prediction of the size-dependent coefficient of diffusion.

of the liquid–crystal interface. This interfacial mobility is determined by the movement of the atoms in the liquid phase as atoms residing in the crystalline phase are far less mobile. Therefore, it is usually assumed that this mobility is proportional to the thermally activated atomic diffusion in the liquid phase. As is well established, $T_m$ suppression happens in a cluster of finite-size due to atomic CN imperfection, which contributes to the free energy of the liquid–crystal interface. However, the kinetics of the highly curved liquid crystal interface is yet unclear.

Using the Stillinger–Weber (SW) empirical potential, Kenlinski [307] studied temperature and size dependence of the growth and dissolution of Si nanosolids and found that there are actually no significant differences between the growth of nanosolids and planar interfaces. However, the $T_m$ of a cluster drops with solid size due to the reduced atomic $E_B$ and the mobility activation energy $E_A$ ($\propto$ atomic $E_B$) of the liquid–crystal interface is essentially the same as that for liquid diffusion. In the study of growth and melting of Si, the crystal front velocity was monitored using the fact that the SW potential consists

of additive two-body and three-body energy terms. The three-body term is zero for the perfect-crystal structure at $T = 0$ K, but even at high temperature the three-body term is assumed relatively low in the crystalline phase (e.g. the three-body energy is about 0.1 eV/atom at $T = 1200$ K). By contrast, the liquid phase is characterized by much larger three-body energy (−1 eV/atom). Using this large difference, Kenlinski calculated the amount of crystal and liquid phase present in the simulated cell simply by monitoring the total three-body energy and using as reference the corresponding values for the bulk liquid and bulk solid at the same temperature.

The size-dependent $T_m(K_j)$ can be investigated by simulating the growth/melt behavior of clusters with various initial sizes as a function of temperature. The free energy of the cluster can be approximated by surface and bulk contribution. The surface contribution, $U_S$, is proportional to the product of surface area and the liquid–solid interfacial free energy, $\gamma_{ls}$, such that $U_S = A\gamma_{ls}K_j^2$, where $A$ is a geometrical constant of order one (for a spherical dot, $A = 4\pi d_0^2$). The bulk contribution, $U_B$, is proportional to the volume of the cluster and the difference between solid and liquid free energy densities, $\Delta u$, such that $U_B = B\Delta u K_j^3$, where $B$ is another geometrical constant (for a spherical cluster $B = 4\pi d_0^3/3$). The difference between crystal and liquid free energy densities in the vicinity of the $T_m$ is proportional to the magnitude of undercooling (or overheating), $\Delta u \sim u_0(T - T_m(K_j))$, where $u_0$ is a constant (note that $\Delta u$ correctly vanishes at $T_m$). For a given temperature, the critical cluster size corresponds to the maximum of the free energy $U = U_S + U_B$. By differentiation of the free energy with respect to the cluster size $K_j$, one finds the maximum at $T = T_m(K_j) - c\gamma_{sl}/K_j$, where $c$ is a constant depending on $A$, $B$ and $u_0$. The linear dependence of the $T_m$ on the inverse of the crystalline size implies that the interfacial energy, $\gamma_{sl}$, does not change significantly with temperature, from the first-order approximation. In reality, the interfacial energy varies with both size and temperature, as discussed in earlier sections.

In order to understand the temperature dependence of growth rate in terms of undercooling and thermally activated interfacial mobility, one may assume that [307], in the classical nucleation theory, growth takes place on an atom-by-atom basis. Hence, the average rates of crystallization and dissolution are:

$$\nu_{\pm} = \nu_0 \exp\{\pm[(\Delta u - (A_{n+1} - A_n)\gamma_{sl})/(2k_BT)] - E_A/k_BT\}$$

where $A_{n+1} - A_n$ is an increase in the interfacial area due to the attachment of an atom to the crystal. The $\nu$ is the thermal vibration frequency of the interfacial atom. The cluster growth velocity resulting from the difference between $\nu_+$ and $\nu_-$ can be then written as:

$$\begin{aligned} V_{grow} &\sim \exp(-E_A/k_BT)\sinh\{[\Delta u - (A_{n+1} - A_n)\gamma_{sl}]/(2k_BT)\} \\ &\cong \{[\Delta u - (A_{n+1} - A_n)\gamma_{sl}]/(2k_BT)\}\exp(-E_A/k_BT) \end{aligned} \quad (47)$$

The argument of the hyperbolic sine is small near the $T_m$ (it is exactly zero at the $T_m(K_j)$). Eq. (47) indicates that the rate of the growth/melting is driven by the lowering of the free energy, $\Delta u - (A_{n+1} - A_n)\gamma_{sl}$, while the interfacial mobility is determined by the $E_A$ for diffusion jumps of the interfacial atoms. Noting that $A_{n+1} - A_n$ is proportional to $K_j^{-1}$ and $\Delta u = u_0(T - T_m(K_j))$, and then the scaling law for melting applies: $\Delta T_m(K_j) \sim \gamma_{sl}/K_j$. ($T_m(K_j)$ is

the temperature at which $V_{\text{grow}} = 0$). For planar growth the interfacial contribution to the free energy disappears; thus $V_{\text{grow}}$ is zero exactly at the $T_{\text{m}}(\infty)$ ($\Delta u = 0$).

For a given cluster size, the free energy term can be expanded around its $T_{\text{m}}(K_j)$ such that

$$V_{\text{grow}}(K_j) \sim \left[\left(T_{\text{m}}(K_j) - T\right)/T\right]\exp(-E_{\text{A}}/k_{\text{B}}T) \tag{48}$$

This process describes the kinetics of liquid–nanosolid dissolution and growth. The $E_{\text{A}}$ obtained from the best fits are $0.75 \pm 0.05$ eV for 2.0 and 2.6 nm solids and $0.85 \pm 0.05$ eV for 3.5 nm solids, respectively. This result complies with the BOLS expectation that the mean atomic $E_{\text{B}}$ increases with solid size. Incorporating the BOLS correlation to the $T_{\text{m}}(K_j)$ and $E_{\text{A}}(K_j)$, Eq. (48) becomes

$$\begin{aligned} &\frac{\Delta E_{\text{A}}(K_j)}{E_{\text{A}}(\infty)} = \frac{\Delta T_{\text{m}}(K_j)}{T_{\text{m}}(\infty)} = \Delta_{\text{B}} \\ &V_{\text{grow}}(D) \sim [(T_{\text{m}}(\infty)(1+\Delta_{\text{B}}) - T)/T]\exp\{-[E_{\text{A}}(\infty)(1+\Delta_{\text{B}})]/k_{\text{B}}T\} \end{aligned} \tag{49}$$

The exponential part is the same to the diffusivity (see Eq. (46)). Results in Fig. 24a show the mobility of the liquid–solid interface that is determined by diffusion in the adjacent bulk liquid, which is exactly the case of homoepitaxial growth.

*5.4.2.2. Vapor phase deposition.* The understanding of size-dependent melting may provide guidelines for growing nanosolids on heated substrates in vapor deposition. For a given substrate temperature ($T_{\text{S}}$), there will be a minimum critical size of the grown particle. Thus, any particle larger than this size will be deposited without change in size. On the other hand, if the incident cluster size is smaller than the critical size, the particles will melt upon deposition and they will coagulate to produce clusters equal to the critical size or larger. If the $T_{\text{S}}$ is higher than the $T_{\text{m}}$, the arriving clusters may merge and then evaporate associated with size reduction of the coagulated solid [203]. This intuitively implies that the deposition temperature should be as low as possible if one wants to obtain smaller particles. This mechanism also applies to the lower sinterability of nanosolids. As found by Hu et al. [53,54], the solid size of an oxide increases with annealing temperature and agglomeration happens at

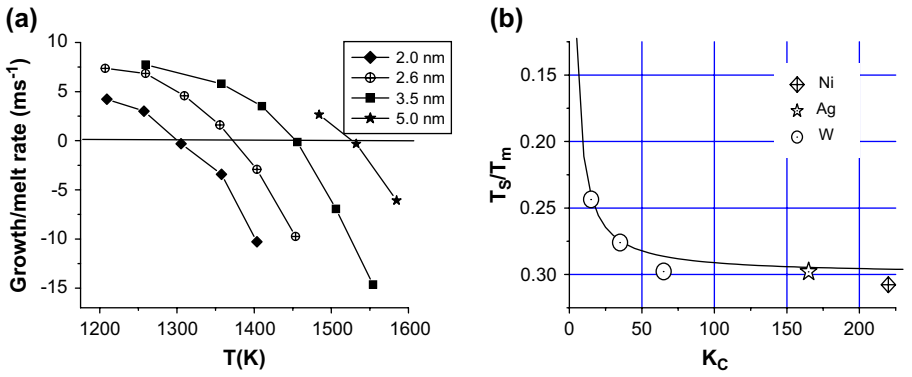


Fig. 24. (a) MD simulation of size and temperature dependence of Si nanosolid melting (negative) and growth (positive) [307]. (b) Agreement between BOLS predictions with measurements [427] of $T_{\text{S}} = 0.3T_{\text{m}}$ dependence of critical sizes for W ($T_{\text{m}}(\infty) = 3695$ K), Ni (1728 K), and Ag (1235 K) nanocrystal growth.

a certain size range at room temperature in the process of ball milling. Recent experimental investigation [428] revealed that the topmost Bi layers on graphite start to lose long-range order at 10–15 K below the Bi bulk melting point, 544.52 K, whereas crystallization occurs from the melt ~125 K below the $T_m(\infty)$, which shows the temperature difference between melting and solidification of the same surface.

Normally, the $T_S(K_j)$ is around 0.3 times the $T_m(K_j)$ [427,429]. The $T_S$ dependence of the critical size $K_C$ can be estimated from the $T_m(K_j)$ expression:

$$T_S(\tau, K_C) = 0.3T_m(\tau, K_j) = 0.3T_m(\infty)(1+\Delta_B)$$
$$\Delta_B \cong \Delta'_B/K_C$$

which gives the thermally stable critical size:

$$K_C = \frac{-\Delta'_B}{1 - T_S(\tau, K_j)/[0.3T_m(\infty)]} = \frac{\tau\sum_3 c_i\left(1 - z_{ib}c_i^{-m}\right)}{1 - T_S(\tau, K_j)/[0.3T_m(\infty)]} \tag{50}$$

It is readily calculated that the constant $\Delta'_B = -2.96$ for a spherical metallic dot ($m = 1$; $\tau = 3$; $K_C > 3$). The critical size and hence the number of atoms in the deposited nanosolid depends on the $T_S(\tau, K_j)/0.3T_m(\infty)$ ratio. The $R_C$ ($=K_C d$) at $T_S$ can be estimated with the known atomic size $d$ and $T_m(\infty)$ as illustrated in Fig. 24b showing agreement between predictions and experimental results [430]. This relation predicts that a monatomic layer of metals ($\tau = 1$) could only grow at $T_S = 0$ K or nearby. Guo et al. has observed that Pd monolayer could hardly form on Si surface at 4 K [368]. The $R_C$ ($K_C d_0$) at $T_S$ can be estimated with the known atomic size $d_0$ and $T_m(\infty)$ as illustrated in Fig. 24b.

*5.4.2.3. Multilayer growth: atom hungering.* The growth of nanostructured multilayer thin films depends largely on how the adatoms aggregate in forming islands of various shapes in the submonolayers. However, little was known about the detailed processes of nucleation and growth in the presence of surfactant at an atomic scale until recently when Wang and coworkers [431,432] initiated and verified a reaction-limited aggregation mechanism, which forms one of the key competitive factors dominating the process of crystal growth. Using first-principle total-energy calculations, they show that an adatom can easily climb up at monatomic-layer-high steps on several representative fcc metal (110) surfaces via a place exchange mechanism. Inclusion of such novel processes of adatom climbing in kinetic Monte Carlo simulations of Al(110) homoepitaxy as a prototypical model system can lead to the existence of an intriguing faceting instability. A fractal-to-compact island shape transition can be induced by either *decreasing* the growth temperature or *increasing* the deposition flux, agreeing with experimental observations. Recent advancements [433,434] in investigating the formation and decay of surface-based nanostructures and in identifying the key rate processes in kinetics-driven atomic processes have further confirmed the novel concept of adatoms ascending at step edges and faceting on fcc metals.

The current BOLS correlation premise might provide a possible complementary mechanism from the perspective of bond making and breaking for the adatom climbing and exchanging position. The thermodynamic process of crystal growth is subject to the competition between atomic cohesion and thermal activation. Bombardment by the energetic deposition flux also supplies energy to the atom participating in the growth. The adatom tends to find a location with optimal total energy that is the sum of binding and heating energies and hence to cross ascend or

descend the step edge in the process of multilayer superlattice growth. At a given temperature, the magnitude of the total energy of an atom with $z$ coordinate is described by (Section 2):

$$E_{\text{total}}(T) = \sum_{z} [\eta_{1l}(T_{\text{m}} - T) + \eta_{2l}]$$

Relocation of the adatom from one site to another with a net gain in the $E_{\text{total}}(T)$ could be the force driving the process as such. The gain of $E_{\text{total}}(T)$ is subject to the difference of atomic CN, the specific heat per bond, $\eta_{1l}$, the melting point of the bond, and the $1/z$ fold entropy for atomization from the molten phase, $\eta_{2l}$. Therefore, the exchanging of positions occurs because of nonequility of binding energy for the exchange specimens. Adatoms ascending or descending across the step edge where the atomic CN is lower can be a clear indication that the thermally activated bond broken is nonsimultaneous and that atoms with fewer bonds at the tip of an edge are generally less stable. However, for Ga and Sn atoms, the $T_{\text{m}}$ becomes higher when the atomic CN is reduced [317–320], as discussed in Section 5.2.4. Therefore, it could be possible to observe that Ga and Sn atoms grow preferably at the tip of an edge under certain conditions, as the binding of such atoms with 2–3 bonds is stronger than even that in the bulk.

### *5.5. Summary*

The BOLS correlation has enabled the thermodynamic behavior of a nanosolid to be consistently formulated and understood in terms of atomic CN imperfection and its effect on atomic cohesion. It is understood that the difference between the cohesive energy of an atom at the surface and that of an atom inside the solid determines the fall or rise of the $T_{\text{m}}$ of a surface and a nanosolid. The approach is in good accordance with existing models based on classical and molecular thermodynamics. Combination of these models should provide deeper insight into the physical origin and the general trends of the melting behavior of a nanosolid.

The Curie temperature suppression for ferromagnetic, ferroelectric, and superconducting nanosolids follows the same trend of $T_{\text{m}}$ suppression that is dictated by the BOLS correlation and the effect of high-order CN imperfection, as well as the criterion of thermal-vibration–exchange-interaction energy equilibration. At $T_{\text{C}}$, the atomic thermal vibration energy overcomes a portion of the atomic $E_{\text{B}}$, which triggers the order–disorder transition of the spin–spin exchange interaction. Numerical match between predictions and measurements for a number of specimens reveals that the short spin–spin correlation dominates the exchange interaction in the ferromagnetic Fe, Co, Ni, and $Fe_3O_2$ nanosolids, whereas the long-range interaction dominates the exchange energy for the ferroelectric $PbTiO_3$, $PbZrO_3$, $SrBi_2Ta_2O_9$, and $BaTiO_3$, and the superconductive $MgB_2$ nanosolids. Consistency between predictions and experimental observations on the $T_{\text{C}}$ suppression of the considered nanosolids evidences the validity of the current premise, which has also been extended to the cases of nano-diffusivity, nano-reactivity and the $E_{\text{A}}$ for atomic dislocation and crystal growth.

## 6. Lattice dynamics: acoustic and optic phonons

### *6.1. Background*

Vibration of atoms at a surface is of high interest because the behavior of phonons influences directly the electrical and optical properties in semiconductor materials, such as electron–phonon coupling, photoabsorption and photoemission, as well as transport dynamics in devices

[435]. With miniaturization of a solid down to the nanometer scale, the transverse and the longitudinal optical (TO/LO) Raman modes shift towards lower frequency (or called optical mode softening) [436], accompanied with generation of low-frequency Raman (LFR) acoustic modes at wave numbers of a few or a few tens $cm^{-1}$. The LFR peak shifts up (called acoustic mode hardening) towards higher frequency when the solid size is being reduced [437,438]. Most of the theoretical studies of phonon modes are based on the continuum dielectric mechanism [439,440]. A microscopic lattice-dynamical calculation has already been developed [438,441]. However, the underlying mechanism behind the red and blue Raman shift is under debate with the possible mechanisms summarized as follows.

The size-dependent Raman shifts can be generalized empirically as [438,436]

$$\omega(K_j) = \omega(\infty) + A_f(d_0/K_j)^{\kappa}$$

where $A_f$ and $\kappa$ are adjustable parameters used to fit the measured data. For the optical redshift, $A_f < 0$. For Si, as an example, $\omega(\infty) = 520\ cm^{-1}$ corresponding to the wavelength of $2 \times 10^4$ nm. The index $\kappa$ varies from 1.08 to 1.44. The $d_0$ is the lattice size that should contract with the solid dimension [677]. For the LFR mode blueshift, $A_f > 0$, $\kappa = 1$. The LFR mode disappears for large particles because $\omega(\infty) = 0$.

### 6.1.1. Acoustic phonon hardening

*6.1.1.1. Quadrupolar vibration.* The LFR peaks have always been attributed to acoustic modes associated with the vibration of the individual nanoparticle as a whole. The phonon energies are size dependent and vary with materials of the host matrix. The LFR scattering from silver nanoclusters embedded in porous alumina [442] and $SiO_2$ [443] and has been suggested to arise from the quadrupolar vibration modes that are enhanced by the excitation of the surface plasmas of the encapsulated Ag particles. The selection of modes by LFR scattering is due to the stronger plasmon–phonon coupling for these modes. For an Ag particle smaller than 4 nm, the size dependence of the peak frequency can be well explained by Lamb's theory [444], which gives vibrational frequencies of a homogeneous elastic body in a spherical form. The mechanism for LFR mode enhancement is analogous to the case of surface-plasma enhanced Raman scattering from molecules adsorbed on rough metal surfaces. The surface acoustic phonons can be described as the eigen frequencies of a homogeneous elastic sphere under stress-free boundary conditions, which give rise to a low-frequency $\omega$ that is in the range of a few to a few tens of $cm^{-1}$ in the vibrational spectra. These modes are suggested to correspond to spheroidal and torsional modes of vibrations of a spherical or an ellipsoidal particle. Spheroidal motions are associated with dilation and strongly depend on the cluster material through $v_t$ and $v_l$, where $v_t$ and $v_l$ are the transverse and longitudinal sound velocities, respectively. The sound velocity in a medium depends functionally on the Young's modulus and the mass density, i.e., $v \sim (Y/\rho)^{0.5} \sim \sqrt{E_b}$ where $E_b$ is the cohesive energy per coordinate [283]. No volume change is assumed in the torsional motion of the particle. These modes are characterized by two indices $l$ and $n$, where $l$ is the angular-momentum quantum number and $n$ is the branch number and $n = 0$ represents the surface modes. It has been shown that spheroidal modes with $l = 0$ and 2 are Raman active and the torsional modes are Raman inactive [445]. The surface quadrupole mode ($l = 2$) appears in both polarized and depolarized geometry, whereas the surface symmetrical mode ($l = 0$) appears only in the polarized geometry. The

relation between the particle size and the frequency of the polarized acoustic phonon can be established from [446]:

$$\sin(\xi) = 4n_{\text{eff}}^2 j_1(\xi)$$

with complex argument,

$$\xi = R(\omega + i\Gamma)/v_{\text{l}} \tag{51}$$

where $\nu$ and $\Gamma$ are the phonon frequency and bandwidth, respectively, for the polarized-confined acoustic phonon of the first order. The term $j_1(\xi)$ is the spherical Bessel function of the first kind with order one, $v_{\text{l}}$ is the longitudinal sound velocity in the nanoparticle, and $n_{\text{eff}}$ is an effective internal acoustic index given by

$$n_{\text{eff}}^2 = n_{\text{p}}^2 - f_{\text{c}}\left\{n_{\text{m}}^2 - (k\xi)^2/\{4[1 - i(k\xi)]\}\right\} \tag{52}$$

where $n_{\text{p}}$ and $n_{\text{m}}$ are the ratios of transverse-to-longitudinal sound velocities in the particle and in the matrix, respectively, $k$ is the ratio between the longitudinal sound velocities in the particle and in the matrix, and $f_{\text{c}}$ is a coupling constant between the particle and the matrix, given by

$$f_{\text{c}} = \rho_{\text{m}}/\left(k^2\rho_{\text{p}}\right)$$

with $\rho_{\text{m}}$ and $\rho_{\text{p}}$ being the mass densities for the matrix and for the particle, respectively. By substituting $n_{\text{eff}}$ in Eq. (52) into Eq. (51), the relation between particle radius $R$ and the phonon frequency $v$ can be obtained from the real part of Eq. (51). The eigen frequencies for the torsional modes and the spheroidal modes with $n = 0$ can be written as [447]:

$$\begin{cases} \omega_{\text{t}}^1 = 0.815v_{\text{t}}/Rc, & \omega_{\text{t}}^2 = 0.4v_{\text{t}}/Rc & \text{(tortional)} \\ \omega_{\text{s}}^0 = 0.18v_{\text{l}}/Rc, & \omega_{\text{s}}^1 = 0.585v_{\text{l}}/Rc, \quad \omega_{\text{s}}^2 = 0.42v_{\text{l}}/Rc & \text{(spheroidal)} \end{cases}$$

where $c$ is the velocity of light in vacuum. For bulk Ag, $v_{\text{t}} = 1660$ m/s and $v_{\text{l}} = 3650$ m/s, the $\omega$ is around $10^2$ cm$^{-1}$ level. This approach fits well the measured LFR data for Ag embedded in $Al_2O_3$ and $SiO_2$ matrices [446,447].

Zi et al. [448] calculated the Raman scattering from acoustic phonons in Si nanocrystals by a lattice-dynamical model. The polarized and depolarized low-frequency Raman peaks were ascribed as confined LA-like and TA-like acoustic phonons, respectively. They found that the effects of the matrix are important, which will lead to a redshift for both polarized and depolarized Raman peaks. Their approaches improve the fit to the measurement compared with calculations using Lamb's model. Atomistic simulations [449] suggested that the morphology of nanoscopic Ag grains (in crystalline, twined icosahedra, Mark's decahedra, and irregular nanograins) introduces a high degree of complexity into the phonon spectra, total and partial vibrational density of states, and phonon localization. For the low-energy, single-crystalline grains present nearly pure torsional and radial phonon modes. When compared to faceted grains of the same size, high-energy, spherical modes that present regular protrusions on the surface have a smaller acoustic gap and a higher total DOS. The twined icosahedra have a breathing mode. Nanograins with grain boundaries and surface disorder do not have degenerate frequencies and the acoustic gap is significantly reduced. These nanograins are the only ones that exhibit low-frequency DOS.

*6.1.1.2. Lattice strain.* The blueshift of LFR mode has also been attributed to the effect of lattice contraction induced stain. $CdS_xSe_{1-x}$ nanocrystals embedded in a borosilicate ($B_2O_3$–$SiO_2$) glass matrix [450] have been found to experience size-dependent compressive strain. The lattice strain causes the surface tension to increase when the crystal size is reduced. The observed blueshift of acoustic phonon energies was suggested to be the consequence of the compressive stress overcoming the redshift caused by phonon confinement with negative dispersion. Liang et al. [451] also presented a model for the Raman blueshift by relating the frequency shift to the bond strength and bond length that are functions of the entropy, latent heat of fusion, and the melting point.

*6.1.2. Optical phonon softening*

The high-frequency Raman shift has usually been suggested to be activated by surface disorder [452], and explained in terms of surface stress [453,454] or phonon quantum confinement [455,456], as well as surface chemical passivation. The Raman shifts of $TiO_2$ particles are attributed to the effects of decreasing particle size on the force constants and vibrational amplitudes of the nearest-neighbor bonds [457]. However, the effect of stress can usually be ignored for hydrogenated silicon [458,459], in which hydrogen atoms terminate the surface dangling bonds, which reduce the bond strains and hence the residual stress. The phonon confinement model [455] attributes the redshift of the asymmetric Raman line to relaxation of the q-vector selection rule for the excitation of the Raman active phonons due to their localization. The relaxation of the momentum conservation rule arises from the finite crystalline size and the diameter distribution of the nanosolid in the films. When the size is decreased, the rule of momentum conservation will be relaxed and the Raman active modes will not be limited at the center of the Brillouin zone [453]. A Gaussian-type phonon confinement model [456] that has been used to fit the experimental data indicates that strong phonon damping is present, whereas calculations [460] using the correlation functions of the local dielectric constant ignore the role of phonon damping in the nanosolid. The large surface-to-volume ratio of a nanodot strongly affects the optical properties mainly due to introducing surface polarization and surface states [461]. Using a phenomenological Gaussian envelope function of phonon amplitudes, Tanaka et al. [462] show that the size dependence originated from the relaxation of the $q = 0$ selection rule based on the phonon confinement argument with negative phonon dispersion. The phonon energies for all the glasses are reduced, the values of the phonon energies of CdSe nanodots are found to be quite different for different host glasses. The currently available models for the optical redshift are based on assumptions that the materials are homogeneous and isotropic, which is valid only in the long-wavelength limit. When the size of the nanosolid is in the range of a few nanometers, the continuum dielectric models exhibit limitations.

Hwang et al. [253] indicated that the effect of lattice contraction must be considered to explain the observed differences in the redshift of phonon energies for CdSe nanodots embedded in different glass matrices. To obtain the phonon frequency as a function of the dot radius $K_j$ with contribution of lattice contraction, it was assumed that

$$\omega(K_j) = \omega_L + \Delta\omega_D(K_j) + \Delta\omega_C(K_j) \tag{53}$$

where $\omega_L$ is the LO phonon frequency of the bulk, $\Delta\omega_D(K_j)$, the peak shift due to phonon dispersion and $\Delta\omega_C(K_j)$, the peak shift due to lattice contraction. The phonon dispersion $\Delta\omega_D(K_j)$ is given by

$$\Delta\omega_{\mathrm{D}}(K_j)=\left[\omega_{\mathrm{L}}^2-\beta_{\mathrm{L}}^2\left(\frac{\mu_{np}}{K_jd_0}\right)^2\right]^{1/2}-\omega_{\mathrm{L}}\cong-\left(\frac{\beta_{\mathrm{L}}^2}{2\omega_{\mathrm{L}}}\right)\left(\frac{\mu_{np}}{K_jd_0}\right)^2 \tag{54}$$

where the parameter $\beta_{\mathrm{L}}$ describes the phonon dispersion assumed to be parabolic and $\mu_{np}$ is the nonzero $n_p$th root of the equation of $\tan(\mu_{np})=\mu_{np}$. The phonon frequency shift due to the lattice contraction $\Delta\omega_{\mathrm{C}}(K_j)$ is given as [450]:

$$\Delta\omega_{\mathrm{C}}(K_j)=\omega_{\mathrm{L}}\left[\left(1+\frac{3\Delta d(K_j)}{d}\right)^{-\gamma}-1\right]\cong-3\gamma\omega_{\mathrm{L}}\frac{\Delta d(K_j)}{d}$$

where

$$\frac{\Delta d(K_j)}{d}=(\alpha'-\alpha)(T-T_{\mathrm{g}})-\frac{2\beta_{\mathrm{c}}}{3}\left(\frac{\sigma_\infty}{K_jd_0}+\frac{b}{2(K_jd_0)^2}\right)\cong(\alpha'-\alpha)(T-T_{\mathrm{g}})-\frac{\beta_cb}{3(K_jd_0)^2} \tag{55}$$

$\gamma$ is the Grüneisen parameter, $\alpha'$ and $\alpha$ are the linear thermal expansion coefficients of the host glass and the nanodot, respectively, $T$ and $T_{\mathrm{g}}$ are the testing and the heat-treatment temperatures, respectively, $\beta_{\mathrm{c}}$ and $\sigma_\infty$ are the compressibility and the surface tension of the bulk, respectively, and $b$, the parameter describing the size-dependent surface tension of the crystal. The surface tension for bulk crystals is assumed small. The first term describes the lattice contraction by thermal expansion mismatch between the glass matrix and the crystal, and the second term arises from the increase of surface tension with the decrease of crystal size. Substituting Eq. (55) into Eq. (54), the phonon frequency change at a given temperature is obtained

$$\frac{\Delta\omega(K_j)}{\omega_{\mathrm{L}}}=-3\gamma(\alpha'-\alpha)(T-T_{\mathrm{g}})-\left[\frac{1}{2}\left(\frac{\beta_{\mathrm{L}}\mu_{n_p}}{\omega_{\mathrm{L}}}\right)^2-\gamma\beta_{\mathrm{C}}b\right](K_jd_0)^{-2}=A-BK_j^{-2} \tag{56}$$

For a free surface, $\alpha'=\alpha$ and $b=0$. There are some difficulties, however, to use this equation, as remarked on by Hwang et al. [463] since the thermal expansion coefficient within the temperature range $T-T_{\mathrm{g}}$ is hardly detectable. The value of $B$ in Eq. (56) is given by the difference of the phonon negative dispersion and the size-dependent surface tension. Thus, a positive value of $B$ indicates that the phonon negative dispersion exceeds the size-dependent surface tension and consequently causes the redshift of phonon frequency. On the contrary, if the size-dependent surface tension is stronger than the phonon negative dispersion, blueshift of phonon frequency occurs. In case of balance of the two effects, i.e., $B=0$, the size dependence disappears. Furthermore, the parameter $b$ introduced by the size-dependent surface tension is also unknown. At the lower end of the size limit, the $\omega(K_j)\to-\infty$ diverges in a $K_j^{-2}$ way. Therefore, the existing models could hardly reproduce the Raman frequency shifts satisfactorily near the lower end of the size limit.

## 6.2. Principles

### 6.2.1. Vibration modes

Raman scattering is known to arise from the radiating dipole moment induced in a system by the electric field of incident electromagnetic radiation. The laws of momentum and energy conservation govern the interaction between a phonon and a photon. When we consider a solid containing numerous Bravais unit cells and each cell contains $n$ atoms, there will be $3n$ modes of vibrations. Among the $3n$ modes, there will be three acoustic modes, LA, $TA_1$ and $TA_2$ and $3(n-1)$ optical modes. The acoustic mode represents the in-phase motion of the mass center of the unit cell or the entire solid. Therefore, the LFR should arise from the vibration of the entire nanosolid interacting with the host matrix. For a freestanding nanosolid, the LFR should correspond to intercluster interaction. The optical mode is the relative motion of the individual atoms in a complex unit cell that contains more than one atom. For elemental solids with a simple such as the fcc structure of Ag, there presents only acoustic modes. The structure for silicon or diamond is an interlock of two fcc structures that contains in each cell two atoms in nonequivalent positions, so there will be three acoustic modes and three optical modes.

### 6.2.2. Lattice vibration frequency

The total energy $E_{\text{total}}$ that sums the lattice thermal vibration and interatomic binding can be expressed in a Taylor's series, as given in Eq. (33) (Section 5). When the atom is in an equilibrium position, the bond energy is $E_b$. The second-order term corresponds to the Harmonic vibration energy, in which, the force constant $k = \mathrm{d}^2u(r)/\mathrm{d}r^2\big|_d \propto E_b/d_0^2$ and $k' = \mathrm{d}^3u(r)/\mathrm{d}r^3\big|_{d_0} \propto E_b/d_0^3$. The latter is in the dimension of stress. The vibration amplitude is $x = r - d_0$. The high-order terms correspond to the nonlinear contribution that can be negligible in the first-order approximation. For a single bond, the $k$ and $k'$ are strengthened; for an undercoordinated atom, the resultant $k$ could be lower because of the reduced CN. Since the short-range interaction on each atom results from its neighboring coordinating atoms, the atomic vibrating dislocation is the contribution from all the surrounding coordinates, $z$. Considering the vibration amplitude $x \ll d_0$, it is convenient and reasonable to take the mean contribution from each coordinate to the force constant and to the magnitude of dislocation as the first-order approximation, i.e.,

$$k_1 = k_2 = \cdots = k_z = \mu_i(c\omega)^2$$

and

$$x_1 = x_2 = \cdots = x_z = (r - d_0)/z$$

Therefore, the total energy of a certain atom with $z$ coordinates is the sum over all coordinates [464]:

$$E_c = \sum_z \left[ -E_b + \frac{\mu c^2\omega^2}{2}\left(\frac{r-d_0}{z}\right)^2 + \cdots \right] = -zE_b + \frac{z\mathrm{d}^2u(r)}{2!\mathrm{d}r^2}\bigg|_{d_0}(r-d_0)^2 + \cdots \tag{57}$$

where $\mu$ is the reduced mass of the dimer atoms and $c$ is the speed of light. This relation leads to an expression for the phonon frequency as a function of atomic CN, bond length, and bond energy

$$\omega = \frac{z}{c}\left[\frac{\mathrm{d}^2u(r)}{\mu \mathrm{d}r^2}\bigg|_{d_0}\right]^{\frac{1}{2}} \propto \frac{z(E_\mathrm{b})^{1/2}}{d_0}, \text{ and } \frac{\omega_i}{\omega} = z_{i\mathrm{b}}c_i^{-(m/2+1)} \tag{58}$$

*6.2.3. Size dependence*

Combining Eqs. (58) and (59) gives the size-dependent redshift of optical mode of a nanosolid [where $Q(\infty) = \omega(\infty) - \omega(1)$]:

$$\begin{aligned} &\omega(K_j) - \omega(1) = [\omega(\infty) - \omega(1)](1 + \Delta_R) \\ &\text{or, } \frac{\omega(K_j) - \omega(\infty)}{\omega(\infty) - \omega(1)} = \Delta_R < 0 \\ &\Delta_R = \sum_{i\le 3}\gamma_{ij}\left(\frac{\omega_i}{\omega_\mathrm{b}} - 1\right) = \sum_{i\le 3}\gamma_{ij}\left(z_{i\mathrm{b}}c_i^{-(m/2+1)} - 1\right) \end{aligned} \tag{59}$$

where $\omega_0$ and $\omega_i$ correspond to the vibration frequency of an atom inside the bulk and in the $i$th surface atomic shell, respectively. $\omega(1)$ is the vibrational frequency of an isolated dimer, which is the reference point for the optical redshift upon nanosolid and bulk formation. The frequency decreases from the dimer value with the number of atomic CN and then reaches the bulk value ($z = 12$) that is experimentally detectable.

*6.3. Verification*

*6.3.1. Optical modes and dimer vibration*

In experiment, one can only measure $\omega(\infty)$ and $\omega(K_j)$ in Eq. (59). However, with the known $m$ value derived from the measurement of other quantities such as the melting point or core-level shift, one can determine $\omega(1)$ and the bulk shift $\omega(\infty) - \omega(1)$ by matching the measured data of size dependence to the theoretically predicted line:

$$\Delta\omega(K_j) = \begin{cases} \dfrac{-A'}{K_j^\kappa} & (\text{Measurement}), \\ = \Delta_R[\omega(\infty) - \omega(1)] & (\text{Theory}) \end{cases} \tag{60}$$

Hence, the frequency shift from the dimer bond vibration to the bulk value, $\omega(\infty) - \omega(1) \equiv -A'/(\Delta_R K_j)$, can be obtained. The matching of the prediction with the measurement indicates that $k = 1$ because $\Delta_R \propto K_j^{-1}$. Fig. 25 shows that the BOLS predictions match exceedingly well with the theoretically calculated and the experimentally measured optical redshift of a number of samples, which therefore justifies the validity of the approximation. The derived information about the corresponding dimer vibration is given in Table 7.

*6.3.2. Acoustic modes and intercluster interaction*

Fig. 26 shows the least-square-mean-root fitting of the size-dependent LFR frequency for different nanosolids. The LFR frequency depends linearly on the inverse $K_j$

$$\Delta\omega(K_j) = \omega(K_j) - \omega(\infty) = \frac{-A'}{K_j}$$

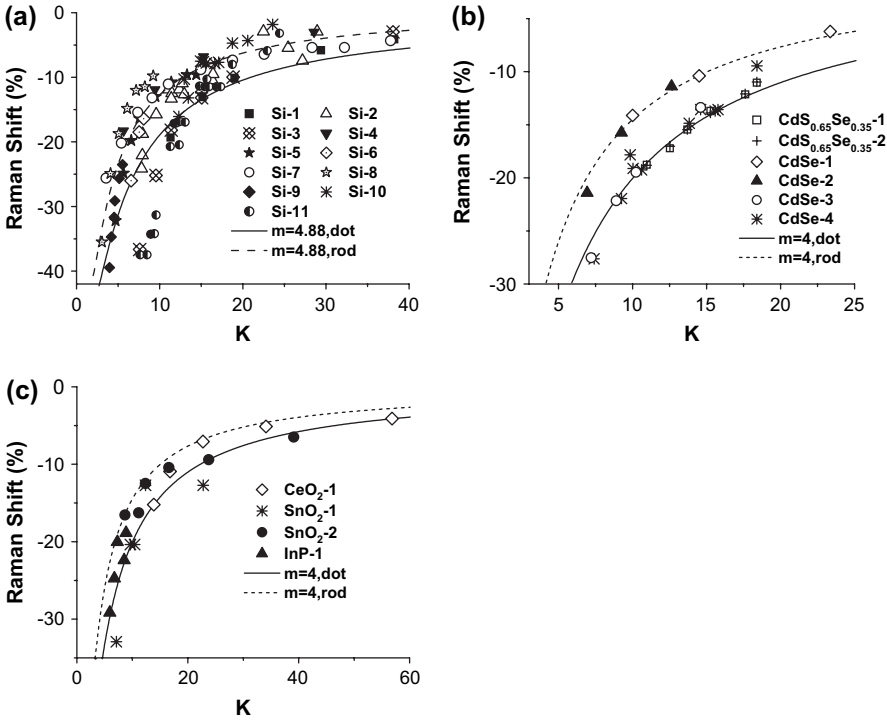


Fig. 25. Comparison of the predictions with observations on the size-dependent TO/LO phonon frequency shift of nanosilicon. Theoretical results: Si-1 was calculated using correlation length model [465]; Si-3 (dot) and Si-4 (rod) were calculated using the bulk dispersion relation of phonons [466]; Si-5 was calculated from the lattice-dynamic matrix [438]; Si-7 was calculated using phonon confinement model [467], and Si-8 (rod) and Si-9 (dot) were calculated using bond polarizability model [436]. Si-2 [468], Si-6 [469], Si-10 and Si-11 [453] are measured data. (b) $CdS_{0.65}Se_{0.35}$-1, $CdS_{0.65}Se_{0.35}$ (in glass)-$LO_2$, $CdS_{0.65}Se_{0.35}$-2, $CdS_{0.65}Se_{0.35}$ (in glass)-$LO_1$ [470], CdSe-1 CdSe (in $B_2O_3SiO_2$)-LO, CdSe-2 CdSe (in $SiO_2$)-LO and CdSe-3 CdSe (in $GeO_2$)-LO [463], CdSe-4 CdSe (in $GeO_2$)-LO [462], (c) $CeO_2$-1 [471], $SnO_2$-1 [472], $SnO_2$-2 [452], and InP-1 [473] are all measurements.

The zero intercept at the vertical axis, $\omega(\infty) = 0$, indicates that when the $K_j$ approaches infinity, the LFR peaks disappear, which implies that the LFR modes and their blueshifts originate from vibration of the individual nanoparticle as a whole, as represented in the quadruple vibration mechanism. It seems to be unnecessary to involve the bond strain at the interface to

Table 7
Vibration frequencies of isolated dimers of various nanosolids and their redshift upon bulk formation derived from simulating the size-dependent redshift of Raman optical modes, as shown in Fig. 25

| Material | Mode | $d_0$ (nm) | $A'$ | $\omega(\infty)$ ($cm^{-1}$) | $\omega(1)$ ($cm^{-1}$) | $\omega(\infty)-\omega(1)$ ($cm^{-1}$) |
|---|---|---|---|---|---|---|
| $CdS_{0.65}Se_{0.35}$ | $LO_1$ CdSe-like | 0.286 | −23.9 | 203.4 | 158.8 | 44.6 |
| | $LO_2$ CdS-like | 0.286 | −24.3 | 303 | 257.7 | 45.3 |
| CdSe | LO | 0.294 | −7.76 | 210 | 195.2 | 14.8 |
| $CeO_2$ | | 0.22 | −20.89 | 464.5 | 415.1 | 49.4 |
| $SnO_2$ | $A_{1g}$ | 0.202 | −14.11 | 638 | 602.4 | 35.6 |
| InP | LO | 0.294 | −7.06 | 347 | 333.5 | 13.5 |
| Si | | 0.2632 | −5.32 | 520.0 | 502.3 | 17.7 |

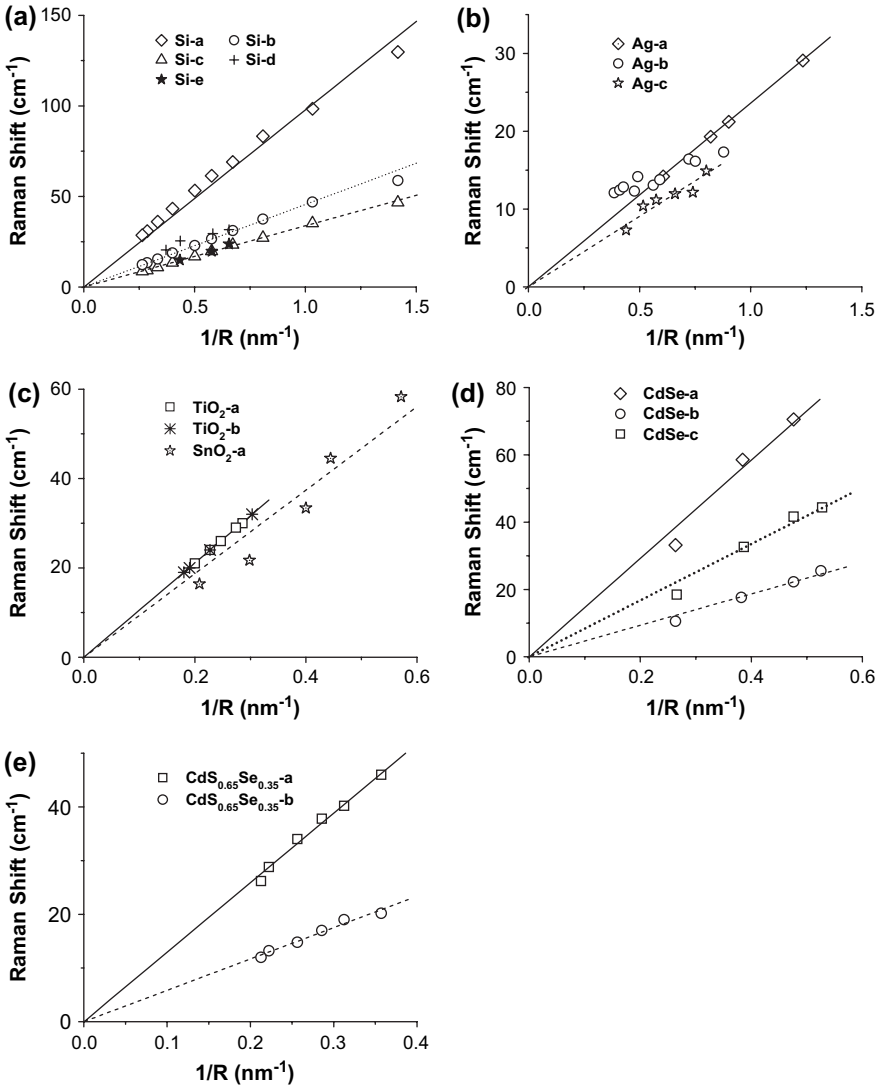


Fig. 26. Generation and blueshift of the LFR spectra where the solid, dotted and dashed lines are the corresponding results of the least squares fitting. (a) The Si-a ($A_1$ mode), Si-b ($T_2$ mode) and Si-c (E mode) were calculated from the lattice-dynamic matrix by using a microscopic valence force field model [438]; the Si-d and Si-e are the experimental results [437]. (b) Ag-a (Ag in $SiO_2$) [475], Ag-b (Ag in $SiO_2$) [443], and Ag-c (Ag in alumina) [442]. (c) $TiO_2$-a [476], $TiO_2$-b [476], and $SnO_2$-a [452]. (d) CdSe-a ($l=0$, $n=2$), CdSe-b ($l=2$, $n=1$) and CdSe-c ($l=0$, $n=1$) [477]. (e) $CdS_{0.65}Se_{0.35}$-a [$CdS_{0.65}Se_{0.35}$ (in glass)-LF2] and $CdS_{0.65}Se_{0.35}$-b [$CdS_{0.65}Se_{0.35}$ (in glass)-LF1] [470] are all measured data.

the LFR modes. Compared with the sophisticated lattice-dynamics calculations in which the polarized and depolarized scattering processes are considered, the current derivatives treat the nanoparticle as a whole and give information about the strength of the interparticle interaction, as summarized in Table 8. This result implies that the mechanical coupling between $CeO_2$ nanoclusters can be assumed to play a key role in the LFR [474]. The slope values for Si

Table 8
Linearization of the LFR acoustic modes of various nanosolids to give information about the sound velocity in the specific solid

| Sample | $A'$ |
|---|---|
| Ag-a and Ag-b | $23.6 \pm 0.72$ |
| Ag-c | $18.2 \pm 0.56$ |
| TiO-a, TiO-b | $105.5 \pm 0.13$ |
| SnO-a | $93.5 \pm 5.43$ |
| CdSe-1-a | $146.1 \pm 6.27$ |
| CdSe-1-b | $83.8 \pm 2.84$ |
| CdSe-1-c | $46.7 \pm 1.39$ |
| CdSSe-a | $129.4 \pm 1.18$ |
| CdSSe-b | $58.4 \pm 0.76$ |
| Si | 97.77 |
| Si | 45.57 |
| Si | 33.78 |

nanosolid are 97.77, 45.57 and 33.78 for the $A_1$, $T_2$ and E modes, corresponding to the stretching (LA) and bending (TA) modes, respectively.

*6.3.3. Surface atom vibration*

According to Einstein's relation, it can be derived that $\mu(c\omega x)^2/2z = k_B T$. At a given temperature, the vibrational amplitude and frequency of a given atom are correlated as $x \propto z^{1/2}\omega^{-1}$, which is CN dependent. The frequency and magnitude of vibration for a surface atom at the surface ($z = 4$) or a metallic monatomic chain (MC with $z = 2$) can be derived as

$$\frac{\omega_1}{\omega_b} = z_{ib} c_1^{-(m/2+1)} = \begin{cases} 0.88^{-3.44}/3 = 0.517 & \text{(Si)} \\ 0.88^{-3/2}/3 = 0.404 & \text{(Metal)} \end{cases}$$

$$\frac{x_1}{x_b} = (z_1/z_b)^{1/2}\omega_b/\omega_1 = (z_b/z_1)^{1/2} c_1^{(m/2+1)} = \begin{cases} \sqrt{3} \times 0.88^{3.44} = 1.09 & \text{(Si)} \\ \sqrt{3} \times 0.88^{3/2} = 1.43 & \text{(Metal)} \end{cases} \quad (61)$$

The vibrational amplitude of an atom at the surface or an MC is indeed greater than that of a bulk atom while the frequency is lower. The magnitude and frequency are sensitive to the $m$ value and vary insignificantly with the curvature of a spherical dot when $K_j > 3$. This result verifies the assumption [41,96] that the vibration amplitude of a surface atom is always greater than the bulk value and it keeps constant at all particle sizes.

*6.4. Summary*

In summary, a combination of the BOLS correlation and the scaling relation has enabled us to correlate the size-created and size-hardened LFR acoustic phonons to the inter-grain interaction and the optical phonon softening to the CN imperfection reduced cohesive energy of atoms near the surface edge. The optical softening and acoustic hardening are realized in a $K_j^{-1}$ fashion. Decoding the measured size dependence of the Raman optical redshift has derived vibrational information on Si, InP, CdS, CdSe, $TiO_2$, $CeO_2$, and $SnO_2$ dimers and their bulk shifts, which is beyond the scope of direct measurement. As the approach proceeds in a way from a bond-by-bond, atom-by-atom, shell-by-shell approach, no other constraints for the continuum medium are applied. The striking significance is that we are able to verify the

correlation between the magnitude and frequency of the vibration of the lower-coordinated atoms. Consistency between the BOLS predictions and observations also verifies the validity of other possible models that incorporate the size-induced Raman shift from different perspectives. The findings gained herewith and progress made so far by the practitioner and coworkers give further evidence of the impact of bond-order loss and the essentiality and validity of the BOLS correlation mechanism in describing the behavior of low-dimensional systems.

## 7. Photon emission and absorption

### *7.1. Background*

For the particular concern of the photoelectronic properties, nanostructured semiconductors exhibit the general trends of the entire band-structure change associated with the reduced dimensions of the solid [44]. The observable changes may be summarized as follows:

(i) The band gap expands with reducing particle size, which gives rise to the blueshift in the PL and photo-absorbance (PA) spectra of nanometric semiconductors such as Si oxides [73,478,479,480], III–V [481] (GaN [482,483], InAs [484], GaP, and InP [485,486]) and II–VI (CdS [487–489], ZnS [490], CdSe [491,492], ZnTe [493], CdTe/CdZnTe [494]) compounds.
(ii) The energies of PL and PA involve the contribution from electron–phonon coupling that shifts the optical band gap $E_G$ from the true $E_G$ by the well-known value of Stokes shift arising from electron–phonon interaction that also changes with solid size [47].
(iii) The energy levels of the core bands and the adsorbate-induced chemical shifts move simultaneously towards higher binding energy (in absolute value). XPS measurements revealed that the main core-level peaks and the oxide satellites of Cu-$2p_{3/2}$ [495] (−932.1, −940.1 eV), Sn-3d (−484.4, −486.7 eV) [496], Sn-4d (−26, −31 eV), Ta-$4f_{5/2}$ (−23.4, −26.8 eV) and Ta-$4f_{7/2}$ (−31.6, −36.5 eV) [496], move simultaneously up and the amounts of change depend on the original core-level position and particle size. These dedicated observations confirm that the particle size and oxidation have important effects on the core-level shift of nanometric compounds, which is of great value in understanding the nature of nanometric systems.
(iv) Because of $E_G$ expansion, the complex dielectric constant of a nanometric semiconductor is significantly suppressed [497], which forms enormous impact in electronic and optical devices. The reduction of dielectric constant can enhance the Coulomb interaction among electrons, holes, and ionized shallow impurities in nanometric devices, and enhances the exciton binding energy [498].

Therefore, it would be more appropriate in modeling practice of the Hamiltonian related properties to consider the simultaneous change of all the properties relating to the Hamiltonian rather than simply separate one phenomenon at a time from others.

### *7.2. Outstanding models*

#### *7.2.1. Quantum confinement*

Among the numerous models for the PL blueshift, "quantum confinement (QC)" theory [69] has been accepted as an elegant solution. Efros and Efros [70] first proposed, in 1982, this

concept based on the experimental findings of the size effect on the blueshift in the main exciton absorption of CuCl (~3 nm across) nanocrystallites [499]. The confinement effect on the band gap, $E_G$, of a nanosolid of radius $R$ was expressed as [70]:

$$E_G(R) = E_G(\infty) + \pi^2\hbar^2/(2\mu R^2) \tag{62}$$

where $\mu(1/\mu = 1/m_h^* + 1/m_e^*)$, being the reduced mass of an electron–hole (e–h) pair, is an adjustable parameter. Eq. (62) indicates that the $E_G$ expansion arises from the kinetic energy of the e–h pairs that are separated by a distance of the particle dimension, $R$, or the quantum well size. In order to improve the simulations, Brus [71] and Kayanuma [72] further extended the QC theory by including the Coulomb interaction of an e–h pair of $R$ separation and the correlation energy $E_R$ being the Rydberg (spatial correlation) energy for the bulk semiconductor. The modified form is given as:

$$E_G(R) = E_G(\infty) + \pi^2\hbar^2/(2\mu R^2) - 1.786e^2/(\varepsilon_r R) + 0.284E_R$$

where,

$$E_R = \mu e^4/(2\varepsilon_r^2\varepsilon_0^2\hbar^2) = 13.56\mu/\varepsilon_r^2 m_e \text{ (eV)} \tag{63}$$

The effective dielectric constant $\varepsilon_r$ and the effective mass, $\mu$, describe the effect of the homogeneous medium in the quantum box, which is a mono-trapping central potential extended from that of a single atom by expanding atomic size to the dimension of the solid. The dictating factor for the QC convention is the production of e–h pairs as their kinetic energy and potential energy dominate the $E_G$ expansion. For CdS, as an example [72,500], it was estimated that $\varepsilon_r = 5.5$, $m_e^* = 0.19$, and $m_h^* = 0.8$.

According to the QC theory, electrons in the conduction band and holes in the valence band are confined spatially by the potential barrier of the surface, or trapped by the potential well of the quantum box. Because of the confinement of both the electrons and the holes, the lowest energy optical transition from the valence to the conduction band increases in energy, effectively increasing the $E_G$. The sum of kinetic and potential energy of the freely moving carriers is responsible for the $E_G$ expansion and therefore the width of the confined $E_G$ grows as the characteristic dimensions of the crystallite decrease.

Later development of the QC theory shows that the relation of $\Delta E_G \propto R^{-n}$ ($n = 1.16$ [501], 1.3 [491], and 1.37 [485]) fits better the size-dependent PL blueshift and the $n$ values vary from source to source. Nevertheless, it is important to recognize that the QC premise is indeed a very helpful first-order approximation, and can be used to estimate changes in energy levels, exciton and related energies, as a function of dot size. However, at the lower end of the size limit, the QC theoretical curve diverges from the true situation that the $E_G$ can never be larger than the separation of the involved energy levels of an isolated atom.

Most recently, Wang and Zunger [502] showed that the optical emission based on the size of quantum dot (QD) depends on changes to dielectric function of the material near the QD surface rather than the overall size of the dot. Measured microscopically, the dielectric function in the core interior of a QD is the same as it is in the bulk material, but in a small dot, the differences are large near the grain boundary. Therefore, the surface shells of the QD are core C independent, agreeing with the present approaches, as discussed in Section 2.

*7.2.2. Other schemes*

A free-exciton collision model [73] proposed for the PL blueshift suggests that the $E_G$ expansion arises from the contribution of thermally activated phonons in the grain boundaries rather than the QC effect. During PL measurement, the excitation laser heats the free-excitons that then collide with the boundaries of the nanometer-sized fragments. The laser heating the free-excitons up to the temperature in excess of the activation energy required for the self-trapping gives rise to the extremely hot self-trapping excitons (STEs). Because the resulting temperature of the STEs is much higher than the lattice temperature, the cooling of the STEs is dominated by the emission of phonons. However, if the STE temperature comes into equilibrium with the lattice temperature, the absorption of lattice phonons becomes possible. As a result, the blueshift of the STE-PL band is suggested to originate from the activation of hot-phonon-assisted electronic transitions. The blueshift of the STE-PL band depends on the temperature of laser-heated free-excitons that in turn is determined by the size of nanometer-sized fragments. This situation arises because the temperature (kinetic energy) of the laser-heated free-exciton increases with the number of collisions with the boundary of confined regions, which tends to be higher with decreasing size of the fragments in nanoscale materials (silica was considered only). The energy gained from laser heating of the exciton increases with decreasing nanosolid diameter in an $\exp(1/R)$ form. Based on the analysis, Glinka et al. [73] indicated that the size-dependent PL blueshift of a nanosolid in general does not need to be related always to the QC effect.

Other phenomenological models for the blueshift in PL of nanosolids include the impurity centers [74], surface states [503], surface alloying [75], cluster interaction and oxidation effect [77]. However, all the models mentioned above are good for the blueshift in the PL and cover various possible sources. These models have their limitations, however, that could explain neither change of Hamiltonian as the origin nor other quantities relating to the Hamiltonain, such as the core-level shift and dielectric suppression, which should be intrinsic to nanostructures.

## *7.3. BOLS consideration*

*7.3.1. Band formation*

Fig. 27 illustrates the evolution of the energy levels of a single atom to the energy bands of a bulk solid containing $N_j$ atoms. Electrons of a single atom confined by the intra-atomic trapping potential, $V_{atom}(r) = \text{constant}$ or $-\infty$, move around the central ion core in a standing-wave form inside the potential well. The corresponding eigen wave functions and the eigen energies are:

$$\phi_\nu(r) \propto \sin^2(2\pi nr/d_0), \quad \text{and} \quad E(n) = 2(n\pi\hbar)^2/\left(m_e d_0^2\right), n = 1, 2, 3, \ldots$$

where the atomic diameter $d_0$ corresponds to the dimension of the potential well of the isolated atom. The branch numbers ($n$) correspond to different energy levels. The energy separation between the closest two levels depends on $(n+1)^2 - n^2 = 2n + 1$.

When a system contains two atoms, the single energy level splits into two separate sublevels and the separation between the sublevels is determined by the interatomic binding energy. Meanwhile, the presence of interatomic interaction shifts the center of the two levels down.

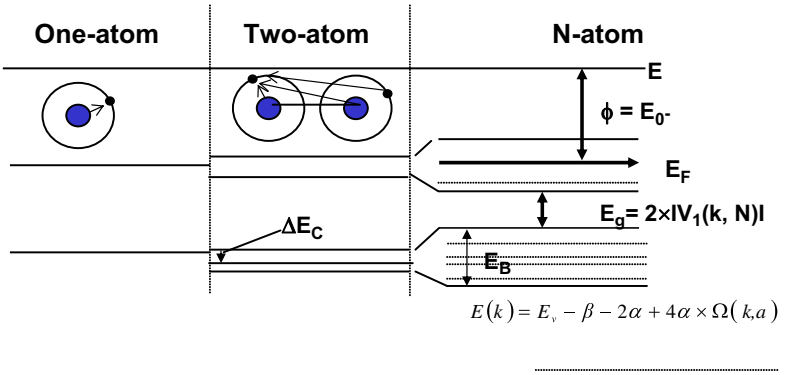


Fig. 27. Evolution of a single energy level into the band structure when particle grows from a single atom to a bulk solid that contains N atoms. Indicated is the work function $\phi$, band gap $E_G$, core level shift $\Delta E_\nu$, and bandwidth $E_B$. The number of allowed sublevels in a certain band equals the number of atoms of the solid. The sublevel spacing is described by the Kubo gap, $4E_F/3N_j$, with $E_F$ being the Fermi level of the bulk [505].

Increasing the number of atoms up to $N_j$, the single energy level will expand into a band within which there are $N_j$ sublevels. The number of atoms $N_j$ in the solid determines the number of the sublevels in a particular energy band. What distinguishes a nanosolid from a bulk solid is that for the former the $N_j$ is accountable, while for the latter the $N_j$ is too large to be accounted. Therefore, the classical band theories are valid for a single nanometric solid that contains any number of atoms. As detected with XPS, the DOS of a core band for a nanosolid exhibits band-like features rather than the discrete spectral lines of a single atom. If the $N_j$ is sufficiently small, the separation between the sublevels is resolvable. The energy-level spacing of the successive sublevels in the valence band, known as the Kubo gap ($\delta_K = 4E_F/3N_j$), decreases with increasing number of valence electrons of the system [12]. For a system containing 1000 silver atoms, the Kubo gap would be 5–10 meV. At room temperature, $k_BT \cong 25$ meV, a 3-nm particle containing 500 atoms or more would be metallic ($k_BT > \delta_K$). At low temperatures, however, the level spacings especially in a small particle may become comparable to $k_BT$ or higher, rendering them nonmetallic [12]. Because of the presence of the $\delta_K$ in an individual nanosolid, properties such as electron conductivity and magnetic susceptibility exhibit quantized features [504]. The resultant discreteness of energy sublevels also brings about fundamental changes in the characteristic spectral features of the nanosolids, especially those related to the valence band.

According to the band theory [283], the Hamiltonian for an electron inside a solid is in the form:

$$\widehat{H} = \widehat{H}_0 + \widehat{H}' = -\frac{\hbar^2\nabla^2}{2m} + V_{\text{atom}}(r) + V_{\text{cry}}(r + R_C) \tag{64}$$

where the $V_{\text{atom}}(r)$ is the intra-atomic trapping potential of an isolated atom and the $\widehat{H}' = V_{\text{cry}}(r) = V_{\text{cry}}(r + R_C)$ is the periodic potential of the crystal, i.e., the interatomic binding potential or crystal potential. $R_C$ is the lattice constant. According to the nearly-free-electron approximation, the $E_G$ originates from the crystal potential and the width of the gap is simply twice that of the first Fourier coefficient of the crystal potential

$$E_G = 2|V_1(k_l)| \tag{65}$$

The energy dispersion of an electron in the $\nu$th core band follows the relation:

$$E_\nu(k) = E_\nu(1) + \Delta E_\nu(\infty) + \Delta E_B(k_l, R_C, z) = E_\nu(1) - (\beta + 2\alpha) + 4\alpha\Omega(k_l, R_C, z) \tag{66}$$

where

- $E_\nu(1) = \langle\phi_\nu(r)|\widehat{H}_0|\phi_\nu(r)\rangle$ is the energy of the core electron of an isolated atom.
- $\beta = -\langle\phi_\nu(r)|V_{cry}(r)|\phi_\nu(r)\rangle$ is the energy of interaction between the crystal potential and the specific core electron at site $r$.
- $\alpha = -\langle\phi_\nu(r)|V_{cry}(r)|\phi_\nu(r - R_C)\rangle$ is the energy of exchange interaction between crystal potential and the overlapping neighboring electrons.
- For an fcc structure example, the structure factor $\Omega(k_l, R_C) = \sum_z \sin^2(k_l R_C/2)$.
- The sum is over all the contributing coordinates ($z$) surrounding the specific atom in the solid.

Eqs. (65) and (66) indicate clearly that the $E_G$, the energy shift $\Delta E_\nu(\infty) = -(\beta + 2\alpha)$ of the $E_\nu(1)$ and the bandwidth $\Delta E_B$ (last term in Eq. (66)) are all functions of the crystal potential. Any perturbation to the crystal potential will vary these quantities. Without the crystal potential, neither the $E_G$ expansion nor the core-level shift would be possible; without the interatomic binding, neither a solid nor even a liquid would form.

*7.3.2. Hamiltonian perturbation*

Considering an assembly composed of $n$ particles of mean size $K_j$ and with each particle, there are $N_j$ atoms, the total binding energy, $V(r, n, N_j)$ [18]:

$$V(r, n, N_j) = \sum_n \sum_{l \neq i} \sum_i v(r_{li}) = \frac{n}{2}\left[N_j \sum_{i=1} v(r_{li}) + \sum_{k \neq j} V(K_{kj})\right] \cong \frac{n}{2}\left[N_j^2 v(d_0) + nV(K_j)\right] \tag{67}$$

$V(r, n, N_j)$ sums over all the $nN_j$ atoms and the $n$ particles. The high order $r_{li}$ is a certain fold of the nearest atomic spacing, $d_0$. Besides, interaction between the nearest clusters, $k$ and $j$, $V(K_{kj})$, should be taken into account. If $K_{kj}$ is considerably large (such as the case of porous Si, or highly dispersed particles), the last term is negligible, which is the case of an isolated particle. Normally, the intercluster interaction, $V(K_j)$, is much weaker than the interatomic interaction. For example, if the cluster is taken as an electrical dipole or a magnetic dipole, the Van der Waals or the super-paramagnetic potential is much weaker. If the intercluster interaction cannot be neglected, Eq. (67) can be developed as follows using the shell structure:

$$
\begin{aligned}
V_{\rm cry}(r,n,N_j) &= \frac{nN_j}{2}\left[N_i v(d_i) + (N_j - N_i)v(d_0) + \frac{n}{N_j}V(K_j)\right] \\
&= \frac{nN_j^2 v(d_0)}{2}\left[\frac{N_i v(d_i)}{N_j v(d_0)} + \left(1 - \frac{N_i}{N_j}\right) + \frac{nV(K_j)}{N_j^2 v(d_0)}\right] \\
&= V_{\rm cry}(d_0,n,N_j)\left\{1 + \gamma_{ij}[v(d_i)/v(d_0) - 1] + \delta_{kj}(K_j)\right\} \\
\frac{\Delta V_{\rm cry}(N_j)}{V_{\rm cry}(\infty)} &= \sum_{j\le 3}\gamma_{ij}\frac{\Delta v}{v} + \delta'_{kj}(K_j) = \sum_{j\le 3}\gamma_{ij}(c_i^{-m} - 1) + \delta'_{kj}(K_j) \\
\delta_{kj} &= \frac{nV(K_j)}{N_j^2 v(d_0)}
\end{aligned}
\tag{68}
$$

The sum is over the outermost three atomic shells of the nanosolid. $V_{\rm cry}(d_0, n, N_j)$ is the crystal potential of the system without the effect of atomic CN imperfection or the intercluster interaction. The pair interatomic binding energy at equilibrium atomic separation, $v(d_i) \propto E_i = c_i^{-m}E_{\rm b}$. This leads to the perturbation to the crystal binding energy (the energy density in the relaxed region rather than the atomic cohesive energy) upon assembly of the nanosolids, as given. The perturbation covers the weighted sum of contribution from the individual surface layers $(c_i^{-m} - 1)$ over the outermost three atomic layers of a nanosolid, and the intercluster interaction, $\delta_{kj}(K_j)$, that is negligible if the particle size is sufficiently large.

The total potential in Eq. (64) becomes $V(\Delta_H) = V_{\rm atom}(r) + V_{\rm cry}(r)[1 + \Delta_H]$. In conjunction with the corresponding Bloch wave functions, the atomic trapping potential, $V_{\rm atom}(r)$, defines the discrete core-level energies of an isolated atom, $E_\nu(1)$. The crystal binding $V_{\rm cry}(r)$ defines not only the $E_{\rm G}$, but also the shift of the core-level energy away from the original position, $\Delta E_\nu(\infty) = E_\nu(\infty) - E_\nu(1)$, as well as other quantities such as the bandwidth and band tails. The dimensionless $\Delta_H$, being independent of the particular form of the interatomic potential, is the contribution from binding energy density in the relaxed surface region.

The perturbation to the Hamiltonian will cause the changes of $E_{\rm G}$ and $E_\nu(K_{\rm j})$, which follows the scaling relation:

$$
\frac{\Delta E_{\rm G}(K_j)}{E_{\rm G}(\infty)} = \frac{\Delta E_\nu(K_j) - \Delta E_\nu(\infty)}{\Delta E_\nu(\infty)} = \Delta_H \tag{69}
$$

We now turn to look at the possible mechanisms that could modify the crystal potential, $V_{\rm cry}(r)$, that depends functionally on atomic distance and the nature of the chemical bond. Bond formation transports charge among the bonding constituents. Different types of interatomic potential describe different kinds of chemical bonds. If the atomic distance, or bond length, relaxes spontaneously, the crystal potential will be enhanced. Chemical reaction in which charge transport dominates not only reduces the ''screening'' effect of the core electrons but also alters the nature of the bond. Therefore, shortened bond length and altered bond nature will enhance the binding energy and, consequently, the crystal potential of the solid. On the other hand, chemical reaction will cause repopulation of electrons in the valence band, which will expand the $E_{\rm G}$ extrinsically [125,506].

In the quantum theory for condensed matter, the key elements are the Hamiltonian and the Bloch wave functions. Nanosolid densification may modify the wave functions slightly as, in this case, no chemical reaction occurs. In the first-order approximation, we may ignore the size effect on the wave function shrinkage. Therefore, the Hamiltonian becomes of key

importance. The potential energy of the Hamiltonian in various modeling consideration is different, and may be compared as follows:

$$V=\begin{cases} V_{\text{atom}}(r), & (r\le r_0), & \text{isolated-atom}\\ V_{\text{dot}}(r)=V_{\text{atom}}(r), & (r\le R), & \text{QC-I}\\ V_{\text{dot}}(r)+V_{\text{e-h}}(R)+E_K(R), & (r\le R), & \text{QC-II}\\ V_{\text{atom}}(r)+V_{\text{cry}}(r), & (-\infty<r<\infty), & \text{Extended-solid}\\ V_{\text{atom}}(r)+V_{\text{cry}}(r)\times(1+\Delta_H), & (r\le R), & \text{BOLS-perturbation}\end{cases} \tag{70}$$

The major difference between the QC theory and the BOLS correlation for a nanosolid lies in that:

(i) The QC effect being an artifact of measurement, is dictated by the presence of e–h pairs that are produced during the measurement. Production of e–h pairs is crucial to trigger the function of the QC theory. The Coulomb potential energy for the e–h pair, $V_{\text{e-h}}$, is of order about $10^{-1}$ eV [507], which is negligibly small compared to the interatomic binding energy (1–7 eV). Furthermore, the radiation recombination of the e–h pair occurs depending on the overlap extent of wave functions of the e–h pair. The localization length of a carrier, $R_0$, is about several Bohr radii [126]. The probability of e–h recombination is proportional to $\exp(-2r_{\text{e-h}}/R_0)$. If the e–h separation, $r_{\text{e-h}}$, is considerably larger than the localization length, $R_0$, the probability of the radiation recombination is extremely small. On the other hand, the involved dielectric constant $\varepsilon_r$ is no longer constant but it is size dependent [498,497].

(ii) The BOLS correlation is dictated, however, by the fact of atomic CN imperfection and its consequences on the Hamiltonian, which focus on the surface shells rather than the entire solid. The BOLS premise adds its perturbation to the crystal potential of an extended solid without e–h pair or the correlation energy being involved. The intra-atomic trapping, $V_{\text{atom}}$, is responsible for the discrete energy levels of an isolated atom. As trapping centers, the $V_{\text{atom}}$ localizes electrons to spend most time moving inside the $V_{\text{atom}}$ in the form of standing waves. The interatomic binding or crystal potential, $V_{\text{cry}}$, is crucial to binding atoms to form a solid. Therefore, the $V_{\text{cry}}$ can never be removed or replaced with other alternatives in dealing with a system containing multiple atoms. Despite the numerical convergence of the $E_G$ at the lower end of the size limit, the BOLS premise is able to formulate not only the entire band-structure change (band gap expansion, the core-level shift, the core bandwidth and band tails) but also other properties such as the strength of electron–phonon coupling.

### *7.4. Verification: photon emission and absorption*

#### *7.4.1. Electron–phonon coupling*

The PL or PA energy is not the band gap but they are determined by the joint effect of crystal binding and electron–phonon coupling. Fig. 28 illustrates the effect of electron–phonon (e–p) coupling and crystal binding on the $E_{\text{PL}}$ and $E_{\text{PA}}$. The energies of the ground state ($E_1$) and the excited state ($E_2$) are expressed as [126]:

$$\begin{cases} E_1(q)=Aq^2\\ E_2(q)=A(q-q_0)^2+E_G\end{cases} \tag{71}$$

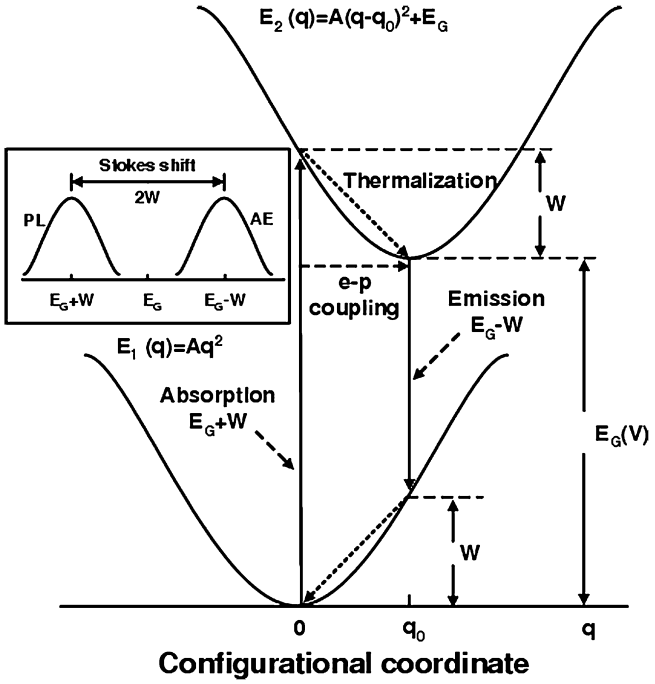


Fig. 28. Mechanisms for $E_{PA}$ and $E_{PL}$ of a nanosemiconductor, involving crystal binding ($E_G$) and electron–phonon coupling ($W$). Insertion illustrates the Stokes shift from $E_{PA}$ to $E_{PL}$ [126]. An electron is excited by absorbing a photon with energy $E_G + W$ from the ground minimum to the excited state and then undergoes a thermalization to the excited minimum, and then transmits to the ground emitting a photon with energy $E_G - W$ [126].

Constant $A$ is the slope of the parabolas. The $q$ is in the dimension of a wave-vector. The vertical distance between the two minima is the real $E_G$ that depends functionally on the crystal potential. The lateral displacement ($q_0$) originates from the e–p coupling that can be strengthened by enhancing lattice vibration. Therefore, the blueshift in the $E_{PL}$ and in the $E_{PA}$ is the joint contribution from the change of crystal binding and e–p coupling. At a surface, the CN imperfection-enhanced bond strength affects both the frequency and magnitude [96,41] of lattice vibration. Hence, at a surface, the e–p coupling and hence the Stokes shift will be enhanced.

In the process of carrier formation and recombination, an electron is excited by a photon with $E_G + W$ energy from the ground minimum to the excited state with the creation of an electron–hole pair. The excited electron then undergoes a thermalization and moves to the minimum of the excited state, and eventually transmits to the ground combining with the hole. The carrier recombination is associated with emission of a photon with energy $E_{PL} = E_G - W$. The transition processes (e–h pair production and recombination) follow the rule of momentum and energy conservation though the conservation law may be subject to relaxation for the short ordered nanosolid. Such conservation law relaxation is responsible for the broad peaks in the PA and PL.

The insertion illustrates the Stokes shift, $2W = 2Aq_0^2$, from $E_{PL}$ to $E_{PA}$. The $q_0$ is inversely proportional to atomic distance $d_i$, and hence, $W_i = A/(c_i d_i)^2$, in the surface region. Based on

this premise, the blueshift of the $E_{PL}$, the $E_{PA}$, and the Stokes shift can be correlated to the CN imperfection-induced bond contraction [508]:

$$\left.\begin{matrix}\dfrac{\Delta E_{PL}(K_j)}{E_{PL}(\infty)}\\ \dfrac{\Delta E_{PA}(K_j)}{E_{PA}(\infty)}\end{matrix}\right\} = \frac{\Delta E_G(K_j) \mp \Delta W(K_j)}{E_G(\infty) \mp W(\infty)} \cong \sum_{i\le 3} \gamma_i \left[\left(c_i^{-m} - 1\right) \mp B\left(c_i^{-2} - 1\right)\right]$$
$$\times \left(B = \frac{A}{E_G(\infty) d^2};\ \ \frac{W(\infty)}{E_G(\infty)} \approx \frac{0.007}{1.12} \approx 0\right) \tag{72}$$

Compared with the bulk $E_G(\infty) = 1.12$ eV, the $W(\infty) \sim 0.007$ eV obtained using empirical tight-binding calculations [509] is negligible. One can easily calculate the size-dependent $E_{PL}$, $E_{PA}$, and $E_G = (E_{PL} + E_{PA})/2$ as well using Eq. (72). Fitting the measured data gives the values of $m$ and $A$ for a specific semiconductor.

*7.4.2. $E_G$ expansion*

The size dependence of both the $E_{PL}(K_j)$ and $E_{PA}(K_j)$ of porous silicon (p-Si) fabricated using electrochemical method has been obtained [508]. The room temperature reflectivity (Fig. 29a) varies with size in the photon energy range of 200–900 nm wavelength, which is related to the change of dimension and geometry of columns and voids on the p-Si surface. The absorption coefficient was obtained by fitting the reflection spectra using the Scout software package [510]. The $E_{PA}$ values were extracted from the absorption spectra (Fig. 29b) using the Tauc plot method [511,512]. The PL and XPS $\Delta E_{2p}$ profiles are given in Fig. 29c and d, compared with the predicted size dependence.

Matching the predictions in Eq. (72) with the measured $E_{PA}$ and $E_{PL}$ data (Fig. 30a) gives coefficient $B = 0.91$ and $m = 4.88$ that refines the original value $m = 4$ of which the e–p interaction was not considered [45]. The refined form is able to discriminate the effect of e–p coupling ($B = 0.91$) from the effect of crystal binding ($m = 4.88$) on the $E_{PL}$ and $E_{PA}$.

Most strikingly, without triggering electron–phonon interaction or electron–hole production, STM/S measurement [48] reveals that the band gap varies from 1.1 to 3.5 eV when the diameter of a Si nanorod is reduced from 7.0 to 1.3 nm and that the surface Si–Si bond contracts by $\sim$12% from the bulk value (0.263 nm) to $\sim$0.23 nm. The STS findings concur convincingly with the BOLS premise: CN imperfection shortens the remaining bonds of the under-coordinated atoms spontaneously with an associated $E_G$ expansion. It is important to note that STS collects *localized* DOS information without needing any energetic stimulus. The bias ($|V_b| < 2$ eV) between the tip and the sample surface is not sufficiently large to break the Si–Si bond. What happens upon being biased is that the tip introduces holes or electrons into the sample rather than produces electron–hole pairs inside the specimen. As such, neither electron excitation from the ground to the excited states nor electron–hole pair production or carrier recombination occurs during STS/M measurement. What contributes to the STS-$E_G$ are states occupied by the covalent bonding electrons and the empty states that are strongly localized at the probed site rather than the Coulomb interaction between the excited electron–hole or kinetic energies of the mobile carriers moving inside, or being confined by, the nanosolid. Without causing e–h production and recombination [506], STS-$E_G$ continues expanding upon the size being reduced. A surface hydride may form upon the sample being

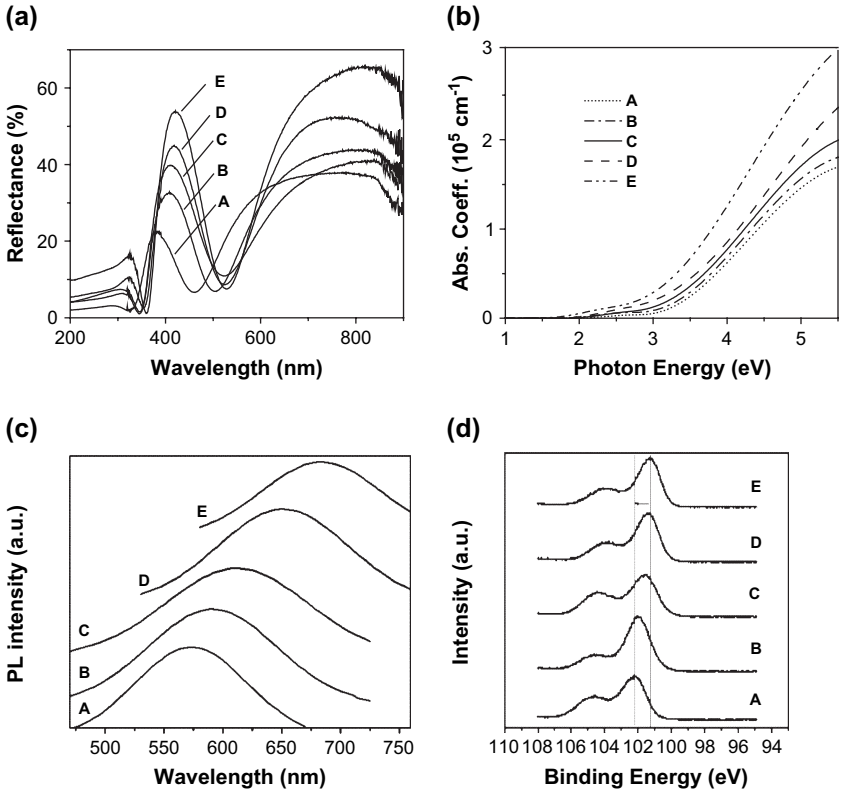


Fig. 29. (a) Reflection and (b) absorption spectra of PS samples with different particle sizes measured at ambient temperature. $E_{PA}$ is obtained with the Tauc plot fitting of the reflection and absorption data. Size dependence of (c) PL spectra and (d) $E$-2p core-level shift in particle size range of $R = 1.4–2.1$ nm [508].

passivated. However, hydride formation reduces the midgap impurity DOS and hence improves the quantum efficiency in the irradiation recombination, and hence, the surface hydride formation could never expand the $E_G$ [126]. As shown in Fig. 30b, the size-enlarged $E_G$ of Si nanorods (STS derived) [46] and Si nanodots (mean value of $E_{PA}$ and $E_{PL}$) follows the BOLS prediction, which involves no events of electron–hole interaction, e–p coupling, or quantum confinement.

### *7.4.3. Nanocompound photoluminescence*

Table 9 lists the parameters used in simulating the size dependence of the PL blueshift of nanometric compound semiconductors. The bond length in the bulk takes the values of covalent bond of the corresponding materials (Appendix A). Fig. 31 compares the predictions with the relative PL shift observed for InP, InAs, CdS, and CdSe nanosolids. It can be seen that the curve of $m = 4$ gives generally a better fit of the PL spectra of these compounds without involving the e–p coupling. This trend also agrees with the $E_G$ expansion determined by XPS from the Si:H nanosolids [16]. The deviation of theory from experiment may arise from the accuracy in determining the shape and size of the particles or from the uncertainty of chemical reaction. The extent of reaction determines the $E_G$ that was used as a scale to normalize the entire set

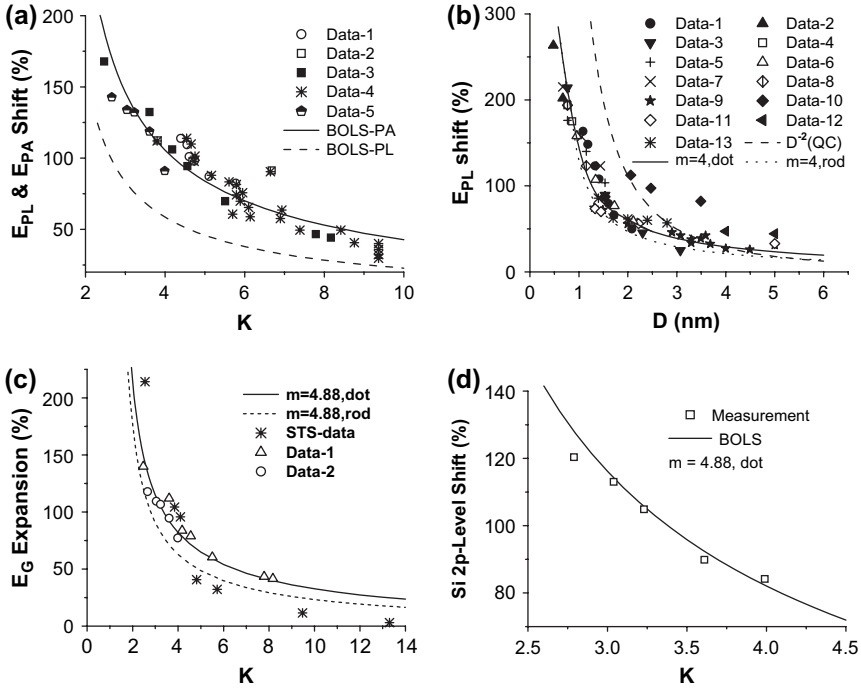


Fig. 30. Comparison between predictions (solid lines) and the measured size dependence. (a) The $E_{PA}$ blueshift of PS with data-1 [511], data-2 [513], data-3 [514], data-4 [515], and data-5 [45]. (b) The $E_{PL}$ blueshift of nano-Si. Data-1 [458], data-2 [516], data-3 [509], data-4 [517], data-5 [518], data-6 [519], data-7 [520], and data-8 [515] are calculation results. Data-9 [515], data-10 [513], data-11 [478], data-12 [521], and data-13 [45] are measurements. (c) The $E_G$-expansion measured using STS [48] and optical method, data-1 ($E_G = E_{PA} - W$) [456] and data-2 ($E_G = (E_{PL} + E_{PA})/2$) [45]. (d) The core level shift of Si [47].

of the PL data. The scattered and broad distribution of the measured data for InP, InAs, CdS, and CdSe should be due to the same reason. However, all the data follow the similar trend of $m = 4-6$. The cluster interaction appears to play an insignificant role in the PL blueshift, which coincides with BOLS predictions, as discussed in Section 7.3.2. The general trends of the predicted PL peak shift show that the size-induced frequency shift varies little with the materials or with the particular crystal structures (Wurtzite and zinc-blend structures in Fig. 31b), as noted by Yoffe [17].

Table 9
Summary of the simulating parameters for the $E_G$ expansion of nanometric semiconductors

| | $E_G$ (bulk) (eV) | $E_G(\infty)$ (eV) |
|---|---|---|
| Si | 1.12 | 1.12 |
| InP | 1.45/1.34 | 1.45 |
| InAs | 0.35 | 0.9 |
| CdS | – | 2.2 |
| CdSe | 1.75 | 1.75 |

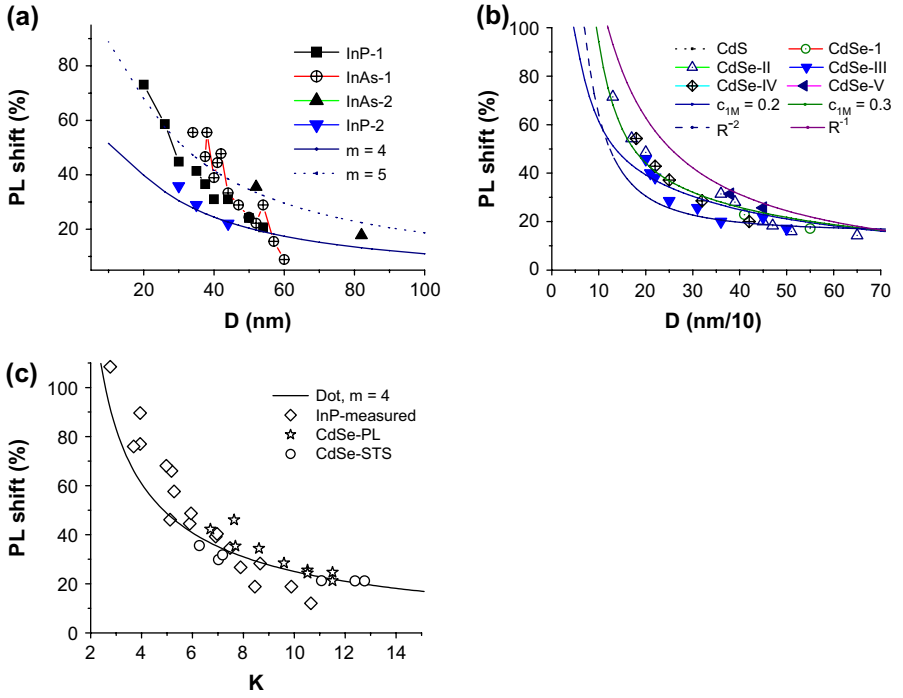


Fig. 31. Comparison of the modeling predictions with the measured PL peak shifts of (a) InAs [484], InP-01 [486,529]; (b) Zn-blende-I and Wurtzite structure-II of CdS and CdSe [481], and CdS-I [487], CdSe-I [524], CdSe-II [525], CdSe-III [526], CdSe-IV [527], and CdSe-V [528] nanosolids. (c) InP [485,529] and CdSe rod measured using STS and PL [534]. The $R^{-1}$ and $R^{-2}$ curves diverge at the lower end of critical size.

It should be noted that the $E_G$ of the bulk compound varies with the extent of chemical reaction [522,523]. For example, the $E_G$ for the $SiO_x$ varies from 1.12 (Si) to 9.0 ($SiO_2$) eV. Therefore, it is not realistic to fit the measured data perfectly without considering the effect of surface passivation. Our attention, however, should focus on the trends of change and their origins. We may compare predictions with experimental observations on the PL blueshift of nanometric semiconductors near the lower end of the size as shown in Figs. 30 and 31. Agreement with PL shift of Si, CdS-I [487], CdSe-I [524], CdSe-II [525], CdSe-III [526], CdSe-IV [527], and CdSe-V [528] nanosolids ($D < 5$ nm) has been realized. The QC theoretical curves of $D^{-\lambda}$ ($1155 \times D^{-1}$ and $80850 \times D^{-2}$) are also compared, which match the PL data only at larger particle size. Fig. 31 compares the BOLS prediction and the measured PL shift of InP nanosolids [485,529,530], and the curves of $R^{-1.04}$ and $100\times\ (5.8D^2 + 27.2D + 10.4)^{-1}$ forms reported by others [531].

The extent of bond contraction varies slightly from CdS to CdSe, as a refinement of the BOLS correlation. The difference should be due to the difference in electronic configuration or the covalent bond length between S ($3p^4$, 0.104 nm) and Se ($4p^4$, 0.114 nm), which is beyond the scope of BOLS correlation. Copper-doped zinc oxide nanowires range from 30 to 100 nm in diameter and show broad and continuous PL spectra extending from the ultraviolet to the red region at room temperature, depending on the excitation wavelength, which is different from that of the bulk [532]. The mechanism of the excitation wavelength dependence of the PL

emission of Cu−$ZnO_2$ is complicated, which should be the joint effect of size and oxidation [533] and Cu doping may add new levels for transition.

### 7.5. Bandwidth and band tails

#### 7.5.1. Bandwidth

The predicted size-dependent bandwidth derived in Section 7.3.2 indicates that the bandwidth is determined by both the crystal potential and the effective atomic CN and the bandwidth shrinks with reducing particle size:

$$\frac{\Delta E_B(K_j)}{E_B(\infty)} = \sum_{i\le 3} \gamma_{ij}\left(\frac{\Delta\alpha_i}{\alpha} + \frac{\Delta z}{z}\right) \tag{73}$$

which agrees with the trends measured using XPS from CuO surface [535]. The observed peak intensity increases and the peak-base width (rather than the full width at half maximum that describes the distribution of the occupied DOS in the core band) decreases with reducing particle size. It is understandable that the number of electrons is conserved in each of the deeper band, as the core electrons do not involve the charge transportation in a process of chemical reaction [3]. If the $z$ reduces to one or two, the bandwidth will approach the single energy level of an isolated atom.

#### 7.5.2. Surface states and band tails: Urbach edge

For an isolated nanosolid or a surface, there are two kinds of surface states. One is the dangling bonds or surface impurities, which add impurity states within the $E_G$ of semiconductors. Termination of the dangling bonds by $H$ adsorption could minimize the impurity states. The other is the contracted bonds localized in the relaxed surface region, which offset the entire band structure associated with $E_G$ enlargement and the presence of band tails.

The difference between an assembly of nanosolids and a bulk solid in amorphous state is the distribution of defects. In the amorphous phase, the randomly distributed CN deficiency causes the bond length and angle of the specific atom to distort in a disordered way, which adds traps randomly in depth inside the bulk. In an amorphous solid, the number of the under-coordinated atoms is hardly controllable as the amorphous state depends heavily on the processing conditions. For a nanosolid or nanocrystallite, CN deficiency only happens in an orderly way at the surface and the number of sites of CN deficiency is controllable by adjusting the shape and size of the nanosolids.

The CN deficiency in both amorphous and nanosolid states bends the energy near the conduction and the valence band edges with production of band tails occupied by the localized states. The resultant of the two band tails gives the Urbach edge appearing in the photoabsorption spectra [126]. According to the BOLS premise, the Urbach edge of a nanosolid resulting from bond contraction due to the CN imperfection in the surface region is comparable to the random traps inside the amorphous bulk solid. The deepened potential traps near the surface edges are responsible for the localization of carriers in the band tails of nanosolids. Therefore, the CN imperfection enhanced interatomic interaction in the surface skin of a nanosolid should also produce such band tails that are identical to the band tails of an amorphous solid though the tail states originate from different sites in real space. As expected, such Urbach edges have been identified from the photoabsorption spectra of InAs [484], InP [485], and the XPS measurement of Si:H nanosolids [16].

### 7.6. Summary

We have thus developed a consistent understanding of the factors dominating the entire band-structure change of nanostructured solids by incorporating the BOLS correlation to the Hamiltonian of an extended solid of which the Hamiltonian contains the intra-atomic trapping and the interatomic binding interactions. Introducing the effect of CN imperfection to the convention of an extended solid in the surface skin has led to a new Hamiltonian that revolves the entire band structure of a nanometric semiconductor. This approach allows us to discriminate the contribution from crystal binding from the effect of e–p coupling in determining the $E_G$ expansion and PL blueshift. In addition, we have shown that the conventional band theories are still valid for a nanosolid that contains numerous atoms in the form of multiple trapping centers in the energy box. It is anticipated that the spontaneous contraction of chemical bonds at the surface is the origin of the size dependency of a nanosolid as all the detectable quantities are functions of interatomic binding energy. Therefore, the CN imperfection induced bond contraction and the rise in the surface-to-volume ratio with reducing particle size cause the change of the band features of nanometric semiconductors and the performance of electrons, phonons, and photons in the small particles. Agreement between modeling predictions and the observed size dependence in the PL of Si and some nanometric III–V and II–VI semiconductors are further evidence of the significance of atomic CN imperfection and the BOLS correlation.

## 8. Electronic structure

### 8.1. Core bands: intra-atomic trapping and crystal binding

#### 8.1.1. Observations

Unlike the valence DOS that provides direct information about charge transportation kinetics during reaction [3], the energy shift of a core level of an isolated atom gives profound information about the intensity of crystal binding that is dominated by interatomic interaction. Alteration of bond nature and variation of bond length will affect the crystal potential and hence shift the core level by a certain extent towards normally higher binding energy if the processes are spontaneous. Being able to discriminate the crystal binding (core-level shift) from the atomic trapping (core level of an isolated atom) of a core electron under various physical and chemical environments is a great challenge, which is beyond the scope of direct measurement using currently available probing technologies. Combining the most advanced laser cooling technology and XPS, one can measure the energy separation between different energy levels of the slowly moving gaseous atoms trapped by the laser beams but, up to now, the individual core-level energy of an statically isolated atom cannot be obtained [536]. What one can measure using XPS are the convoluted broad peaks of the core bands contributing from atomic trapping, crystal binding, crystal orientation, surface relaxation or nanosolid formation and the effect of surface passivation.

In addition to the well-known chemical shift caused by the core-hole ‘screening’ due to charge transportation in reaction, relaxed atomic layer spacings at a surface can split the core-level of a specimen into a few components, as illustrated in Fig. 32. However, the assignment for the components induced by surface relaxation is quite confusing, as summarized in Table 10, due to the lack of guidelines for determining which peak arises from the surface and which one comes from the bulk. With the widely used sign convention, a positive shift relates the high-energy component to the surface contribution ($S_i$, $i = 1, 2,\ldots,$B) while the low-energy component relates to the bulk origin (B) (Fig. 32). The resultant peak is often located in between the components and the

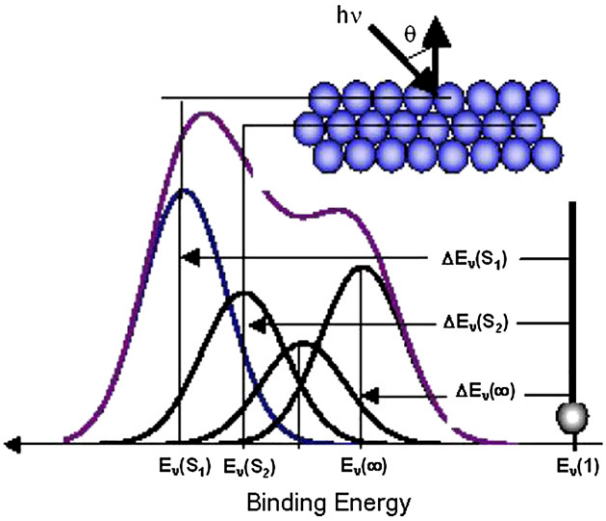


Fig. 32. Illustration of the positive shift ($S_1$, $S_2$,…, B) of the core-band components with respect to the energy level of an isolated atom, $E_v(1)$. $\Delta E_v(S_i) = \Delta E_v(\infty)[1 + \Delta_i]$. Measurements show that the intensities of the low-energy bulk component often decrease with incident beam energy and with the increase of the angle between the incident beam and surface normal.

exact position of the resultant peak varies with experimental conditions, which is perhaps why the recorded values for the core-level energy of a specimen vary from source to source. XPS measurements [495,537–540] reveal that the intensity of the low-energy component often increases with the incident beam energy or with decreasing the angle between the incident beam and the surface normal in the XPS measurement (Fig. 32). The intensity of the low-energy component also increases with decreasing the surface atomic density under the same beam conditions (energy and incident angle). For example, at 390 eV beam energy, two $3d_{5/2}$ components at 334.35 and 334.92 eV have been identified from Pd(110, 100, 111) surfaces. The lower 334.35 eV peak intensity decreases with the variation of the surface geometry from (110) to (111) [541] (with atomic density $n_{110}$:$n_{100}$:$n_{111} = 1/\sqrt{2}$:1:2/$\sqrt{3}$). The 306.42 eV component of the Rh(111) $3d_{5/2}$ level measured under 380 eV beam energy is relatively higher than the same peak of Rh(110) measured using 370 eV beam energy

Table 10
Specifications and the possible origins of the surface-induced core-level splitting

| Specification ($\|E_v\|$: high → low) | Samples |
|---|---|
| Positive shift: | Nb(001) [495,538], graphite [537], |
| $S_1$, $S_2$, …, and B | Tb(0001)-4f [539], Ta(001)-4f [540], |
| | Ta(110) [542], Mg(10$\bar{1}$0) [543], Ga(0001) [544] |
| Negative shift: | Be(0001) [545], Be(10$\bar{1}$0) [543,546,547], |
| B, $S_4$, $S_3$, $S_2$, and $S_1$ | Ru(10$\bar{1}$0) [548], Mo(110) [549], |
| B, $S_2$, $S_3$, $S_4$, and $S_1$ | Al(001) [550], W(110) [551], W(320) [552], |
| | Pd(110,100, 111) [541] |
| Mixed shift: | Si(111) [553], Si(113) [554] |
| $S_1$, B, $S_{\text{dimer-up}}$, $S_{\text{dimer-down}}$ | Ge(001) [555] |
| $S_2$, B, $S_1$ | Ru(0001) [556] |
| $S_1$, B, $S_2$ | |
| $S_2$, $S_3 + S_4$, $S_1$, B | Be(10$\bar{1}$0) [557] |

compared with the high-energy component at 307.18 eV [541]. The energy of individual component should be intrinsic disregarding the surface atomic density but the resultant peak changes with crystal orientation due to the contribution from the individual component. The dependence of the low-energy-component intensity on the beam conditions and atomic density implies that the surface relaxation induces most likely a positive shift in the XPS measurement due to the varied penetration depth of the incident beams.

Upon reacting with electronegative elements such as oxygen, the core-level also splits with the production of high-energy satellites. This well-known 'chemical shift' arises from core-hole production due to bond formation that weakens the 'screening' of the crystal potential acting on the specific core electrons. Interestingly, the effects of surface relaxation and chemical reaction on the core-level shift can be distinguished easily. For instance, two distinct Ru-$3d_{5/2}$ core-level components were resolved from a clean Ru(0001) surface due to the relaxation. Both components then shift up simultaneously further by up to 1.0 eV upon oxygen adsorption [553]. The Rh-$3d_{5/2}$ core-level of Rh(100) surface has a split of 0.65 eV relative to the main peak of the bulk, while with oxygen addition both of the components shift 0.40 eV further towards high binding energy [558]. XPS spectra in Fig. 33c shows the Ta-4f spectra taken after removing about 30% (upper) and 50% (lower) of the surface nanoparticles of a gate device by sputtering [496]. The first pair of doublets (Ta-$4f_{5/2}$ and Ta-$4f_{7/2}$) at (23.4 and 26.8 eV) arises from $TaSi_x$ and $Ta_2O_5$, respectively. The second pair of doublets (at 31.6 and 34.5 eV) is the corresponding satellites due to the size effect. This size effect that can be weakened by removing the nanoparticles causes a simultaneous shift of both the oxide coated nanoparticle and its metallic environment by about 8 eV (bold arrow). These observations confirm that both surface relaxation and catalytic reaction could shift the core-level positively by an amount that may vary depending not only on the original core-level position but also on the extent of reaction.

When a solid reduces its size down to the nanometer scale, the entire core-level features (both the main peak and the chemical satellites) move simultaneously towards higher binding energy and the amounts of shift depend on not only the original core-level position but also the shape and size of the particle. This trend has been confirmed using XPS to study the size dependence of the main core-level peaks and the oxide satellites, as introduced in Section 8.1. The trend of Au-4f core-level shift coincides with the change of the inverse capacitance of the Au particles measured using STS [559]. Compared with the mono-peak of S-2p and S-2s core bands of a bulk solid, ZnS and CdS nanosolids exhibit three components of each the S-2p and S-2s core band [185,560]. These components have been ascribed as the contribution, from high to low binding energy, from the outmost capping layer (0.2–0.3 nm thick), surface layer (0.2–0.3 nm thick), and the core of the nanosolid, as shown in Fig. 33a and b. This specification is in accordance with the surface positive shift. The energy value of each component changes insignificantly with particle size but the resultant peak varies considerably with the atomic portions of the capping, surface and the core of the nanosolid. For example, when the particle size is reduced, the intensity of the core component decreases while the capping component increases, which follows the size dependence of the surface-to-volume ratio of a nanosolid. This convention has enabled an effective method of determining the particle size to be developed [186,560], which is competent with transition electron microscopy (TEM) and XRD.

Generally, the core-level shift of a nanosolid follows the scaling relation with a slope $B$ that changes depending on surface treatment, particle dimensionality and particle–substrate interaction [561]. Photoemission from highly oriented pyrolytic graphite (HOPG) [537] shows two $C_{1s}$ components separated in binding energy by 0.12 eV. The higher binding-energy component of the $C_{1s}$ is ascribed to electrons of atoms in the outermost atomic layer and the other to the bulk. The Cu-$2p_{3/2}$ peak of Cu nanosolids deposited on HOPG and CYLC (polymer) substrates [562], the Au-4f peak of Au

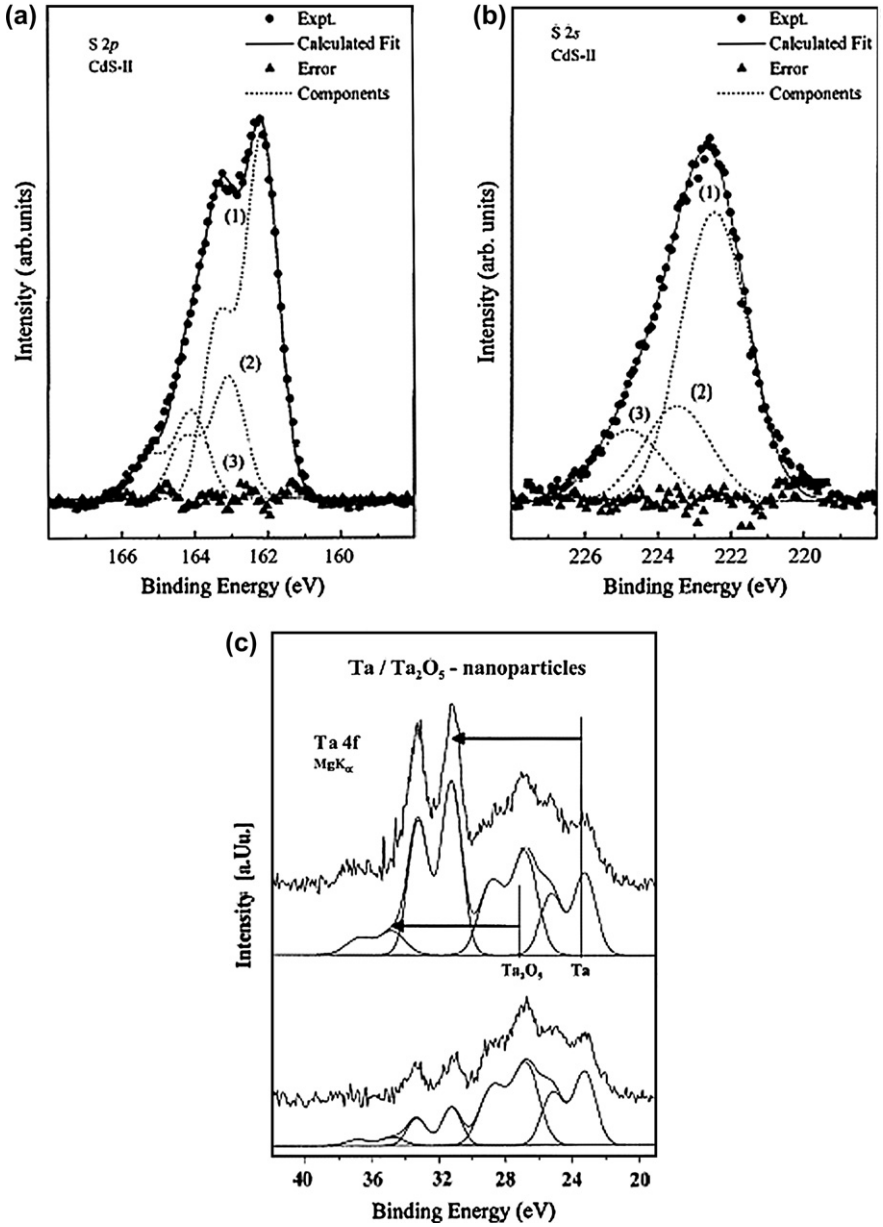


Fig. 33. XPS spectra (a) S-2p and (b) S-2s of CdS nanosolids show the core (1), surface (2) and capping (3) features. The intensity of feature (1) decreases whereas the intensities of features (2) and (3) increase with the decreases of particle size. XPS profiles in (c) show both the size and oxidation effect on the core-level shift of Ta oxide [185,560].

nanosolids deposited on octanedithiol [559], $TiO_2$ [563] and Pt(001) [564] substrates as well as the Pd/HOPG [504] follow exactly the scaling relation. Therefore, for purely physical reasons (without charge transport being involved), surface relaxation and nanosolid formation play an equivalent but as yet unclear role in splitting and shifting the core levels of a specimen.

*8.1.2. Outstanding models*

The underlying mechanism for the surface- and size-induced core-level shift is under debate with the following major arguments:

(i) The high-energy component of the core-level shift was attributed to the surface interlayer contraction [540]. For Nb(001)-$3d_{3/2}$ as an example, the first layer spacing was found to contract by 12% with an associated 0.50 eV core-level shift [495]. A $(10 \pm 3)$% contraction of the first layer spacing has caused the Ta(001)-$4f_{5/2(7/2)}$ level to shift by 0.75 eV [540]. The corresponding positive shift was explained as the enhanced interlayer charge density and the enhanced resonant diffraction of the incident light irradiation due to the surface bond contraction [495,540].

(ii) The size-induced Cu-2p core-level shift of a CuO nanosolid was ascribed as the size-enhanced *ionicity* of copper and oxygen [535]. This suggestion means that an oxygen atom bonds more strongly to the Cu atoms in a nanosolid than does the oxygen atom to the Cu atoms inside the bulk.

(iii) The size-enhanced Sn-3d, Sn-4d and Ta-4f core-level shift of the O–Sn and O–Ta covered metallic clusters was considered as the contribution from the *interfacial dipole* formation between the substrate and the particles [496]. The number of dipoles or the momentum of the dipoles was expected to increase with reducing particle size.

(iv) The thermo-chemical or the 'initial (neutral, un-ionized specimen with $n$ electrons)–final (radiation beam ionized specimen with $n-1$ electrons) states' model [538,539] defines the core-level shift as the difference in cohesive energy that is needed to remove a core electron either from a surface atom or from a bulk atom. The surface atom is assumed as a '$Z+1$ impurity' sitting on the substrate metal of $Z$ atomic number. The final states of atoms at a flat surface or at the curved surface of a nanosolid were expected to increase/decrease while the initial states would decrease/increase when the particle size is reduced. This model has been generally accepted though a negative or mixed surface shift is often derived by the model in theoretical calculations.

(v) Experimental investigations [565,566] have shown that the 'initial–final states' effects cannot explain all the observations and that a metal-to-nonmetal transition mechanism was therefore suggested to occur with a progressive decrease in cluster size [12]. The increase in the core-level binding energy in small particles was also attributed to the poor screening of the core-hole and hence a manifestation of the size-induced metal–nonmetal transition that happens at particle sizes in the range of 1–2 nm diameter consisting of $300 \pm 100$ atoms [504]. However, the metal–insulator transition for Au nanoparticles deposited on diamond is excluded based on an XPS observation and the occurrence of the band offset was assigned to the range of cluster sizes [567].

(vi) Yang and Wu [568] investigated the core-level shifts in sparse Au clusters on oxides, Au/MgO(001) and Au/$TiO_2$(110), with a varying coverage and in the presence of surface oxygen vacancies, by using the DFT full-potential-linearized augmented plane-wave method. The final-state effects are treated self-consistently by moving one core electron to the valence band. They concluded that it is not the final-state contribution but the presence of surface O vacancies that causes the positive core-level shifts in Au nanosolids.

Briefly, signs show that surface relaxation and nanosolid formation share indeed a common yet unclear origin in splitting and shifting the core-level to higher binding energy. However, definition of the components is quite confusing and the origin for the surface- and size-induced

core-level shift is under debate. Therefore, consistent understanding of the effect of surface relaxation and nanosolid formation on the core-level shift is therefore highly desirable. The BOLS correlation mechanism allows us to unify the core-level shift to the origin of atomic CN imperfection and the associated rise of binding energy density in the relaxed surface region on the electronic properties of a surface and a nanosolid. The BOLS correlation favors strongly the mechanisms of (i), (ii), (v), and (vi) with the bond order deficiency as origin.

*8.1.3. BOLS consideration*

According to the band theory and the BOLS correlation, the surface relaxation induced and the size-induced shift of the energy level of an isolated atom $E_\nu(1)$ follows the same relation ($1 = i, j$) to the $E_G(\infty)$ expansion:

$$\begin{cases} V(\Delta_l) = V_{\text{atom}}(r) + V_{\text{cry}}(r)[1+\Delta_l] & \text{(a)} \\ E_\nu(\Delta_l) = E_\nu(1) + [E_\nu(\infty) - E_\nu(1)](1+\Delta_l), & \text{or} \\ E_\nu(\Delta_l) = E_\nu(\infty) + [E_\nu(\infty) - E_\nu(1)]\Delta_l & \text{(b)} \end{cases} \tag{74}$$

where $E_\nu(\infty) - E_\nu(1) = \Delta E_\nu(\infty)$ plays an equivalent role of $E_G(\infty)$ in determining the relative band gap expansion and it is independent of crystal size, surface relaxation, or chemical reaction. $\Delta_l$ can be expressed as

$$\Delta_l = \begin{cases} \Delta_i(S_i) = \dfrac{E_i - E_b}{E_b} = c_i^{-m} - 1 & \text{(surface)} \\ \Delta_j(K_j) = \sum_{i\le 3} \gamma_{ij}\Delta_i & \text{(nanosolid)} \end{cases} \tag{75}$$

$\Delta_l$ is the contribution from interlayer bond contraction ($\Delta_i$) or its sum over the outmost two or three atomic layers ($\Delta_j$). At the lower end of the size limit, the perturbation to the Hamiltonian of a nanosolid relates directly to the behavior of a single bond, being the case of the outermost surface layer and a monatomic chain. Thus, we have the relation for the relaxed surface

$$\begin{aligned} &\frac{E_\nu(\Delta_l) - E_\nu(1)}{E_\nu(\Delta_{l'}) - E_\nu(1)} = \frac{1+\Delta_l}{1+\Delta_{l'}}, \quad (l' \neq l), \text{ or} \\ &\frac{E_\nu(\Delta_l) - E_\nu(\infty)}{E_\nu(\Delta_{l'}) - E_\nu(\infty)} = \frac{\Delta_l}{\Delta_{l'}}, \quad (l' \neq l) \end{aligned} \tag{76}$$

Not surprisingly, given an XPS profile with clearly identified $E_\nu(\Delta_i)$ and $E_\nu(\infty)$ components of a surface ($l = i = 1, 2, \ldots, B$), or a set XPS data collected from a certain type of nanosolid of different sizes ($l = j = 1, 2, \ldots$), one can easily calculate the energy level of an isolated atom, $E_\nu(1)$, and the bulk shift, $\Delta E_\nu(\infty)$ as well, with the following relations derived from Eq. (76):

$$\begin{cases} E_\nu(1) & = \dfrac{(1+\Delta_{l'})E_\nu(\Delta_l) - (1+\Delta_l)E_\nu(\Delta_{l'})}{\Delta_{l'} - \Delta_l}, \quad (l \neq l') \\ \Delta E_\nu(\infty) & = E_\nu(\infty) - E_\nu(1) \end{cases}$$

or

$$E_\nu(1) = E_\nu(\infty) - \frac{E_\nu(\Delta_l) - E_\nu(\infty)}{\Delta_l} \tag{77}$$

If $l$ (>2) components are given, the $E_\nu(1)$ and the $\Delta E_\nu(\infty)$ should take the mean value of the $C_l^2 = l!/[(l-2)!2!]$ possible combinations with a standard deviation $\sigma$ as both $E_\nu(1)$ and $\Delta E_\nu(\infty)$ are independent of particle dimension or surface relaxation. Chemical reaction changes neither of these two quantities. Accuracy of determination is subject strictly to the XPS data calibration and the bond length that may not always follow exactly the BOLS specification (Section 2). Nevertheless, furnished with this approach, we would be able to elucidate, in principle, the core-level positions of an isolated atom and the strength of bulk crystal binding using the conventional XPS measurement.

### 8.1.4. Verification

*8.1.4.1. Surfaces.* The $E_\nu(1)$ and $\Delta E_\nu(\infty)$ values of several surfaces have been derived based on the available XPS database and Eq. (77). As listed in Table 11, the small deviation $\sigma$ values evidence that the BOLS correlation describes adequately the real situations and that the parameters of $m$ and $z_i$ represent the true situations. Interestingly, a slight refinement of the mid-component $E_\nu(S_2)$ within the XPS resolution reduces the $\sigma$ values to less than 0.1%, which indicates that the XPS precision is critical and the developed method is sensitive and reliable.

Results show that the crystal binding is stronger to the electrons in the outer shells than to the electrons in the inner ones. For example, the binding to the C-1s electrons is weaker ($\sim$0.8 eV) than the binding to the Be-1s ($\sim$5.6 eV) electrons. The former is screened by the four electrons ($2s^2 2p^2$) and the latter by the two $2s^2$ electrons only.

*8.1.4.2. Nanosolids.* BOLS prediction yields a simpler form for elucidating the $E_\nu(1)$ from a set of data of size-dependent core-level shifts, which follows the scaling law (Eq. (13) in Section 2). The $Q(\infty) = \Delta E_\nu(\infty) - \Delta E_\nu(1) = B/(\Delta_j \times K_j)$ varies simply with the parameter $m$ and the given dimensionality ($\tau$) and size ($K_j$) of the solid because $\Delta_j \propto K_j^{-1}$. There are only two independent variables, $m$ and $\Delta E_\nu(\infty)$, in the calculations. If a certain known quantity $Q(\infty)$ in the scaling law, such as the $T_m(\infty)$ or the $E_G(\infty)$, and the measured size-dependent $Q(K_j)$ of the considered system are given, the $m$ can be readily obtained by equilibrating both the theoretical and

Table 11
Calculated atomic $E_\nu(1)$, bulk shift $\Delta E_\nu(\infty)$, and the standard deviation $\sigma$ for different surfaces based on available XPS database

| Surface | XPS components | | | Calculation results | | |
|---|---|---|---|---|---|---|
| | $E_\nu(S_1)$ | $E_\nu(S_2)$-refined | $E_\nu(\infty)$ | $E_\nu(1)$ | $\Delta E_\nu(\infty)$ | $\sigma$ (%) |
| Poly C 1s [537] | 284.42 | – | 284.30 | | | – |
| Pd-$3d_{5/2}$ [541] | 334.92 | – | 334.35 | 330.34 | 4.01 | – |
| Rh-$3d_{5/2}$ [541] | 307.18 | – | 306.42 | 301.17 | 5.35 | – |
| Ru(0001) $3d_{1/2}$[556] | 280.21 | 279.955 | 279.73 | 276.344 | 3.3856 | 0.003 |
| W(110) $4f_{7/2}$ [551] | 31.50 | 31.335 | 31.19 | 29.006 | 2.1835 | 0.003 |
| Nb(100) $3d_{5/2}$[495] | 202.80 | 202.54 | 202.31 | 198.856 | 3.4544 | 0.002 |
| Be($10\bar{1}0$) 1s [546] | 111.85 | 111.475 | 111.1 | 105.817 | 5.2835 | 0.002 |
| Be(0001) 1s [545] | 111.9 | 111.48 | 111.1 | 105.465 | 5.6350 | 0.007 |

For elemental surface, $m = 1$. $z_1 = 4$, $z_2 = 6$ and $z_3 = 8$ are used in calculation. Refinement of the $E_\nu(S_2)$ within XPS resolution reduces the $\sigma$ to <0.1%, indicating the importance of accuracy in XPS calibration.

experimental scaling law. With the determined $m$, any other unknown quantities $Q(\infty)$ such as the crystal binding intensity, $\Delta E_\nu(\infty)$, of the same system, and hence the energy level of an isolated atom, $E_\nu(1)$, can be determined uniquely with the above relations.

The $\Delta E_\nu(\infty)$ and $E_\nu(1)$ for Cu-2p, Au-4f and Pd-3d were calculated by using Eq. (13). Fig. 34 compares the predicted (solid) curves with the measured size dependence of the core-level shifts of these samples (scattered data). In order to find the intercepts and slopes in the scaling relation, all the experimental results were linearized with the least-root-mean-square optimization method. Intercepts at vertical axis provide calibration of the measurement as the intercepts reflect the space charging effect or the system error. The slopes are the major concern in the current decoding exercises. The $E_\nu(1)$ and $\Delta E_\nu(\infty)$ of Cu-2p can be obtained by calculating the Cu/HOPG system with $m = 1$ using Eq. (13). The reason to take $m = 1$ is that Cu atoms hardly react with the carbon surface at room temperature [569], and that $m = 1$ always holds for elemental metallic solid. Decoding gives rise to the atomic trapping energy $E_{2p}(1) = -931.0$ eV for the Cu-2p electrons of an isolated Cu atom and the bulk crystal binding energy $\Delta E_{2p}(\infty) = -1.70$ eV for an extended Cu solid. Taking the obtained Cu-$\Delta E_{2p}(\infty)$ value as reference in simulating the measured size-dependent $\Delta E_{2p}(K_j)$ for Cu on CYCL gives $m = 1.82$, which adds the contribution from the reactivity of Cu to CYCL polymer substrate

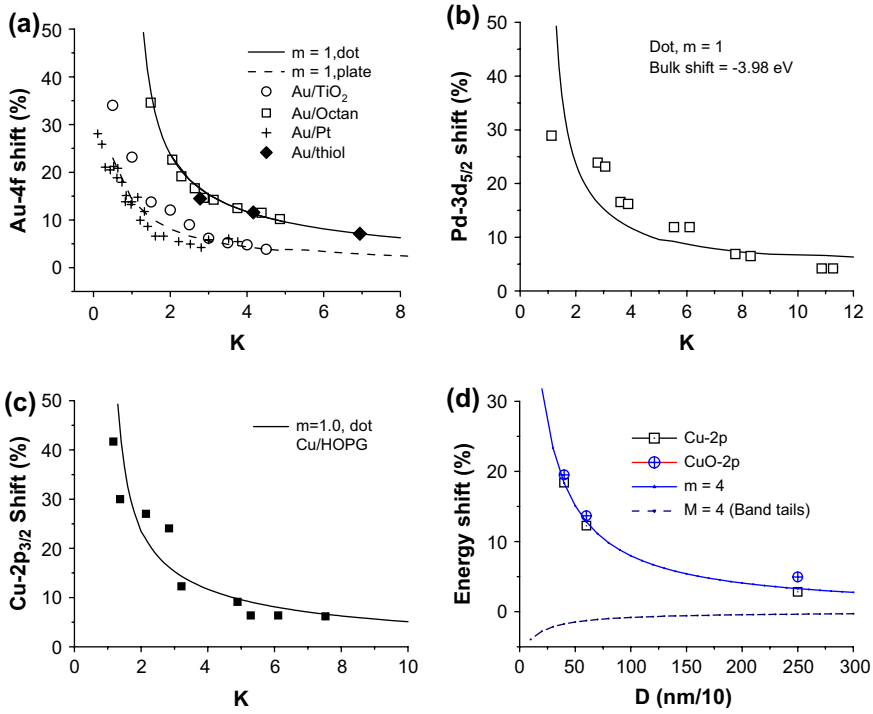


Fig. 34. Comparison of the BOLS prediction with the measured size dependence of the core-level shift. (a) Thiol-capped Au [188] and Au on octan [559] shows three-dimensional features while Au on $TiO_2$ [563] and on Pt [564] show plate pattern of formation. (b) Pd on HOPG substrate [504]. The different $m$ values in (c) of Cu on HOPG and CYCL [562] indicate the contribution from the reaction between Cu nanosolid and polymer CYCL substrate. (d) Core-level shift and bandwidth of CuO nanoparticles.

to the $m = 1$. Therefore, the change of $m$ value provides information about particle–substrate interaction.

For the Au nanosolid, $m = 1$ has been confirmed in decoding the size-dependent melting temperature of Au on C and on W substrates [80]. Fitting the measured $\Delta E_{4f}(K_j)$ of Au on octan with $m = 1$ gives $E_{4f}(1) = -81.50$ eV for an isolated Au atom and $\Delta E_{4f}(\infty) = -2.86$ eV for the Au bulk bonding. Simulations with the derived $\Delta E_{4f}(\infty) = -2.86$ eV as reference reveal that Au growth on $TiO_2$ and on Pt(001) substrates proceeds in a layer-by-layer mode, agreeing with the growth modes as reported by the initial researchers [563,564]. Simulating the XPS data of both Pd surfaces [541] and Pd/HOPG nanosolids [504] led to the value of $\Delta E_{Pd\text{-}3d}(\infty) = -4.00 \pm 0.02$ eV and $E_{Pd\text{-}3d}(1) = -330.34$ eV [570]. Incorporating an $m = 4.88$ value into the simulation of the measured size dependence of the Si-2p level shift gives $E_{2p}(1) = -96.74$ eV for a Si atom and $\Delta E_{2p}(\infty) = -2.46$ eV for Si bulk.

Calculation results from counting the capping, surface and the core of the ZnS and CdS nanosolids show that the crystal binding to S-2p of ZnS is stronger than that of CdS, as compared in Table 12, because the Zn–S bond [30] is shorter than the Cd–S [48] bond. $E_\nu(1)$ should not change under any circumstance. However, the crystal binding to the same levels of an atom may be offset when the atom forms compounds with different elemental atoms. Surface charging also affects the measurement. Therefore, the measured S-2s and S-2p peaks of CdS should shift up or down consistently against the same peaks of ZnS. Compared with the measured S-2s and S-2p peaks from CdS, it can be found that the S-2p peak from ZnS goes slightly down while the S-2s peak floats up with respect to those of CdS. This may cause the $E_{2p}(1)$ values of S in the two samples to vary slightly.

Assuming $m = 4$ for O–Cu, we can use the measured data [535] to estimate the $E_{2p}(1)$ and the $\Delta E_{2p}(\infty)$ of bulk Cu and bulk CuO, as given in Table 12. The estimated values seem to be too large to be reasonably compared with those obtained from Cu/HOPG or Cu/CYCL. As mentioned earlier, the accuracy is strictly subject to the precision of the XPS data. The modeling predictions agree also with the trends of the core-level shift for O–Sn and O–Ta compound nanosolids, of which both the satellites and the main peaks in the XPS profiles shift towards higher binding energy with reducing particle size (Table 13).

*8.1.4.3. Conductor–insulator transition.* In the current modeling approach, we have found that the interfacial bond nature (character $m$) changes with atomic CN. For instance, the $m$ value for Sn and Ga nanosolids increases from one to seven when the solid size decreases from the bulk to the lower end of the size limit, as shown in Section 5.3. For an isolated metallic nanosolid,

Table 12
Calculated atomic $E_\nu$, bulk shift $\Delta E_C(\infty)$ and the standard deviation $\sigma$ for different nanosolids based on the available XPS database. (For compounds, $m = 4$, $z_1 = 4$, $z_2 = 6$, and $z_3 = 8$ are used in calculation)

| Nanosolid | XPS measurement | | | Calculated | | |
|---|---|---|---|---|---|---|
| | $E_\nu$ (cap) | $E_\nu$ (surf) | $E_\nu$ (core) | $E_\nu(1)$ | $\Delta E_\nu(\infty)$ | $\sigma$ |
| CdS-S $2p_{3/2}$ [560] | 163.9 | 162.7 | 161.7 | 158.56 | 3.14 | 0.002 |
| ZnS-S 2p [185] | 164.0 | 162.4 | 161.4 | 157.69 | 3.71 | 0.002 |
| CdS-S 2s [560] | 226.0 | 224.7 | 223.8 | 220.66 | 3.14 | 0.001 |
| ZnS-S 2s [185] | 229.0 | 227.3 | 226.3 | 222.32 | 3.92 | 0.001 |
| CuO-Cu $2p_{3/2}$ [535] | 936.0/934.9 (4/6 nm) | 932.9 (25 nm) | 932.1 (bulk) | 919.47 | 12.63 | 0.36 (2.8%) |
| CuO-Cu $2p_{3/2}$ refined data | 935.95/934.85 (4/6 nm) | 932.95 (25 nm) | 932.1 (bulk) | 919.58 | 12.52 | 0.30 (2.4%) |

Table 13
The $E_v(1)$ of isolated Au, Cu and Si atoms and the crystal binding energy of $\Delta E_v(\infty)$ obtained from decoding the size-dependent $E_v(K_j)$ of the corresponding nanosolids

| | Au/octan | Au/$TiO_2$ | Au/Pt | Cu/HOPG | Cu/CYCL | Si | Pd |
|---|---|---|---|---|---|---|---|
| $m$ | 1 | | | | 1.82 | 4.88 | 1 |
| $\tau$ | 3 | 1 | 1 | 3 | 3 | 3 | 3 |
| $d_0$/nm | 0.288 | | | 0.256 | | 0.263 | 0.273 |
| $E_v(\infty)$/eV | −84.37(4f) | | | −932.7(2p) | | −99.20(2p) | −334.35(3d) |
| $E_v(1)$/eV | −81.504 | −81.506 | −81.504 | −931.0 | | −96.74 | −330.34 |
| $\Delta E_v(\infty)$/eV | −2.866 | −2.864 | −2.866 | −1.70 | | −2.46 | −3.98 |

the metallic bond suffers from relaxation due to CN imperfection but no change in its nature if no chemical process is involved. Metal–nonmetal transition may happen at a certain critical size, 1–2 nm. Such transition was suggested to originate from the Kubo-gap expansion in which no bond character is involved. However, from the bond relaxation point of view, the bonds in the surface skin become shorter and stronger and the trapping potential wells become deeper. The BOLS correlation indicates that it is the deepened trapping potential well that confines the moving electrons to be more localized, and hence, the conductivity of the metallic nanosolid becomes lower [571]. At the lower end of the size limit (1–2 nm) no core exists, all the bonds will contract by 20–30% associated with 30–50% deepening of the trapping potential wells, see Fig. 5 in Section 2. As a complementary mechanism to the Kubo-gap expansion, the BOLS correlation may provide a scenario in real space to explain why the conductivity drops and how the conductor–insulator transforms for a metallic nanosolid.

*8.1.4.4. Electroaffinity versus valence DOS shift.* Potential well suppression and energy densification in the skin of a solid will perturb the Hamiltonian that determines the entire band structure and related properties, including electroaffinity, $\varepsilon$. The electroaffinity is defined as the separation between the vacuum level, $E_0$, and the conduction band edge, which represents the ability of holding the bonding electrons. In comparison, the difference in electronegativity between two elements represents the capability of the more electronegative element catching electrons from the less electronegative one. One specimen with a larger value of $\varepsilon$ has higher tendency to hold the caught electrons more firmly.

The enlargement of electroaffinity of the specimen results from the conduction band shift and the band gap expansion (for semiconductors only, which is not shown in the diagram). The affinity change follows the relation:

$$\begin{aligned}\Delta\varepsilon(\tau,K_j) &= \Delta E_C(\tau,K_j) - \Delta E_C(\infty) - \Delta E_G(\tau,K_j)/2 \\ &= [\Delta E_C(\infty) - \Delta E_G(\infty)/2] \times \Delta_H(\tau,K_j)\end{aligned} \tag{78}$$

The conduction band edge drops sharply from the $E_C(1)$ value of an isolated atom to a maximum at $E_C(K_j \sim 1.5)$, and then recovers in a $K_j^{-1}$ manner until the bulk value of $\Delta E_C(\infty)$ is reached. The value of $K_j = 1.5$ corresponds to $z_i = 2$, which is the case of a monatomic chain ($\tau = 1$) or a unit cell ($\tau = 3$) containing 13 atoms of an fcc structure, for instance. Measurement [572] using X-ray absorption spectroscopy has recently clarified that the occupied $E_{2p}$ DOS shifts positively by ~0.9 eV from the $E_{2p}(1)$ value of 573.5 eV monotonically to the $E_{2p}(13)$ value of 574.4 eV. With the $\Delta E_C(\infty)$ data obtained as above [123,562], the maximal $\Delta\varepsilon_M$ value, or the valence DOS shift of the conduction band, of $Cu_{3d}$ ($\Delta E_{3d}(\infty) = 2.12$ eV, $\Delta\varepsilon_M = 0.99$ eV)

and $Au_{4f}$ ($\Delta E_{3d}(\infty) = 2.87$ eV; $\Delta\varepsilon_M = 1.34$ eV) nanospheres can be derived using the parameters of $\tau = 3$, $m = 1.0$, and $\Delta_H(1.5) = 0.7^{-1} - 1 = 43\%$. For a semiconductor Si nanosphere ($\tau = 3$ and $m = 4.88$), the electroaffinity will be enlarged by $\Delta_H(1.5) = 0.7^{-4.88} - 1 = 470\%$. Employing the $\Delta E_{2p}(\infty) = 2.46$ eV and $E_G(\infty) = 1.12$ eV, the estimated $\Delta\varepsilon_M$ for Si at least is 5.8 eV. The actual $\Delta\varepsilon_M$ for Si should be larger as the $\Delta E_{3p}(\infty)$ for the conduction band is larger than the $\Delta E_{2p}(\infty)$. If the $m$ increases with reducing $z_i$, the $\Delta\varepsilon_M$ value becomes enormous. At a flat surface ($z_i = 4$), the energy level will shift positively by $0.88^{-1} - 1 = 13.6\%$ for metals and $0.88^{-4.88} - 1 = 87\%$ for Si. The enlarged electroaffinity may further explain why the bond nature alteration occurs in the III-A nanosolids and why the IV-A covalent bond becomes even stronger at $z_i \leq 3$.

### 8.2. Work function

#### 8.2.1. Chemical modulation

The work function ($\Phi$) of a specimen is the energy required to get an electron from or to add an electron into the surface. The $\Phi$ or the threshold in cold-cathode field emission of materials such as diamond, diamond like carbon (a-C) or carbon nanotubes (CNTs), can be chemically modulated/enhanced by doping the materials with proper impurities as well as by geometric enhancement of the emitters [573]. It has been realized that co-doping O or N with low-$\Phi$ metals to form metal dipoles at the surface could be a promising route [574,575] in lowering the $\Phi$ at the surface. For example, ZnO nanopins and Ga-doped ZnO nanorods show a low field emission threshold $\sim$2.0 V/μm at a current density of 0.1 μA cm$^{-1}$ [576,577]. The lone-pair-induced antibonding dipole states that are located at energy levels higher than the Fermi level are responsible for the $\Phi$ reduction. However, the production of the H-type bond at the surface due to O or N overdosing may have detrimental effects on the $\Phi$ reduction, such as the case of carbon nanotubes with over-doped oxygen [577]. Lower doses of oxygen to the tubes improve significantly the field emission characteristics while overdosing with oxygen makes electron emission difficult. Therefore, appropriate amounts of impurity density are necessary [575] to avoid H-bond like formation that narrows the antibonding band [3,579]. The chemical effect on the $\Phi$ has been intensively discussed in the previous reports on the electronic process of oxidation and nitridation [3,4].

#### 8.2.2. Geometric modulation

The current BOLS correlation argument indicates that the bond contraction not only deepens the atomic potential well but also enhances the charge density in the relaxed surface region. The confined electrons near the surface edge are denser and more localized. For an isolated nanosolid of size $K_j$, the $\Phi$ satisfies ($V \propto d^{\tau}$):

$$\Phi = E_0 - E_F; \quad \text{and} \quad E_F \propto n^{2/3} = (N_e/V)^{2/3} \propto (\overline{d})^{-2\tau/3} \tag{79}$$

The total number of electrons $N_e$ of a nanosolid is conserved. At the lower end of the size limit of a spherical or semispherical dot ($R \sim 1$ nm, $\tau = 3$), the average bond length is around 20% shorter than the bulk value and hence the $\Phi$ will reduce from the original value by 30% ($E_F$ shifts up by $0.8^{-2} - 1$), according to Eq. (79). Using He-II ultraviolet beam source of 21.2 eV, Abbott et al. [580] measured the $\Phi$ of diamond {111} surface to be about 4.8 eV at grain size of 108 μm, as shown in Fig. 35a. The $\Phi$ of the diamond decreases with particle size to a minimum of 3.2 eV at an average grain size of about 4 μm, and then the $\Phi$ recovers to a maximum of 5.1 eV at a diamond particle size of 0.32 μm. Kelvin force probe microscopy detected that work function of single

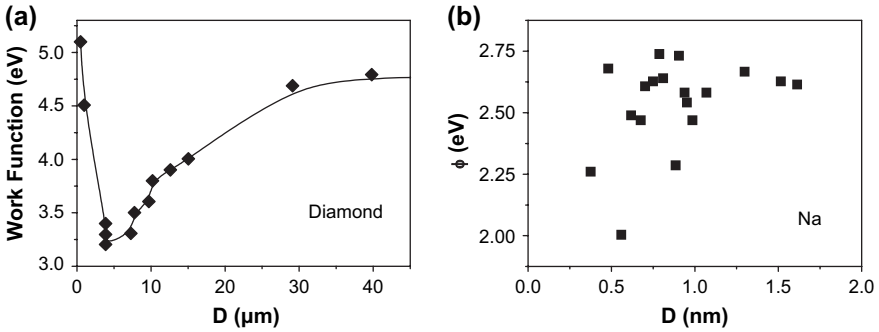


Fig. 35. Size modulated work function of (a) diamond [580] and (b) Na [582] nanocrystals. Recovery of the work function is due to the geometrical flatness [584].

InAs dot on GaAs(001) is lower than that of an InAs wetting layer, and increases with decreasing dot height [581]. Rouse et al. [267] measured at room temperature that the field-emission threshold decreases from 3.8 to 3.4 V/μm for polycrystalline diamond films on molybdenum tips as the diamond average grain size increases from 0.25 to 6 μm. They related the $\Phi$ change to the increases of negative electron affinity within the grain due to increased surface hydrogen bonding and with perhaps a contribution from surface defect states. The $\Phi$ of Na particles around 0.4–2.0 nm size was measured to vary inversely with the size $R$ and lowered the bulk value from 2.75 to 2.25 eV (by 18%) [582]. The majority of the nanotubes have a $\Phi$ of 4.6–4.8 eV at the tips, which is 0.2–0.4 eV lower than that of carbon (graphite) bulk. A small fraction of the nanotubes have a $\Phi$ value of $\sim$5.6 eV, about 0.6 eV higher than that of carbon (graphite). This discrepancy is suggested to arise from the metallic and semiconductive characteristics of the nanotubes. The average $\Phi$ of porous Si with different crystalline columnar dimensions was measured using a retarding field diode method and shown to increase as the crystalline size decreases [583]. The variation of the $\Phi$ was attributed to the etching effect and the formation of impurity Si–H, Si–O, and Si–H–O bonds at the surface [583].

It appears that the measured size-dependent $\Phi$ change for diamond is in conflict with the BOLS prediction. However, one needs to note that if the emitters are packed too closely, the system is identical to a smooth surface. It has been found [584] that hydrogen-rich or oxygen-containing CVD precursors could promote electron emission from discrete diamond particles and *non-continuous* diamond films but not for high quality and continuous diamond films, nanocrystalline diamond, and glassy carbon coatings even if they contain conductive graphitic carbon. The $\Phi$ at the tips of individual multi-walled carbon nanotubes was measured using a TEM to show no significant dependence on the diameter of the nanotubes in the range of 14–55 nm [585]. Although the calibrated diamond particles are much larger the curvature of the tips should be much higher. The particle size corresponds only to the separation of the sharp emitters. This phenomenon indicates the significance of CN imperfection on the $\Phi$ reduction that is subject to the separation between the nanoparticles and surface chemical states.

### *8.2.3. Hydrophobic–hydrophilic transition*

The wettability that governs the surface chemical states and geometric structures is an important factor influencing the properties of functional materials. Special wettabilities, such

as superhydrophilicity and superhydrophobicity, have aroused great interest in recent years because of their advantages in applications, such as anti-contamination, anti-oxidation, and prevention of current conduction. Superhydrophobicity and superhydrophobicity have been observed on as grown and alkylfluorosilane (NaF) modified carbon nanotubes [586] and other aligned nanostructures [587]. Interestingly, reversible switching between superhydrophilicity and superhydrophobicity through constructing special surface structures on the respective surfaces becomes possible by surface conditioning [588,589]. On a poly(*N*-isopropylacrylamide)-modified rough silicon substrate [588], switching from superhydrophobicity to superhydrophilicity can be achieved at temperatures 302–313 K because of the inverse competition between intermolecular and intramolecular hydrogen bonding in the polymer chains. However, on an aligned ZnO nanorod surface [589], switching can be achieved by UV irradiation ($365 \pm 10$ nm) and dark aging, which is considered the result of the reversible generation and annihilation of the photo-generated surface oxygen vacancies.

The combination of the BOLS and the BBB correlation premises may provide a possible complementary mechanism in terms of bond formation and relaxation for the superhydrophilicity and superhydrophobicity [586–589]. As demonstrated, charge densification in the relaxed flat or curved surface region could lower the local work function by as much as 30% at the expense of raising the chemical potential ($E_F$) of the nanosolid. Furthermore, sp-orbital hybridization of electronegative elements such as N, O, and F will produce nonbonding lone pairs that polarize electrons of the neighboring atoms to form antibonding dipoles. Dipole formation lowers the local work function by about 1.2 eV for N and O involvement. The joint effect of nanostructures and antibonding states could be responsible for the superhydrophobicity arising from the raised chemical potential. By warming up the passivated samples to a certain temperature [590], irradiated by light of a certain wavelength, or bombarded by energetic beams, dehybridization occurs. An external stimulus such as heating breaks the lone pairs and hence the antibonding dipoles, as observed for the O–Cu(001) surface of which the lone-pair DOS feature disappears upon annealing at ''dull red color''. The lone-pair DOS feature of the annealed O–Cu(001) surface is restored after cooling down and aging for a while or for some time. If overdosed with electronegative additives to the surface, H-like bonds may form, which reduces the number of antibonding dipoles and hence restore the work function, as the dipoles become positive ions due to charge transport. This happens for carbon nanotubes overdosed with oxygen [578]. A small amount of oxygen lowers the work function while overdosing with oxygen raises the work function to a value that is even higher than the undoped case. Changing the dosage of electronegative elements could be a new manner in which to switch the superhydrophilicity and superhydrophobicity nature, and further experimental verification of this is required.

### *8.2.4. Mechanical modulation*

Amorphous carbon (a-C) films have a uniquely intrinsic stress ($\sim$12 GPa) that is almost one order of magnitude higher than those found in other amorphous materials such as a-Si, a-Ge, or metals (<1 GPa) [591]. Although it is known from theoretical studies [592] that by applying pressure to a material one can modify its electronic properties, e.g., band structure, resistivity, work function, etc., the influence of the intrinsic stress on the electron emission properties of a material has not been clear. Poa et al. [191,591] investigated electron emission from highly compressive carbon films obtained by bombardment in a noble gas plasma and found a correlation between the stress and the threshold field for electron emission, as shown in Fig. 36. By carefully controlling deposition conditions, they varied the internal stresses from 1 to 12 GPa, which is associated with suppression of the electron emission threshold field. The lowering of

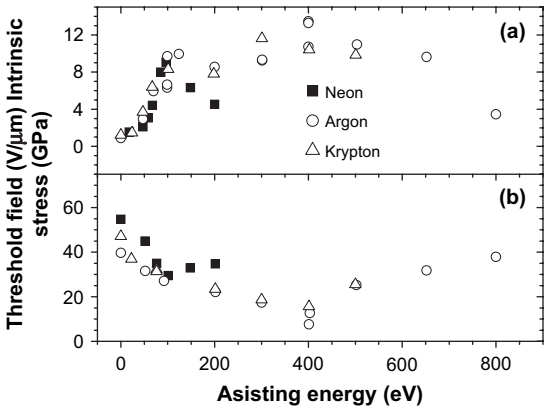


Fig. 36. Correlation between the threshold field (upper panel) and intrinsic stress (lower panel) of amorphous carbon as a function of the assisting energy when bombarded by different noble gases [191].

the threshold field is related to the enhanced stress that pushes the $\pi$ and the $\pi^*$ bands together with a reduced gap between them to even an overlap by gathering the $sp^2$ clusters closer to each other. Such a band overlap increases the electron conductivity and hence the drop of the threshold. On the other hand, the "*c*-axis" spacing of the $sp^2$ clusters is likely to be smaller than that of crystalline graphite under the intrinsic stress. The reduced lattice spacing will densify the charge in the compressed region, which suppresses internally the threshold field. Applying an external stress by bending a-C films or carbon nanotubes has the same effect on reducing the threshold for electron emission [593]. However, the threshold will restore when it reduces to a certain value if further stress is applied.

Using extended near-edge XAFS, Lacerda et al. [594] investigated the effect of trapping noble gases (Ar, Kr, and Xe) in an a-C matrix on the internal stress of the a-C films. When an internal stress of 1–11 GPa is generated by controlling the size of the pores within which noble gases are trapped, they found an approximate1 eV lowering of the core-level binding energy of the entrapped gases associated with 0.05 nm expansion of the atomic distance of the noble gases. For Ar (Xe), the first interatomic separation varies from 0.24 (0.29) nm to 0.29 (0.32) nm in the 1–11-GPa pressure range. This enhancement indicates clearly that the gas entrapped pores expand and the interfacial C–C bonds contract. An external pressure around 11 GPa could suppress the interplanar distance of microcrystalline graphite by $\sim$15% [595], gathering the core/valence electrons and carbon atoms closer together. The resistivity of a-C films decreases when the external hydrostatic pressure is increased [596]. These results are in agreement with the recent work of Umemoto et al. [597] who proposed a dense, metallic, and rigid form of graphitic carbon with characteristics being very similar to the findings of Poa et al. However, the spontaneous lattice contraction could raise the resistivity, instead, as the densified charges are strongly trapped within the lowered potential well though both the intrinsic and extrinsic pressure could densify the mass, charge, and the stress (energy) of a highly $sp^2$ rich a-C film.

We may suggest a possible mechanism for the intrinsic and extrinsic stress enhanced threshold field of carbon films. Nanopore formation creates under-coordinated atoms at the interfaces between the gas-trapped pores and the a-C matrix. The CN imperfection induced lattice contraction of the host matrix will apply to the pores and hence act to expand the atomic distance between the inter-trapped atoms. The bond expansion is associated with weakening of

interatomic binding of the noble gas atoms confined in the pores, as observed. The interfacial C–C bond contraction leads to simultaneous enhancement of both the charge density and the internal stress, associated with a drop of the local work function by as high as 30%, as derived in the previous section. Therefore, the internal stress affects the work function by enhancing the local charge density trapped in the deep potential well. From this perspective, an $sp^2$ cluster with a shortened bond ($\leq$0.142 nm) would be beneficial to the field emission properties when compared with an $sp^3$ cluster (0.154 nm bond length) despite the less localized Van der Waals bond electrons that should add a DOS feature in the midgap. Therefore, atomic CN imperfection enhances the charge density and hence the magnitude of the N(E).

In contrast, external stress could raise the atomic binding and the total energy between a pair of atoms, being the same in effect as heating and thus weakening the bond. Therefore, heating or pressing should raise the N(E) higher and, as a consequence, minimize the gap between the $\pi$ and $\pi^*$ bands, as proposed by Poa et al. Overstressing the specimen tends to break bonds so that dangling bonds are formed, which adds DOS features in the midgap despite the enlarged gap between the emitter and the grid in the measurement. This understanding may provide a possible mechanism for the threshold recovery, which occurs upon being overstressed. Therefore, this mechanism for the external pressure lowered $\Phi$ should differ from that of intrinsic pressure though the effects are the same. The intrinsic stress amplifies the N(E) magnitude and raises the resistivity; whereas the external one ''pumps'' the N(E) up, and raises the conductivity. Lu and coworkers [8,58] have demonstrated that for an as grown nanosolid, the resistivity increases with the inverse of solid size but, under stretching, the electrical conductivity remains comparable to that of bulk copper, which could be evidence for the recommended effect of intrinsic and extrinsic stress on the conductivity behavior of a metallic nanosolid.

### *8.3. Summary*

The BOLS correlation premise has enabled us to unify the core-level physical shift induced by surface relaxation and nanosolid formation into the same origin of atomic CN imperfection. The mechanism of surface interlayer relaxation [540] induced positive shift and the specification of the capping and surface layers in CdS and ZnS nanosolids are highly favored. Atomic CN imperfection also enhances the ionicity of the constituent atoms such as oxygen and metals [535]. The artifacts added to the XPS spectrum due to photovoltaic effects in experiments and the excited final states could be removed by proper calibration of the data. The CN imperfection enhanced binding strength acts on the core electrons of an atom disregarding the atomic states whether it is in the neutral initial or the ionized final state.

In addition, we have developed an effective yet straightforward method to determine the core-level energies of an isolated atom and hence to discriminate the contribution of crystal binding from the effect of atomic trapping to the core electrons at energy levels shifted by bulk formation, surface relaxation or nanosolid formation. The developed method not only allows the predicted size dependence of core-level shift to match with observations but also enables conventional XPS to provide comprehensive information about the behavior of electrons in the deeper shells of an isolated atom and the influence of crystal formation.

Understanding of the effect of intrinsic and extrinsic stress and factors controlling work function, resistivity, and the intrinsic stress should provide guidelines for materials design and fabrication for applications of electron emission and superhydrophilicity–superhydrophobicity transition.

## 9. Dielectric suppression

### 9.1. Background

The complex dielectric constant, $\varepsilon_r(\omega) = \mathrm{Re}\left[\varepsilon_r(\infty)\right] + i\,\mathrm{Im}\left[\varepsilon'_r(\omega)\right]$, is a direct measure of electron polarization response to external electric field, which has enormous impact on the electrical and optical performance of a solid and related devices. For example, low $\varepsilon_r(\infty)$ media are required for the replacement of Al with Cu in microelectronic circuitry to prevent the 'cross-talk' between connections while media of higher $\varepsilon_r(\infty)$ are required for the miniaturized conductor–metal–oxide–semiconductor gate devices. Miniaturizing a semiconductor solid to nanometer scale often causes the $\varepsilon_r(K_j)$ to decrease [502,598]. The $\varepsilon_r(K_j)$ reduction enhances the Coulomb interaction between charged particles such as electrons, holes, and ionized shallow impurities in nanometric devices, leading to abnormal responses. The increase of exciton activation energy in nanosemiconductors due to $\varepsilon_r(K_j)$ reduction would significantly influence optical absorption and transport properties of the devices. Both the ac conductivity and dielectric susceptibility of amorphous Se films drop with thickness in the range of 15–850 [599]. The complex dielectric constant decreases when the frequency is increased and the temperature is decreased in the range of 300 and 350 K. Carrier motion is suggested to be the dominant mechanism in both ac polarization and dc conduction. A thermodynamic analysis [600] suggests a drastic variation in the polarization near the dislocation due to the coupling of the stress field of the dislocation and the polarization. These polarization gradients result in strong depolarizing fields that suppress the polarization in a region that extends over several nanometers. In epitaxial ferroelectric films, these polarization gradients should result in the formation of dead layers that severely degrade ferroelectric properties. The detrimental effect of such regions will be enhanced in ultrathin ferroelectric thin films, and hence play a critical and extrinsic role in size effect studies of ferroelectrics. A progressive reduction of tetragonal distortion, heat of transition, Curie temperature, and relative dielectric constant has been observed on dense $BaTiO_3$ ceramics with grain size decreasing from 1200 to 50 nm [374]. From experimental trends it is estimated that the critical size for disappearance of ferroelectricity is 10–30 nm. The strong depression of the relative permittivity observed for the nanocrystalline ceramics can be ascribed to the combination of the intrinsic size effect and of the size-dependent ''dilution'' effect of a grain boundary ''dead'' layer.

The relative changes of the dielectric susceptibility, $\chi = \varepsilon_r - 1$, have been modeled as:

$$\Delta\chi(K_j)/\chi(\infty) = \begin{cases} -\left[1 + \left(K_j/\alpha\right)^{\lambda}\right]^{-1} & \text{(Penn)} \\ \dfrac{-2\Delta E_G(K_j)}{E_G(\infty)} & \text{(Tsu)} \\ \dfrac{-2}{1-\left(E/E_G(\infty)\right)^2}\left(\dfrac{\Delta E_G(K_j)}{E_G(\infty)}\right) & \text{(Chen)} \end{cases}$$

where $\alpha$ and $\lambda$ in the Penn's empirical model [601] are freely adjustable parameters that vary from situation to situation as listed in Table 14. Tsu and Babic [602] related the susceptibility change directly to the offset of $E_G(K_j)$. Considering the contribution from incident photon energy, $E = \hbar\omega$, Chen et al. [603,604] modified Tsu's model and studied the dielectric response of nanosolid Si embedded in a $SiO_2$ matrix using ellipsometry. They suggested that the dielectric suppression varies with the photon beam energy that should be lower than the intrinsic $E_G(\infty)$

Table 14
Simulation results in Penn's model

| | $\varepsilon_r$ (bulk) | $\alpha$/nm | $\lambda$ |
|---|---|---|---|
| CdSe [180] | 6.2 | 0.75 | 1.2 |
| Si-a [497,602] | 11.4 | 2.2 | 2 |
| Si-b [610] | 11.4 | 1.84 | 1.18 |
| Si-c [610] | 10.38 | 0.85 | 1.25 |
| Si-d [610] | 9.5 | 0.69 | 1.37 |

of Si. Delerue et al [605] deposited PbSe nanocrystals of several nanometers in height on an Au(111) substrate and measured the thickness-dependent dielectric function. Compared with electronic structure calculations of the imaginary part of the dielectric function of PbSe nanocrystals they suggested that the size-dependent variation of the dielectric function is affected by quantum confinement at well-identifiable points in the Brillouin zone, instead of the band–gap transition. The size-induced decrease of the average dielectric response is also suggested to be mainly due to the breaking of the polarizable bonds at the surface [606] rather than the $E_G$ expansion or quantum confinement. A recent calculation [607] of the microscopic dielectric response function for quantum dots using first-principle methods suggests that the response is bulk-like inside the quantum dots, and the reduction of the macroscopic dielectric constants is a surface effect. This indicates that the quantum dots are more ''superficial'' than first thought in terms of quantum confinement [608]. A theoretical study [609] of the third-order susceptibility for an Ag dielectric composite suggests the saturation of optical transitions between discrete states of conduction electrons in metal dots. Saturation effects lead to a decrease of the local field enhancement factor that is of particular importance for surface-enhanced phenomena, such as Raman scattering and nonlinear optical responses.

One may note that the modified models [602,603] suit only the cases where $\Delta E_G(K_j)/E_G(\infty) < 0.5$, otherwise $\chi < 0$, which is physically forbidden, as commented by Chen. Generally, the $E_G$ often expands beyond this critical value such as the case of Si nanorods with $E_G = 3.5$ eV [46]. Therefore, understanding of dielectric suppression of nanosolid semiconductors is still under debate. Furthermore, the size dependence of the imaginary part of the dielectric constant and of the photoabsorption coefficient needs yet to be established. Therefore, deeper and consistent insight into the origin and a clearer and complete expression for the size dependence of the complex dielectric constant of a nanosolid semiconductor is necessary.

### 9.2. BOLS consideration

#### 9.2.1. Electron polarization

Electronic polarization through a process of transition from the lower ground states (valence band or the midgap impurity states) to the upper excited states in the conduction band takes the responsibility for complex dielectrics. This process is subject to the selection rule of energy and momentum conservation, which determines the optical response of semiconductors and reflects how strongly the electrons in ground states are coupling with the excited states that shift with lattice phonon frequencies [515]. Therefore, the $\varepsilon_r$ of a semiconductor is directly related to its band gap $E_G$ at zero temperature, as no lattice vibration occurs at 0 K.

Since the involvement of electron–phonon coupling, electron excitation from the ground states to the excited upper states is complicated, as illustrated in Fig. 28. The energy for photon absorption, or energy difference between the upper excited state $E_2(q)$ and the lower ground state $E_1(q)$, at $q$ is given as:

$$\hbar\omega = E_2(q) - E_1(q) = E_G - Aq_0^2 + 2Aqq_0 = E_{PL} + 2Aqq_0 \tag{80}$$

The imaginary part, $\varepsilon_r'(\omega)$, describes the electromagnetic wave absorption and is responsible for the energy loss of incident irradiation through the mechanism of electron polarization. The $\varepsilon_r'(\omega)$ can be obtained by inserting the gradient of Eq. (80) into the relation [283,611]

$$\varepsilon_r'(\omega) = \frac{F}{\omega^2}\int \mathrm{d}s \frac{f_{CV}}{|\nabla[E_C(q) - E_V(q)]|} = \frac{\pi F f_{CV}}{A\omega^2}q = \frac{\pi F f_{CV}}{2A^2}\frac{\hbar\omega - E_{PL}}{q_0\omega^2} \propto \frac{\hbar\omega - E_{PL}}{q_0\omega^2}$$

where the gradient and the elemental area for integral are derived as follows [612]:

$$\begin{aligned} &\nabla[E_C(q) - E_V(q)] = 2Aq_0 \\ &\mathrm{d}s = 2\pi q_0 \mathrm{d}q \end{aligned} \tag{81}$$

The $s$ is the area difference of the two curved surfaces in $q$ space of the upper excited band and the lower ground band. $F$ is a constant. $f_{CV}$, the probability of inter-subband (Kubo gap) transition, is size dependent. However, the size-induced change of transition probability between the sublevels is negligibly small, and for the first-order approximation, $f_{CV}$ is taken as constant.

### 9.2.2. Complex dielectrics

*9.2.2.1. Dielectric susceptibility.* The Kramers–Kronig relation correlates the real part to the imaginary part of the complex dielectric function by [613]

$$\begin{aligned} \varepsilon_r(\infty) - 1 = \chi &= \frac{2}{\pi}\int_{\omega_0}^{\infty} \frac{\varepsilon_r'(\omega)}{\omega}\mathrm{d}\omega(\omega_0 = E_{PL}/\hbar) = \frac{Ff_{CV}}{A^2q_0}\int_{\omega_0}^{\infty}\frac{\hbar\omega - E_{PL}}{\omega^3}\mathrm{d}\omega \\ &= \frac{G}{q_0E_{PL}}, \quad \left(G = \hbar^2 F f_{CV}/2A^2\right) \end{aligned} \tag{82}$$

where $\hbar\omega - E_{PL} = 2Aqq_0$ as given in Eq. (80). Hence, the size-suppressed dielectric susceptibility depends functionally on the characteristics of e–p interaction and the PL energy. Using the relation of $\Delta E_{PL}(K_j)/E_{PL}(\infty) = \Delta_H - B\Delta_{e-p}$ (Section 7), the size-induced relative change of both the $\chi$ and the $\varepsilon_r'(\omega)$ can be obtained as:

$$\begin{aligned} &\frac{\Delta\chi(K_j)}{\chi(\infty)} = -\frac{\Delta E_{PL}(K_j)}{E_{PL}(\infty)} - \frac{\Delta q_0(K_j)}{q(\infty)} = -\frac{\Delta E_{PL}(K_j)}{E_{PL}(\infty)} + \frac{\Delta d_i(K_j)}{d_0} = -\left(\Delta_H - B\Delta_{e-p}\right) + \Delta_d, \\ &\frac{\Delta\varepsilon_r'(K_j,\omega)}{\varepsilon_r'(\infty)} = \frac{-E_{PL}(\infty)}{\hbar\omega - E_{PL}(\infty)}\frac{\Delta E_{PL}(K_j)}{E_{PL}(\infty)} + \frac{\Delta d_i(K_j)}{d_0} = \frac{-E_{PL}(\infty)}{\hbar\omega - E_{PL}(\infty)}\left(\Delta_H - B\Delta_{e-p}\right) + \Delta_d \end{aligned} \tag{83}$$

where $B$ is the e–p coupling coefficient. $\Delta_H$ and $\Delta_{e-p}$ represent the contribution from the CN-imperfection perturbed Hamiltonian and the e–p coupling in the

relaxed surface skin. The last term is the bond length change ($q \propto d^{-1}$). They are given as [45]:

$$\begin{cases} \Delta_H & = \sum_{i\leq 3} \gamma_{ij}\left(c_i^{-m}-1\right), \quad \text{(Hamiltonian-perturbation)} \\ \Delta_{\text{e-p}} & = \sum_{i\leq 3} \gamma_{ij}\left(c_i^{-2}-1\right), \quad \text{(e–p-coupling)} \\ \Delta_d & = \sum_{i\leq 3} \gamma_{ij}(c_i-1), \quad \text{(bond-contraction)} \end{cases} \tag{84}$$

For a spherical silicon dot, $B = 0.91$, $m = 4.88$, $z_2 = 6$, and $z_3 = 12$. Compared with the relations given in Eq. (83), the complex dielectric performance of a nanosolid semiconductor depends functionally on crystal binding and e–p coupling. The imaginary dielectric constant depends also functionally on the photon energy. Both components drop with solid size, which follow the BOLS correlation.

*9.2.2.2. Direct and indirect band transition.* For direct and indirect band gap optical transition, the $\varepsilon_{\text{r}}'(\omega)$ can be traditionally simplified as [498,614]:

$$\begin{aligned} \varepsilon_{\text{r}}'(\omega) &= \begin{cases} \dfrac{B'}{\omega^2}(\hbar\omega - E_{\text{G}})^{1/2} & (\text{direct} - E_{\text{G}}) \\ A'(T)(\hbar\omega - E_{\text{G}})^2 & (\text{indirect} - E_{\text{G}}) \end{cases} \\ B' &= \pi\left(2\mu/\hbar^2\right)^{\frac{3}{2}} f_{cv}, \quad A(\hbar\omega > E_{\text{G}}) \end{aligned} \tag{85}$$

where $A'(T)$, containing parameters for band structure and temperature describes the momentum contribution of phonons to the indirect $E_{\text{G}}$ transition. The probability of interband transition, $f_{\text{cv}}$ and $A'(T)$, should also vary with the particle size. It would be reasonable to assume that the size-induced transition-probability change is negligibly small despite the availability of the exact correlation of the transition probability to the Kubo gaps.

Compared with Eq. (83), the traditional form of size-dependent $\varepsilon_{\text{r}}'$ varies with the $E_{\text{G}}$ and the incident beam energy:

$$\frac{\Delta\left[\varepsilon_{\text{r}}'\left(K_j,\omega\right)\right]}{\varepsilon_{\text{r}}'(\infty,\omega)} = \frac{\alpha' E_{\text{G}}(\infty)}{E_{\text{G}}(\infty)-\hbar\omega}\left(\frac{\Delta E_{\text{G}}\left(K_j\right)}{E_{\text{G}}(\infty)}\right) = \frac{\alpha' E_{\text{G}}(\infty)}{E_{\text{G}}(\infty)-\hbar\omega}\Delta_H \tag{86}$$

where $\alpha' = 1/2$ and 2 correspond to direct and indirect $E_{\text{G}}$ transition, respectively. The traditional form at a certain optical energy, $\hbar\omega > E_{\text{G}}(\infty)$, decreases with $E_{\text{G}}$ expansion, $\Delta_H$, without involvement of bond contraction and e–p interaction.

*9.2.2.3. Photon absorption.* The absorption coefficient, $\alpha$, the refractive index, $n$ ($=\sqrt{\varepsilon_{\text{r}}}$), and the complex dielectric function are correlated as $\alpha(\omega) = 2\pi\varepsilon_{\text{r}}'(\omega)/n\lambda$, and the transmittance of light is given as $T \propto \exp(-\alpha x)$, where $x$ is the thickness of the medium for light transmission. This relation leads to the size-induced change of $\alpha$ as:

$$\frac{\Delta\alpha(K_j,\omega)}{\alpha(\infty,\omega)}=\frac{\Delta\varepsilon_r'(K_j,\omega)}{\varepsilon_r'(\infty,\omega)}-\frac{\Delta\varepsilon_r(K_j)}{2\varepsilon_r(\infty)}$$
$$=-\left[\frac{\chi(\infty)}{\chi(\infty)+1}+\frac{\alpha' E_G(\infty)}{\hbar\omega-E_G(\infty)}\right]\Delta_H \quad \text{(convention)}$$
$$\text{or} \quad =\left[\frac{\chi(\infty)}{2[\chi(\infty)+1]}-\frac{E_{PL}(\infty)}{\hbar\omega-E_{PL}(\infty)}\right]\times\left(\Delta_H-B\Delta_{e-p}\right)+\frac{\chi(\infty)+2}{2[\chi(\infty)+1]}\times\Delta_d \ \text{(BOLS)} \tag{87}$$

The traditional form $\left[\Delta\chi(K_j)/\chi(\infty)=-2\Delta_H\right]$ discriminates the direct and indirect $E_G$ transition by the $\alpha'$ while the BOLS form $\left[\Delta\chi(K_j)/\chi(\infty)=\Delta_d-\left(\Delta_H-B\Delta_{e-p}\right)\right]$ counts the contribution from e–p coupling, lattice relaxation, and crystal binding.

### 9.3. Verification

#### 9.3.1. Dielectric suppression

It is possible to discriminate the dielectric contribution of the nanosolid Si backbone from the measured effective $\varepsilon_{eff}$ of p-Si by matching the prediction with the measured impedance spectra. p-Si samples were prepared and their impedance was measured at ambient temperature in the frequency range of 50 Hz–1.0 MHz under 100 mV potential. Silver paste was used for an ohmic contact. The samples were then dried at 353 K for 1 h to make the experimental data reproducible.

The impedance behavior can be described by Debye's formula for a serial-parallel resistor-capacitor (RC) circuit [615] with elements that correspond to the dielectric behavior of different components. The high temperature impedance behavior can be described by a series of triple parallel RC circuit elements [615] that correspond to the dielectric behavior of grain interior, grain boundary and electrode/film interface, respectively, as shown in Fig. 37. The complex impedance response commonly exhibits semicircular forms in the measured Cole–Cole plot [616] as shown in Fig. 38. At higher temperatures, two or more semicircles present corresponding different transition mechanisms [617]. The grain-boundary resistance is normally higher than the grain interior

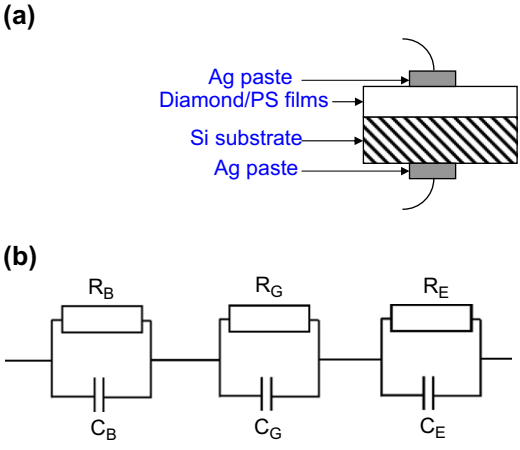


Fig. 37. Effective circuits for the impedance measurement of a sample containing several components.

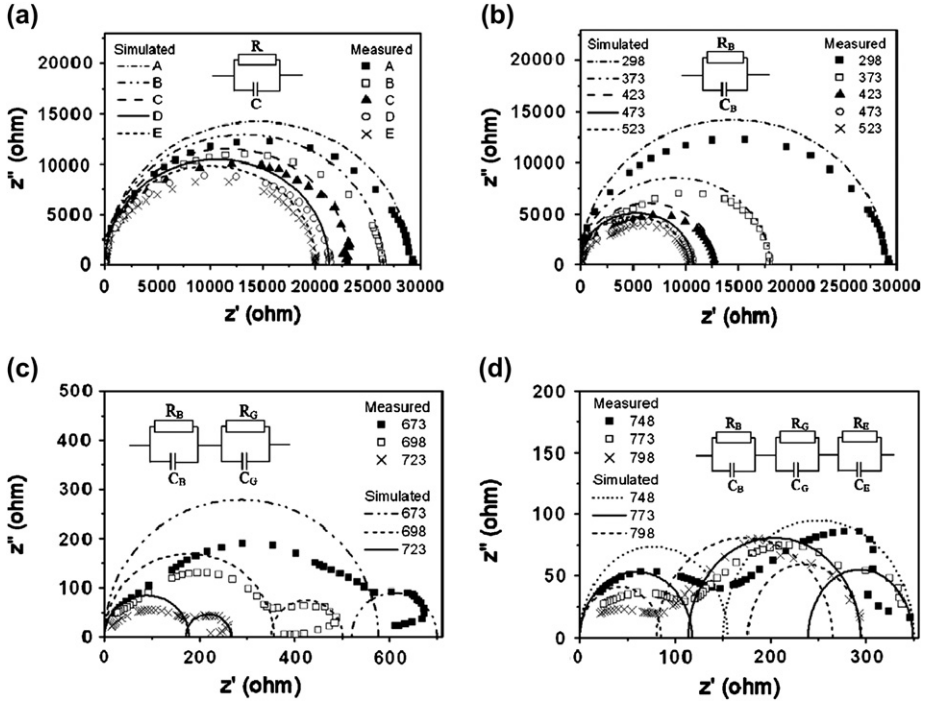


Fig. 38. Simulated and measured (a) size and (b) temperature dependence of Cole–Cole plots of p-Si and the RC parallel circuit model (inset) for typical dielectric materials [612]. The intercepts of the semicircles shift away from the orgion, indicating that solid size reduction or temperature depression increases the nanograin resistance, due to the potential well depression that traps the electrons in the surface skins.

and the electrode/film interface resistance is higher than that of the boundary. The larger radius of the Cole–Cole plot in frequency space corresponds to contribution from a constituent of lower resistance. Therefore, the first semicircle in the high-frequency region can be attributed to the behavior of grain interior while the intermediate and tertiary semicircles in the lower frequency region correspond to the grain boundary and the electrode/film interface, respectively.

The fitting procedure used here is the same as the one described by Kleitz and Kennedy [618]. The complex impedance $Z^*$ measured by RCL meter can be expressed as:

$$\begin{cases} Z^* = Z' - jZ'' \\ Z' = \sum_1 \dfrac{R_1}{1+\omega^2 R_1^2 C_1^2}; Z'' = \sum_1 \dfrac{\omega R_1^2 C_1}{1+\omega^2 R_1^2 C_1^2} \end{cases} \tag{88}$$

where $\omega$ is the angular frequency. The resistance $R_1$ represents ionic or electronic conduction mechanisms, while the capacitance $C_1$ represents the polarizability of the sample from different components labeled l, which are related to grain interior, grain boundary, and electrode or interface [612]. Curves A–E in Fig. 38(a) denote the responses of different samples (Table 15) measured at the ambient temperature. The complex impedance plots show only one depressed single semicircular arc, indicating that only one primary mechanism, corresponding to the bulk grain behavior, dominates the polarization and easy path for conductance within the specimen. The second intercept on the lateral real axis made by the semicircle corresponds

Table 15
Summary of the $D$-dependent $\varepsilon_{\text{nano-Si}}$ derived from the measured $E_{\text{PL}}$, porosity, and $\varepsilon_{\text{eff}}$, p-Si

| Sample | $D$ (nm) | $E_{\text{PL}}$ (eV) | Porosity (%) | $\varepsilon_{\text{eff}}$ | $\varepsilon_{\text{nano-Si}}$ |
|---|---|---|---|---|---|
| A | 1.7 | 2.08 | 85 | 1.43 | 6.27 |
| B | 2.0 | 1.82 | 76 | 1.84 | 7.29 |
| C | 2.1 | 1.81 | 71 | 2.11 | 7.7 |
| D | 2.2 | 1.79 | 68 | 2.28 | 7.86 |
| E | 2.4 | 1.76 | 66 | 2.45 | 8.29 |

to the resistance in the bulk grain. As it is seen, the intercept of the semicircles shifts away from the origin as the solid size decreases, indicating an increase of the nanograin resistance, due to the lowering of the atomic potential well that traps the electrons in the surface region.

The capacitance and dielectric constant is extracted by using the relation: $Z'' = 1/(\omega C)$ from the data measured in the high-frequency range of $10^5$–$10^6$ Hz [619]. The bulk grain capacitance $C$ of the sample is given by the slope of the straight line determined by the variation of $Z''$ as a function of $1/\omega$. Then, the effective dielectric constant $\varepsilon_{\text{eff}}$ of the porous structure is calculated based on the equation $\varepsilon_{\text{eff}} = Cx/(\varepsilon_0 S)$. With the measured $\varepsilon_{\text{eff}}$, we can calculate the $\varepsilon_{\text{nano-Si}}$ based on the Looygenga approximation [620]:

$$\varepsilon_{\text{eff}}^{1/3} = (1-p)\varepsilon_{\text{nano-Si}}^{1/3} + p\varepsilon_{\text{air}}^{1/3}$$

where $\varepsilon_{\text{air}}$ ($\approx 1$) is the dielectric constant of air and $p$ is the porosity of the p-Si. Results in Table 15 show that the $\varepsilon_{\text{nano-Si}}$ decreases with solid size.

Fig. 39(b) compares the $\varepsilon_{\text{nano-Si}}$ derived herein and other sophisticated calculations of nanosolid Si and the third-order dielectric susceptibility of Ag nanodots [605]. Although the dielectric susceptibility does not follow the BOLS prediction, it shows the suppressed trend. Consistency in trends between BOLS predictions and the measured results evidences that the BOLS correlation describes adequately the true situation in which the $\varepsilon_{\text{nano-Si}}$ suppression is dictated by atomic CN imperfection. Other factors may contribute to dielectric suppression, which makes the prediction deviate from measurement compared with other simulations reported in previous sections. The apparent factors are the accuracy and uniformity of the shape

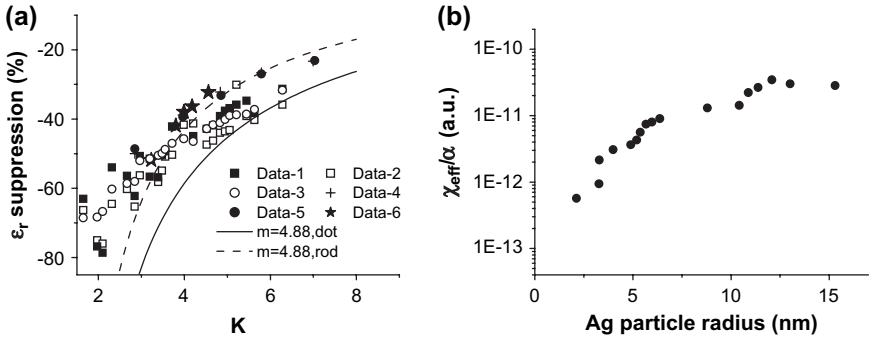


Fig. 39. Comparison of the BOLS predictions with the sophisticated calculation and measurement results on the size-dependent dielectric constants of (a) silicon nanosolids with calculated data-1, 2, 3 [610]; data-4 and 5 [502]; and data-6 [612]; and (b) the third-order dielectric susceptibility of Ag nanosolid [609]. Note that a logarithmic $y$-axis has been used for clarity.

and size of porous Si and the porosity. Atomic CN at a negatively curved surface of a pore is higher than that at the positively curved surface of a dot. As the numerical solution sums the contribution from crystal binding ($E_G$ expansion), electron–phonon coupling, and bond contraction, errors accumulate from the three aspects, contributing to the observed deviation. However, from a physical and chemical insight point of view, the first (main) order approximation would be acceptable as other artifacts from measurement or from impurities are hardly controllable.

### 9.3.2. Blueshift of photoabsorption

The coefficient of photon absorption is calculated based on the following relation:

$$\begin{aligned}\frac{\Delta\alpha(K_j,\omega)}{\alpha(\infty,\omega)} &= \frac{\Delta\varepsilon_r'(K_j,\omega)}{\varepsilon_r'(\infty,\omega)} - \frac{\Delta\varepsilon_r(K_j)}{2\varepsilon_r(\infty)} \\ &= -\left[\frac{\chi(\infty)}{\chi(\infty)+1} + \frac{\alpha' E_G(\infty)}{\hbar\omega - E_G(\infty)}\right]\Delta_H \qquad \text{(convention)} \\ \text{or} \quad &= \left[\frac{\chi(\infty)}{2[\chi(\infty)+1]} - \frac{E_{PL}(\infty)}{\hbar\omega - E_{PL}(\infty)}\right] \times \left(\Delta_H - B\Delta_{e-p}\right) + \frac{\chi(\infty)+2}{2[\chi(\infty)+1]} \times \Delta_d \ \text{(BOLS)}\end{aligned} \tag{87}$$

For Si, $\chi(\infty) = 10.4$ and $E_{PL}(\infty) \sim E_G(\infty) = 1.12$ eV. It is surprising that, as shown in Fig. 40, a blueshift of the absorption edge takes place for the nano-Si. The threshold of absorption for the indirect band gap is slightly higher than that of the direct band gap materials. Such a blueshift of absorption edges should be advantageous in designing devices for optical communication of nanometer-scaled wires, tubes or superlattice structures. The lowered absorption coefficient and refractive index make a nanometer-sized adsorbate more transparent, which may form the basis of quantum lasers, as observed at room temperature from nanostructured ZnO tubes which emit ultraviolet laser at $393 \pm 3$ nm under 355 nm optical excitation [621].

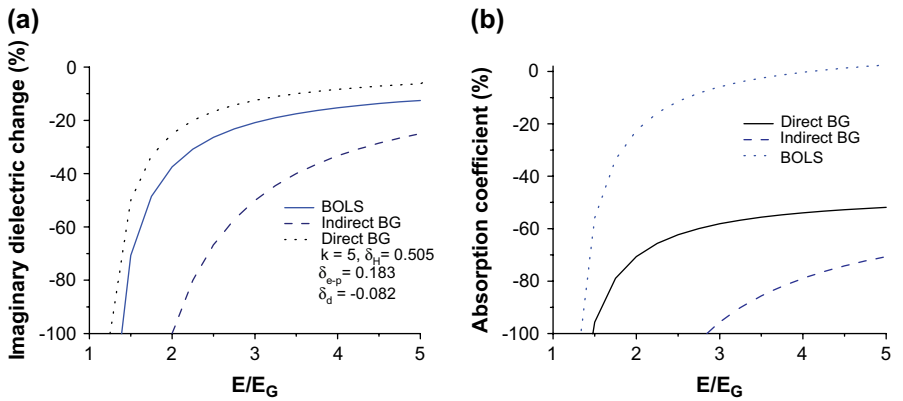


Fig. 40. Energy dependence of (a) imaginary dielectrics and (b) photoabsorption coefficient in conventional and BOLS approaches. Spherical size $K_j = 5$ is used corresponding to $\Delta_H = 0.506$, $\Delta_{e-p} = 0.182$ and $\Delta_d = -0.083$.

### 9.4. Summary

The BOLS correlation has enabled us to derive numerical solutions for the first time to unify the complex dielectric constants and the coefficient of photoabsorption of nanosemiconductors to the often-overlooked event of atomic CN imperfection and its effect on crystal binding and electron–phonon coupling. The solution applies to the whole range of measuring energies. The dielectric constant drops dramatically at the surface edge of the solid due to bond-order loss. This mechanism can be used to trap and amplify light within the nanosolid by internal reflection, which may form a possible mechanism for random lasers. Understanding could be of use in designing photonic crystals with thermal and electrical tunability for optical switches and in fabricating wave guides for light trapping and amplifying device applications [622].

In addition, the BOLS correlation has also allowed us to formulate and understand the dielectric suppression, dispersion, and conductivity and dielectric transition of nanosemiconductors. The effects of temperature and frequency on the dielectric transition and relaxation of nanosolid Si and nanodiamond were also examined, which derives the activation energy for conductivity and dielectric transition of both nanodiamond and nanosilicon, giving information about the impurity midgap states of the corresponding systems. Interested readers may refer to Refs. [612,617].

## 10. Magnetic modulation

### 10.1. Background

#### 10.1.1. Observations

When a ferromagnetic solid is reduced to the nanometer scale, the magnetic properties of the solid will change. For example, the Curie temperature $T_C$ drops [349,623,624] and the coercivity ($H_C$) increases for embedded nanograins; whereas for an isolated nanosolid, the $H_C$ drops [625–628]. Generally, the saturation magnetization ($M_S$) increases at low temperature with quantized features, whereas the $M_S$ drops at ambient temperatures when the solid size is reduced [629–632]. When the size of the ferromagnetic (Pt/Co)–antiferromagnet (FeMn) coupled nanostructure is reduced, the exchange biasing field and the blocking temperature decrease while the $H_C$ increases [633,634]. Fig. 41a and b shows the magnetic oscillation of small Ni and Rh particles at temperatures close to 0 K.

*10.1.1.1. Surface magnetron.* In the case of surfaces and thin films, the magnetic moment of an atom ($\mu_i$) in the surface region is larger than the corresponding bulk value ($\mu_b$) [635,636]. For instance, compared to the bcc Fe bulk moment of 2.2 $\mu_B$, the $\mu$ for a surface Fe atom has been found theoretically to be enhanced by: (i) 15% to 2.54 $\mu_B$ for 1 monolayer (ML) Fe on 5 ML W(110) and (ii) 29% to 2.84 $\mu_B$ for 2 ML Fe on 5 ML W(110) surface. The significant surface relaxation (−12%) of Fe(310) [140] and Ni(210) [141] surfaces has also been found to enhance the atomic $\mu$ by up to 27%. The $\mu_B$ is the Bohr magneton.

*10.1.1.2. Nanosolid at low temperature.* The surface effects become stronger in the case of a nanosolid since a larger fraction of atoms of the system is located at the curved surface. However, controversy remains in the measured trend of the $M_S(K_j)$ values [629–632,637–640]. One trend in measurement shows that at temperatures below 200 K, the $M_S(K_j)$ increases with the inverse of size [640–644]. For example, the $M_S$ per atom of Fe,

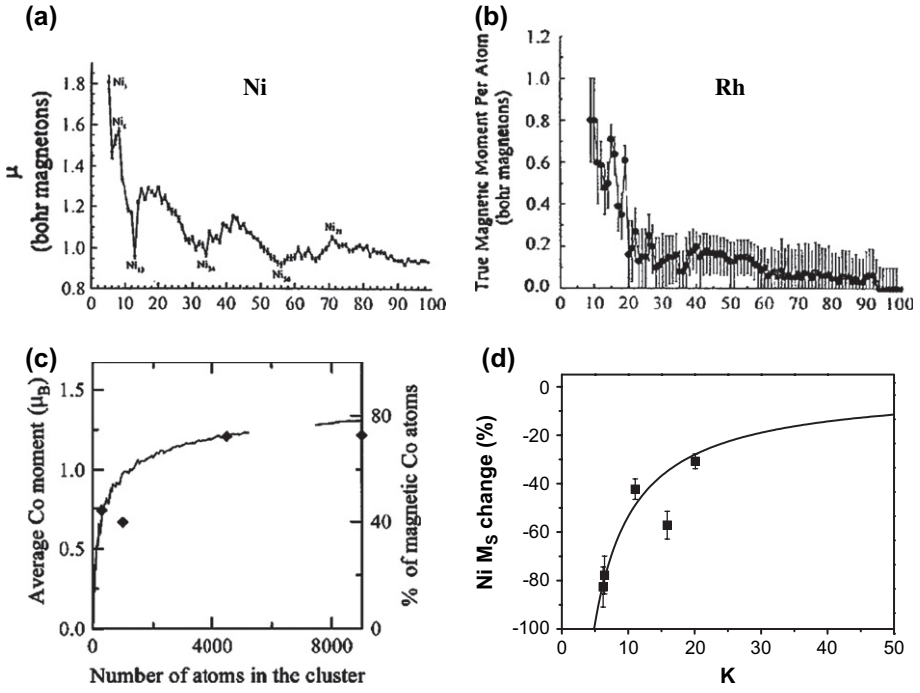


Fig. 41. Size dependence of magnetic moments of (a) $Ni_n$ [647] and (b) $Rh_n$ [648] particles measured at low temperature shows the size-enhanced and quantized $M_S(N_j)$ with oscillating features; (c) cobalt particles [632] and (d) Ni thin films [627] measured at room temperature show size-tailed $M_S(K_j)$, instead.

Co and Ni (at 78–120 K) was measured [644] to increase up to the value of the free atom when the solid size was reduced to a cluster that contains 30 atoms or less. As the size is increased up to 700 atoms, the magnetic moment approaches the bulk limit. The $M_S$ of Ni clusters also increases inversely with size at temperatures between 73 and 198 K [341]. $Co_n$ particles of 1.8–4.4 nm sizes carry magnetic moments that are ~20% higher than the bulk value [341].The moment of a Co surface atom is enhanced by 32% compared to the bulk value of 1.73 $\mu_B$ [645]. In the temperature range of 77–570 K, the $M_S$ of Fe–Ni alloy films increase gradually when the film thickness is decreased from 75 to 35 nm [646]. In a Stern-Gerlach experiment conducted at ~20 K, Cox et al. [638] measured the magnetic properties of isolated iron-atom clusters containing 2–17 atoms and Fe monoxide and dioxide clusters and found that the spin per atom of iron clusters was larger than that of the bulk counterpart. It was therefore widely accepted that size reduction could enhance the magnetization of the small ferromagnetic particles.

*10.1.1.3. Nanosolid at ambient temperature.* Since the observation of Cox in 1985 [638], numerous experiments have been conducted on various ferromagnetic nanosolids. Repeating the same Stern–Gerlach deflections of Fe clusters in a molecular beam, Heer et al. [629] found instead that the average magnetic moments for small iron clusters (50–230 atoms) drops with the number of atoms when the molecular beam nozzle temperatures are around 300 K. This trend is similar to those observed at room temperature of Co [632], $Pd_{96}Fe_4$ [631,630], $Pd_{97.1}Fe_{2.9}$ [631], $NiFe_2O_4$ [23] and $Ni_3Fe$ [637] alloy particles. Similarly, a remarkable reduction of magnetization for Fe–Ni invar alloy (<40 nm) [649] and Ni thin films has been

observed at room temperature [627,650]. The $M_S$ for $Fe_3O_4$ thin films [651] drops rapidly when the film decreases from 70 nm. For $\gamma$-$Fe_2O_3$ nanoparticles, coercivity rises whereas the saturation magnetization drops with increasing particle size [652]. Fig. 41c and d shows the magnetic suppression of Co clusters [632,637] and Ni films. Small $Pd_{100-x}Fe_x$, grains with $x = 4$, 6, 8, 12 and a radius of approximately 5 nm at 4.2, 100, and 295 K show typical superparamagnetic features with $M_S$ values that are substantially smaller than those observed for the bulk [630]. However, for MnBi films [653], the magnetic momentum changes with neither thickness nor chemical composition. Therefore, it was surprising that some measurements give conflicting data and show magnetic elevation whereas some show suppression without taking the operating temperature into consideration.

*10.1.1.4. Coercive performance.* An isolated magnetic domain or highly dispersed ones often show no hysteresis at any temperature. When the size of an isolated ferromagnetic solid is reduced to a certain critical size, the coercivity of the isolated nanosolid will approach zero [654]. $Fe_{69}Ni_9CO_2$ powders of 10–15 nm grain sizes show almost no hysteresis, being indicative of superparamagnetic characteristics [655]. However, when the particles get closer together, the superparamagnetic behavior vanishes and the coercivity is present [654,656]. The coercivity increases with the inverse of grain size, which follows a $H_C \sim 1/K_j$ relation [626,654,657]. Investigation on the $Fe_{74.5-x}Cu_xNb_3Si_{13.5}B_9$ ($x = 0$–1 at.%) ribbons with grain sizes between 10 and 300 nm suggests that the $H_C$ increases following a $K_j^6$ dependence and then drops in a $1/K_j$ fashion at the critical size of 50 nm. A similar trend of transition has been observed for Fe, Ni, and Co metal films, with corresponding critical sizes of 20, 40, and 30 nm [658]. Fig. 42a shows the size-enhanced $H_C$ of Ni thin films consisting of 3–10 nm grains. Panel b shows the CN imperfection enhanced magnetization of Ni, Fe, and Co particles and panel c the Monte Carlo simulated $M_S(T, N_j)$ profiles [659].

### *10.1.2. Possible mechanisms*

*10.1.2.1. Magnetization.* A number of outstanding theories have been developed to explain the unusual behavior of ferromagnetic nanosolids, in particular the oscillatory behavior at low-$T$ (see Fig. 41a, b) [640,644] and the inconsistent trends of $M_S$ measured at different temperature ranges. Several shell structural models have been proposed for the size-enhanced magnetization [644,661] and suggested that the magnetic moment of an individual atom is determined by its atomic CN [661]. By assuming bulk-like structures (such as fcc and bcc) and different global cluster shapes (cube, octahedron, cube octahedron), the average magnetic moment was found to oscillate with the cluster size, coinciding with observations. Therefore, the magnetic ''shell structure'' reflects the progressive formation of concentric atomic layers [662].

Without considering the effect of temperature, the magnetic properties of transition metals are described by using a simple rectangular d-band approximation [642] together with the second-moment approximation, as the first-order approximation [663]. It was assumed that the d-band splitting between the major and the minor spin caused by exchange interaction is invariant for the cluster to the bulk solid, leading to the following expression [636]:

$$\frac{\mu_i}{\mu_b} = \begin{cases} \mu_{dim}/\mu_b, & \text{if} \quad z_i \le z_b(\mu_b/\mu_{dim})^2 \\ (z_b/z_i)^{1/2}, & \text{otherwise} \end{cases} \tag{89}$$

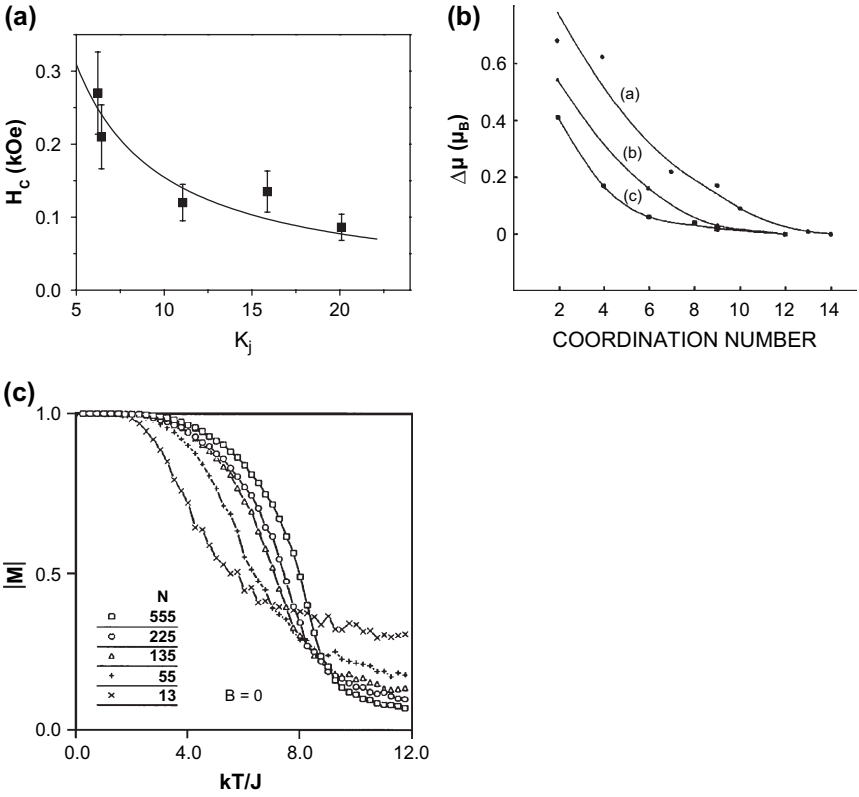


Fig. 42. (a) Size-enhanced $H_C$ of Ni films [627] measured at room temperature and (b) CN dependence of the magnetic moment in (a) Fe, (b) Co, and (c) Ni as a function of nearest-neighbor coordination (in various structures) [660]. (c) Monte Carlo simulated $M_S(T, N_j)$ profiles [659].

where $\mu_{dim}$ is the magnetic moment of one atom with one neighbor [659]. In the case of Fe, $\mu_b = 2.22\ \mu_B$ [115] and $\mu_{dim} = 3.2\ \mu_B$ [660]. If $z_b = 12$, the step function transits at $z_i = 5.775-6$. The magnetic moment of an atom will take the dimer value if its CN is 6 or less. Considering the geometrical arrangement of atoms in different lattice structures of various shapes, the oscillation features could be reproduced using the shell structure [636,664]. Calculations using the tight-binding theory [660] also show that the magnetic moment of Fe, Co, and Ni atoms increases towards the atomic value when the CN is reduced, as shown in Fig. 42b.

The $M_S$ suppression at mid-$T$ was explained with the following mechanisms:

(i) Surface spins are weakly coupled and more disordered at ambient temperatures compared to the bulk spins. The magnetization is then dominated by the interior bulk spins that drop in number when the solid size is decreased [665].
(ii) $T_C$ suppression of the nanosolid lowers the $M_S$. In the shell structure, the surface layer is magnetically molten, which contributes little to the total $M_S$ of the system [659].
(iii) The anomalous behavior of $Fe_3O_2$ was explained in terms of the redistribution of $Fe^{3+}$ ions, depending on the particle size [652]. The increase of coercive field with decreasing

particle size was also attributed to the lattice strain that increases with the decrease of particle size [666].

(iv) In contrast, Monte Carlo simulations, as shown in Fig. 42c, suggest that the $M_S$ of a small cluster is never higher than the bulk value due to the reduction of exchange bonds of the surface atoms. Based on an assumption that the clusters undergo a super-paramagnetic relaxation, Khanna and Linderoth [667] derived that the effective $M_S$ of small Fe and Co clusters decreases with size, which was explained as a consequence of fluctuations due to thermal vibration and rotation effects on the domain when considered as a giant spinner.

*10.1.2.2. Coercivity.* It is known that both the inter-spin interaction within a domain and the inter-grain interaction within a solid composed of nanograins can be described using the same Ising model, or other approaches such as the mean field approximation as well. We prefer using the Ising model, as it is sufficient for the first-order approximation. Considering a domain as a giant spinner with a moment $J$, the exchange energy of the spinner ($E_{exc,i}$) interacting with its $z$ nearest giant spin neighbors follows the Ising relation. The $d_i$ is then replaced with grain diameter, $D_j$ (also structural correlation length), if uniform grain size is assumed. The $H_C(D_j)$ transition from $D_j^6$ to $D_j^{-1}$ can be expressed as [668]:

$$H_C \sim \frac{1}{20}\frac{K_2^4 D_j^6}{A^3 M_0} \Rightarrow H_C \propto \frac{1}{2} H_S \propto E'_{exc} \propto z D_j^{-1}$$

where $K_2$ is the strength of local uniaxial anisotropy, $M_0$, the magnitude of the local magnetization vector and $A$ is the exchange stiffness parameter. The former corresponds to the random anisotropy mechanism of domain-wall pinning at grain boundaries; the latter relates herewith to the inter-grain and grain–substrate interaction, which dominates the anisotropy energy [668].

A model is highly desirable to reconcile the size and temperature dependence of $M_S(K_j, T)$ and the $M_S(K_j \sim 0, T \sim 0)$ oscillation in experimental and theoretical observations. Here we show that incorporating the BOLS mechanism to the Ising model could reproduce all the observed trends using MC calculations and hence reconcile the discrepancy in the unusual magnetic behavior of a ferromagnetic nanosolid of different shapes and crystal structures at different temperatures.

## 10.2. BOLS consideration

### 10.2.1. Charge localization

The CN imperfection-enhanced bond energy deepens the atomic trapping potential well of the under-coordinated atom from one unit to $c_i^{-m}$. Electrons inside the trap are then more localized. If the localization probability is proportional to the trapping well depth, then the densely localized electrons contribute to the $\mu_i$ of the under-coordinated atom. The corresponding change of the mean $\mu(K_j)$ varies monotonically with the coefficient of bond contraction:

$$\begin{cases} \mu_i(z_i) = c_i^{-m}\mu_b \\ \dfrac{\Delta\mu(K_j)}{\mu_b} = \sum_{i\le 3} r_{ij}\left(c_i^{-m} - 1\right) \end{cases} \tag{90}$$

The effective magnetic momentum along the applied field direction of a $z_i$ coordinated atom is $\mu_{iz} = Jg_J\mu_B$. Note that the Lande $g$-factor ($g_J = 1-2$) is a function of the orbital ($L$) and spin ($S_p$) angular momentum: $g_J = 1 + [J(J+1)+S_p(S_p+1)-L(L+1)]/[2J(J+1)]$, which is also affected by the CN imperfection. However, in the first-order approximation, we neglect this effect that may influence the precision of $m$ parameterization. For a dimer Fe atom ($z_i = 2$, $c_i \sim 0.7$), $\mu_i = 0.7^{-1}$, $\mu_b = 3.25\,\mu_B$, which is 1.43 times the bulk value, agreeing with measured value of $\mu_{dim} = 3.2\,\mu_B$. Compared with the model given in Eq. (89), here we use a smooth function rather than a step transiting at $z_i \sim 6$, in spite of the difference in physical origin. As the effective CN of an atom at a flat or a curved surface is 4 or lower, the BOLS premise predicts a $0.88^{-1} = 112\%$ or higher magnetic enhancement of a surface atom at 0 K, agreeing with theoretical predictions [141,139]. Therefore, it is reasonable to suggest that it is the very atomic CN imperfection deepened atomic potential that traps the electrons with high probability of localization to contribute to the $\mu_i$ of the undercoordinated atom. By taking the effect of atomic CN imperfection and the pronounced portion of surface atoms into consideration, the magnetic properties of the ferromagnetic nanosolids should differ from those of the bulk.

*10.2.2. Brillouin function*

The inter-spin interaction dominates the order of the spin system and hence the $M_S$ and $T_C$. At low temperatures, the total angular moment of an atom changes its direction in a quantum tunneling process [669]. At higher temperatures, the spin direction will fluctuate due to thermal agitation. The easiness of fluctuation is determined by the strength of inter-spin coupling that varies with atomic CN as well. Because of fluctuation, the magnetic momentum will reduce and eventually vanish at the $T_C$. In the first-order approximation to the size and temperature dependence of the $\mu_S(T, K_j)$, we use the concept of ''molecular field'' [666], to describe the spontaneous magnetization at $T$ in terms of Brillouin function, $B_J(y)$:

$$\begin{cases} \mu(T) = g_J J \mu_B B_J(y) \\ B_J(y) = \dfrac{2J+1}{2J}\coth\dfrac{2J+1}{2J}y - \dfrac{1}{2J}\coth\dfrac{y}{2J} \\ y = \dfrac{Jg_J\mu_B}{k_B T}H_m \end{cases} \tag{91}$$

where $g_J$ is the Lande's $g$-factor, $J$ is the total angular momentum and $E_{exc} \sim E_{coh}$ is the molecular field. When $T$ approaches $0.8\,T_C$, $\mu(T) \approx \mu_S(T)$ [670]. Therefore, the $\mu_S(K_j, T)$ can be obtained by replacing the bulk $J$ and $H_m$ with the size-dependent $J(K_j)$ and $E_{exc}(K_j)$ that are given as:

$$\begin{aligned} E_{exc}(K_j) &= E_{exc}(\infty)\left[1 + \sum\nolimits_{i\le 3}\gamma_{ij}\left(z_{ib}c_i^{-m} - 1\right)\right] \\ J(K_j) &= J\left[1 + \sum\nolimits_{i\le 3} r_{ij}\left(c_i^{-m} - 1\right)\right] \end{aligned} \tag{92}$$

Differentiating Eq. (91) against $E_{exc}(K_j)$ leads to the size and temperature dependent $\mu_S(K_j, T)$:

$$\frac{\Delta\mu_S(K_j,T)}{\mu_S(\infty,T)} = \left\{\frac{1}{2J}\mathrm{csch}^2\left[\frac{2g_J\mu_B}{2k_BT}AE_{exc}(\infty)\right] - \frac{2J+1}{2J}\mathrm{csch}^2\left[\frac{(2J+1)g_J\mu_B}{2k_BT}AE_{exc}(\infty)\right]\right\} \times \frac{\Delta E_{exc}(K_j)}{E_{exc}(\infty)} = \alpha(T)\sum_{i\le 3}\gamma_i\left(z_{ib}c_i^{-m}-1\right) \quad (93)$$

parameter $\alpha(T)$ is also material dependent. Eq. (93) indicates that for a specific ferromagnetic solid and at a given temperature, the $\mu_S(K_j, T)$ changes with the atomic cohesive energy. One needs to note that Eq. (93) does not apply to an isolated atom without exchange interaction being involved though the isolated atom possesses intrinsically higher magnetic momentum.

### *10.3. Verification*

#### *10.3.1. Ni films at ambient temperature*

Ni films with grain sizes in the range of 3–10 nm were grown on Si(100) substrates using physical vapor deposition. The grain size was calibrated using XRD profiles and Scherrer's equation. The in-plane magnetic properties were measured using vibrational sample magnetometer at room temperature [627].

Figs. 41d and 42a compare the predicted (with $m = 1$) and the measured size dependence of the $M_S$ and the $H_C$ for the Ni films. The match of $M_S(K_j)$ at 300 K is realized with $\alpha(J, T) = 4.0$. When the particle size is reduced to $K_j = 5$ ($D_j = 2.5$ nm), $M_S = 0$. This result is consistent with the findings of the size induced $T_C$ suppression of ferromagnetic nanosolids, as discussed in Section 5.3.3. For a Ni particle of $K_j = 5$, the $T_C$ drops by $\sim$ 51% from 631 K to 309 K and the $M_S$ is not detectable [623] (Fig. 43).

#### *10.3.2. Monte Carlo simulation*

In order to examine the model consideration, Monte Carlo simulation was carried out based on the BOLS incorporated Ising convention in comparison with the modified Brillouin function. The atomic CN imperfection enhanced magnetic moment was taken into consideration by varying the spin value $S_i'$ for each atom. We employed six kinds of nanosolids to investigate the size, shape, and crystal structure effects on the $\mu_S$ at various temperatures. The fcc spherical dots are formed in such a way that layers of successive atoms are added to the initial central atom. Fig. 44a shows, for example, the fcc spherical dot containing $N_{141}$ atoms with $S = 9$ shells and $K_j = 3.3$ atomic size. Here we only consider those clusters with completely closed outermost shells as a convention. The rod and the plate systems are also formed based on the fcc lattice along the ⟨100⟩ direction. The length of the rod is maintained at $K_j = 28.3$ and variation of this has an insignificant effect on the result. The radius of the rod ranges from $S = 1$ to 11 ($K_j = 0.5$–$3.66$). The width and length of the plate are maintained at $K_j = 28.3$. The thickness ranges from $S = 1$ to 14 ($K_j = 0.5$–$5.1$). Fig. 44b and c illustrates an fcc rod and plate with $S = 3$, $K_j = 1.9$ and $S = 2$, $K_j = 1.7$, respectively.

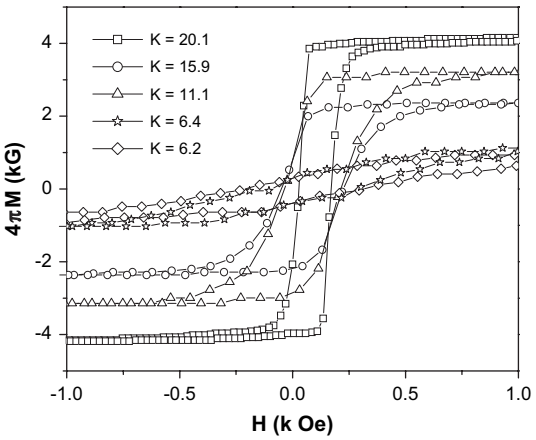


Fig. 43. The magnetic hysteretic loops of Ni films of different grain sizes measured at room temperature [627].

Calculations were also conducted using the ordered structures of icosahedra, decahedra and the close-packed fcc truncated octahedra that are favored from the energetic point of view. Fig. 44d–f show the close-packed structures with a total number of $N_{101}$, $N_{147}$, and $N_{201}$ atoms, respectively. Icosahedra and decahedra are noncrystalline structures that cannot be found in bulk crystals because of the fivefold symmetry. Icosahedra are quasispherical, where atoms are arranged in the concentric shells. Marks-truncated decahedra have reentrant (111) facets that are introduced via a modified-Wulff construction. Fcc truncated octahedra possess a crystalline structure and have the open (100) facets.

To compute effectively, we use cool state initialization at low temperature ($k_BT/J_{exc} < 6$) and hot state initialization at relatively high temperature ($k_BT/J_{exc} \geq 6$) [120]. In the hot state, spins orientate randomly; and in the cool state, spins align parallel to the applied magnetic field. For a certain spin system, the value of the Hamiltonian $H_{ex,k-1}$ was calculated. A spin $S_i'$ was chosen randomly and the orientation was flipped from $S_i'$ to $S_{i,trial}$. The $H_{ex,k}$ was optimized to satisfy the Metropolis criterion [671]:

$$\begin{cases} \exp(-\Delta H_{ex}/kT) > \delta_{mc} \\ \Delta H_{ex} = H_{ex,k} - H_{ex,k-1} \end{cases}$$

$\Delta H_{ex}$ is the energy change for a spin reorientation and $\delta_{mc}$ is a uniform random deviate. After several MC steps of sweeping over all lattice sites of the spin system, the spin system of a specific size at a specific temperature reaches thermal equilibrium. In simulation, each atom is taken as an independent spin with $\mu_i$ in unit of the bulk $\mu_b$. For the bulk value, $S$ takes the values of $+1$ or $-1$ for the up and down flip. The energy change is calculated for the spin flip from $k-1$ to $k$ step due to thermal vibration: $\Delta H_{ex} = H_{ex,k} - H_{ex,k-1}$. At a given temperature, the system will reach a stable state after sufficient steps of operation. The magnetization is then calculated as $\langle M \rangle = [\sum_N M(s_1^{(i)}, s_2^{(i)}, \ldots s_N^{(i)})]/N$ with 5000 thermalization steps for each spin to reach thermal equilibrium state.

Fig. 45 shows the MC simulated $M_S(K_j, T)$ curves at zero applied magnetic field for an (a) fcc dot, (b) fcc rod, (c) fcc plate and (d) icosahedra spin system. Generally, at a very

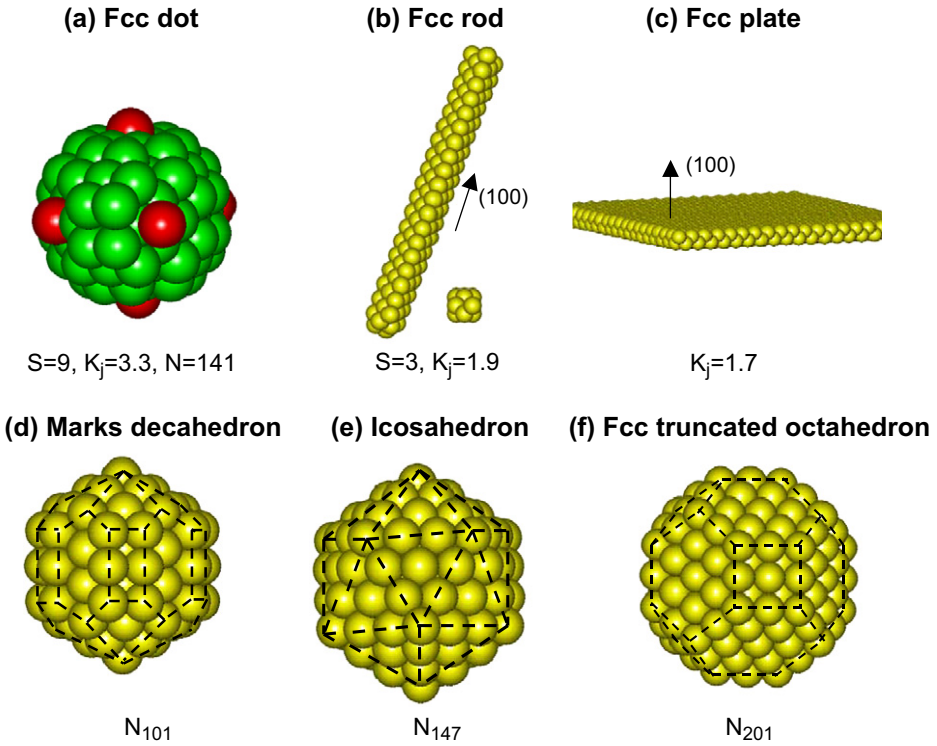


Fig. 44. Illustration of atomic configurations of (a) an fcc dot of nine shells with $K_j = 3.3$, (b) an fcc rod of three shells with $K_j = 1.9$, and (c) an fcc plate of $K_j = 1.7$ thickness, (d) an icosahedron with $N_{147}$ atoms, (e) a Marks decahedron with $N_{101}$ and (f) an fcc truncated octahedron with $N_{201}$ atoms [120].

low temperature region ($k_BT/J_{exc} < 3$), the $M_S(K_j, T)$ increases with oscillatory features as the solid size is reduced. At mid-$T$ region ($k_BT/J_{exc} \sim 6$), the $M_S$ drops with size. In the paramagnetic region, the residual $M_S$ increases as the size is reduced. These features are intrinsically common depending less on the shape and the crystal structure of the specimen. Fig. 46 shows the BOLS predicted $M_S(K_j, T)$ counterplot for a spherical dot. No oscillatory features are given as the smooth function for the surface-to-volume ratio was employed.

*10.3.2.1. $M_S(K_j, T \sim 0\ K)$ enhancement.* It is seen from Fig. 45a that for a specific size $K_j$, the $M_S$ of the fcc dot is higher than that of the fcc plate because a spherical dot has higher $\gamma_{ij}$ value. It is understood that when $T \to 0$, $y \to \infty$, and then $B_J(y) \to 1$, Eq. (91) can then be approximated as $\mu_S(T \to 0) = Jg_j\mu_B$. Using a shell structure in the BOLS correlation that calculates the magnetic moment of every atom layer-by-layer leads to the size-enhanced $M_S$ for a nanosolid at very low temperature, which follows Eq. (90).

Fig. 47 compares the BOLS predictions with the measured low-temperature $M_S(K_j)$ of Fe, Ni and Co particles [644]. As the measured data are much scattered, it is hard to reach a conclusion though the trends generally match; however, the close match of $T_C(K_j)$ suppression and lattice contraction, as shown earlier in this report evidences sufficiently the validity of the BOLS correlation as the origin of the unusual magnetic behavior of the ferromagnetic nanosolids at different temperatures.

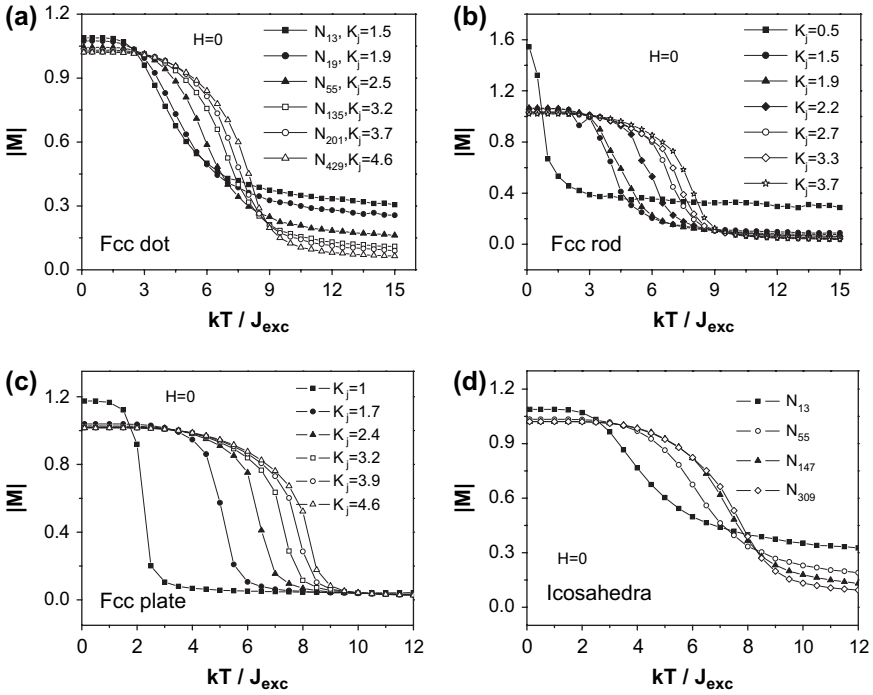


Fig. 45. MC simulated temperature and size dependence of the $M_S$ for an (a) fcc dot, (b) fcc rod, (c) fcc plate and (d) icosahedral spin system.

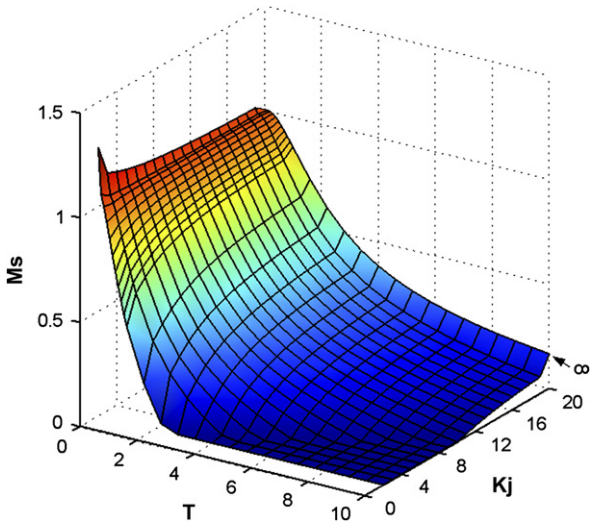


Fig. 46. Counterplot of the BOLS predicted $M_S(T, K_j)$, which shows that $M_S$ increases with inverse size at low temperature and decreases with size at mid-temperature. The $M_S$ is normalized by $M_S(T=0, K_j=\infty)$ and $T$ is normalized by $AE_{exc}(\infty)$.

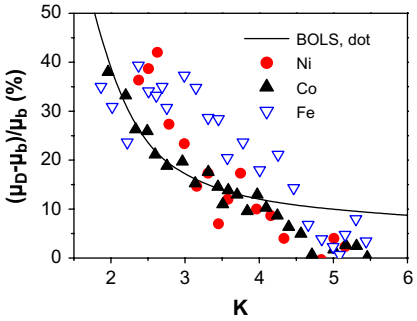


Fig. 47. Comparison of BOLS predictions with measured size dependence of $M_S$ at low $T$.

*10.3.2.2. $M_S(K_j, T \sim T_C)$ suppression.* Fig. 48b shows the matching between predictions with $\alpha(J, T) = 1.4$ and the MC simulated results at mid-$T$. The calculated trend is consistent with the measurement with $\alpha(J, T)$ value that is different from Ni sample. The calculation takes the surface CN to the half number of the bulk (12) but in the BOLS premise, the effective surface CN is 4 or less. In the paramagnetic phase as shown in Fig. 48c, the

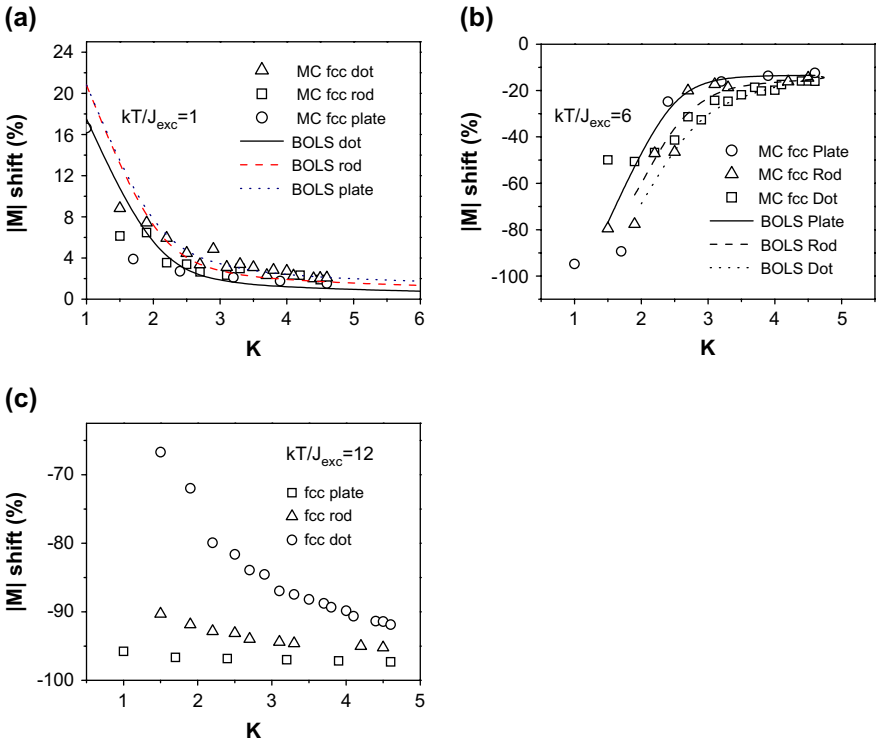


Fig. 48. Size dependence of the $M_S$ at temperature (a) $k_BT/J_{exc} = 1$, (b) $k_BT/J_{exc} = 6$ and (c) $k_BT/J_{exc} = 12$ for fcc nanosolids shows three outstanding regions, where $|M|$ shift $= [|M|(K) - |M|(\infty)]/|M|(\infty) \times 100\%$.

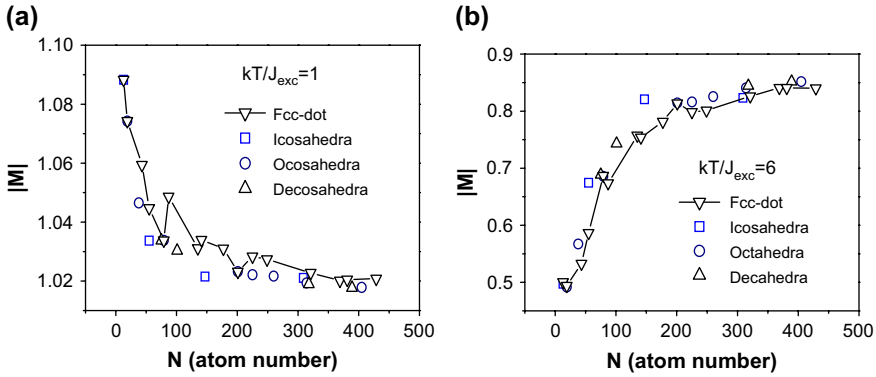


Fig. 49. Magnetic oscillation features of different crystal structures at different temperatures.

remnant magnetism is higher for smaller particles, which has been attributed to the slower temperature decay in the MC study and to the increasing fluctuations with decrease in cluster size [659].

*10.3.2.3. $M_S(K_j)$ oscillation and structural stability*. The oscillation behavior of $M_S$ at smaller sizes, as shown in Fig. 49, depends less on the crystal structures. This relation suggests that the oscillatory originates from the surface-to-volume ratio because some particles may have fewer atoms at the surface with smaller $\gamma_{ij}$ value than those of the adjacent larger or smaller sizes, as illustrated in Section 2 for the fcc and bcc structures [647]. Therefore, it is not surprising to resolve the $M_S$ oscillation in the low temperature measurement of smaller nanostructures with quantized surface-to-volume ratios.

The physical properties of nanosolids in molecular regime typically exhibit a very irregular dependence on their aggregate size, namely, magic numbers, while they behave in a regular way in the mesoscopic regime. The icosahedron, Marks-decahedron, and the fcc truncated-octahedron have lower $M_S$ in the low-$T$ region, especially, the small icosahedral particles of $N_{55}$ and $N_{147}$ atoms, compared to other structures. An icosahedron has fewer low-CN atoms at the surface with most compact structures. The mass spectra of nanosolids usually exhibit especially abundant sizes that often reflect particularly stable structures, especially reactive nanosolids, or closed electronic shells [672]. These ''magic number'' sizes are of theoretical interest since many of them correspond to compact structures that are especially stable. The simulative results presented herein show the magic numbers of $N_{13}$, $N_{55}$, $N_{147}$ for icosahedron magnetic nanoparticles [643]. However, when the $N$ is larger than 300, the fcc truncated-octahedron is magnetically most stable compared with the decahedra, icosahedra and the fcc spherical dot. The MC simulation results here are consistent with experimental findings that the icosahedral structure transits at $\sim$3.8 nm to the fcc truncated structure when the particle size is increased [673]. The competition between the surface energy reduction and the strain energy enhancement determines the structural stability. Therefore, icosahedra are the most stable at small sizes due to their low surface energy and good quasispherical structures, while decahedra are favorable at intermediate sizes, and regular crystalline structures are favored for large objects.

### *10.4. Summary*

Incorporating the BOLS correlation to the Ising premise and the Brillouin function, we have conducted the MC simulations, and BOLS predictions to examine the size, shape, structural and temperature dependence of the magnetization of ferromagnetic nanosolids with experimental verification. MC simulations and BOLS predictions have produced all the observable features at various temperatures, including the oscillatory ones with clear physical insight into the origin of the changes. Conclusions may be drawn as follows:

(i) For a ferromagnetic nanosolid, the magnetic moment at very low temperature increases with the inverse of size compared with the bulk value due to the deepening of the intra-atomic potential well that trap the surface charges contributing to the angular momentum of the under-coordinated atoms of a nanosolid.
(ii) The $M_S$ at temperature around $T_C$ reduces, which is dominated by the decrease of exchange energy that dominates the thermal stability of a nanosolid.
(iii) The oscillation of $M_S$ with the change of the total number of atoms arise from nothing more than the surface-to-volume ratio of the solid.
(iv) The $H_C$ is dominated by inter-grain interaction.
(v) Structure transition from icosahedron to fcc truncated-octahedron happens at size containing 300 atoms, which is common to observations using other means.

Consistency in the MC calculations, BOLS predictions and experimental observations clarifies for the first time the long-standing confusion on magnetic behavior of a ferromagnetic nanosolid at various temperatures. The joint contribution from the CN imperfection and the associated bond energy rise lowers the exchange energy that tailors the temperature of phase transition. Therefore, it is not surprising that some measurements show the enhanced $M_S$ at low temperature while some observed the tailoring of the $M_S$ at temperatures close to the $T_C$ [674–676].

## 11. Concluding remarks

### *11.1. Attainment*

As demonstrated, the impact of the often-overlooked event of atomic CN imperfection is indeed tremendous, which has enabled us to view the performance of a surface, a nanosolid and a solid in amorphous state consistently in a way from the perspective of bond relaxation and its consequences on bond energy. Progress made can be summarized as follows:

(i) The unusual behavior of a surface and a nanosolid in mean lattice contraction [677,678], mechanical strength [679], phase transition, thermal stability, acoustic and optical phonons, optoelectronics, magnetism, dielectrics [680], and chemical reactivity [681] has been consistently predicted and experimentally verified with formulations depending on atomic CN imperfection and its consequences.
(ii) Most encouragingly, single energy levels of *isolated* Si, Pd, Au, Ag and Cu atoms and their shift upon bulk and nanosolid formation have been quantified by matching

predictions to the observed size-and-shape dependence of the XPS data. This attempt enhances in turn the capability of the XPS, providing an effective way of discriminating the contribution from intra-atomic trapping from the contribution of crystal binding to the specific electrons. Attainment is beyond the scope of a combination of XPS and laser cooling that measures the energy level separation of the slowly moving atoms/clusters in gaseous phase [682].

(iii) Quantitative information about dimer vibration [683] and e–p interaction has been elucidated by matching predictions to the measured shape and size dependence of Raman and photoemission/absorption spectra of Si and other III–V and II–VI compounds. The CN imperfection of different orders unifies the phase stability of ferromagnetic, ferroelectric and superconductive nanosolids. In conjunction with the previous bond-band-barrier correlation mechanism, the present approach allows us to distinguish the extent of oxidation [684] and contribution of surface passivation [685] to the dielectric susceptibility of porous silicon.

(iv) The bonding identities such as the length, strength, extensibility, and thermal and chemical stability [686], in metallic monatomic chains (MCs) [687], and in the CNTs have been determined. Understanding has been extended to the mechanical strength and ductility of metallic nanowires, and the inverse Hall–Petch relationship that shows the mechanical strength transition from hard to soft in the nanometer regime.

(v) In combination with the bond-band-barrier correlation for chemical reaction, the BOLS premise has also enabled us to discriminate the extent of oxidation and the effect of fluorine passivation on the performance of nanostructured silicon. The latter two topics would form the subject of nanometrology, and further pursue is in progress.

The significance of the approach is that it covers the whole range of sizes from a dimer bond to the bulk solid and covers the states of surface, amorphous, and nanosolid of various shapes to bulk solid with defects inside, with few adjustable parameters and almost no assumptions. Almost all of the imaginable and detectable quantities are consistently related to the BOLS correlation and the population of the under-coordinated atoms as well. For instance, the surface energy, interfacial energy, surface stress, the local mass density of liquid and solid are all functions of atomic separation and bond energy that are subject to the effect of atomic CN imperfection. The difficulties encountered by other theories in describing the photoluminescence blueshift at the lower end of the size limit and the melting point oscillation over the whole range of sizes have been completely resolved. The parameters involved are just the bond nature represented by the parameter $m$ and the corresponding bulk values of quantities of concern, which are independent of the particularity of element, crystal structures, or the form of interatomic potentials.

Consistency between the BOLS prediction and the measurements evidences not only the essentiality and validity of the BOLS correlation premise but also the significance of atomic CN imperfection to the low-dimensional and disordered systems that are dominated by atomic CN deficiencies. Understanding gained insofar should be able to help us in predicting nanosolid performance and hence provide guidelines in designing process and fabricating materials with desired functions.

### *11.2. Limitations*

One may wonder that there is often competition between various origins for a specific phenomenon. As demonstrated in the context, the atomic CN imperfection affects almost

all the aspects of concern, and therefore, the atomic CN imperfection should dominate the performance of a nanosolid through the competition factors. For instance, the atomic cohesive energy dictates the phase transition or melting while the binding energy density dominates angular momentum and mechanical strength. These two competition factors determine the unusual behavior of a nanosolid in magnetism and mechanical strength under various conditions.

One may also wonder about the effect of impurities such as surface oxidation on the measurement. Although XRD and XPS revealed no impurities in the Ni samples, for instance, we cannot exclude the existence of trace impurities. However, if all the samples were prepared and measured under the same conditions and we use the relative change of the quantities, artifacts caused by impurities should be minimized, and the results are purely size dependent.

The BOLS premise does not apply to the so-called dangling bond, as a dangling bond is not a real bond that forms between two neighboring atoms. It is true that the concept of localized bond is not applicable to metallic systems due to the demoralized valence electrons whose wave function often extends to the entire solid. However, the demoralized valence electrons are often treated as a Fermi sea and the metal ions are arranged regularly in the Fermi-sea background. As a standard practice, the metallic bond length corresponds to the equilibrium atomic separation and the bond energy is defined as the division of the atomic cohesive energy $E_B$ by the atomic CN in a real system. For the tetrahedral bond of diamond and Si, the full CN is not 4 as the tetrahedron is an interlock of fcc structures. Therefore, the BOLS premise is valid for any solid disregarding the nature of the chemical bond. The pair interatomic potential for metallic interatomic interaction also holds, as the pair potential represents the resultant effect of various orders of coordination and the charge-density distribution. DFT calculations on the dimer bond contraction and bond-strength gain of Ni, Cu, Ag, Au, Pt and Pd evidence sufficiently the validity of the current BOLS correlation for metallic systems.

Stimuli in measurement may affect the data acquired. For example, in mechanical strength detection, the stress–strain profiles of a nanosolid may not be symmetric under tension and compression, and the flow stress is strain rate, loading mode, and materials' compactness as well as size distribution dependent. However, one could not expect to cover the fluctuations of mechanical (strain rate, stress direction, loading mode, etc.), thermal (self-heating during process and electron bombardment in TEM), crystal structure orientation, or grain-size distributions in a theoretical model, as these fluctuations add random artifacts that are hardly controllable. These effects can be minimized in the present approach by using relative changes that are intrinsic in physics.

As the current approach is the first (but main) order approximation, there is still plenty of room for improvement by involving other high-order effects that contribute to the physical properties. If counting atom-by-atom in a specific crystal structure, the theoretical curves at the lower end of the size limit should show oscillation features with ''magic number'' of atoms due to the surface-to-volume ratio. For illustration purpose, it would be adequate to employ the smooth function for the surface-to-volume ratio in the present approach, as one should focus, in the first place, on the nature, trend, origins, and limitations for the size-induced changes and to grasp with factors controlling the property change.

It should be emphasized that all the models mentioned in the context are successful from different physical perspectives, and with the BOLS correlation as complementary origin, they would be complete and in good accordance.

### 11.3. Prospectus

Although the imaginable and detectable quantities of a nanosolid have been preliminarily formulated and verified with experimental measurements in terms of the BOLS correlation, there are still more exciting challenges ahead of us:

(i) Further attention is needed to address the joint effect of physical size and chemical reaction. At an interface, no significant CN imperfection is expected but chemical bonds may evolve when an alloy or compound is formed. The chemical effect alters the nature of the bond while the physical size causes the bond contraction. Both will modify the atomic trapping, crystal binding, electron–phonon coupling, which should be the origin for the detectable physical properties of a solid including transport properties. Switching between superhydrophilicity and superhydrophobicity of chemically treated nanostructure could be a successful sample for the joint effect of the BOLS and BBB promises.

(ii) Traditional practice in theoretical calculations may be subject to modification at the lower end of the size limit to involve the effect of CN imperfection. Consideration of the real boundary conditions with atomic CN imperfection instead of the ideal periodic boundary conditions would be necessary. As demonstrated, the atomic CN imperfection and the large portion of surface/interface atoms play key roles in determining the performance of small structures. Recent tight-binding potential MD calculations of tetrahedron carbon (t-C) graphitization by Zheng et al. [688] reveal that the graphitization of t-C cluster with hundreds of atoms happens at a temperature that is 10% higher than that measured (1100–1200 K). A first-principle calculation [689] predicted that the hardness of the optimal $BC_2N$ structure is lower than the measured extreme hardness of $BC_2N$ nanocomposites. It is suggested that the effects of the nanocrystalline size and the bonding with the amorphous carbon matrix in $BC_2N$ nanocomposites likely play a crucial role in producing the extreme hardness measured in experiments. If the effect of bond-order loss on the atomic cohesive energy and binding energy density in the contracted surface region is considered for the large number of surface atoms instead of the ideally periodic boundary condition, the transition temperature of t-C would be lowered to a value closer to that measured and the calculated hardness of $BC_2N$ with approach the measured values.

(iii) Excitingly, in situ $T_C$ and valence DOS measurement of atomic-layered growth of superconductive Pb on stepped Si substrate by Guo et al. [368] revealed oscillation of both $T_C$ and the valence DOS peak near the $E_F$ when the film thickness was increased by one atomic layer at a time. The $T_C$ increases gradually to the bulk-value at about 30 layers in a saw-tooth-like oscillatory fashion. The oscillation is in about 0.5 K in magnitude and in a period of every other layer. The two DOS peaks at 0 and 0.3 eV below $E_F$ dominate alternatively with the layer-by-layer growth. These discoveries provide direct evidence for the BOLS premise, which indicates that the atomic cohesive energy (and $T_C$) drops associated with the deepened potential well of trapping as the atomic CN decreases. Therefore, the $T_C$ valley and the dominance of the DOS peak away from the $E_F$ are suggested to arise from the large number of under-coordinated atoms, which correspond to the deepened potential well (DOS peak away from $E_F$) and the lowered atomic cohesive energy ($T_C$). The $T_C$ peak and the dominance of the DOS peak near the $E_F$ are a consequence of the small number of under-coordinated atoms.

(iv) Transport in thermal conductivity and electric conductivity plays an important role in the performance of nanostructured devices, which would be more challenging for studies.

Employing the BOLS crystal potential for a nanosolid and for an assembly of nanosolids could improve the understanding on the kinetic and dynamic performance of a nanosolid under external stimuli.

(v) An extension of the BOLS to liquid surface and interfacial junction interfaces would lead to knowledge about the surface and interface states that are critical in practical applications.

(vi) The new freedom of size allows us to tune the physical properties of a nanosolid by simply changing the shape and size. Far beyond that, the new freedom provides us with opportunities to gain information such as dimer vibration and the single energy level of an isolated atom, which could form important impact in basic science.

(vii) A combination of the new freedom of size with traditional ones such as temperature, pressure, etc. would be even more challenging.

(viii) Application of the BOLS and its derivative to process and materials design is important in practical applications. If we know what is intrinsic and what the limit is, we may save our spirit and resources in fabricating devices and materials. For example, those working in microelectronics often expect to expand the limit of dielectrics to the lower end for interconnection and to the higher end for gate devices by changing the grain size. The BOLS derivative is able to tell us that it is unlikely that it is possible to raise the dielectrics by reducing the particle size and one has to seek other chemical routes for the objectives. One cannot expect proper functioning of a ferromagnetic, ferroelectric and a superconductive nanosolid when the solid size is smaller than 2.5 nm, as derived in the present work.

These topics would form challenging branches of study towards profound knowledge and practical applications and this report just scratches the skin of this vast field whilst further investigation is in progress.

## Acknowledgments

The practitioner would like to express his sincere gratitude to Professors P.J. Jennings, S.Y. Tong, C.L. Bai, M.F. Ashby, C. Humphreys, S Veprek, T.C. Chiang, J.A. Rodriguez, J.S. Colligon, R.H. Baughman, A.A. Zakhidov, S.R.P. Silva, D.H. Feng, Y.H. Tzeng, F.G. Shi, X. Yao, A. Bhalla, E. Sacher, M. Subramanian, M. Wautelet, W. Gao, P. Chu, A. Stelbovics, Leo Tan, H.G. Ang, C.H. Lai, C.H. Kam, Y.C. Soh, T.J. White, O.K. Tan, J.Y. Lin, Q.K. Xue, B.R. Mehta, S.X. Dou, K.P. Loh, A.T.S. Wee, H.C. Zeng, A. Mookerjee, and E.Y. Jiang for their encouragement and valuable communications. The author is indebted to S. Li, B.K. Tay, W.G. Zhu, C.M. Li, F.R. Zhu, K. Liao, Z.L. Dong, H. Huang, Y.Q. Fu, H.L. Bai, J. Zhou, S.Y. Xu, S.Y. Fu, W.T. Zheng, Q. Jiang, L.K. Pan, and W.H. Zhong for their support and input in one way or another. A fascinating and encouraging discussion in person with Dr Alan G. MacDiarmid at University of Texas at Dallas is particularly gratefully acknowledged. Permission of reprinting diagrams from Elsevier, IOP, APS, ACS, and AIP is also acknowledged.

## Appendix A

The table gives the values of electronegativity ($\eta$), metallic (ionic) valency and metallic (ionic) radius of the elements. $R(v)$ is the ionic radius and $v$, the valence value. $R(\mathrm{CN}=12)$ and $R(1)$ are the corresponding bond radii. [From Pauling L, J Am Chem Soc 1947;69:542 (see Eq. (10)), and Goldshmidt VM, Ber Deut Chem Ges 1927;60:1270 (see Eq. (9))]

Appendix A (*continued*)

| | | | | | | | | | | | | | | | | | |
|---|---|---|---|---|---|---|---|---|---|---|---|---|---|---|---|---|---|
| ($\eta$) | Li | Be | | | | H | | | | | | | B | C | N | O | F |
| | (1.0) | (1.6) | | | | (2.2) | | | | | | | (2.0) | (2.5) | (3.0) | (3.5) | (4.0) |
| $R(v)$ | 0.78 | 0.34 | | | | 1.27 | | | | | | | – | 2.60 | 1.71 | 1.32 | 1.33 |
| | (+) | (2) | | | | (−) | | | | | | | | (−4) | (−3) | (−2) | (−) |
| $R$(CN = 12) | 1.549 | 1.123 | | | | – | | | | | | | 0.98 | 0.914 | 0.88, 0.92 | – | – |
| $R$(1) | 1.225 | 0.889 | | | | 0.529 | | | | | | | 0.80 | 0.771 | 0.70, 0.74 | 0.66, 0.74 | 0.64, 0.72 |
| ($\eta$) | Na | Mg | | | | | | | | | | | Al | Si | P | S | Cl |
| | (0.9) | (1.3) | | | | | | | | | | | (1.5) | (1.9) | (2.1) | (2.5) | (3.0) |
| $R(v)$ | 0.98 | 0.78 | | | | | | | | | | | 0.57 | 0.41 | – | 1.72 | 1.81 |
| | (+) | (2) | | | | | | | | | | | (3) | (4) | | (−2) | (−) |
| $R$(CN = 12) | 1.896 | 1.598 | | | | | | | | | | | 1.429 | 1.316 | 1.28 | 1.27 | – |
| $R$(1) | 1.572 | 1.364 | | | | | | | | | | | 1.248 | 1.173 | 1.10 | 1.04 | 0.994 |
| ($\eta$) | K | Ca | Se | Ti | V | Cr | Mn | Fe | Co | Ni | Cu | Zn | Ga | Ge | As | Se | Br |
| | (0.8) | (1.0) | (1.4) | (1.5) | (1.6) | (1.7) | (1.6) | (1.8) | (1.9) | (1.9) | (1.9) | (1.7) | (1.6) | (2.0) | (2.0) | (2.4) | (2.8) |
| $R(v)$ | 1.33 | 1.06 | 0.83 | 0.68 | −(5) | (2.90,5.87) | 0.91 | 0.83 | 0.82 | 0.78 | 0.53 | 0.83 | 0.63 | 0.53 | – | 1.91 | 1.96 |
| | (+) | (2) | (3) | (4) | | | (2) | (2) | (2) | (2) | (1) | (2) | (3) | (4) | | (02) | (−) |
| $R$(CN = 12) | 2.349 | 1.970 | 1.620 | 1.467 | 1.338 | 1.357, 1.267 | 1.306, 1.26 | 1.260 | 1.252 | 1.244 | 1.276 | 1.379 | 1.408 | 1.366 | 1.39 | 1.40 | – |
| $R$(1) | 2.025 | 1.736 | 1.439 | 1.324 | 1.224 | 1.172 | 1.168 | 1.165 | 1.157 | 1.149 | 1.173 | 1.249 | 1.245 | 1.223 | 1.21 | 1.17 | 1.142 |
| ($\eta$) | Rb (0.8) | Sr (1.0) | Y (1.2) | Zr (1.3) | Nb (1.6) | Mo (2.2) | Te (1.9) | Ru (2.2) | Rh (2.3) | Pd (2.2) | Ag (1.9) | Cd (1.7) | In (1.7) | Sn (2.0) | Sb (1.9) | Te (2.1) | I (2.5) |
| $R(v)$ | 1.49 (+) | 1.27 (2) | – | 0.79 (4) | – | −(6) | (5.78) | (5.78) | (5.78) | (5.78) | 1.00 (1) | 1.03 (2) | (3.44) | (2.44, 4) | – | 2.03 (−2) | 2.20 (−) |
| $R$(CN = 12) | 2.48 | 2.148 | 1.797 | 1.597 | 1.456 | 1.386 | – | 1.336 | 1.342 | 1.373 | 1.442 | 1.543 | 1.660 | 1.620, 1.542 | 1.59 | 1.60 | – |
| $R$(1) | 2.16 | 1.914 | 1.616 | 1.454 | 1.342 | 1.291 | – | 1.241 | 1.252 | 1.283 | 1.339 | 1.413 | 1.497 | 1.412, 1.399 | 1.41 | 1.37 | 1.334 |
| ($\eta$) | Cs (0.8) | Ba (0.9) | La (1.1) | Hf (1.3) | Ta (1.5) | W (2.2) | Re (1.9) | Os (2.2) | Ir (2.2) | Pt (2.3) | Au (2.5) | Hg (2.0) | Tl (1.8) | Pb (2.3) | Bi (1.9) | Po (2.0) | At (2.0) |
| $R(v)$ | 1.65 (+) | 1.43 (2) | – | – | – | (5.78) | (5.78) | (5.78) | (5.78) | (5.78) | (5.44) | 1.12 (2) | 1.05 (3) | (2.44) | – | – | – |
| $R$(CN = 12) | 2.67 | 2.215 | 1.871 | 1.585 | 1.457 | 1.394 | 1.373 | 1.350 | 1.355 | 1.385 | 1.439 | 1.570 | 1.712 | 1.746 | 1.70 | 1.76 | – |
| $R$ (1) | 2.35 | 1.981 | 1.690 | 1.442 | 1.343 | 1.299 | 1.278 | 1.255 | 1.260 | 1.290 | 1.336 | 1.440 | 1.549 | 1.538 | 1.52 | 1.53 | – |
| ($\eta$) | Fa | Ra | Ae | Th | Pa | U | Np | Pu | Am | Cm | | | | | | | |
| | (0.7) | (0.9) | | | | | | | | | | | | | | | |
| $R$ ($v$) | – | – | 89–94 | – | | (5.78) | | | | | | | | | | | |
| $R$(CN = 12) | | | (1.1–1.4) | 1.795 | | 1.516 | | | | | | | | | | | |
| r (1) | | | | 1.652 | | 1.421 | | | | | | | | | | | |
| ($\eta$) | | | | Ce | Pr | Nd | Pm | Sm | Eu | Gd | Tb | Dy | Ho | Er | Tm | Yb | Lu |
| $R(v)$ | | | | (3.2) | (3.1) | (3.1) | | (2.8) | (2) | (3) | (3) | (3) | (3) | (3) | (3) | (2) | (3) |
| $R$(CN = 12) | | | | 1.818 | 1.824 | 1.818 | | 1.85 | 2.084 | 1.795 | 1.773 | 1.770 | 1.761 | 1.748 | 1.743 | 1.933 | 1.738 |
| $R$ (1) | | | | 1.646 | 1.648 | 1.642 | | 1.66 | 1.850 | 1.614 | 1.592 | 1.589 | 1.580 | 1.567 | 1.562 | 1.699 | 1.557 |

## References


[1] Pauling L. Atomic radii and interatomic distances in metals. J Am Chem Soc 1947;69:542–53.
[2] Goldschmidt VM. Ber Deut Chem Ges 1927;60:1270.
[3] Sun CQ. Oxidation electronics: bond-band-barrier correlation and its applications. Prog Mater Sci 2003;48:521–685.
[4] Zheng WT, Sun CQ. Electronic process of nitriding: mechanism and applications. Prog Solid State Chem, 2006;34:1–20.
[5] Ashby MF, Lu TJ. Metal foams: a survey. Sci China B 2003;46:521–32.
[6] Edelstein AS, Cammarata RC. Nanomaterials: synthesis, properties and applications. Inst Phys Bristol 1996.
[7] Gleiter H. Nanocrystalline materials. Prog Mater Sci 1989;33:223–315.
[8] Lu L, Sui ML, Lu K. Superplastic extensibility of nanocrystalline copper at room temperature. Science 2000;287:1463–6.
[9] Mintova S, Olson NH, Valtchev V, Bein T. Mechanism of zeolite A nanocrystal growth from colloids at room temperature. Science 1999;283:958–60.
[10] Horch S, Lorensen HT, Helveg S, Laegsgaard E, Stensgaard I, Jacobsen KW, et al. Enhancement of surface self-diffusion of platinum atoms by adsorbed hydrogen. Nature (London) 1999;398:134–6.
[11] Tan OK, Zhu W, Yan Q, Kong LB. Size effect and gas sensing characteristics of nanocrystalline $SnO_2$-$(1-x)\alpha$-$Fe_2O_3$ ethanol sensors. Sensor Actuat B 2000;65:361–5.
[12] Rao CNR, Kulkarni GU, Thomas PJ, Edwards PP. Size-dependent chemistry: properties of nanocrystals. Chem Euro J 2002;8:28–35.
[13] Goldstein N, Echer CM, Alivistos AP. Melting in semiconductor nanocrystals. Science 1992;256:1425–7.
[14] Christenson HK. Confinement effects on freezing and melting. J Phys Condens Matter 2001;13:95–133.
[15] Zhang Z, Li ZC, Jiang Q. Modelling for size-dependent and dimension-dependent melting of nanocrystals. J Phys D Appl Phys 2000;33:2653–6.
[16] van Buuren T, Dinh LN, Chase LL, Siekhaus WJ, Terminello LJ. Changes in the electronic properties of Si nanocrystals as a function of particle size. Phys Rev Lett 1998;80:3803–6.
[17] Yoffe AD. Semiconductor quantum dots and related systems: electronic, optical, luminescence and related properties of low dimensional systems. Adv Phys 2001;50:1–208.
[18] Sun CQ, Gong HQ, Hing P, Ye H. Behind the quantum confinement and surface passivation of nanoclusters. Surf Rev Lett 1999;6:L171–6.
[19] Modrow H. Tuning nanoparticle properties – the X-ray absorption spectroscopic point of view. Appl Spec Rev 2004;39:183–290.
[20] Brauman JI. Small clusters hit the big time. Science 1996;271:889–99.
[21] Service RF. Semiconductor clusters, nanoparticles, and quantum dots. Science 1996;271:890.
[22] Collins RT, Faucher PM, Tischler MA. Porous silicon: from luminescence to LEDs. Phys Today 1997: 25–31.
[23] Kodama RH, Berkowitz AE, McNiff Jr EJ, Foner S. Surface spin disorder in $NiFe_2O_4$ nanoparticles. Phys Rev Lett 1996;77:394–7.
[24] Berkowitz AE, Takano K. Exchange anisotropy. J Magn Magn Mater 1999;200:552–70.
[25] Gerberich WW, Mook WM, Perrey CR, Carter CB, Baskes MI, Mukherjee R, et al. Superhard silicon nanospheres. J Mech Phys Solids 2003;51:979–92.
[26] Chen CQ, Shi Y, Zhang YS, Zhu J, Yan YJ. Size dependence of Young's modulus in ZnO nanowires. Phys Rev Lett 2006;96:075505.
[27] Dalton AB, Collins S, Munoz E, Razal JM, Ebron VH, Ferraris JP, et al. Super-tough carbon-nanotube fibres – these extraordinary composite fibres can be woven into electronic textiles. Nature 2003;423:703.
[28] Baughman RH. Materials science – muscles made from metal. Science 2003;300:268–9.
[29] Veprek S. Electronic and mechanical properties of nanocrystalline composites when approaching molecular size. Thin Solid Films 1997;297:145–53.
[30] Veprek S, Reiprich S. A concept for the design of novel superhard coatings. Thin Solid Films 1995;268:64–71.
[31] Zhao M, Li JC, Jiang Q. Hall–Petch relationship in nanometer size range. J Alloys Comp 2003;361:160–4.
[32] Jiang B, Weng GJ. A theory of compressive yield strength of nano-grained ceramics. Int J Plast 2004;20(11):2007–26.
[33] Wang YM, Ma E, Chen MW. Enhanced tensile ductility and toughness in nanostructured Cu. Appl Phys Lett 2002;80:2395–7.

[34] Champion Y, Langlois C, Guerin-Mailly S, Langlois P, Bonnentien JL, Hytch MJ. Near-perfect elastoplasticity in pure nanocrystalline copper. Science 2003;300:310–1.
[35] Lu L, Shen YF, Chen XH, Qian LH, Lu K. Ultrahigh strength and high electrical conductivity in copper. Science 2004;304:422–6.
[36] Huang JY, Chen S, Wang ZQ, Kempa K, Wang YM, Jo SH, Chen G, Dresselhaus MS, Ren ZF. Superplastic carbon nanotubes - Conditions have been discovered that allow extensive deformation of rigid single-walled nanotubes. Nature 2006;439:281.
[37] Weissmuller J, Viswanath RN, Kramer D, Zimmer P, Wurschum R, Gleiter H. Charge-induced reversible strain in a metal. Science 2003;300:312–5.
[38] Wong EW, Sheehan PE, Lieber CM. Nanobeam mechanics: elasticity, strength and toughness of nanorods and nanotubes. Science 1997;277:1971–5.
[39] Ren Y, Fu YQ, Liao K, Li F, Cheng HM. Fatigue failure mechanisms of single-walled carbon nanotube ropes embedded in epoxy. Appl Phys Lett 2004;84:2811–3.
[40] An B, Fukuyama S, Yokogawa K, Yoshimura M. Surface superstructures of carbon nanotubes on highly oriented pyrolytic graphite annealed at elevated temperatures. Jpn J Appl Phys 1998;137:3809–11.
[41] Shi FG. Size-dependent thermal vibrations and melting in nanocrystals. J Mater Res 1994;9:1307–13.
[42] Allan G, Delerue C, Lannoo M, Martin E. Hydrogenic impurity levels, dielectric constant, and Coulumb charging effects in silicon crystallites. Phys Rev B 1995;52:11982–8.
[43] Chen XS, Zhao JJ, Wang GH, Shen XC. The effect of size distributions of nanoclusters on photoluminescence from ensembles of Si nanoclusters. Phys Lett A 1996;212:285–9.
[44] Alivisatos AP. Semiconductor clusters, nanocrystals, and quantum dots. Science 1996;271:933–7.
[45] Pan LK, Sun CQ, Tay BK, Chen TP, Li S. Photoluminescence of Si nanosolids near the lower end of the size limit. J Phys Chem B 2002;106:11725–7.
[46] Sun CQ, Li S, Tay BK, Chen TP. Upper limit of blue shift in the photoluminescence of CdSe and CdS nanosolids. Acta Mater 2002;50:4687–93.
[47] Sun CQ, Pan LK, Fu YQ, Tay BK, Li S. Size dependence of the 2p-level shift of nanosolid silicon. J Phys Chem B 2003;107:5113–5.
[48] Ma DDD, Lee CS, Au FCK, Tong SY, Lee ST. Small-diameter silicon nanowire surfaces. Science 2003;299:1874–7.
[49] Shi J, Gider S, Babcock K, Awschalom DD. Magnetic clusters in molecular beams, metals, and semiconductors. Science 1996;271:937–41.
[50] Tong WP, Tao NR, Wang ZB, Lu J, Lu K. Nitriding iron at lower temperatures. Science 2003;299: 686–8.
[51] Shibata T, Bunker BA, Zhang ZY, Meisel D, Vardeman CF, Gezelter JD. Size-dependent spontaneous alloying of Au–Ag nanoparticles. J Am Chem Soc 2002;124:11989–96.
[52] Kennedy MK, Kruis FE, Fissan H, Mehta BR, Stappert S, Dumpich G. Tailored nanoparticle films from monosized tin oxide nanocrystals: particle synthesis, film formation, and size-dependent gas-sensing properties. J Appl Phys 2003;93:551–60.
[53] Hu Y, Tan OK, Cao W, Zhu W. Fabrication and characterization of nano-sized $SrTiO_3$-based oxygen sensor for near-room temperature operation. IEEE Sens J 2005;5:825–32.
[54] Hu Y, Tan OK, Pan JS, Yao X. A new form of nano-sized $SrTiO_3$ material for near human body temperature oxygen sensing applications. J Phys Chem B 2004;108:11214–8.
[55] Balamurugan B, Mehta BR, Shivaprasad SM. Surface-modified CuO layer in the size-stabilized $Cu_2O$ nanoparticles. Appl Phys Lett 2001;79:3176–8.
[56] Zhou J, Sun CQ, Pita K, Lam YL, Zhou Y, Ng SL, et al. Thermally tuning of the photonic band-gap of $SiO_2$ colloid-crystal infilled with ferroelectric $BaTiO_3$. Appl Phys Lett 2001;78:661–3.
[57] Li B, Zhou J, Hao LF, Hu W, Zong RL, Cai MM, et al. Photonic band gap in $(Pb,La)(Zr,Ti)O_3$ inverse opals. Appl Phys Lett 2003;82:3617–9.
[58] Lu K. Nanocrystalline metals crystallized from amorphous solids: nanocrystallization, structure, and properties. Mater Sci Eng R 1996;16:161–221.
[59] Agraït N, Yeyati AL, van Ruitenbeek JM. Quantum properties of atomic-sized conductors. Phys Rep 2003;377:81–279.
[60] Halporin WP. Quantum size effects in metal particles. Rev Mod Phys 1966;58:533–97.
[61] Binns C. Nanoclusters deposited on surfaces. Surf Sci Rep 2001;44:1–49.
[62] Baletto F, Ferrando R. Structural properties of nanoclusters: energetic, thermodynamic, and kinetic effects. Rev Mod Phys 2005;77:371–423.

[63] Baretzky B, Baro MD, Grabovetskaya GP, Gubicza J, Ivanov MB, Kolobov YR, et al. Fundamentals of interface phenomena in advanced bulk nanoscale materials. Rev Adv Mater Sci 2005;9:45–108.
[64] Nobuera C. Insulating oxides in low dimensionality: a theoretical review. Surf Rev Lett 2001;8:121–67.
[65] Moriarty P. Nanostructured materials. Rep Prog Phys 2001;64(3):297–381.
[66] Fernandez-Garcia M, Martinez-Arias A, Hanson JC, Rodriguez JA. Nanostructured oxides in chemistry, characterization and properties. Chem Rev 2004;104(9):4063–104.
[67] Rao CNR, Deepak FL, Gundiah G, Govindaraj A. Inorganic nanowires. Prog Solid State Chem 2003;31(1–2): 5–147.
[68] Wang CX, Yang GW. Thermodynamics of metastable phase nucleation at the nanoscale. Mater Sci Eng R-Reports 2005;49(6):157–202.
[69] Trwoga PF, Kenyon AJ, Pitt CW. Modeling the contribution of quantum confinement to luminescence from silicon nanoclusters. J Appl Phys 1998;83:3789–94.
[70] Efros AL, Efros AL. Interband absorption of light in a semiconductor sphere. Sov Phys Semicond 1982;16:772–5.
[71] Brus JE. On the development of bulk optical properties in small semiconductor crystallites. J Lumin 1984;31:381–4.
[72] Kayanuma Y. Quantum-size effects of interacting electrons and holes in semiconductor microcrystals with spherical shape. Phys Rev 1988;B38:9797–805.
[73] Glinka YD, Lin SH, Hwang LP, Chen YT, Tolk NH. Size effect in self-trapped exciton photoluminescence from $SiO_2$-based nanoscale materials. Phys Rev B 2001;64:085421.
[74] Qin GG, Song HZ, Zhang BR, Lin J, Duan JQ, Yao GQ. Experimental evidence for luminescence from silicon oxide layers in oxidized porous silicon. Phys Rev B 1996;54:2548–55.
[75] Koch F, Petrova-Koch V, Muschik T, Nikolov A, Gavrilenko V. Microcrystalline semiconductors: materials science and devices, vol. 283. Pittsburgh, PA: Materials Research Society; 1993. p. 197.
[76] Prokes SM. Surface and optical properties of porous silicon. J Mater Res 1996;11:305–19.
[77] Iwayama TS, Hole DE, Boyd IW. Mechanism of photoluminescence of Si nanocrystals in $SiO_2$ fabricated by ion implantation: the role of interactions of nanocrystals and oxygen. J Phys Condens Matter 1999;11:6595–604.
[78] Lindemann FA. The calculation of molecular natural frequencies. Phys Z 1910;11:609–12.
[79] Born M. Thermodynamics of crystals and melting. J Chem Phys 1939;7:591–603.
[80] Buffat P, Borel JP. Size effect on the melting temperature of gold particles. Phys Rev A 1976;13:2287–98.
[81] Pawlow P. The dependency of the melting point on the surface energy of a solid body. (Supplement.) Z Phys Chem (Munich) 1909;65:545–8.
[82] Reiss H, Mirabel P, Whetten RL. Capillarity theory for the ''coexistence'' of liquid and solid clusters. J Phys Chem 1988;92:7241–6.
[83] Sakai H. Surface-induced melting of small particles. Surf Sci 1996;351:285–91.
[84] Ubbelohde AR. The molten state of materials. New York: Wiley; 1978.
[85] Hanszen KJ. Theoretische untersuchungen uber den schmelzpunkt kleiner kugelchen – ein beitrang zur thermodynamik der grenzflachen. Z Phys 1960;157:523–53.
[86] Couchman PR, Jesser WA. Thermodynamic theory of size dependence of melting temperature in metals. Nature (London) 1977;269:481–3.
[87] Vanfleet RR, Mochel JM. Thermodynamics of melting and freezing in small particles. Surf Sci 1995;341:40–50.
[88] Vekhter B, Berry RS. Phase coexistence in clusters:an ''experimental'' isobar and an elementary model. J Chem Phys 1997;106:6456–9.
[89] Jiang Q, Liang LH, Li JC. Thermodynamic overheating and relevant interface stability of low-dimensional metallic crystals. J Phys Condens Matter 2001;13:565–71.
[90] Jiang Q, Tong HY, Hsu DT, Okuyama K, Shi FG. Thermal stability of crystalline thin films. Thin Solid Films 1998;312:357–61.
[91] Jiang Q, Shi HX, Li JC. Finite size effect on glass transition temperatures. Thin Solid Films 1999;354:283–6.
[92] Wen Z, Zhao M, Jiang Q. The melting temperature of molecular nanocrystals at the lower bound of the mesoscopic size range. J Phys Condens Matter 2000;12:8819–24.
[93] Jiang Q, Liang LH, Zhao M. Modelling of the melting temperature of nano-ice in MCM-41 pores. J Phys Condens Matter 2001;13:L397–401.
[94] Nanda KK, Sahu SN, Behera SN. Liquid-drop model for the size-dependent melting of low-dimensional systems. Phys Rev A 2002;66:013208.
[95] Wautelet M. Estimation of the variation of the melting temperature with the size of small particles, on the basis of a surface-phonon instability model. J Phys D 1991;24:343–6.
[96] Jiang Q, Zhang Z, Li JC. Overheating of nanocrystals embedded in matrix. Chem Phys Lett 2000;322:549–52.

[97] Vallee R, Wautelet M, Dauchot JP, Hecq M. Size and segregation effects on the phase diagrams of nanoparticles of binary systems. Nanotechnology 2001;12:68–74.
[98] Wales DJ. Structure, dynamics, and thermodynamics of clusters: tales from topographic potential surfaces. Science 1996;271:925–9.
[99] Sun CQ. Oxygen-reduced inner potential and work function in VLEED. Vacuum 1997;48:865–9.
[100] Sun CQ. Spectral sensitivity of the VLEED to the bonding geometry and the potential barrier of the O–Cu(001) surface. Vacuum 1997;48:491–8.
[101] Sun CQ, Bai CL. Modelling of non-uniform electrical potential barriers for metal surfaces with chemisorbed oxygen. J Phys Condens Matter 1997;9:5823–36.
[102] Jones RO, Jennings PJ, Jepsen O. Surface barrier in metals: a new model with application to W(001). Phys Rev B 1984;29:6474–80.
[103] Jennings PJ, Sun CQ. Low energy electron diffraction. In: O'Connor DJ, Sexton BA, Smart RC, editors. Surface analysis methods in materials science. 2nd ed. Berlin/New York: Springer-Verlag; 2003 [Chapter 13].
[104] Sinnott MJ. The solid state for engineers. New York: Wiley and Sons; 1963.
[105] Shpyrko OG, Grigoriev AY, Steimer C, Pershan PS, Lin B, Meron M, et al. Anomalous layering at the liquid Sn surface. Phys Rev B 2004;B 70:224206.
[106] Povey MJW, Hindle SA, Aarflot A, Hoiland H. Melting point depression of the surface layer in *n*-alkane emulsions and its implications for fat destabilization in ice cream. Crystal Growth Design 2005;5:297–301.
[107] Mahnke H-E, Haas H, Holub-Krappe E, Koteski V, Novakovic N, Fochuk P, et al. Lattice distortion around impurity atoms as dopants in CdTe. Thin Solid Films 2005;480–481:279–82.
[108] Srinivasan SG, Liao XZ, Baskes MI, McCabe RJ, Zhao YH, Zhu YT. Compact and dissociated dislocations in aluminum: implications for deformation. Phys Rev Lett 2005;94:125502.
[109] Feibelman PJ. Relaxation of hcp(0001) surfaces: a chemical view. Phys Rev B Condens Matter 1996;B53:13740–6.
[110] Sun CQ, Bai HL, Tay BK, Li S, Jiang EY. Dimension, strength, and chemical and thermal stability of a single C–C bond in carbon nanotubes. J Phys Chem B 2003;107:7544–6.
[111] Sun CQ, Li CM, Bai HL, Jiang EY. Melting point oscilation of a solid over the whole range of sizes. Nanotechnology 2005;16:1290–3.
[112] Bahn SR, Jacobsen KW. Chain formation of metal atoms. Phys Rev Lett 2001;87:266101.
[113] Sun CQ, Wang Y, Tay BK, Li S, Huang H, Zhang YB. Correlation between the melting point of a nanosolid and the cohesive energy of a surface atom. J Phys Chem B 2002;106:10701–5.
[114] Kocks UF, Argon AS, Ashby AS. Thermodynamics and kinetics of slip. Prog Mater Sci 1975;19:1–281.
[115] Kittel C. Introduction to solid state physics. 6th ed. New York: Wiley; 1986.
[116] Harrison WA. Electronic structure and the properties of solids. San Francisco: Freeman; 1980.
[117] Crain JN, Pierce DT. End states in one-dimensional atom chains. Science 2005;307:703.
[118] Hensel JC, Tung RT, Poate JM, Unterwald FC. Specular boundary scattering and electrical transport in single-crystal thin films of $CoSi_2$. Phys Rev Lett 1985;54:1840–3.
[119] Tesanovic Z, Jaric MV. Quantum transport and surface scattering. Phys Rev Lett 1986;57:2760–3.
[120] Zhong WH, Sun CQ, Li S, Bai HL, Jiang EY. Impact of bond order loss on surface and nanosolid magnetism. Acta Mater 2005;53:3207–14.
[121] Au Yeung TC, Chiam TC, Chen CK, Sun CQ, Shangguan WZ, Wong WK, et al. Effect of surface bond-order loss on the electrical resistivity of metallic polycrystalline thin films. Phys Rev B 2005;B 72: 155417.
[122] Sun CQ. Surface and nanosolid core-level shift: impact of atomic coordination number imperfection. Phys Rev B 2004;69:045105.
[123] Sun CQ, Pan LK, Chen TP, Sun XW, Li S, Li CM. Distinguishing the effect of crystal-field screening from the effect of valence recharging on the 2p3/2 and 3d5/2 level energies of nanostructured copper. Appl Surf Sci 2006;252(6):2101–7.
[124] Sun CQ, Li S. Oxygen derived DOS features in the valence band of metals. Surf Rev Lett 2000;7:L213–7.
[125] Sun CQ. A model of bonding and band-forming for oxides and nitrides. Appl Phys Lett 1998;72:1706–8.
[126] Street RA. Hydrogenated amorphous silicon. Cambridge: Cambridge University Press; 1991.
[127] Tománek D, Mukherjee S, Bennemann KH. Simple theory for the electronic and atomic structure of small clusters. Phys Rev B 1983;28:665–73.
[128] Baraldi G, Silvano L, Comelli G. Oxygen adsorption and ordering on Ru(1010). Phys Rev B 2001;63:115410.
[129] Over H, Kleinle G, Ertl G, Moritz W, Ernst KH, Wohlgemuth H, et al. LEED structural analysis of the Co(1010) surface. Surf Sci 1991;254:L469–74.

[130] Davis HL, Hannon JB, Ray KB, Plummer EW. Anomalous interplanar expansion at the (0001) surface of Be. Phys Rev Lett 1992;68:2632–5.
[131] Halicioglu T. Calculation of surface energies for low index planes of diamond. Surf Sci 1991;259: L714–8.
[132] Sun CQ. Exposure-resolved VLEED from the O–Cu(001): bonding dynamics. Vacuum 1997;48:535–41.
[133] Sun CQ. Origin and processes of O–Cu(001) and the O–Cu(110) biphase ordering. Int J Mod Phys B 1998;12:951–64.
[134] Sun CQ. O–Cu(001): I. Binding the signatures of LEED, STM and PES in a bond-forming way. Surf Rev Lett 2001;8:367–402.
[135] Sun CQ. O–Cu(001): II. VLEED quantification of the four-stage $Cu_3O_2$ bonding kinetics. Surf Rev Lett 2001;8:703–34.
[136] Sun CQ, Tay BK, Lau SP, Sun XW, Zeng XT, Bai H, et al. Bond contraction and lone pair interaction at nitride surfaces. J Appl Phys 2001;90:2615–7.
[137] Nautiyal T, Youn SJ, Kim KS. Effect of dimensionality on the electronic structure of Cu, Ag, and Au. Phys Rev B 2003;68:033407.
[138] Zhao YH, Zhang K, Lu K. Structure characteristics of nanocrystalline element selenium with different grain sizes. Phys Rev B 1997;56:14322–9.
[139] Qian X, Hübner W. First-principles calculation of structural and magnetic properties for Fe monolayers and bilayers on W(110). Phys Rev B 1999;60:16192–7.
[140] Geng WT, Freeman AJ, Wu RQ. Magnetism at high-index transition-metal surfaces and the effect of metalloid impurities: Ni(210). Phys Rev B 2001;63:064427.
[141] Geng WT, Kim M, Freeman AJ. Multilayer relaxation and magnetism of a high-index transition metal surface: Fe(310). Phys Rev B 2001;63:245401.
[142] Batra IP. Lattice relaxation in aluminum monolayers. J Vac Sci Technol A 1985;3:1603–6.
[143] Banerjee R, Sperling EA, Thompson GB, Fraser HL, Bose S, Ayyub P. Lattice expansion in nanocrystalline niobium thin films. Appl Phys Lett 2003;82:4250–2.
[144] Walko DA, Robinson IK. Structure of Cu(115): clean surface and its oxygen-induced facets. Phys Rev B 1999;59:15446–58.
[145] Durukanolu S, Rahman TS. Structure of Ag(410) and Cu(320). Phys Rev B 2003;67:205406.
[146] Jona F, Marcus PM, Zanazzi E, Maglietta M. Structure of Ag(410). Surf Rev Lett 1999;6:355–9.
[147] Nascimento VB, Soares EA, de Carvalho VE, Lopes EL, Paniago R, de Castilho CM. Thermal expansion of the Ag(110) surface studied by low-energy electron diffraction and density-functional theory. Phys Rev B 2003;68:245408.
[148] Galanakis I, Papanikolaou N, Dederichs PH. Applicability of the broken-bond rule to the surface energy of the fcc metals. Surf Sci 2002;511:1–12.
[149] Sun CQ. Theory of size, confinement, and oxidation effects [Chapter 1]. In: Fernandez-Garcia M, Rodríguez JA, editors. Synthesis and applications of oxide nanoparticles. John Wiley & Sons; Nov. 2005.
[150] Champion Y, Bernard F, Millot N, Perriat P. Surface adsorption effects on the lattice expansion of copper nanocrystals. Appl Phys Lett 2005;86(23):231914.
[151] Duan Y, Li J. Structure study of nickel nanoparticles. Mater Chem Phys 2004;87:452–4.
[152] Li JG, Qin Y, Kou XL, Huang JJ. Microstructure and magnetic properties of $Fe_xNi_{1-x}$ alloy nanoplatelets. J Nanosci Nanotechnol 2005;5(10):1699–706.
[153] Duan YW, Kou XL, Li JG. Size dependence of structure and magnetic properties of $La_{0.7}Sr_{0.3}MnO_3$ nanoparticles. Phys B Condens Matter Jan 31, 2005;355(1–4):250–4.
[154] Montano PA, Schulze W, Tesche B, Shenoy GK, Morrison TI. Extended x-ray-absorption fine-structure study of Ag particles isolated in solid argon. Phys Rev B 1984;30:672–7.
[155] Lamber R, Wetjen S, Jaeger NI. Size dependence of the lattice parameter of small palladium particles. Phys Rev B 1995;51:10968–71.
[156] Mi WB, Li ZQ, Wu P, Jiang EY, Bai HL, Hou DL, et al. Facing-target sputtered Fe–C granular films: structural and magnetic properties. J Appl Phys 2005;97:043903.
[157] Yu XF, Liu X, Zhang K, Hu ZQ. Lattice contraction of nanometre-sized Sn and Bi particles produced by an electrohydrodynamic technique. J Phys Condens Matter 1999;11:937–44.
[158] Reddy DR, Reddy BK. Laser-like mechanoluminescence in ZnMnTe-diluted magnetic semiconductor. Appl Phys Lett 2002;81:460–2.
[159] Aruna I, Mehta BR, Malhotra LK. Faster H recovery in Pd nanoparticle layer based Gd switchable mirrors: size-induced geometric and electronic effects. Appl Phys Lett 2005;87:103101.

[160] Montano PA, Shenoy GK, Alp EE, Schulze W, Urban J. Structure of copper microclusters isolated in solid argon. Phys Rev Lett 1986;56:2076–9.
[161] Hansen LB, Stoltze P, Nørskov JK. Is there a contraction of the interatomic distance in small metal particles? Phys Rev Lett 1990;64:3155–8.
[162] Weissker HC, Furthmuller J, Bechstedt F. Structural relaxation in Si and Ge nanocrystallites: influence on the electronic and optical properties. Phys Rev B 2003;67:245304.
[163] Liu HH, Jiang EY, Bai HL, Wu P, Li ZQ. Impact of shell structure on atomic cluster. Chem Phys Lett 2005;412(1–3):195–9.
[164] Kara A, Rahman TS. Vibrational properties of metallic nanocrystals. Phys Rev Lett 1998;81:1453–6.
[165] Buttard D, Dolino G, Faivre C, Halimaoui A, Comin F, Formoso V, et al. Porous silicon strain during in situ ultrahigh vacuum thermal annealing. J Appl Phys 1999;85:7105–11.
[166] Mays CW, Vermaak JS, Kuhlmann-Wilsdorf D. On surface stress and surface tension II Determination of the surface stress of gold. Surf Sci 1968;12:134–40.
[167] Stoneham AM. The lattice contraction of nanometer sized Sn and Bi particles. J Phys Condens Matter 1999;11:8351–2.
[168] Wasserman HJ, Vermaak JS. On the determination of a lattice contraction in very small silver particles. Surf Sci 1970;22:164–72.
[169] Nanda KK, Behera SN, Sahu SN. The lattice contraction of nanometre-sized Sn and Bi particles produced by an electrohydrodynamic technique. J Phys Condens Matter 2001;13:2861–4.
[170] Jiang Q, Liang LH, Zhao DS. Lattice contraction and surface stress of fcc nanocrystals. J Phys Chem B 2001;105:6275–7.
[171] Liang LH, Li JC, Jiang Q. Size-dependent melting depression and lattice contraction of Bi nanocrystals. Physica B Condens Matter 2003;334:49–53.
[172] Toyama T, Adachi D, Okamoto H. Electroluminescent devices with nanostructured ZnS:Mn emission layer operated at 20 V0-p. Mater Res Symp Proc 2000;621:q441–6.
[173] Woltersdorf J, Nepijko AS, Pippel E. Dependence of lattice parameters of small particles on the size of the nuclei. Surf Sci 1981;106:64–9.
[174] Zhao M, Zhou XH, Jiang Q. Comparison of different models for melting point change of metallic nanocrystals. J Mater Res 2001;16:3304–8.
[175] Müller H, Opitz C, Strickert K, Skala LZ. Phys Chem Leipzig 1987;268:634.
[176] Kellermann G, Craievich AF. Structure and melting of Bi nanocrystals embedded in a $B_2O_3$–$Na_2O$ glass. Phys Rev B 2002;65:134204.
[177] Apai G, Hamilton JF. Extended x-ray absorption fine structure of small copper and nickel clusters: binding energy and bond length changes with cluster size. Phys Rev Lett 1979;43:165–8.
[178] Wasserman HJ, Vermaak JS. On the determination of the surface stress of copper and platinum. Surf Sci 1972;32:168–74.
[179] Liu JP, Zaumseil P, Bugiel E, Osten HJ. Epitaxial growth of $Pr_2O_3$ on Si(111) and the observation of a hexagonal to cubic phase transition during postgrowth $N_2$ annealing. Appl Phys Lett 2001;79:671–3.
[180] Wang LW, Zunger A. Pseudopotential calculations of nanoscale CdSe quantum dots. Phys Rev B Condens Matter 1996;B 53:9579–82.
[181] Leung K, Whaley KB. Surface relaxation in CdSe nanocrystals. J Chem Phys 1999;110:11012–22.
[182] Rabani E. Structure and electrostatic properties of passivated CdSe nanocrystals. J Chem Phys 2001;115:1493–7.
[183] Puzder A, Williamson AJ, Reboredo FA, Galli G. Structural stability and optical properties of nanomaterials with reconstructed surfaces. Phys Rev Lett 2003;91:1574051–4.
[184] Gilbert B, Huang F, Zhang H, Waychunas GA, Banfield JF. Nanoparticles: strained and stiff. Science 2004;305:651–4.
[185] Nanda J, Sarma DD. Photoemission spectroscopy of size selected zinc sulfide nanocrystallites. J Appl Phys 2001;90:2504–10.
[186] Sklyadneva YI, Rusina GG, Chulkov EV. Vibrational states on vicinal surfaces of Al, Ag, Cu and Pd. Surf Sci 1998;416:17–36.
[187] Kara A, Durukanoglu S, Rahman TS. Local thermodynamic properties of a stepped metal surface: Cu(711). Phys Rev B 1996;53:15489–92.
[188] Zhang P, Sham TK. X-ray studies of the structure and electronic behavior of alkanethiolate-capped gold nanoparticles: the interplay of size and surface effects. Phys Rev Lett 2003;90:245502.
[189] Ibach H. Role of surface stress in reconstruction, epitaxial growth and stabilization of mesoscopic structures. Surf Sci Rep 1997;29:193–263.

[190] Haiss W. Surface stress of clean and adsorbate-covered solids. Rep Prog Phys 2001;64:59–648.
[191] Poa CHP, Lacerda RG, Cox DC, Silva SRP, Marques FC. Stress-induced electron emission from nanocomposite amorphous carbon thin films. Appl Phys Lett 2002;81:853–5.
[192] de Boer FR, Boom R, Mattens WCM, Miedema AR, Niessen AK. Cohesion in metals, vol. 1. Amsterdam: North-Holland Publishing Company; 1998.
[193] Vitos L, Ruban AV, Skriver HL, Kollár J. Surface energy of metals. Surf Sci 1998;411:186–202.
[194] Mattsson AE, Jennison DR. Computing accurate surface energies and the importance of electron self-energy in metal/metal-oxide adhesion. Surf Sci 2002;520:L611–8.
[195] Methfessel M, Hennig D, Scheffler M. Trends of the surface relaxations, surface energies, and work functions of the 4d transition metals. Phys Rev B 1992;46:4816–29.
[196] Skriver HL, Rosengaard NM. Surface energy and work function of elemental metals. Phys Rev B 1992;46: 7157–68.
[197] Mehl MJ, Papaconstantopoulos DA. Applications of a tight-binding total-energy method for transition and noble metals: elastic constants, vacancies, and surfaces of monatomic metals. Phys Rev 1996;B54: 4519–30.
[198] Rodríguez AM, Bozzolo G, Ferrante J. Multilayer relaxation and surface energies of FCC and BCC metals using equivalent crystal theory. Surf Sci 1993;289:100–26.
[199] Alden M, Skriver HL, Mirbt S, Johansson B. Calculated surface-energy anomaly in the 3d metals. Phys Rev Lett 1992;69:2296–8.
[200] Moriarty JA, Phillips R. First-principles interatomic potentials for transition-metal surfaces. Phys Rev Lett 1991;66:3036–9.
[201] Thomson Kelvin W. Philos Mag 1871;42:448.
[202] Rytkönen A, Valkealahti S, Manninen M. Melting and evaporation of argon clusters. J Chem Phys 1997;106:1888–92.
[203] Nanda KK, Maisels A, Kruis FE, Fissan H, Stappert S. Higher surface energy of free nanoparticles. Phys Rev Lett 2003;91:106102.
[204] Lu HM, Jiang Q. Comment on: higher surface energy of free nanoparticles. Phys Rev Lett 2004;92:179601.
[205] Desjonquères MC, Spanjaard D. Concepts in surface physics. Springer series in surface, vol. 30. Berlin, Heidelberg: Springer-Verlag; 1993.
[206] Jiang Q, Lu HM, Zhao M. Modelling of surface energies of elemental crystals. J Phys Condens Matter 2004;16:521–30.
[207] Baskes MI. Many-body effects in fcc metals: a Lennard–Jones embedded-atom potential. Phys Rev Lett 1999;83:2592–5.
[208] Sun CQ, Li S, Li CM. Impact of bond-order loss on surface and nanosolid mechanics. J Phys Chem B 2005;109:415–23.
[209] Shi X, Tay BK, Flynn DL, Sun Z. Tribological properties of tetrahedral carbon films deposited by filtered cathodic vacuum arc technique. Mat Res Symp Proc 1997;436:293–8.
[210] Caceres D, Vergara I, Gonzalez R, Monroy E, Calle F, Munoz E, et al. Nanoindentation on AlGaN thin films. J Appl Phys 1999;86:6773–8.
[211] Mirshams RA, Parakala P. Nanoindentation of nanocrystalline Ni with geometrically different indenters. Mater Sci Eng A 2004;372:252–60.
[212] Wang YH, Moitreyee MR, Kumar R, Wu SY, Xie JL, Yew P, et al. The mechanical properties of ultra-low-dielectric-constant films. Thin Solid Films 2004;462–463:227–30.
[213] Price WJ, Leigh SA, Hsu SM, Patten TE, Liu GY Measuring the size dependence of young's modulus using force modulation atomic force microscopy. J Phys Chem A 2006;110:1382–8.
[214] Liu E, Shi X, Tan HS, Cheah LK, Sun Z, Tay BK, et al. The effect of nitrogen on the mechanical properties of metrahedral amorphous carbon films deposited with a filtered cathodic vacuum arc. Surf Coat Technol 1999;120–121:601–6.
[215] Zhao M, Slaughter WS, Li M, Mao SX. Material-length-scale-controlled nanoindentation size effects due to strain-gradient plasticity. Acta Mater 2003;51:4461–9.
[216] Dodson BW. Many-body surface strain and surface reconstructions in fcc transition metals. Phys Rev Lett 1988;60:2288–91.
[217] Streitz FH, Cammarata RC, Sieradzki K. Surface-stress effects on elastic properties: I. Thin metal films. Phys Rev B Condens Matter 1994;B49:10699–706.
[218] Liu M, Shi B, Guo J, Cai X, Song H. Lattice constant dependence of elastic modulus for ultrafine grained mild steel. Scr Mater 2003;49:167–71.

[219] Horstemeyer MF, Baskes MI, Plimpton SJ. Length scale and time scale Dects on the plastic Cow of fcc metals. Acta Mater 2001;49:4363–74.
[220] Kim JJ, Choi Y, Suresh S, Argon AS. Nanocrystallization during nanoindentation of a bulk amorphous metal alloy at room temperature. Science 2002;295:654–7.
[221] Baker SP, Vinci RP, Arias T. Elastic and anelastic behavior of materials in small dimensions. MRS Bull 2002;27:26–9.
[222] Murayama M, Howe JM, Hidaka H, Tokai S. Atomic level observation of disclination diposes in mechanically milled, nanocrystalline Fe. Science 2002;295:2433–5.
[223] Veprek S, Argon AS. Mechanical properties of superhard nanocomposites. Surf Coat Technol 2001;146–147:175–82.
[224] Ferro D, Teghil R, Barinov SM, D'Alessio L, DeMaria G. Thickness-dependent hardness of pulsed laser ablation deposited films of refractory carbides. Mater Chem Phys 2004;87:233–6.
[225] Yamakov V, Wolf D, Salazar M, Phillpot SR, Gleiter H. Length-scale Dects in the nucleation of extended dislocations in nanocrystalline Al by molecular-dynamics simulation. Acta Mater 2001;49:2713–22.
[226] Cantor B, Chang ITH, Knight P, Vincent AJB. Microstructural development in equiatomic multicomponent. Mater Sci Eng A 2004;375–377:213–8.
[227] Gao F, He J, Wu E, Liu S, Yu D, Li D, et al. Hardness of covalent crystals. Phys Rev Lett 2003;91:015502.
[228] Cohen ML, Bergstresser TK. Band structures and pseudopotential form factors for fourteen semiconductors of the diamond and zinc-blende structures. Phys Rev 1966;141:789–96.
[229] Philips JC. Covalent bonding in crystals, molecules and polymers. Chicago: Chicago University Press; 1969.
[230] Liu AY, Cohen L. Prediction of new low compressibility solids. Science 1989;245:841–2.
[231] Korsunskii BL, Pepekin VP. Usp Khim 1977;66:1003.
[232] Litovchenko V. Analysis of the band structure of tetrahedral diamondlike crystals with valence bonds: prediction of materials with superhigh hardness and negative electron affinity. Phys Rev B 2002;65:153108.
[233] Wang EG. Research on carbon nitrides. Prog Mater Sci 1997;41:241–300.
[234] Wang EG. New development in covalently bonded carbon-nitride and related materials. Adv Mater 1999;11:1129–33.
[235] Zheng WT, Sjostrom H, Ivanov I, Xing KZ, Broitman E, Salaneck WR, et al. Reactive magnetron sputter deposited $CN_x$: effects of $N_2$ pressure and growth temperature on film composition, bonding, and microstructure. J Vac Sci Technol A 1996;14:2696–701.
[236] Veprek S. Conventional and new approaches towards the design of novel superhard materials. Surf Coat Technol 1997;97:15–22.
[237] Van Swygenhoven H, Derlet PM, Hasnaoui A. Atomic mechanism for dislocation emission from nanosized grain boundaries. Phys Rev B 2002;66:024101.
[238] Arzt E, Ashby MF. Threshold stresses in materials containing dispersed particles. Scr Met 1982;16:1285–90.
[239] Cheng S, Spencer JA, Milligan WW. Strength and tension/compression asymmetry in nanostructured and ultrafine-grain metals. Acta Mater 2003;51:4505–18.
[240] Schiøtz J, Jacobsen KW. A maximum in the strength of nanocrystalline copper. Science 2003;301:1357–9.
[241] Schiotz J. Atomic-scale modeling of plastic deformation of nanocrystalline copper. Scr Mater Oct 2004;51(8):837–41.
[242] Conrad H, Jung K. Effect of grain size from millimeters to nanometers on the flow stress and deformation kinetics of Ag. Mater Sci Eng A 2005;391(1–2):272–84.
[243] Zhong WL, Jiang B, Zhang PL, Ma JM, Cheng HM, Yang ZH, et al. Phase transition in $PbTiO_3$ ultrafine particles of different sizes. J Phys Condens Matt 1993;5:2619–24.
[244] Bata V, Pereloma EV. An alternative physical explanation of the Hall–Petch relation. Acta Mater 2004;52:657–65.
[245] Wang GF, Feng XQ, Yu SW. Interfacial effects on effective elastic moduli of nanocrystalline materials. Mat Sci Eng A 2003;363:1C8.
[246] Wolf D, Yamakov V, Phillpot SR, Mukherjee AK. Deformation mechanism and inverse Hall–Petch behavior in nanocrystalline materials. Zeitschrift fur Metallkunde 2003;94:1091–7.
[247] Yamakov V, Wolf D, Phillpot SR, Mukherjee AK, Gleiter H. Deformation-mechanism map for nanocrystalline metals by molecular-dynamics simulation. Nat Mater 2004;3:43–7.
[248] Kumar KS, Van Swygenhoven H, Suresh S. Mechanical behavior of nanocrystalline metals and alloys. Acta Mater 2003;51:5743–74.
[249] Qi WH, Wang MP. Size effect on the cohesive energy of nanoparticle. J Mater Sci Lett 2002;21:1743–5.

[250] Xie D, Wang MP, Qi WH. A simplified model to calculate the surface-to-volume atomic ratio dependent cohesive energy of nanocrystals. J Phys Condens Matter 2004;16:L401–5.
[251] Qi WH, Wang MP, Xu GY. The particle size dependence of cohesive energy of metallic nanosolids. Chem Phys Lett 2003;372:632–4.
[252] Jiang Q, Li JC, Chi BQ. Size-dependent cohesive energy of nanocrystals. Chem Phys Lett 2002;366:551–4.
[253] Kim HK, Huh SH, Park JW, Jeong JW, Lee GH. The cluster size dependence of thermal stabilities of both molybdenum and tungsten nanoclusters. Chem Phys Lett 2002;354:165–72.
[254] Gorecki T. Vacancies and changes of physical-properties of metals at melting-point. Z Metallkde 1974;65:426–31.
[255] Finis MW. The Harris functional applied to surface and vacancy formation energies in aluminium. J Phys Condens Matter 1990;2:331–42.
[256] Brooks H. Impurities and imperfection. Cleveland: American Society for Metals; 1955.
[257] Qi WH, Wang MP. Size dependence of vacancy formation energy of metallic nanosolids. Phys B 2003;334: 432–5.
[258] Brands EA. Smithells metals reference book. 6th ed. London: Butterworths; 1983. p. 15–22.
[259] Miedema AR. Surface energies of solid metals. Zeitschrift fur Metallkunde 1978;69:287–92.
[260] Dash JG. History of the search for continuous melting. Rev Mod Phys 1999;71:1737–43.
[261] Penfold J. The structure of the surface of pure liquids. Rep Prog Phys 2001;64:777–814.
[262] Akhter JI. Size-dependent overheating in confined Pb(111) films. J Phys Condens Matter 2005;17:53–60.
[263] Sheng HW, Ren G, Peng LM, Hu ZQ, Lu K. Overheating and melting-point depression of Pb nanosolids embedded in Al matrices. Philos Mag Lett 1996;73:179–86.
[264] Sheng HW, Ren G, Peng LM, Hu ZQ, Lu K. Epitaxial dependence of the melting behavior of In nanosolids embedded in Al matrices. J Mater Res 1997;12:119–23.
[265] Lereah Y, Deutscher G, Cheyssac P, Kofman R. A direct observation of low-dimensional effects on melting of small lead particles. Europhys Lett 1990;12:709–13.
[266] Rouse AA, Bernhard JB, Sosa ED, Golden DE. Variation of field emission and photoelectric thresholds of diamond films with average grain size. Appl Phys Lett 1999;75:3417–9.
[267] Hamada N, Sawada A, Oshiyama A. New one-dimensional conductors: graphitic microtubules. Phys Rev Lett 1992;68:1579–81.
[268] Skripov VP, Koverda VP, Skokov VN. Size effect on melting of small particles. Phys Status Solidi A 1981;66:109–18.
[269] Pcza JF, Barna A, Barna PB. Formation processes of vacuum-deposited indium films and thermodynamical properties of submicroscopic particles observed by in situ electron microscopy. J Vac Sci Technol 1969;6:472–5.
[270] Lee YJ, Lee EK, Kim S, Nieminen RM. Effect of potential energy distribution on the melting of clusters. Phys Rev Lett 2001;86:999–1002.
[271] Santucci SC, Goldoni A, Larciprete R, Lizzit S, Bertolo M, Baraldi A, et al. Calorimetry at surfaces using high-resolution core-level photoemission. Phys Rev Lett 2004;93:106105.
[272] Bergese P, Colombo I, Gervasoni D, Depero LE. Melting of nanostructured drugs embedded into a polymeric matrix. J Phys Chem B 2004;108:15488–93.
[273] Hwang I-S, Chang S-H, Fang C-K, Chen L-J, Tsong TT. Observation of finite-size effects on a structural phase transition of 2D nanoislands. Phys Rev Lett 2004;93:106101.
[274] Miao L, Bhethanabotla VR, Joseph B. Melting of Pd clusters and nanowires: a comparison study using molecular dynamics simulation. Phys Rev B 2005;72:134109.
[275] Zhang M, Yu Efremov M, Schiettekatte F, Olson EA, Kwan AT, Lai SL, et al. Size-dependent melting point depression of nanostructures: nanocalorimetric measurements. Phys Rev B 2000;62:10548–57.
[276] Jin ZH, Gumbsch P, Lu K, Ma E. Melting mechanisms at the limit of overheating. Phys Rev Lett 2001;87:055703.
[277] Defay R, Prigogine I. Surface tension and adsorption. New York: Wiley; 1951.
[278] Peters KF, Cohen JB, Chung YW. Melting of Pb nanocrystals. Phys Rev B 1998;57:13430–8.
[279] Tartaglino U, Zykova-Timan T, Ercolessi F, Tosatti E. Melting and nonmelting of solid surfaces and nanosystems. Phys Rep 2005;411:291–321.
[280] Yang QW, Zhu RZ, Wei JA, Wen YH. Surface-induced melting of metal nanoclusters. Chin Phys Lett Nov 2004;21(11):2171–4.
[281] Rose JH, Smith JR, Ferrante J. Universal features of bonding in metals. Phys Rev B 1983;28:1835–45.
[282] Tateno J. An empirical relation for the melting temperature of some ionic crystals. Solid State Commun 1972;10:61–2.
[283] Omar MA. Elementary solid state physics: principles and applications. New York: Addison-Wesley; 1975.

[284] Pluis B, Frenkel D, van der Veen JF. Surface-induced melting and freezing: II. A semi-empirical Landau-type model. Surf Sci 1990;239:282–300.
[285] Wautelet M, Dauchot JP, Hecq M. Phase diagrams of small particles of binary systems:a theoretical approach. Nanotechnology 2000;11:6–9.
[286] Wautelet M. Phase stability of electronically excited Si nanoparticles. J Phys Condens Matter 2004;16:L163–6.
[287] Wang J, Chen X, Wang G, Wang B, Lu W, Zhao J. Melting behavior in ultrathin metallic nanowires. Phys Rev B 2002;66:085408.
[288] Hu WY, Xiao SG, Yang JY, Zhang Z. Melting evolution and diffusion behavior of vanadium nanoparticles. Euro Phys J B Jun 2005;45(4):547–54.
[289] Lai SL, Guo JY, Petrova V, Ramanath G, Allen LH. Size-dependent melting properties of small tin particles: nanocalorimetric measurements. Phys Rev Lett 1996;77:99–102.
[290] Jiang Q, Lang XY. Glass transition of low-dimensional polystyrene. Macromol Rapid Commun 2004;25:825–8.
[291] Ding XZ, Liu XH. The Debye temperature of nanocrystalline titania measured by two different methods. Phys Status Solidi A 1996;158:433–9.
[292] Schmidt M, Kusche R, von Issendorff B, Haberland H. Irregular variations in the melting point of size-selected atomic clusters. Nature (London) 1998;393:238–40.
[293] Lai SL, Carlsson JRA, Allen LH. Melting point depression of Al clusters generated during the early stages of film growth: nanocalorimetry measurements. Appl Phys Lett 1998;72:1098–100.
[294] Bottani CE, Bassi AL, Tanner BK, Stella A, Tognini P, Cheyssac P, et al. Melting in metallic Sn nanoparticles studied by surface Brillouin scattering and synchrotron-x-ray diffraction. Phys Rev B 1999;59:R15601–4.
[295] Zhong J, Zhang LH, Jin ZH, Sui ML, Lu K. Overheating of Ag nanoparticles embedded in Ni matrix. Acta Mater 2001;49:2897–904.
[296] Lu L, Schwaiger R, Shan ZW, Dao M, Lu K, Suresh S. Nano-sized twins induce high rate sensitivity of flow stress in pure copper. Acta Mater 2005;53:2169–79.
[297] Veprek S, Veprek-Heijman MGJ, Karvankova P, Prochazka J. Different approaches to superhard coatings and nanocomposites. Thin Solid Films 2005;476:1–29.
[298] Ding F, Rosén A, Bolton K. Size dependence of the coalescence and melting of iron clusters: a molecular-dynamics study. Phys Rev B 2004;70:075416.
[299] Sun CQ, Shi Y, Li CM, Li S, Au Yeung TC. Size-induced undercooling and overheating in phase transitions in bare and embedded clusters. Phys Rev B 2006;73:075408.
[300] Dick K, Dhanasekaran T, Zhang Z, Meisel D. Size-dependent melting of silica-encapsulated gold nanoparticles. J Am Chem Soc 2002;124:2312–7.
[301] Eckert J, Holzer JC, Ahn CC, Fu Z, Johnson WL. Melting behavior of nanocrystalline alminum powders. Nanostruct Mater 1993;2:407.
[302] Lai SL, Ramanath G, Allen LH, Infante P. Heat capacity measurements of Sn nanostructures using a thin-film differential scanning calorimeter with 0.2 nJ sensitivity. Appl Phys Lett 1997;70:43–5.
[303] Allen GL, Gile WW, Jesser WA. Melting temperature of microcrystals embedded in a matrix. Acta Metall 1980;28:1695–701.
[304] Unruh KM, Huber TE, Huber CA. Melting and freezing behavior of indium metal in porus glasses. Phys Rev B 1993;48:9021–7.
[305] David TB, Lereah Y, Deutscher G, Kofmans R, Cheyssac P. Solid–liquid transition in ultra-fine lead particles. Philos Mag A 1995;71:1135.
[306] Goldstein N. The melting of silicon nanocrystals submicro thin-film structures derived from nanocrystal precursors. Appl Phys A 1996;62:33–7.
[307] Kenlinski P. Thermodynamics and kinetics of melting and growth of crystalline silicon clusters. Mat Res Soc Symp Proc 1999;536:311–6.
[308] Wu Y, Yang P. Melting and welding semiconductor nanowires in nanotubes. Adv Mater 2001;13:520–1.
[309] Peppiat SJ. Proc R Soc London Ser A 1975;345:401.
[310] Itoigawa H, Kamiyama T, Nakamura Y. Bi precipitates in $Na_2O-B_2O_3$ glasses. J Non-Cryst Solids 1997;210:95–100.
[311] Morishige K, Kawano K. Freezing and melting of methyl chloride in a single cylindrical pore: anomalous pore-size dependence of phase-transition temperature. J Phys Chem B 2000;104:2894–900.
[312] Molz E, Wong AP, Chan MHW, Beamish JR. Freezing and melting of fluids in porous glasses. Phys Rev B 1993;48:5741–50.
[313] Saka H, Nishikawa Y, Imura T. Temperature dependence of the stacking fault energy in silver-base alloys. Philos Mag A 1983;57:859–68.

[314] Gråback L, Bohr J. Overheating and undercooling of lead precipitates in aluminum. Phys Rev Lett 1990;64: 934–7.
[315] Zhang L, Jin ZH, Zhang LH, Sui ML, Lu K. Overheating of confined Pb thin films. Phys Rev Lett 2000;85:1484–7.
[316] Chattopadhyay K, Goswami R. Melting and overheating of metals and alloys. Prog Mater Sci 1997;42:287–300.
[317] Breaux GA, Benirschke RC, Sugai T, Kinnear BS, Jarrold MF. Hot and solid gallium clusters: too small to melt. Phys Rev Lett 2003;91:215508.
[318] Chacko S, Joshi K, Kanhere DG. Why do gallium clusters have a higher melting point than the bulk. Phys Rev Lett 2004;92:135506.
[319] Lu ZY, Wang CZ, Ho KM. Structures and dynamical properties of Cn, Sin, Gen, and Snn clusters with n up to 13. Phys Rev B 2000;61:2329–34.
[320] Chuang FC, Wang CZ, SerdarÖüt, Chelikowsky JR, Ho KM. Melting of small Sn clusters by ab initio MD simulations. Phys Rev B 2004;69:165408.
[321] Joshi K, Kanhere DG, Blundell SA. Abnormally high melting temperature of the Sn10 cluster. Phys Rev B 2002;66:155329.
[322] Breaux GA, Neal CM, Cao B, Jarrold MF. Tin clusters that do not melt: calorimetry measurements up to 650 K. Phys Rev B 2005;71:073410.
[323] Olson EA, Efremov MY, Zhang M, Zhang Z, Allen LH. Size-dependent melting of Bi nanoparticles. J Appl Phys 2005;97:034304.
[324] Zheng WT, Zheng B. Private communications. JIlin University; July 2005.
[325] Jones RO. Simulated annealing study of neutral and charged clusters: AlN and GaN. J Chem Phys 1993;99:1194–206.
[326] Shvartsburg AA, Liu B, Lu ZY, Wang CZ, Jarrold MF, Ho KM. Structures of germanium clusters:where the growth patterns of silicon and germanium clusters diverge. Phys Rev Lett 1999;83:2167–70.
[327] Lu GH, Deng S, Wang T, Kohyama M, Yamamoto R. Theoretical tensile strength of an Al grain boundary. Phys Rev B 2004;69:134106.
[328] Carling K, Wahnstrüm G, Mattsson TR, Mattsson AE, Sandberg N, Grimvall G. Vacancies in metals:from first-principles calculations to experimental data. Phys Rev Lett 2000;85:3862–5.
[329] Ogata S, Li J, Yip S. Ideal pure shear strength of aluminum and copper. Science 2002;298:807–11.
[330] Liu HH, Jiang EY, Bai HL, Wu P, Li ZQ, Sun CQ. Possible paths of magic clusters growth. J Theor Chem 2005;728:203–7.
[331] Haberland H, Hippler T, Donges J, Kostko O, Schmidt M, von Issendorff B. Melting of sodium clusters: where do the magic numbers come from? Phys Rev Lett 2005;94(3):035701.
[332] Sun CQ, Li CM, Li S, Tay BK. Breaking limit of atomic distance in an impurity-free monatomic chain. Phys Rev 2004;B67:245402.
[333] Bachels T, Guntherodt HJ, Schafer R. Melting of isolated tin nanoparticles. Phys Rev Lett 2000;85:1250–3.
[334] Breaux GA, Neal CM, Cao B, Jarrold MF. Melting, premelting, and structural transitions in size-selected aluminum clusters with around 55 atoms. Phys Rev Lett 2005;94:173401.
[335] Huang FF, Mankey GJ, Kief MT, Willis RF. Finite-size scaling behavior of ferromagnetic thin films. J Appl Phys 1993;73:6760–2.
[336] Kenning GG, Slughter JM, Cowen JA. Finite-size effects in a CuMn spin-glass. Phys Rev Lett 1997;59:2596–9.
[337] Qiu ZQ, Person J, Bader SD. Asymmetry of the spin reorientation transition in ultrathin Fe films and wedges grown on Ag(100). Phys Rev Lett 1993;70:1006–9.
[338] Ishikawa K, Yoshikawa K, Okada N. Size effect on the ferroelectric phase transition in $PbTiO_3$ ultrafine particles. Phys Rev 1988;B37:5852–5.
[339] Yu T, Shen ZX, Toh WS, Xue JM, Wang JJ. Size effect on the ferroelectric phase transition in $SrBi_2Ta_2O_9$ nanoparticles. J Appl Phys 2003;94:618–20.
[340] Pogrebnyakov AV, Redwing JM, Jones JE, Xi XX, Xu SY, Li Q, et al. Thickness dependence of the properties of epitaxial $MgB_2$ thin films grown by hybrid physical–chemical vapor deposition. Appl Phys Lett 2003;82: 4319–21.
[341] Tsai AP, Chandrasekhar, Chattopadhyay N. Size effect on the superconducting transition of embedded lead particles in an Al–Cu–V amorphous matrix. Appl Phys Lett 1999;75:1527–8.
[342] Giaever I, Zeller HR. Superconductivity of small tin particles measured by tunneling. Phys Rev Lett 1968;20:1504–7.
[343] Stampanoni M, Vaterlaus A, Aeschlimann M, Meier F. Magnetism of epitaxial bcc Iron on Ag(001) observed by spin-polarized photoemission. Phys Rev Lett 1987;59:2483–5.

[344] Baibich MN, Broto JM, Fert A, Van Dau FN, Petrou F, Eitenne P, et al. Giant magnetoresistance of (001)Fe/(001)Cr magnetic superlattices. Phys Rev Lett 1988;61:2472–5.
[345] Liu C, Moog R, Bader SD. Polar Kerr-effect observation of perpendicular surface anisotropy for ultrathin fcc Fe grown on Cu(100). Phys Rev Lett 1998;60:2422–5.
[346] Schneider CM, Bressler P, Schuster P, Kirschner J, de Miguel JJ, Miranda R. Curie temperature of ultrathin films of fcc-cobalt epitaxially grown on atomically flat Cu(100) surfaces. Phys Rev Lett 1990;64:1059–62.
[347] Hu X, Kawazoe Y. Mean-field theory for critical phenomena in bilayer systems. Phys Rev B 1994;50:12647–58.
[348] Ou JT, Wang F, Lin DL. Critical behavior of magnetic films in the Ising model. Phys Rev E 1997;56:2805–10.
[349] Li Y, Baberschke K. Dimensional crossover in ultrathin Ni(111) films on W(110). Phys Rev Lett 1992;68:1208–11.
[350] Tischer M, Arvanitis D, Yokoyanma T, Lederer T, Troger L, Baberschke K. Temperature dependent MCXD measurements of thin Ni films on Cu(100). Surf Sci 1994;307–309:1096–101.
[351] Tjeng LH, Idzerda YU, Rudolf P, Sette F, Chen CT. Soft-X-ray magnetic circular dichroism. A new technique for probing magnetic properties of magnetic surfaces and ultrathin films. J Magn Magn Mater 1992;109:288–92.
[352] Jiang JS, Chien CL. Magnetization and finite-size effects in Gd/W multilayers. J Appl Phys 1996;79:5615–7.
[353] Jiang JS, Davidovic D, Reich DH, Chien CL. Oscillatory superconducting transition temperature in Nb/Gd multilayers. Phys Rev Lett 1995;74:314–7.
[354] Zhou PH, Xue DS. Finite-size effect on magnetic properties in Prussian blue nanowire arrays. J Appl Phys Jul 1 2004;96(1):610–4.
[355] Fisher ME, Barber MN. Scaling theory for finite-size effects in the critical region. Phys Rev Lett 1972;28:1516–9.
[356] Richie DS, Fisher ME. Finite-size and surface effects in Heisenberg films. Phys Rev B 1973;7:480–94.
[357] Barber MN. In: Domb C, Lebowita J, editors. Phase transitions and critical phenomena, vol. 8. New York: Academic; 1983.
[358] Binder K, Hohenberg PC. Surface effects on magnetic phase transitions. Phys Rev B 1974;9:2194–214.
[359] Zhang R, Willis RF. Thickness-dependent curie temperatures of ultrathin magnetic films: effect of the range of spin–spin interactions. Phys Rev Lett 2001;86:2665–8.
[360] Nikolaev VI, Shipilin AM. The influence of breaking of exchange bonds on the curie temperature. Phys Solid State 2003;45:1079–80.
[361] Sadeh B, Doi M, Shimizu T, Matsui MJ. Dependence of the Curie temperature on the diameter of $Fe_3O_4$ ultra-fine particles. J Magn Soc Jpn 2000;24:511–4.
[362] Degennes PG. Superconductivity of metals and alloys. New York: Benjamin; 1966.
[363] Coswami R, Banerjee S, Chattopadhyay K, Raychaudhuri AK. Superconductivity in rapidly quenched metallic systems with nanoscale structure. J Appl Phys 1993;73:2934–40.
[364] Kubo R. Electronic properties of metallic fine particles. 1. J Phys Soc Jpn 1962;17:975.
[365] Anderson PW. Theory of dirty superconductors. J Phys Chem Solids 1959;11:26–30.
[366] Strongin M, Thompson RS, Karnmerer OF, Crow JE. Destruction of superconductivity in disordered near-monolayer films. Phys Rev B 1970;1:1078–91.
[367] Muhlschlegel B, Scalapino DJ, Denton R. Thermodynamic properties of small superconducting particles. Phys Rev B 1972;6:1767–77.
[368] Guo Y, Zhang YF, Bao XY, Han TZ, Tang Z, Zhang LX, et al. Superconductivity modulated by quantum size effects. Science 2004;306:1915–7.
[369] Pogrebnyakov AV, Redwing JM, Raghavan S, Vaithyanathan V, Schlom DG, Xu SY, et al. Enhancement of the superconducting transition temperature of $MgB_2$ by a strain-induced bond-stretching mode softening. Phys Rev Lett 2004;93:147006.
[370] Nagamatsu J, Nakagawa N, Muranaka T, Zenitani Y, Akimitsu J. Superconductivity at 39 K in magnesium diboride. Nature (London) 2001;410:63–4.
[371] Hur N, Sharma PA, Guha S, Cieplak MZ, Werder DJ, Horibe Y, et al. High-quality $MgB_2$ films on boron crystals with onset Tc of 417 K. Appl Phys Lett 2001;79:4180–2.
[372] Yildirim T, Gulseren O. A simple theory of 40 K superconductivity in $MgB_2$:first-principles calculations of Tc, its dependence on boron mass and pressure. J Phys Chem Solids 2002;63:2201–6.
[373] Honebecq V, Huber C, Maglione M, Antonietti M, Elissalde C. Dielectric properties of pure (BaSr)$TiO_3$ and composites with different grain sizes ranging from the nanometer to the micrometer. Adv Funct Mater 2004;19:899–904.
[374] Zhao Z, Buscaglia V, Viviani M, Buscaglia MT, Mitoseriu L, Testino A, et al. Grain-size effects on the ferroelectric behavior of dense nanocrystalline $BaTiO_3$ ceramics. Phys Rev B 2004:70. 024107.

[375] Hong J, Song HW, Choi J, Kim SK, Kim Y, No K. Dependence of ferroelectricity on film thickness in nano-scale Pb(Zr,Ti)O-3 thin films. Integr Ferroelectr 2004;68:157.
[376] Wang CL, Xin Y, Wang XS, Zhong WL. Size effects of ferroelectric particles described by the transverse Ising model. Phys Rev B 2000;62:11423–7.
[377] Jiang B, Bursill LA. Phenomenological theory of size effects in ultrafine ferroelectric particles of lead titanate. Phys Rev B 1999;60:9978–82.
[378] Huang HT, Sun CQ, Zhang TS, Hing P. Grain-size effect on ferroelectric $Pb(Zr_{1-x}Ti_x)O_3$ solid solutions induced by surface bond contraction. Phys Rev B 2001;63:184112.
[379] Huang HT, Sun CQ, Hing P. Surface bond contraction and its effect on the nanometric sized lead zirconate titanate. J Phys Condens Matter 2000;12:L127–32.
[380] Tanaka M, Makino Y. Finite size effects in submicron barium titanate particles. Ferroelectr Lett 1998;24:13–23.
[381] Munkholm A, Streiffer SK, Murty MVR, Eastman JA, Thompson C, Auciello O, et al. Antiferrodistortive reconstruction of the $PbTiO_3$(001) surface. Phys Rev Lett 2002;88:016101.
[382] Huang H, Zhou LM, Guo J, Hng HH, Oh JT, Hing P. F spots and domain patterns in rhombohedral PbZr0.9Ti0.1O3. Appl Phys Lett 2003;83:3692–4.
[383] Huang H, Sun CQ, Tianshu Z, Hong Z, Oh JT, Hing P. Stress effect on the pyroelectric properties of lead titanate thin films. Integr Ferroelectr 2003;51:81–90.
[384] Jiang Q, Cui XF, Zhao M. Size effects on Curie temperature of ferroelectric particles. Appl Phys A 2004;78: 703–4.
[385] Zysler ED, Firani D, Testa AM, Suber L, Agostnelli E, Godinho M. Size dependence of the spin–flop transition in hematite nanosolids. Phys Rev B 2003;68:212408.
[386] Amin A, Arajs S. Morin temperature of annealed submicronic $\alpha$-$Fe_2O_3$ particles. Phys Rev B 1987;35:4810–1.
[387] Weschke E, Ott H, Schierle E, Schüßler-Langeheine C, Vyalikh DV, Kaindl G, et al. Finite-size effect on magnetic ordering temperatures in long-period antiferromagnets: holmium thin films. Phys Rev Lett 2004;93:57204.
[388] Fullerton EE, Riggs KT, Sowers CH, Bader SD, Berger A. Suppression of biquadratic coupling in Fe /Cr(001) superlattices below the Néel transition of Cr. Phys Rev Lett 1995;75:330–3.
[389] Rao SS, Anuradha KN, Sarangi S, Bhat SV. Weakening of charge order and antiferromagnetic to ferromagnetic switch over in $Pr_{0.5}Ca_{0.5}MnO_3$ nanowires. Appl Phys Lett 2005;87:182503.
[390] Von Braun F, Delft J. Superconductivity in ultrasmall metallic grains. Phys Rev B 1999;59:9527–44.
[391] Bergholz R, Gradmann U. Structure and magnetism of oligatomic Ni(111)-films on Re(0001). J Magn Magn Mater 1984;45:389–98.
[392] Uchina K, Sadanaga Y, Hirose T. J Am Ceram Soc 1999;72:1555.
[393] Chattopadhyay S, Ayyub P, Palkar VR, Gurjar AV, Wankar RM, Multani M. Finite-size effects in antiferroelectric $PbZrO_3$ nanoparticles. J Phys Condens Matter 1997;9:8135–45.
[394] Li S, White T, Plevert J, Sun CQ. Superconductivity of nano-crystalline $MgB_2$. Supercond Sci Technol 2004;17:S589–94.
[395] Li S, White T, Sun CQ, Fu YQ, Plevert J, Lauren K. Discriminating lattice structural effects from electronic contributions to the superconductivity of doped $MgB_2$ with nanotechnology. J Phys Chem B 2004;108:6415–9.
[396] Schlag S, Eicke HF, Stern WB. Size driven phase transition and thermodynamic properties of nanocrystalline $BaTiO_3$. Ferroelectrics 1995;173:351–69.
[397] Valiev RZ, Islamgaliev RK, Alexandrov IV. Bulk nanostructured materials from severe plastic deformation. Prog Mater Sci 2000;45:103–89.
[398] Ouyang G, Wang CX, Yang GW. Anomalous interfacial diffusion in immiscible metallic multilayers: a size-dependent kinetic approach. Appl Phys Lett 2005;86(17). 171914.
[399] Razumovskii IM, Kornelyuk LG, Valiev RZ, Sergeev VI. Diffusion along nonequilibrium grain boundaries in a nickel-base superalloy. Mater Sci Eng A 1993;167:123–7.
[400] Horvath J. Diffusion in nanocrystalline materials. Diffusion and defect data – solid state data, Part A: defect and diffusion forum 1989;66–69:207–27.
[401] Mütschele T, Kirchheim R. Segregation and diffusion of hydrogen in grain boundaries of palladium. Scr Met 1987;21:135–40.
[402] Kolobov YR, Grabovetskaya GR, Ratochka IV, Kabanova ER, Naidenkin EV, Lowe T. Effect of grain-boundary diffusion fluxes of copper on the acceleration of creep in submicrocrystalline nickel. Ann Chim Sci des Materiaux 1996;21:483–91.
[403] Wurschum R, Kubler A, Gruss S, Acharwaechter P, Frank W, Valiev RZ, et al. Tracer diffusion and crystallite growth in ultra-fine-grained Pd prepared by severe plastic deformation. Ann Chim Sci Mater 1996;21: 471–82.

[404] Wang ZB, Tao NR, Tong WP, Lu J, Lu K. Diffusion of chromium in nanocrystalline iron produced by means of surface mechanical attrition treatment. Acta Mater 2003;51:4319–29.
[405] Mishin YM, Razumovskii IM. Development of boundary diffusion models. Scripta Metall 1991;25:1375–80.
[406] Kim HC, Alford TL, Allee DR. Thickness dependence on the thermal stability of silver thin films. Appl Phys Lett 2002;81:4287–9.
[407] Li CM, Cha CS. Electrodes with surface intercalated powder of catalysts: II. Microelectrodes with surface-intercalated powder of catalysts. Acta Chim Sin 1988;1:14–20.
[408] Li CM, Cha CS. Powder microelectrodes: II. Irreversible electrode system. Acta Phy-Chim Sin 1988;4:273–7.
[409] Cha CS, Li CM, Yang HX, Liu PF. Powder microelectrodes. J Electroanal Chem 1994;368:47–51.
[410] Li CM, Cha CS. Porous carbon/Teflon composite enzyme glucose sensors. Front Biosci 2004;9:3324–30.
[411] Schumacher S, Birringer R, Strauss R, Gleiter H. Diffusion of silver in nanocrystalline copper between 303 and 373 K. Acta Metall 1989;37:2485–8.
[412] Suryanarayana C. Mechanical alloying and milling. Prog Mater Sci 2001;46:1–184.
[413] Calka A, Nikolov JI, Williams JS. Formation, structure and stability of iron nitrides made by reactive ball milling. Mater Sci Forum 1996;225–227:527–32.
[414] El-Eskandarany MS, Sumiyama K, Aoki K, Suzuki K. Mater Sci Forum 1992;88–90:801–6.
[415] Mongis J, Peyre JP, Tournier C. Nitriding of nicroalloyed steels. Heat Treat Metals 1984;3:71–5.
[416] Meier J, Schiotz J, Liu P, Norskov JK, Stimming U. Nano-scale effects in electrochemistry, source. Chem Phys Lett 2004;390:440–4.
[417] Gillet M, Aguir K, Bendahan M, Mennini P. Grain size effect in sputtered tungsten trioxide thin films on the sensitivity to ozone. Thin Solid Films July 22, 2005;484(1–2):358–63.
[418] Campbell CT. The active site in nanoparticle gold catalysis. Science 2004;306:234–5.
[419] Hu Z, Boiadjiev V, Thundat T. Nanocatalytic spontaneous ignition and self-supporting room-temperature combustion. Energy Fuels 2005;19:855–8.
[420] Ajayan PM, Terrones M, de la Guardia A, Huc V, Grobert N, Wei BQ, et al. Nanotubes in a flash – ignition and reconstruction. Science 2002;296:205.
[421] Chen MS, Goodman DW. The structure of catalytically active gold on titania. Science 2004;306:252–5.
[422] Liu Z, Gao W, Dahm K, Wang F. Oxidation behaviour of sputter-deposited Ni–Cr–Al micro-crystalline coatings. Acta Metallurg Mater 1998;46:1691–700.
[423] Gao W, Liu Z, Li Z. Nano- and micro-crystal coatings and their high-temperature applications. Adv Mater 2001;13:1001–4.
[424] Liu Z, Gao W, He Y. Surface nano-crystallisation of 310s stainless steel and its effect on the oxidation behaviour. J Mater Eng Perf 1998;7:88–92.
[425] Sun CQ, Xie H, Zhang W, Ye H, Hing P. Preferential oxidation of diamond {111}. J Phys D 2000;33:2196–9.
[426] Lopez N, Janssens TVW, Clausen BS, Xu Y, Mavrikakis M, Bligaard T, et al. On the origin of the catalytic activity of gold nanoparticles for low-temperature CO oxidation. J Catal 2004;223:232–5.
[427] Alymov ML, Maltina EI, Stepanov YN. Nanostruct Mater 1994;4:737.
[428] Zayed MK, Elsayed-Ali HE. Condensation on (002) graphite of liquid bismuth far below its bulk melting poin. Phys Rev B 2005;72:205426.
[429] Jiang Q, Shi FG. Size-dependent initial sintering temperature of ultrafine particles. J Mater Sci Tech 1998;14:171–2.
[430] Röder H, Hahn E, Brune H, Bucher JP, Kern K. Building one- and two-dimensional nanostructures by diffusion-controlled aggregation at surfaces. Nature (London) 1993;366:141–3.
[431] Liu BG, Wu J, Wang EG, Zhang Z. Two-dimensional pattern formation in surfactant-mediated epitaxial growth. Phys Rev Lett 1999;83:1195–8.
[432] Li MZ, Wendelken JF, Liu BG, Wang EG, Zhang Z. Decay characteristics of surface mounds with contrasting interlayer mass transport channels. Phys Rev Lett 2001;86:2345–8.
[433] Zhu WG, Mongeot FB, Valbusa U, Wang EG, Zhang Z. Adatom ascending at step edges and faceting on fcc metal (110) surfaces. Phys Rev Lett 2004;92:106102.
[434] Wu J, Wang EG, Varga K, Liu BG, Panfelides ST, Zhang Z. Island shape selection in Pt(111) submonolayer homoepitaxy without or with CO as adsorbates. Phys Rev Lett 2002;89:146103.
[435] Takagahara T. Electron–phonon interactions and excitonic dephasing in semiconductor nanocrystals. Phys Rev Lett 1993;71:3577–80.
[436] Zi J, Büscher H, Falter C, Ludwig W, Zhang KM, Xie XD. Raman shifts in Si nanocrystals. Appl Phys Lett 1996;69:200–2.

[437] Fujii M, Kanzawa Y, Hayashi S, Yamamoto K. Raman scattering from acoustic phonons confined in Si nanocrystals. Phys Rev B 1996;54:R8373–6.
[438] Cheng W, Ren SF. Calculations on the size effects of Raman intensities of silicon quantum dots. Phys Rev B 2002;65:205305.
[439] Klein MC, Hache F, Ricard D, Flytzanis C. Size dependence of electron–phonon coupling in semiconductor nanospheres: the case of CdSe. Phys Rev B 1990;42:11123–32.
[440] Trallero-Giner C, Debernardi A, Cardona M, Menendez-Proupi E, Ekimov AI. Optical vibrons in CdSe dots and dispersion relation of the bulk material. Phys Rev B 1998;57:4664–9.
[441] Hu XH, Zi J. Reconstruction of phonon dispersion in Si nanocrystals. J Phys Condens Matter 2002;14:L671–7.
[442] Palpant B, Portales H, Saviot L, Lerme J, Prevel B, Pellarin M, et al. Quadrupolar vibrational mode of silver clusters from plasmon-assisted Raman scattering. Phys Rev B 1999;60:17107–11.
[443] Fujii M, Nagareda T, Hayashi S, Yamamoto K. Low-frequency Raman scattering from small silver particles embedded in $SiO_2$ thin films. Phys Rev B 1991;44:6243–8.
[444] Lamb H. Proc London Math Soc 1882;13:189.
[445] Duval E. Far-infrared and Raman vibrational transitions of a solid sphere: selection rules. Phys Rev B 1992;46:5795–7.
[446] Verma P, Cordts W, Irmer G, Monecke J. Acoustic vibrations of semiconductor nanocrystals in doped glasses. Phys Rev B 1999;60:5778–85.
[447] Ferrari M, Gonella F, Montagna M, Tosello C. Detection and size determination of Ag nanoclusters in ion-exchanged soda-lime glasses by waveguided Raman spectroscopy. J Appl Phys 1996;79:2055–9.
[448] Zi J, Zhang K, Xie X. Microscopic calculations of Raman scattering from acoustic phonons confined in Si nanocrystals. Phys Rev B 1998;58:6712.
[449] Narvaez GA, Kim J, Wilkins JW. Effects of morphology on phonons of nanoscopic silver grains. Phys Rev 2005;B 72:155411.
[450] Scamarcio G, Lugara M, Manno D. Size-dependent lattice contraction in $CdS_{1-x}Se_x$ nanocrystals embedded in glass observed by Raman scattering. Phys Rev B 1992;45:13792–5.
[451] Liang LH, Shen CM, Chen XP, Liu WM, Gao HJ. The size-dependent phonon frequency of semiconductor nanocrystals. J Phys Condens Matt 2004;16:267–72.
[452] Dieguez A, Romano-Rodrýguez A, Vila A, Morante JR. The complete Raman spectrum of nanometric $SnO_2$ particles. J Appl Phys 2001;90:1550–7.
[453] Iqbal Z, Vepřek S. Raman scattering from hydrogenated microcrystalline and amorphous silicon. J Phys Condens Matter 1982;15:377–92.
[454] Anastassakis E, Liarokapis E. Polycrystalline Si under strain: elastic and lattice-dynamical considerations. J Appl Phys 1987;62:3346–52.
[455] Richter H, Wang ZP, Ley L. One phonon Raman spectrum in microcrystalline silicon. Solid State Commun 1981;39:625–9.
[456] Campbell IH, Fauchet PM. Eeffects of microcrystal size and shape on the phonon Raman spectra of of crystalline semiconductors. Solid State Commun 1986;58:739–41.
[457] Choi HC, Jung YM, Kim SB. Size effects in the Raman spectra of $TiO_2$ nanoparticles. Vib Spectrosc 2005;37:33–8.
[458] Wang X, Huang DM, Ye L, Yang M, Hao PH, Fu HX, et al. Pinning of photoluminescence peak positions for light-emitting porous silicon: an evidence of quantum size effect. Phys Rev Lett 1993;71:1265–7.
[459] Andújar JL, Bertran E, Canillas A, Roch C, Morenza JL, Influence of pressure and radio frequency power on deposition rate and structural properties of hydrogenated amorphous silicon thin films prepared by plasma deposition. J Vac Sci Technol A 1991;9:2216–21.
[460] Ohtani N, Kawamura K. Theoretical investigation of Raman scattering from microcrystallites. Solid State Commun 1990;75:711–5.
[461] Banyai L, Koch SW. Semiconductor quantum dots. Singapore: World Scientific; 1993.
[462] Tanaka A, Onari S, Arai T. Raman scattering from CdSe microcrystals embedded in germanate glass matrix. Phys Rev B 1992;45:6587–92.
[463] Hwang YN, Shin S, Park HL, Park SH, Kim U, Jeong HS, et al. Effect of lattice contraction on the Raman shifts of CdSe quantum dots in glass matrices. Phys Rev B Condens Matter 1996;B54:15120–4.
[464] Pan LK, Sun CQ, Li CM. Elucidating Si–Si dimer vibration from the size-dependent Raman shift of nanosolid Si. J Phys Chem B 2004;108:L3404–6.
[465] Viera G, Huet S, Boufendi L. Crystal size and temperature measurements in nanostructured silicon using Raman spectroscopy. J Appl Phys 2001;90:4175–83.

[466] Fauchet PM, Campbell IH. Raman-spectroscopy of low-dimensional semiconductors, CRC. Crit Rev Solid State Mater Sci 1988;14:S79–101.
[467] Sood AK, Jayaram K, Victor D, Muthu S. Raman and high-pressure photoluminescence studies on porous silicon. J Appl Phys 1992;72:4963–5.
[468] Ossadnik C, Vepřek S, Gregora I. Applicability of Raman scattering for the characterization of nanocrystalline silicon. Thin Solid Films 1999;337:148–51.
[469] Cheng GX, Xia H, Chen KJ, Zhang W, Zhang XK. Raman measurement of the grain size for silicon crystallites. Phys Status Solidi A 1990;118:K51–4.
[470] Verma P, Gupta L, Abbi SC, Jain KP. Confinement effects on the electronic and vibronic properties of CdS0.65Se0.35 nanoparticles grown by thermal annealing. J Appl Phys 2000;88:4109–16.
[471] Spanier JE, Robinson RD, Zhang F, Chan SW, Herman IP. Size-dependent properties of $CeO_2$ nanoparticles as studied by Raman scattering. Phys Rev B 2001;64:245407.
[472] Shek CH, Lin GM, Lai JKL. Effect of oxygen deficiency on the Raman spectra and hyperfine interactions of nanometer $SnO_2$. Nanosruct Mater 1999;11:831–5.
[473] Seong MJ, Micic OI, Nozik AJ, Mascarenhas A, Cheong HM. Size-dependent Raman study of InP quantum dots. Appl Phys Lett 2003;82:185–7.
[474] Talati M, Jha PK. Low-frequency acoustic phonons in nanometric $CeO_2$ particles. Phys E-Low-D Systems & Nanostructures 2005;28:171–7.
[475] Gangopadhyay P, Kesavamoorthy R, Nair KGM, Dhandapani R. Raman scattering studies on silver nanoclusters in a silica matrix formed by ion-beam mixing. J Appl Phys 2000;88:4975–9.
[476] Gotić M, Ivanda M, Sekulić A, Musić S, Popović S, Turković A, Furić K. Microstructure of nanosized $TiO_2$ obtained by sol–gel synthesis. Mater Lett 1996;28:225–9.
[477] Saviot L, Champagnon B, Duval E, Kudriavtsev IA, Ekimov AI. Size dependence of acoustic and optical vibrational modes of CdSe nanocrystals in glasses. J Non-Crystal Solids 1996;197:238–46.
[478] Schuppler S, Friedman SL, Marcus MA, Adler DL, Xie YH, Ross FM, et al. Size, shape, and composition of luminescent species in oxidized Si nanocrystals and H-passivated porous Si. Phys Rev B 1995;52:4910–25.
[479] Heikkila L, Kuusela T, Hedman HP. Electroluminescence in Si/SiO2 layer structures. J Appl Phys 2001;89:2179–84.
[480] Garrido B, Lopez M, Gonzalez O, Perez-Rodrýguez A, Morante JR, Bonafos C. Correlation between structural and optical properties of Si nanocrystals embedded in $SiO_2$: the mechanism of visible light emission. Appl Phys Lett 2000;77:3143–5.
[481] Tomasulo A, Ramakrishna MV. Quantum confinement effects in semiconductor clusters II. J Chem Phys 1996;105:3612–26.
[482] Jain SC, Willander M, Narayan J, van Overstraeten R. III—nitrides: growth, characterization, and properties. J Appl Phys 2000;87:965–1006.
[483] Ramvall P, Tanaka S, Nomura S, Riblet P, Aoyagi Y. Observation of confinement-dependent exciton binding energy of GaN quantum dots. Appl Phys Lett 1998;73:1104–6.
[484] Guzelian AA, Banin U, Kadavanich AV, Peng X, Alivisatos AP. Colloidal chemical synthesis and characterization of InAs nanocrystal quantum dots. Appl Phys Lett 1996;69:1432–4.
[485] Micic OI, Sprague J, Lu Z, Nozik AJ. Highly efficient band-edge emission from InP quantum dots. Appl Phys Lett 1996;68:3150–2.
[486] Ferreyra JM, Proetto CR. Quantum size effects on excitonic Coulomb and exchange energies in finite-barrier semiconductor quantum dots. Phys Rev B 1999;60:10672–5.
[487] Wang Y, Herron N. Quantum size effects on the exciton energy of CdS clusters. Phys Rev B 1990;42:7253–5.
[488] Krishna MVR, Friesner RA. Exciton spectra of semiconductor clusters. Phys Rev Lett 1991;67:629–32.
[489] Lippens PE, Lannoo M. Comparison between calculated and experimental values of the lowest excited electronic state of small CdSe crystallites. Phys Rev B 1989;41:6079–81.
[490] Chu DS, Dai CM. Quantum size effects in CdS thin films. Phys Rev B 1992;45:11805–10.
[491] Albe V, Jouanin C, Bertho D. Confinement and shape effects on the optical spectra of small CdSe nanocrystals. Phys Rev B 1998;58:4713–20.
[492] Bawendi MG, Wilson WL, Rothberg L, Carroll PJ, Jedju TM, Steigerwald ML, et al. Electronic structure and photoexcited-carrier dynamics in nanometer-size CdSe clusters. Phys Rev Lett 1990;65:1623–6.
[493] Hayashi S, Sanda H, Agata M, Yamamoto K. Resonant Raman scattering from ZnTe microcrystals: evidence for quantum size effects. Phys Rev B 1989;40:5544–8.
[494] Gourgon C, Dang LS, Mariette H. Optical properties of CdTe/CdZnTe wires and dots fabricated by a final anodic oxidation etching. Appl Phys Lett 1995;66:1635–7.

[495] Fang BS, Lo WS, Chien TS, Leung TC, Lue CY, Chan CT, et al. Surface band structures on Nb(001). Phys Rev B 1994;50:11093–101.
[496] Schmeißer D, Böhme O, Yfantis A, Heller T, Batchelor DR, Lundstrom I, et al. Dipole moment of nanoparticles at interfaces. Phys Rev Lett 1999;83:380–3.
[497] Tsu R, Babic D, Loriatti Jr L. Simple model for the dielectric constant of nanoscale silicon particle. J Appl Phys 1997;82:1327–9.
[498] Sun CQ, Sun XW, Tay BK, Lau SP, Huang H, Li S. Dielectric suppression and its effect on photoabsorption of nanometric semiconductors. J Phys D 2001;34:2359–62.
[499] Ekimov AI, Onushchenko AA. Quantum size effect in the optical spectra of semiconductor microcrystals. Sov Phys Semicon 1982;16:775–8.
[500] Steigerwald ML, Brus LE. Semiconductor crystallites:a class of large molecules. Acc Chem Res 1990;23:183–8.
[501] Fu H, Zunger A. Local-density-derived semiempirical nonlocal pseudopotentials for InP with applications to large quantum dots. Phys Rev B 1997;55:1642–53.
[502] Wang LW, Zunger A. Dielectric constants of silicon quantum dots. Phys Rev Lett 1994;73:1039–42.
[503] Wang X, Qu L, Zhang J, Peng X, Xiao M. Surface-related emission in highly luminescent CdSe quantum dots. Nanolett 2003;3:1103–6.
[504] Aiyer HN, Vijayakrishnan V, Subbanna GN, Rao CNR. Investigations of Pd clusters by the combined use of HREM, STM, high-energy spectroscopies and tunneling conductance measurements. Surf Sci 1994;313:392–8.
[505] Sun CQ, Chen TP, Tay BK, Li S, Huang H, Zhang YB, et al. An extended quantum confinement theory: surface-coordination imperfection modifies the entire band structure of a nanosolid. J Phys D 2001;34:3470–9.
[506] Yang DQ, Kabashin AV, Pilon-Marien VG, Sacher E, Meunier M. Optical breakdown processing: influence of the ambient gas on the properties of the nanostructured Si-based layers formed. J Appl Phys 2004;95:5722–8.
[507] Bawendi MG, Carroll PJ, Wilson WL, Brus LE. Luminescence properties of CdSe quantum crystallites: resonance between interior and surface localized states. J Chem Phys 1992;96:946–54.
[508] Pan LK, Sun CQ. Coordination imperfection enhanced electron–phonon interaction. J Appl Phys 2004;95:3819–21.
[509] Sanders GD, Chang YC. Theory of optical properties of quantum wires in porous silicon. Phys Rev 1992;B45:9202–13.
[510] Theiss W, Scout thin film analysis software handbook, hard and software: M Theiss, Aachen, Germany, 2001, www.mtheiss.com.
[511] Furukawa S, Miyasato T. Quantum size effects on the optical band gap of microcrystalline Si:H. Phys Rev B 1988;38:5726–9.
[512] Guha S, Steiner P, Lang W. Resonant Raman scattering and photoluminescence studies of porous silicon membranes. J Appl Phys 1996;79:8664–8.
[513] Kanemitsu Y, Uto H, Masumoto Y, Matsumoto T, Futagi T, Mimura H. Microstructure and optical properties of free-standing porous silicon films: size dependence of absorption spectra in Si nanometer-sized crystallites. Phys Rev B 1993;48:2827–30.
[514] von Behren J, van Buuren T, Zacharias M, Chimowitz EH, Fauchet PM. Quantum confinement in nanoscale silicon: the correlation of size with bandgap and luminescence. Solid State Commun 1998;105:317–22.
[515] Canham L. Properties of porous silicon. London: INSPEC; 1997. p. 213.
[516] Dorigoni L, Bisi O, Bernardini F, Ossicini S. Electron states and luminescence transition in porous silicon. Phys Rev B 1996;53:4557–64.
[517] Hybertsen MS, Needels M. First-principles analysis of electronic states in silicon nanoscale quantum wires. Phys Rev B 1993;48:4608–11.
[518] Ohno T, Shiraishi K, Ogawa T. Intrinsic origin of visible light emission from silicon quantum wires: electronic structure and geometrically restricted exciton. Phys Rev Lett 1992;69:2400–3.
[519] Yeh CY, Zhang SB, Zunger A. Confinement, surface, and chemisorption effects on the optical properties of Si quantum wires. Phys Rev B 1994;50:14405–15.
[520] Read AJ, Needs RJ, Nash KJ, Canham LT, Calcott PDJ, Qteish A. First-principles calculations of the electronic properties of silicon quantum wires. Phys Rev Lett 1992;69:1232–5.
[521] Pavesi L, Giebel G, Ziglio F, Mariotto G, Priolo F, Campisano SU, et al. Nanocrystal size modifications in porous silicon by preanodization ion implantation. Appl Phys Lett 1994;65:2182–4.
[522] Hasegawa S, Matsuda M, Kurata Y. Bonding configuration and defects in amorphous SiN$x$:H films. Appl Phys Lett 1991;58:741–3.
[523] Brongersma ML, Polman A, Min KS, Boer E, Tambo T, Atwater HA. Tuning the emission wavelength of Si nanocrystals in $SiO_2$ by oxidation. Appl Phys Lett 1998;72:2577–9.

[524] Nogami N, Suzuki S, Nagasaka K. Sol–gel processing of small-sized CdSe crystal-doped silica glasses. J Non-Cryst Solids 1991;135:182–8.
[525] Bawendi MG, Carroll PJ, Wilson WL, Brus LE. Luminescence properties of CdSe quantum crystallites: resonance between interior and surface localized states. J Chem Phys 1992;96:946–54.
[526] Katari JEB, Colvin VL, Alivisatos AP. X-ray photoelectron spectroscopy of CdSe nanocrystals with applications to studies of the nanocrystal surface. J Phys Chem 1994;98:4109–17.
[527] Hoheisel W, Colvin VL, Johnson CS, Alivisatos AP. Threshold for quasicontinuum absorption and reduced luminescence efficiency in CdSe nanocrystals. J Chem Phys 1994;101:8455–60.
[528] Alivisatos AP, Harris RD, Brus LE, Jayaraman A. Resonance Raman scattering and optical absorption studies of CdSe microclusters at high pressure. J Chem Phys 1988;89:5979–82.
[529] Micic OI, Cheong HM, Fu H, Zunger A, Sprague JR, Mascarenhas A, et al. Size-dependent spectroscopy of InP quantum dots. J Phys Chem B 1997;101:4904–12.
[530] Micic OI, Jones KM, Cahill A, Nozik AJ. Optical, electronic, and structural properties of uncoupled and close-packed arrays of InP quantum dots. J Phys Chem B 1998;102:9791–6.
[531] Sapra S, Viswanatha R, Sarma DD. An accurate description of quantum size effects in InP nanocrystallites over a wide range of sizes. J Phys D 2003;36:1595–8.
[532] Xu CX, Sun XW, Zhang XH, Ke L, Chua SJ. Photoluminescent properties of copper-doped zinc oxide nanowires. Nanotechnology 2004;15:856–61.
[533] Sun CQ, Sun XW, Gong HQ, Huang H, Ye H, Jin D, et al. Frequency shift in the photoluminescence of nanometric $SiO_x$: surface bond contraction and oxidation. J Phys Condens Matt 1999;11:L547–50.
[534] Katz D, Wizansky T, Millo O, Rothenberg E, Mokari T, Banin U. Size-dependent tunneling and optical spectroscopy of CdSe quantum rods. Phys Rev Lett 2002;89:086801.
[535] Borgohain K, Singh JB, Rao MVR, Shripathi T, Mahamuni S. Quantum size effects in CuO nanoparticles. Phys Rev B 2000;61:11093–6.
[536] Phillips WD. Laser cooling and trapping of neutral atoms. Rev Mod Phys 1998;70:721–41.
[537] Balasubramanian T, Andersen JN, Wallden L. Surface-bulk core-level splitting in graphite. Phys Rev B 2001;64:205420.
[538] Aldén M, Skriver HL, Johansson B. Ab initio surface core-level shifts and surface segregation energies. Phys Rev Lett 1993;71:2449–52.
[539] Navas EE, Starke K, Laubschat C, Weschke E, Kaindl D. Surface core-level shift of 4f states for Tb(0001). Phys Rev B 1993;48:14753–5.
[540] Bartynski RA, Heskett D, Garrison K, Watson G, Zehner DM, Mei WN, et al. The first interlayer spacing of Ta(100) determined by photoelectron diffraction. J Vac Sci Technol A 1989;7:1931–6.
[541] Andersen JN, Hennig D, Lundgren E, Methfessel M, Nyholm R, Scheffler M. Surface core-level shifts of some 4d-metal single-crystal surfaces: experiments and ab initio calculations. Phys Rev B 1994;50: 17525–33.
[542] Riffe DM, Wertheim GK. Ta(110) surface and subsurface core-level shifts and 4f7/2 line shapes. Phys Rev B 1993;47:6672–9.
[543] Cho JH, Kim KS, Lee SH, Kang MH, Zhang Z. Origin of contrasting surface core-level shifts at the Be(10 -10) and Mg(10-1 0) surfaces. Phys Rev B 2000;61:9975–8.
[544] Fedorov AV, Arenholz E, Starke K, Navas E, Baumgarten L, Laubschat C, et al. Surface shifts of 4f electron-addition and electron-removal states in Gd(0001). Phys Rev Lett 1994;73:601–4.
[545] Johansson LI, Johansson HI, Andersen JN, Lundgren E, Nyholm R. Three surface-shifted core levels on Be(0001). Phys Rev Lett 1993;71:2453–6.
[546] Lizzit S, Pohl K, Baraldi A, Comelli G, Fritzsche V, Plummer EW, et al. Physics of the Be(10-10) surface core level spectrum. Phys Rev Lett 1998;81:3271–4.
[547] Johansson HIP, Johansson LI, Lundgren E, Andersen JN, Nyholm R. Core-level shifts on Be(10-10). Phys Rev B 1994;49:17460–3.
[548] Baraldi A, Lizzit S, Comelli G, Goldoni A, Hofmann P, Paolucci G. Core-level subsurface shifted component in a 4d transition metal: Ru(1010). Phys Rev B 2000;61:4534–7.
[549] Lunsgren E, Johansson U, Nyholm R, Anderson JN. Surface core-level shift of the Mo(110) surface. Phys Rev B 1993;48:5525–9.
[550] Nyholm R, Andersen JN, van Acker JF, Qvarford M. Surface core-level shifts of the Al(100) and Al(111) surfaces. Phys Rev B 1991;44:10987–90.
[551] Riffe DM, Kim B, Erskine JL, Shinn ND. Surface core-level shifts and atomic coordination at a stepped W(110) surface. Phys Rev B 1994;50:14481–8.

[552] Cho JH, Oh DH, Kleinman L. Core-level shifts of low coordination atoms at the W(320) stepped surface. Phys Rev B 2001;64:115404.
[553] Karlsson CK, Landemark E, Chao YC, Uhrberg RIG. Atomic origins of the surface components in the Si 2p core-level spectra of the Si(111)7 × 7 surface. Phys Rev B 1994;50:5767–70.
[554] Scholz SM, Jacobi K. Core-level shifts on clean and adsorbate-covered Si(113) surfaces. Phys Rev B 1995;52:5795–802.
[555] Pi TW, Wen JF, Ouyang CP, Wu RT. Surface core-level shifts of Ge(100)-2×1. Phys Rev B 2001;63:153310.
[556] Lizzit S, Baraldi A, Groso A, Reuter K, Ganduglia-Pirovano MV, Stampfl C, et al. Surface core-level shifts of clean and oxygen-covered Ru(0001). Phys Rev B 2001;B63:205419.
[557] Glans PA, Johansson LI, Balasubramanian T, Blake RJ. Assignment of the surface core-level shifts to the surface layers of Be(10-10). Phys Rev B 2004;70:033408.
[558] Zacchigna M, Astaldi C, Prince K, Sastry M, Comicioli C, Rosei R, et al. Photoemission from atomic and molecular adsorbates on Rh(100). Surf Sci 1996;347:53–62.
[559] Ohgi T, Fujita D. Consistent size dependency of core-level binding energy shifts and single-electron tunneling effects in supported gold nanoclusters. Phys Rev B 2002;66:115410.
[560] Nanda J, Kuruvilla A, Sarma DD. Photoelectron spectroscopic study of CdS nanocrystallites. Phys Rev B 1999;B59:7473–9.
[561] Sun CQ, Pan LK, Bai HL, Li ZQ, Wu P, Jiang EY, Effects of surface passivation and interfacial reaction on the size-dependent 2p-level shift of supported copper nanosolids. Acta Mater 2003;51:4631–6.
[562] Yang DQ, Sacher E. Initial- and final-state effects on metal cluster/substrate interactions, as determined by XPS: copper clusters on Dow Cyclotene and highly oriented pyrolytic graphite. Appl Surf Sci 2002;195: 187–95.
[563] Howard A, Clark DNS, Mitchell CEJ, Egdell RG, Dhanak VR. Initial and final state effects in photoemission from Au nanoclusters on $TiO_2$(110). Surf Sci 2002;518:210–24.
[564] Salmon M, Ferrer S, Jazzar M, Somojai GA. Core- and valence-band energy-level shifts in small two-dimensional islands of gold deposited on Pt(100): the effect of step-edge, surface, and bulk atoms. Phys Rev B 1983;28:1158–60.
[565] Vijayakrishnan VA, Chainani A, Sarma DD, Rao CNR. Metal–insulator-transitions in metal clusters. A high-energy spectroscopy study of Pd and Ag clusters. J Phys Chem 1992;96:8679–82.
[566] Mason MG. In: Pacchioni G, editor. Cluster models for surface and bulk phenomena. New York: Plenum; 1992.
[567] Boyen HG, Herzog T, Kastle G, Weigl F, Ziemann P, Spatz JP, et al. X-ray photoelectron spectroscopy study on gold nanoparticles supported on diamond. Phy Rev B 2002;65:075412.
[568] Yang ZN, Wu R. Origin of positive core-level shifts in Au clusters on oxides. Phys Rev B 2003;67:081403.
[569] Egelhoff Jr WF, Tibbetts GG. Growth of copper, nickel, and palladium films on graphite and amorphous carbon. Phys Rev B 1979;19:5028–35.
[570] Sun CQ. Atomic-coordination-imperfection-enhanced Pd-3d5/2 crystal binding energy. Surf Rev Lett 2003;10:1009–13.
[571] Kästle G, Boyen HG, Schröder A, Plettl A, Ziemann P. Size effect of the resistivity of thin epitaxial gold films. Phys Rev B 2004;70:165414.
[572] Reif M, Glaser L, Martins M, Wurth W. Size-dependent properties of small deposited chromium clusters by x-ray absorption spectroscopy. Phys Rev B 2005;72:155405.
[573] Amaratunga GAJ, Silva SRP. Nitrogen containing hydrogenated amorphous carbon for thin-film field emission cathodes. Appl Phys Lett 1996;68:2529–31.
[574] Pickett WE. Negative electron affinity and low work function surface Cesium on oxygenated diamond (100). Phys Rev Lett 1994;73:1664–7.
[575] Lin LW. The role of oxygen and fluorine in the electron emission of some kinds of cathodes. J Vac Sci Technol A 1998;6:1053–7.
[576] Xu CX, Sun XW. Field emission from zinc oxide nanopins. Appl Phys Lett 2003;83:3806–8.
[577] Xu CX, Sun XW, Chen BJ. Field emission from gallium-doped zinc oxide nanofiber array. Appl Phys Lett 2004;84:1540–2.
[578] Wadhawan A, Stallcup RE, Stephens KF, Perez JM, Akwani IA. Effects of $O_2$, Ar, and $H_2$ gases on the field-emission properties of single-walled and multiwalled carbon nanotubes. Appl Phys Lett 2001;79:1867–9.
[579] Zheng WT, Li JJ, Wang X, Li XT, Jin ZS, Tay BK, et al. Mechanism for the nitrogen-lowered threshold in carbon nitride cold-cathode. J Appl Phys 2003;94:2741–5.
[580] Abbott P, Sosa ED, Golden DE. Effect of average grain size on the work function of diamond films. Appl Phys Lett 2001;79:2835–7.

[581] Yamauchi T, Tabuchi M, Nakamura A. Size dependence of the work function in InAs quantum dots on GaAs(001) as studied by Kelvin force probe microscopy. Appl Phys Lett 2004;84(19):3834–6.
[582] Kappes MM, Kunz RW, Schuhmacher E. Production of large sodium clusters (NAX,X less-than 65) by seeded beam expansions. Chem Phys Lett 1982;91:413–8.
[583] Bhave TM, Bhoraskar SV. Surface work function studies in porous silicon. J Vac Sci Technol B 1998;16:2073–8.
[584] Tzeng Y, Liu C, Hirata A. Effects of oxygen and hydrogen on electron field emission from microwave plasma chemically vapor deposited microcrystalline diamond, nanocrystalline diamond, and glassy carbon coatings. Diamond Rel Mater 2003;12:456–63.
[585] Gao R, Pan Z, Wang ZL. Work function at the tips of multiwalled carbon nanotubes. Appl Phys Lett 2001;78:1757–9.
[586] Li H, Wang X, Song Y, Liu Y, Li Q, Jiang L, et al. Super-amphiphobic aligned carbon nanotube films. Angew Chem Int Ed Engl 2001;40:1743–6.
[587] Feng L, Li S, Li H, Zhai J, Song Y, Jiang L, et al. Super-hydrophobic surface of aligned polyacrylonitrile nanofibers. Angew Chem Int Ed Engl 2002;41:1221–3.
[588] Sun T, Wang G, Feng L, Liu B, Ma Y, Jiang L, et al. Reversible switching between superhydrophilicity and superhydrophobicity. Angew Chem Int Ed Engl 2004;43:357–60.
[589] Feng X, Feng L, Jin M, Zhai J, Jiang L, Zhu D. Reversible super-hydrophobicity to super-hydrophilicity transition of aligned ZnO nanorod films. J Am Chem Soc 2004;126:62–3.
[590] Sun CQ. Time-resolved VLEED from the O–Cu(001): atomic processes of oxidation. Vacuum 1997;48:525–30.
[591] Poa CHP, Lacerda RG, Cox DC, Marques FC, Silva SRP. Effects of stress on electron emission from nanostructured carbon materials. J Vac Sci Technol B 2003;21:1710–4.
[592] Uher C, Hockey RL, Ben-Jacob E. Pressure dependence of the *c*-axis resistivity of graphite. Phys Rev B 1987;35:4483–8.
[593] Poa CHP, Smith RC, Silva SRP, Sun CQ. Influence of mechanical stress on electron field emission of multiwalled carbon nanotube-polymer composites. J Vac Sci Technol B 2005;B 23:698–701.
[594] Lacerda RG, dos Santos MC, Tessler LR, Hammer P, Alvarez F, Marques FC. Pressure-induced physical changes of noble gases implanted in highly stressed amorphous carbon films. Phys Rev B 2003;68:054104.
[595] Lynch RW, Drickamer HG. Effect of high pressure on the lattice parameters of diamond, graphite, and hexagonal boron nitride. J Chem Phys 1966;44:181–4.
[596] Bhattacharyya S, Subramanyam SV. Metallic conductivity of amorphous carbon films under high pressure. Appl Phys Lett 1997;71:632–4.
[597] Umemoto K, Saito S, Berber S, Tomanek D. Carbon foam: spanning the phase space between graphite and diamond. Phys Rev B 2001;64:193409.
[598] Walter JP, Cohen ML. Wave-vector-dependent dielectric function for Si, Ge, GaAs, and ZnSe. Phys Rev B 1970;2:1821–6.
[599] Deger D, Ulutas K. Conduction and dielectric polarization in Se thin films. Vacuum 2003;72:307–12.
[600] Alpay SP, Misirlioglu IB, Nagarajan V, Ramesh R. Can interface dislocations degrade ferroelectric properties? Appl Phys Lett 2004;85:2044–6.
[601] Penn DR. Wave-number-dependent dielectric function of semiconductors. Phys Rev 1962;128:2093–7.
[602] Tsu R, Babic D. Doping of a quantum dot. Appl Phys Lett 1994;64:1806–8.
[603] Chen TP, Liu Y, Tse MS, Tan OK, Ho PF, Liu KY, et al. Dielectric functions of Si nanocrystals embedded in a $SiO_2$ matrix. Phys Rev B 2003;68:153301.
[604] Chen TP, Liu Y, Tse MS, Ho PF, Dong G, Fung S. Depth profiling of Si nanocrystals in Si-implanted $SiO_2$ films by spectroscopic ellipsometry. Appl Phys Lett 2002;81:4724–6.
[605] Hens Z, Vanmaekelbergh D, Kooij ES, Wormeester H, Allan G, Delerue C. Effect of quantum confinement on the dielectric function of PbSe. Phys Rev Lett 2004;92:026808.
[606] Delerue C, Lannoo M, Allan G. Concept of dielectric constant for nanosized systems. Phys Rev B 2003;68:115411–4.
[607] Cartoixà X, Wang L-W. Microscopic dielectric response functions in semiconductor quantum dots. Phys Rev Lett 2005;94:236804.
[608] Winn H. Quantum dot may be more ‘‘superficial’’ than first thought. SPIE OE Magazine 2005;8:10.
[609] Drachev VP, Buin AK, Nakotte H, Shalaev VM. Size-dependent $\chi(3)$ for conduction electrons in Ag nanoparticles. Nano Lett 2004;4:1535–9.
[610] Lannoo M, Delerue C, Allan G. Screening in semiconductor nanocrystallites and its consequences for porous silicon. Phys Rev Lett 1995;74:3415–8.

[611] Greenway DL, Harbeke G. Optical properties and band structure of semiconductors. New York: Pergamon Press; 1968.
[612] Pan LK, Huang HT, Sun CQ. Dielectric transition and relaxation of nanosolid silicon. J Appl Phys 2003;94:2695–700.
[613] Brown FG. The physics of solids. New York: Benjamin Press; 1968.
[614] Blatt FJ. Physics of electronic conduction in solids. New York: McGraw-Hill; 1967.
[615] Macdonald JR. Impedance spectroscopy. New York: Wiley; 1987 [Chapter 4].
[616] Orton JW, Powell MJ. The Hall effect in polycrystalline and powdered semiconductors. Rep Prog Phys 1980;43:1263–307.
[617] Ye HT, Sun CQ, Huang HT, Hing P. Dielectric transition of nanostructured diamond films. Appl Phys Lett 2001;78:1826–8.
[618] Kleitz M, Kennedy JH. Fast ion transport in solids. In: Vashishta P, Mundy JN, Shenoy GK, editors. Noth Holland: Elsevier; 1979. p. 185.
[619] Lanfredi S, Carvalho JF, Hernandes AC. Electric and dielectric properties of $Bi_{12}TiO_{20}$ single crystals. J Appl Phys 2000;88:283–7.
[620] Looyenga H. Dielectric constants of heterogeneous mixtures. Physica 1965;31:401.
[621] Sun XW, Yu SF, Xu CX, Yuen C, Chen BJ, Li S. Room-temperature ultraviolet lasing from zinc oxide microtubes. Jpn J Appl Phys 2003;42:L1229–31.
[622] Zhou J, Zhou Y, Ng SL, Zhang X, Que WX, Lam YL, et al. Three-dimensional photonic band gap structure of a polymer-metal composite. Appl Phys Lett 2000;76:3337–9.
[623] Zhong WH, Sun CQ, Tay BK, Li S, Bai HL, Jiang EY. Curie temperature suppression of ferromagnetic nanosolids. J Phys Condens Mater 2002;14:L399–405.
[624] Sun CQ, Zhong WH, Li S, Tay BK. Coordination imperfection suppressed phase stability of ferromagnetic, ferroelectric, and superconductive nanosolids. J Phys Chem B 2004;108:1080–4.
[625] Tronc E, Noguès M, Chanéac C, Lucari F, D'Orazio F, Grenèche JM, et al. Magnetic properties of $\gamma$-$Fe_2O_3$ dispersed particles: size and matrix effects. J Magn Magn Mater 2004;272–276:1474–5.
[626] Seehra MS, Punnoose A. Particle size dependence of exchange-bias and coercivity in CuO nanoparticles. Solid State Commun 2003;128:299–302.
[627] Zhong WH, Sun CQ, Li S. Size effect on the magnetism of nanocrystalline Ni films at ambient temperature. Solid State Commun 2004;13:603–6.
[628] Li J, Qin Y, Kou X, Huang J. The microstructure and magnetic properties of Ni nanoplatelets. Nanotechnology 2004;15:982–6.
[629] De Heer WA, Milani P, Chatelain A. Spin relaxation in small free iron clusters. Phys Rev Lett 1990;65:488–91.
[630] Guzman M, Delplancke JL, Long CJ, Delwiche J, Hubin-Franskin MJ, Grandjean F. Morphologic and magnetic properties of $Pd_{1-x}Fe_x$ nanoparticles prepared by ultrasound assisted electrochemistry. J Appl Phys 2002;92:2634–60.
[631] Taniyama T, Ohta E, Sato T, Takeda M. Magnetic properties of Pd–29 at% Fe fine particles. Phys Rev B 1997;55:977–82.
[632] Qiang Y, Sabiryanov RF, Jaswal SS, Liu Y, Haberland H, Sellmyer DJ. Manetism of Co nanocluster films. Phys Rev B 2002;66:064404.
[633] Sort J, Dieny B, Fraune M, Koenig C, Lunnebach F, Beschoten B, et al. Perpendicular exchange bias in antiferromagnetic–ferromagnetic nanostructures. Appl Phys Lett 2004;84:3696–8.
[634] Baltz V, Sort J, Rodmacq B, Dieny B, Landis S. Size effects on exchange bias in sub-100 nm ferromagnetic-antiferromagnetic dots deposited on prepatterned substrates. Appl Phys Lett 2004;84:4923–5.
[635] Falicov LM, Pierce DT, Bader SD, Gronsky R, Hathaway KB, Hopster HJ, et al. Surface, interface, and thin-film magnetism. J Mater Res 1990;5:1299–340.
[636] Aguilera-Granja F, Moran-Lepez JL. Ising model of phase transitions in ultrathin films. Solid State Commun 1990;74:155–8.
[637] Chinnasamy CN, Narayanasamy A, Ponpandian N, Chattopadhyay K, Saravanakumar M. Order–disorder studies and magnetic properties of mechanically alloyed nanocrystalline $Ni_3Fe$ alloy. Mater Sci Eng A 2001;304: 408–12.
[638] Cox GM, Trevor DJ, Whetten RL, Rohifing EA, Kaldor A. Magnetic behavior of free-iron and iron oxide clusters. Phys Rev B 1985;32:7290–8.
[639] Bucher JP, Douglas DC, Xia P, Haynes B, Bloomfield LA. Magnetic properties of free cobalt clusters. Phys Rev Lett 1991;66:3052–5.

[640] Billas IML, Becker JA, Chatelain A, de Herr WA. Magnetic moments of iron clusters with 25 to 700 atoms and their dependence on temperature. Phys Rev Lett 1993;71:4067–70.
[641] Ohnishi S, Freeman AJ, Weinert M. Surface magnetism of Fe(001). Phys Rev B 1983;28:6741–8.
[642] Pastor GM, Dorantes-Dvaila J, Bennemann KH. Size and structural dependence of the magnetic properties of small 3d-transition-metal clusters. Phys Rev B 1989;40:7642–54.
[643] Yang CY, Johnson KH, Salahub DR, Kaspar J, Messmer RP. Iron clusters: electronic structure and magnetism. Phys Rev B 1981;24:5673–90.
[644] Billas IML, Chatelain A, De Heer WA. Magnetism from the atom to the bulk in iron, cobalt, and nickel clusters. Science 1994;265:1682–4.
[645] Ney A, Poulopoulos P, Baberschke K. Surface and interface magnetic moments of Co/Cu(001). Europhys Lett 2001;54:820–5.
[646] Konno M. Anomalous thickness dependence of the saturation magnetization in Fe–Ni Invar alloy films. J Phys Soc Jpn 1980;49:1185–6.
[647] Apsel SE, Emmert JW, Deng J, Bloomfield LA. Surface-enhanced magnetism in nickel clusters. Phys Rev Lett 1996;76:1441–4.
[648] Cox AJ, Louderback JG, Apsel SE, Bloomfield LA. Magnetism in 4d-transition metal clusters. Phys Rev B 1994;49:12295–8.
[649] Sumiyama K, Sato T, Graham GM. Thickness dependence of magnetization in Fe–Ni Invar alloy film. Solid State Commun 1976;19:403–4.
[650] Wedler G, Schneck H. Galvanomagnetic and magnetic properties of evaporated thin nickel films: II. Thickness dependence of the Hall coefficients, the magnetoresistivity and the saturation magnetization. Thin Solid Films 1977;47:147–53.
[651] Ohta S, Terada A, Ishii Y, Hattori S. Thickness dependence of magnetic properties and read–write characteristics for iron oxide thin films. Trans Inst Electr Commun Eng Jap 1985;E68:173.
[652] Mukadam MD, Yusuf SM, Sharma P, Kulshreshtha SK. Particle size-dependent magnetic properties of gamma-$Fe_2O_3$ nanoparticles. J Magn Magn Mater 2004;272:1401–3.
[653] Kempter K, Maurer I, Harms H. Saturation magnetization of MnBi films with different thicknesses and composition. Appl Phys 1975;7:7–9.
[654] Manaf A, Buckley RA, Davies HA, Leonowicz M. Enhanced magnetic properties in rapidly solidified Nd–Fe–B based alloys. J Magn Magn Mater 1991;101:360–2.
[655] Shafi KVPM, Gedanken A, Prozorov R, Revesz A, Lendvai J. Preparation and magnetic properties of nanosized amorphous ternary Fe–Ni–Co alloy powders. J Mater Res 2000;15:332–7.
[656] Degauque J, Astié B, Porteseil JL, Vergne R. Influence of the grain size on the magnetic and magnetomechanical properties of high-purity iron. J Magn Magn Mater 1982;26:261–3.
[657] Herzer G. Grain size dependence of coercivity and permeability in nanocrystalline ferromagnets. IEEE Trans Mag 1990;26:1397–402.
[658] Sato F, Tezuka N, Sakurai T, Miyazaki T. Grain diameter and coercivity of Fe, Ni, and Co metals. IEEE Trans Mag Jpn 1994;9:100–6.
[659] Merikoski J, Timonen J, Manninen M. Ferromagnetism in small clusters. Phys Rev Lett 1991;66:938–41.
[660] Liu F, Press MR, Khanna SN, Jena P. Magnetism and local order: ab initio tight-binding theory. Phys Rev B 1989;39:6914–24.
[661] Jensen PJ, Bennemann KH. Theory for the atomic chshell structure of the cluster magnetic-moment and magnetoresistance of a cluster ensemble. Z Phys D 1995;35:273–8.
[662] Aguilera-Granja F, Montejano-Carrizales JM, Morán-López JL. Magnetic moments of iron clusters: a simple theoretical model. Phys Lett 1998;A242:255–60.
[663] Zhao J, Chen X, Sun Q, Liu E, Wang G. A simple d-band model for the magnetic property of ferromagnetic transition-metal clusters. Phys Lett A 1995;205:308–12.
[664] Montejano-Carrizales JM, Aguilera-Granja F, Moran-Lσpez JL. Direct enumeration of the geometrical characteristics of clusters. Nanostruct Mater 1997;8:269–87.
[665] Han DH, Wang JP, Luo HL. Crystallite size effect on saturation magnetization of fine ferrimagnetic particles. J Magn Mang Mater 1994;136:176–82.
[666] Lopez M, Marin P, Kulik T, Hernando A. Influence of measuring temperature in size dependence of coercivity in nano structured alloys. J Magn Magn Mater Apr 2005;290:171–4.
[667] Khanna SN, Linderoth S. Magnetic behavior of clusters of ferromagnetic transition metals. Phys Rev Lett 1991;67:742–5.
[668] Alben R, Becker JJ, Chi MC. Random anisotropy in amorphous ferromagnets. J Appl Phys 1978;49:1653–8.

[669] Sangregorio C, Ohm T, Paulsen C, Sessoli T, Gatteschi D. Quantum tunneling of the magnetization in an iron cluster nanomagnet. Phys Rev Lett 1997;78:4645–8.
[670] Dai DS, Qian KS. Ferromagnetism. Beijing: Sci Press; 2000.
[671] Metropolis N, Rosenbluth AW, Rosenbluth MH, Teller A, Teller E. Equation of state calculations by fast computing machines. J Chem Phys 1953;21:1087–92.
[672] Sakurai M, Watanabe K, Sumiyama K, Suzuki K. Magic numbers in transition metal (Fe, Ti, Zr, Nb, and Ta) clusters observed by time-of-flight mass spectrometry. J Chem Phys 1999;111:235–8.
[673] Reinhard D. Size-dependent icosahedral-to-fcc structure change confirmed in unsupported nanometer-sized copper clusters. Phys Rev Lett 1997;79:1459–62.
[674] Du Y, Wu J, Lu H, Wang T, Qiu ZQ, Tang H, et al. Magnetic properties of fine iron particles. J Appl Phys 1987;61:3314–6.
[675] Gangopadhyay S, Hahjipanayis GC, Sorensen CM, Klabunde KJ. Magnetic properties of ultrafine Co particles. IEEE Trans Magn 1992;28:3174–6.
[676] Sánchez RD, Rivas J, Vaqueiro P, López-Quintela MA, Caeiro D. Particle size effects on magnetic garnets prepared by a properties of yttrium iron sol–gel method. J Magn Magn Mater 2002;247:92–8.
[677] Sun CQ, Li S, Tay BK. Laser-like mechanoluminescence in ZnMnTe-diluted magnetic semiconductor. Appl Phys Lett 2003;82:3568–9.
[678] Sun CQ. The lattice contraction of nanometersized Sn and Bi particles. J Phys Condens Matter 1999;11:4801–3.
[679] Zeng XT, Zhang S, Sun CQ, Liu YC. Nanometric-layered CrN/TiN thin films: mechanical strength and thermal stability. Thin Solid Films 2003;424:99–102.
[680] Pan LK, Sun CQ, Chen TP, Li S, Li CM, Tay BK. Dielectric suppression of nanosolid silicon. Nanotechnology 2004;15:1802–6.
[681] Pan LK, Ee YK, Sun CQ, Yu GQ, Zhang QY, Tay BK. Band-gap expansion, core-level shift and dielectric suppression of porous Si passivated by plasma fluorination. J Vac Sci Technol B 2004;22:583–7.
[682] Sun CQ, Tay BK, Fu YQ, Li S, Chen TP, Bai HL, et al. Discriminating crystal bonding from the atomic trapping of a core electron at energy levels shifted by surface relaxation or nanosolid formation. J Phys Chem B 2003;107:L411–4.
[683] Sun CQ, Pan LK, Li CM, Li S. Size-induced acoustic hardening and optic softening of phonons in CdS, InP, $CeO_2$, $SnO_2$, and Si nanostructures. Phys Rev B 2005;72:134301.
[684] Pan LK, Sun CQ, Li CM. Estimating the extent of surface oxidation by measuring the porosity dependent dielectrics of oxygenated porous silicon. Appl Surf Sci 2005;240:19–23.
[685] Pan LK, Sun CQ, Yu GQ, Zhang QY, Fu YQ, Tay BK. Distinguishing the effect of surface passivation from the effect of size on the photonic and electronic behavior of porous silicon. J App Phys 2004;96:1074–5.
[686] Sun CQ, Bai HL, Li S, Tay BK, Jiang EY. Size effect on the electronic structure and the thermal stability of a gold nanosolid. Acta Mater 2004;52:501–5.
[687] Sun CQ, Bai HL, Li S, Tay BK, Li CM, Chen TP, et al. Length, strength, extensibility and thermal stability of an Au–Au bond in the gold monatomic chain. J Phys Chem B 2004;108:2162–7.
[688] Zheng B, Zheng WT, Yu SS, Tian HW, Meng FL, Wang YM, et al. Growth of tetrahedral amorphous carbon film: tight-binding MD study. Carbon 2005;43:1976–83.
[689] Zhang Y, Sun H, Chen C. Superhard cubic $BC_2N$ compared to diamond. Phys Rev Lett 2004;93:195504.